

DTIC FILE COPY

(2)

CSM MT-CWR-087-041

AD-A196 834

FINAL REPORT

INVESTIGATION OF HIGH TEMPERATURE DUCTILITY LOSSES IN
ALPHA-BETA TITANIUM ALLOYS

by:

B.K. Damkroger*, B.B. Rath**, and G.R. Edwards*

*Center for Welding and Joining Research
Colorado School of Mines
Golden, Colorado 80401

**Naval Research Laboratory
Materials Science & Component Technology
Washington, DC 20375-5000

DISTRIBUTION STATEMENT A

Approved for public release
Distribution Unlimited

April, 1988

DTIC
ELECTE
JUN 16 1988
S D

CSM



CENTER FOR WELDING RESEARCH
Colorado School of Mines
Golden, Colorado 80401

88 5 05 020

T-3393

INVESTIGATION OF HIGH TEMPERATURE
DUCTILITY LOSSES IN ALPHA-BETA
TITANIUM ALLOYS



Accession For	
NTIS CRA&I	<input checked="checked" type="checkbox"/>
DTIC TAB	<input type="checkbox"/>
Unannounced	<input type="checkbox"/>
Justification	
By <i>ltr. on file</i>	
Distribution/	
Availability Codes	
Dist	Avail and/or Special
<i>A-1</i>	

This Manuscript is the Colorado
School of Mines PhD Thesis of
Mr. Brian K. Damkroger

ABSTRACT

Under certain conditions, alpha-beta titanium alloys can show severely reduced high-temperature ductility. These conditions consist of loading in tension during cooling from a thermal excursion to above the beta transus. A model for this behavior, which relates the ductility loss to the volumetric incompatibility between the beta and alpha lattices during the beta to alpha transformation, has been previously proposed. This model was developed and investigated as part of an overall investigation of the ductility loss with respect to several metallurgical variables. It was found that the high-temperature ductility loss is ubiquitous in alpha-beta titanium alloys, but could not be directly related to lattice incompatibility. It was instead found that the ductility loss resulted from gross localized deformation within a particular microstructural component, lamellar Widmanstatten colonies. *Keynote*
on the same subject as long as the material is in the beta phase
However, the relationship between the colony microconstituent and ductility was found to exist only at high temperature, indicating that the deformation characteristics of the material changed with temperature.

TABLE OF CONTENTS

	<u>Page</u>
ABSTRACT	iii
LIST OF FIGURES	viii
LIST OF TABLES	xvii
ACKNOWLEDGMENTS	ix

SECTION

1. Statement of Problem	1
2. Introduction	5
2.1 General Characteristics of Ti Alloys	5
2.1.1 Alloy Additions and Classification	6
2.1.2 Alpha Alloys	6
2.1.3 Near-Alpha Alloys	10
2.1.4 Alpha-Beta Alloys	11
2.1.5 Metastable Beta Alloys	12
2.2 Microstructures in Alpha-Beta Alloys	13
2.2.1 Prior Beta Grain Shape	13
2.2.2 Transformation Rate	14
2.2.3 Alpha-Beta Interface Phase	16
2.3 Microstructure-Property Correlations	19
2.3.1 Near-Alpha Alloys	19
2.3.2 Alpha-Beta Alloys	21
2.3.3 Failure Modes	22
Overall Fracture Models	23
Void Nucleation	25
Void Growth	28
Summary	32

3.	Elevated Temperature Behavior and Models . . .	34
3.1	Review of Work to Date	34
3.1.1	Lewis and Caplan	34
3.1.2	Starke, et. al.	41
3.1.3	Inouye and David	45
3.1.4	Ushkov	47
3.1.5	Krishnamohanrao, et. al.	50
3.1.6	CSM Welding Research	54
3.1.7	Summary	63
3.2	Analysis of Existing Models	64
3.2.1	Solute Partitioning	64
3.2.2	Differential Strength	68
3.2.3	Summary	72
3.3	Lattice Incompatibility Model	73
4.	Experimental Procedure	84
4.1	Initial Screening Tests	85
4.1.1	Annealing Time and Temperature	85
4.1.2	Effective Strain Rate	89
4.1.3	Results of Initial Tests	94
4.2	CCT Diagram Development	94
4.3	Lattice Incompatibility Measurements	102
4.3.1	X-Ray Diffraction	103
	Specimen Loading Correction	109
	Systematic Error Correction	113
4.3.2	Lattice Incompatibility	114
4.4	Hot Ductility Testing	118
4.5	Microstructural Analysis	121

5.	Results and Discussion	123
5.1	Phase Stability and Transformations . . .	124
5.1.1	CCT Diagrams	126
	Aluminum Additions	147
	Beta Stabilizer Elements	148
5.1.2	Microstructures	151
	Cooling Rate Effect	151
	Alloy Effects	156
5.1.3	Overall Transformation Mechanism .	156
5.1.4	Transformation Kinetics Model . .	161
	Widmanstätten Colony Growth . .	163
	Grain Boundary Allotriomorph . .	163
	Basketweave Widmanstätten . . .	165
	Additivity Principle	165
	Calibration to Ti-6Al-4V	170
	Effects of System Changes	171
5.1.5	Rabbit Ears Martensite	184
5.2	Lattice Incompatibility	189
5.2.1	Lattice Parameter Measurements . .	192
	Overall General Trends	198
	Alloy Effects	213
	Summary	224
5.2.2	High Speed Dilatometry	225
5.2.3	Lattice Incompatibility	232
	Beta to Alpha	232
	Beta to Widmanstätten Colonies .	236
5.2.4	Summary of Lattice Incompatibility Calculations .	241
5.3	High Temperature Ductility	244
5.3.1	Effect of Alloy Content.	245
5.3.2	Effect of Lattice Incompatibility	279

5.3.3	Microstructural Effects	288
	Prior Beta Grain Size	291
	Grain Boundary Alpha Thickness	294
	Widmanstatten Colony Structure	296
	Alpha Prime Martensite	316
5.4	Deformation of the Colony Structure	321
5.5	Overall Deformation Behavior	324
6.	Summary and Conclusions	331
7.	Future Work	335
	
	LIST OF REFERENCES	337
	APPENDICES	
A.	In-Situ Measurements of Transformation Kinetics Using Neutron Diffraction	350
B.	Lattice Parameter Measurements Made Using Synchrotron Radiation and Neutron Diffraction	363
C.	X-Ray Diffraction Data Processing Methods and BASIC Computer Programs	369
D.	Errors Involved in Lattice Incompatibility Measurements and Calculations	386

LIST OF FIGURES

<u>Figure</u>	<u>Page</u>
1.1 Hot Ductility Testing Results of Lewis and Caplan (6)	3
2.1 Schematic Binary Phase Diagram for an Alpha-Stabilized Titanium Alloy System	7
2.2 Schematic Binary Phase Diagram for a Beta-Stabilized Titanium Alloy System	8
2.3 Micrographs of Ti-6Al-2Mo Cooled at four Different Cooling Rates	15
3.1 Ti-6211 Ductility Map of Lewis (49)	36
3.2 Net Section Strength Versus Temperature Data of Lewis (6)	38
3.3 Lewis (49) Ductility Map and Vareststraint Test Results	40
3.4 Ductility Versus Temperature Results of Ushkov (59)	48
3.5 Unalloyed Titanium and Ti-6Al-4V Fracture Maps of Rao, et. al. (60, 61)	51
3.6 Macrographs of Vareststraint Weld Cracks (63).	56
3.7 Fractographs of Vareststraint Weld Cracks (63)	57
3.8 Micrographs of Ti-6211, Region Adjacent to Vareststraint Weld Cracks (63).	58
3.9 Micrographs of Ti-6Al-4V Weld Fusion and Heat-Affected Zones (63)	60
3.10 Affects of Oxygen and Nitrogen Additions on the Vareststraint Weld Cracking of Ti-6211 (64)	61
3.11 Schematic of the Differential Strength Model of Starke, et. al. (55)	65

<u>Figure</u>	<u>Page</u>
3.12 Schematic of the Solute Partitioning Model of Lewis, et. al. (6)	69
3.13 Ti-6211 Dilatometric Curve	74
3.14 Schematic of the Lattice Incompatibility Model of Rath (70)	75
3.15 Lattice Parameter Data on Binary Titanium Alloys, Compiled by Pearson (71)	77
4.1 Gleeble Specimen Configuration	91
4.2 Thermal Gradient Present in Gleeble Specimens Tested at High Temperature	92
4.3 Percent Reduction in Area Versus Temperature for Ti-6211, Ti-6Al-4V, and Ti-6Al-2V-2Zr, Cooled at 10°C/s	95
4.4 Gleeble Radial Dilatometry Fixture	99
4.5 Continuous Cooling Transformation (CCT) Diagram of Ti-6211	101
4.6 High-Temperature X-Ray Diffraction Specimen Configurations	106
4.7 High-Temperature X-Ray Diffraction Specimen Holder and Chamber	108
4.8 Ti-6211 Dilatometry Trace, Including Size Versus Temperature Calculations	116
4.9 Schematic Illustrating the Calculation of Lattice Incompatibility	117
5.1 Partial CCT Diagram of Grade 2 Unalloyed Titanium	127
5.2 Partial CCT Diagram of Ti-6Al	128
5.3 Partial CCT Diagram of Ti-6Al-2V	129
5.4 Partial CCT Diagram of Ti-6Al-4V	130

<u>Figure</u>	<u>Page</u>
5.5 Partial CCT Diagram of Ti-6Al-6V	131
5.6 Partial CCT Diagram of Ti-6Al-2Mo	132
5.7 Partial CCT Diagram of Ti-6Al-4Mo	133
5.8 Partial CCT Diagram of Ti-6Al-6Mo	134
5.9 Partial CCT Diagram of Ti-6Al-2Nb	135
5.10 Partial CCT Diagram of Ti-6Al-4Nb	136
5.11 Partial CCT Diagram of Ti-6Al-6Nb	137
5.12 Partial CCT Diagram of Ti-6Al-2V-2Nb	138
5.13 Partial CCT Diagram of Ti-6211	139
5.14 Micrographs of Ti-6Al-2V, Ti-6Al-4V, Ti-6Al-6V and Ti-6211, Cooled at 10°C/s	142
5.15 Psuedo-Binary Phase Diagrams for the Systems Ti-6Al-V, Ti-6Al-Mo, and Ti-6Al-Nb	143
5.16 Titanium-Aluminum Binary Phase Diagram (S)	146
5.17 Micrographs of Ti-6211, As-Received and After Cooling at Three Different Rates	152
5.18 Micrographs of Ti-6Al-2V, Cooled at Four Different Rates	153
5.19 Micrographs of Ti-6Al-6V, Cooled at Four Different Rates	154
5.20 Titanium-Aluminum-Vanadium Ternary Phase Diagram (M)	155
5.21 Volume Percent Transformed Versus Temperature for Model Alloy BKD-007	172

<u>Figure</u>	<u>Page</u>
5.22 Transformation Rates for Colony and Basketweave Microconstituents, Model Alloy 3KD-007	173
5.23 Volume Percent Basketweave Microconstituent Versus Cooling Rate for Model Alloys BKD-005, BKD-007, and BKD-009	175
5.24 Predicted Transformation Temperatures for Model Alloys BKD-005, BKD-007, and BKD-009, Superimposed on the CCT Diagrams of Ti-6Al-2V, Ti-6Al-4V, and Ti-6Al-6V	177
5.25 Micrographs of Ti-6211, Cooled at 20°C/s	185
5.26 Micrographs of Ti-6Al-4Nb, Cooled at 50°C/s	186
5.27 Micrographs of Ti-6Al-2Mo, Cooled at 50°C/s	187
5.28 Micrograph of Ti-6Al-2Mo, Cooled at 10°C/s	190
5.29 Lattice Volume Versus Temperature for Grade 2 Unalloyed Titanium	199
5.30 Lattice Volume Versus Temperature for Ti-6Al	200
5.31 Lattice Volume Versus Temperature for Ti-6Al-2V	201
5.32 Lattice Volume Versus Temperature for Ti-6Al-4V	202
5.33 Lattice Volume Versus Temperature for Ti-6Al-6V	203
5.34 Lattice Volume Versus Temperature for Ti-6Al-2Mo	204
5.35 Lattice Volume Versus Temperature for Ti-6Al-4Mo	205

<u>Figure</u>	<u>Page</u>
5.36 Lattice Volume Versus Temperature for Ti-6Al-6Mo	206
5.37 Lattice Volume Versus Temperature for Ti-6Al-2Nb	207
5.38 Lattice Volume Versus Temperature for Ti-6Al-4Nb	208
5.39 Lattice Volume Versus Temperature for Ti-6Al-6Nb	209
5.40 Lattice Volume Versus Temperature for Ti-6211	210
5.41 Lattice Volume Versus Temperature for Ti-6Al-2V-2Nb	211
5.42 Lattice Volume Versus Temperature of Ti-6Al-4V Beta Phase, Illustrating the Effect of Composition on Lattice Volume	214
5.43 Lattice Volume Versus Temperature Summary Curves for the Alpha Phase of Several Alloys	215
5.44 Lattice Volume Versus Temperature Summary Curves for the Beta Phase of the Alloys Tested	218
5.45 Lattice Volume Versus Temperature Summary Curves for the Beta Phase of Alloys Containing 4% Beta Stabilizer	219
5.46 Lattice Volume Versus Temperature Summary Curves for Vanadium Containing Alloys	221
5.47 Lattice Volume Versus Temperature Summary Curves for Niobium Containing Alloys	222
5.48 Lattice Volume Versus Temperature Summary Curves for Molybdenum Containing Alloys	223
5.49 Beta Phase Dilatometry Curves for Several Alloys Cooled At 10°C/s	228

<u>Figure</u>	<u>Page</u>
5.50 Beta Phase Dilatometry Curves for Vanadium Containing Alloys, Cooled at 10°C/s	230
5.51 Beta Phase Dilatometry Curves for Ti-6Al-4V, Cooled at Different Rates	231
5.52 Schematic Illustrating the Lattice Incompatibility Calculation Procedure	234
5.53 Schematic Illustrating High-Temperature Ductility Loss Behavior	246
5.54 Ductility Versus Temperature for Grade 2 Unalloyed Titanium	247
5.55 Ductility Versus Temperature for Ti-6Al	248
5.56 Ductility Versus Temperature for Ti-6Al-2V	249
5.57 Ductility Versus Temperature for Ti-6Al-4V	250
5.58 Ductility Versus Temperature for Ti-6Al-6V	251
5.59 Ductility Versus Temperature for Ti-6Al-4Nb	252
5.60 Ductility Versus Temperature for Ti-6Al-2V-2Nb	253
5.61 Ductility Versus Temperature for Ti-6211	254
5.62 Schematic Illustrating Procedure for Calculation of Net Ductility Loss	258
5.63 Minimum Hot Ductility Versus Cooling Rate for All Alloys Tested	261
5.64 Net Ductility Loss Versus Cooling Rate for All Alloys Tested	251
5.65 Ultimate Tensile Strength (UTS) Versus Temperature for Grade 2 Unalloyed Titanium	266
5.66 UTS Versus Temperature for Ti-6Al	267

<u>Figure</u>	<u>Page</u>
5.67 UTS Versus Temperature for Ti-6Al-2V	268
5.68 UTS Versus Temperature for Ti-6Al-4V	269
5.69 UTS Versus Temperature for Ti-6Al-6V	270
5.70 UTS Versus Temperature for Ti-6Al-4Nb	271
5.71 UTS Versus Temperature for Ti-6Al-2V-2Nb	272
5.72 UTS Versus Temperature for Ti-6211	273
5.73 UTS Versus Temperature Summary Curves for All Alloys Tested, Cooled at 10°C/s	275
5.74 UTS Versus Temperature Summary Curves for Vanadium Containing Alloys Cooled at Rates Chosen to Produce Microstructural Similarity	277
5.75 Minimum Hot Ductility Versus Beta to Alpha Lattice Incompatibility	280
5.76 Net Ductility Loss Versus Beta to Alpha Lattice Incompatibility	281
5.77 Minimum Hot Ductility Versus Beta to Colony Lattice Incompatibility	283
5.78 Net Ductility Loss Versus Beta to Colony Lattice Incompatibility	284
5.79 Ductility Versus Temperature for Ti-6Al-2V Samples with Different Prior Beta Grain Sizes	292
5.80 Net Ductility Loss for Ti-6211 Samples with Different Prior Beta Grain Sizes	293
5.81 Volume Percent Widmanstatten Colony Structure Versus Cooling Rate for All Alloys Tested	300
5.82 Widmanstatten Colony Width Versus Cooling Rate for All Alloys Tested	301

<u>Figure</u>	<u>Page</u>
5.83 Micrographs of Longitudinal Sections of a Failed Ti-6211 Gleeble Specimen	302
5.84 Minimum Hot Ductility Versus Volume Percent Widmanstatten Colony Structure for All Alloys Tested	304
5.85 Net Ductility Loss Versus Volume Percent Widmanstatten Colony Structure for All Alloys Tested	305
5.86 Hall-Petch Plot of Minimum Hot Ductility Versus Widmanstatten Colony Width	310
5.87 Hall-Petch Plot of Net Ductility Loss Versus Widmanstatten Colony Width	311
5.88 True Stress-True Strain Curves for Ti-6Al-2V Tested at 800°C	313
5.88 True Stress-True Strain Curves for Ti-6Al-2V Tested at 100°C	314
5.89 Fractograph and Micrograph of Ti-6211 Martensitic Sample	319
5.90 Fractograph and Micrograph of Ti-6Al-2V Tested at 800°C	320
5.91 Fractographs of Ti-6211, Tested in Martensitic and Non-Martensitic Conditions	321
5.92 True Stress-True Strain Curves for Ti-6211 Tested at 750°C	328
A.1 Experimental Apparatus used in Neutron Diffraction Transformation Kinetics Measurements	354
A.2 Photomicrographs of Ti-6Al-2V and Ti-6Al-6V Cooled at 10°C/s	356
A.3 Beta Phase Diffraction Peaks at Increasing Times Showing Decrease in Intensity as Transformation Proceeds	334

T-3393

<u>Figure</u>	<u>Page</u>
A.4 Relative Integrated Intensity of the Beta Phase Plotted Against Cooling Time from 1200°C	335
A.5 Relative Integrated Intensity of the Beta Phase Plotted Against Temperature	336

LIST OF TABLES

<u>Table</u>	<u>Page</u>
3.1 Test Results of Starke, et. al. (55)	43
4.1 Compositions and Sources of Material Used	86
4.2 Alloy and Test Matrix	96
4.3 Room Temperature Diffraction Peak Positions, Standard Values	110
4.4 X-Ray Diffraction Peak Position Correction Procedure	112
4.5 Cooling Rates Used in Hot Ductility Testing	120
5.1 Transformation Temperatures for All Alloys Tested	140
5.2 Compositional Driving Force Factors for the Systems Ti-6Al-V, Ti-6Al-Nb, and Ti-6Al-Mo	181
5.3 Measured Room Temperature Lattice Parameters of All Alloys Tested	194
5.4 Published Lattice Parameters of Unalloyed Titanium and Ti-5Al	195
5.5 Relative Sample Size at Several Temperatures During Rapid Cooling, Data for Four Alloys	226
5.6 Beta to Alpha Lattice Incompatibility of All Alloys Tested	235
5.7 Beta to Colony Lattice Incompatibility of All Alloys Tested	237
5.8 Minimum Hot Ductility and Net Ductility Loss for All Alloys Tested	259
5.9 Volume Percent Widmanstatten Colony and Colony Width for All Alloys Tested	297

<u>Table</u>	<u>Page</u>
B.1 Lattice Parameter Measurements Made using Synchrotron Radiation (114)	365
B.2 Lattice Parameters Measured Using Neutron Diffraction	366
B.3 Beta Phase Lattice Parameters Measured by X-Ray and Neutron Diffraction	368
C.1 Examples of Lattice Parameters Obtained with Various Data Processing Methods	375
C.2 Published and Measured Peak Positions Compared with Peak Positions Back-Calculated from Lattice Parameters	377
D.1 Examples of Lattice Parameters Obtained with Various Data Combinations and Processing Methods	389

T-3393

ACKNOWLEDGEMENTS

Support for this work was provided by the Office of Naval Research, Contract, No. N0014-80-C-0607. The support and encouragement of Dr. Bruce MacDonald, now at the National Science Foundation, is gratefully acknowledged.

STATEMENT OF PROBLEM

Titanium and its alloys are attractive structural materials because of their high specific strength, elevated-temperature capabilities, and inherent corrosion resistance. Titanium alloys have densities in the range of 4-5 g/cc compared to 2.70 and 7.87 g/cc for aluminum and iron, respectively. Titanium alloys typically have tensile strengths of 80-300 ksi, roughly spanning the range of strengths available in commercial steels and aluminum alloys. The melting point of titanium is 1668°C, above that of iron and aluminum, and its modulus of elasticity is 16.8×10^6 psi, midway between the values for aluminum and iron (1). The high specific properties of alpha-beta and beta titanium alloys have led to their extensive use in the aerospace industry. Unalloyed titanium and alpha titanium alloys have been and are being increasingly used in the food and chemical industries due to their excellent corrosion resistance.

Two classes of titanium alloys, near-alpha and alpha-beta alloys, can be used to great advantage in marine environments. Good corrosion and stress corrosion cracking resistance in salt water environments combined with high specific strength and rigidity make these classes of

titanium alloys promising for such applications (3). However, the use of these alloys in any structural capacity requires that they be fabricated by processes such as hot rolling, forging, and welding, processes which involve a combination of stress and exposure to elevated temperatures. Certain alpha-beta and near-alpha alloys have proven to be susceptible to low-ductility failure under these conditions. This phenomenon has been named and will be referred to as the hot ductility dip. Two common manifestations of this phenomenon are edge cracking during hot rolling and weld cracking (4,5).

Lewis and Caplan experimentally isolated and identified this behavior using Gleeble simulation of GTAW thermal cycles, Figure 1.1 (6). They found that Ti-6Al-4V (Ti-64), Ti-6Al-2Nb-1Ta-0.8Mo (Ti-6211), and Ti-6Al suffered severe drops in ductility when tensile tested at approximately 800°C. This ductility loss only occurred on cooling following a thermal excursion above the beta transus or on heating during a subsequent thermal cycle. Ti-3Al-2.5V and unalloyed titanium had little or no ductility loss, indicating that the hot ductility dip is a function of alloy content. The efficient utilization of these alloys requires that this loss of high-temperature ductility be characterized, and that its causes be defined in terms of

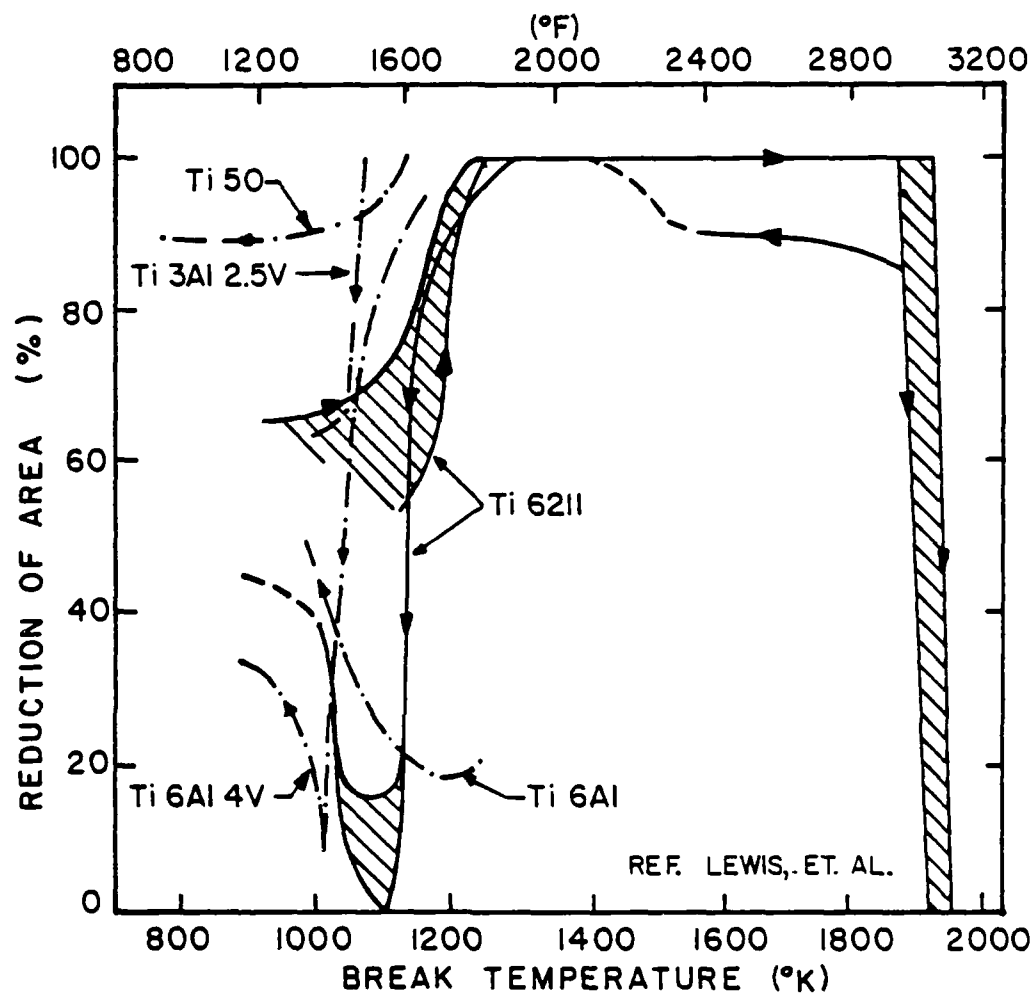


Figure 1.1 High temperature ductility behavior of several titanium alloys showing severe ductility loss in alloys containing 6% aluminum (6).

traditional metallurgical principles so that it can be eliminated.

INTRODUCTION

The introduction of this thesis is designed to function as an overview of the physical metallurgy of titanium alloys in general, and of alpha-beta alloys in particular. This section will consist of three parts. The first sub-section will outline the classification of titanium alloys and describe the general characteristic of each of the major classes of titanium alloys. The second sub-section will discuss the relationships between phase stability, heat treatment, and microstructures in alpha-beta and near-alpha alloys. The third sub-section contains a brief review of several investigations into the microstructure-property relationships in alpha-beta and near-alpha alloys.

2.1 General Characteristics of Titanium Alloys

The physical metallurgy of titanium and titanium alloys is dominated by the allotropic phase transformation between the bcc beta phase which is stable at high temperatures and one or more phases which exist at lower temperatures. Under equilibrium conditions, titanium transforms on cooling from bcc beta to hcp alpha ($c/a = 1.587$) at 883°C . Titanium may also undergo a displacive transformation during rapid cooling to form hexagonal alpha' martensite (1).

2.1.1 Alloy Additions and Alloy Classification

Alloying additions to titanium are classified on the basis of their effect on the stability of either the alpha or beta phase. Aluminum, gallium, germanium, and the interstitials oxygen, carbon and nitrogen stabilize the alpha phase. A schematic binary phase diagram for an alpha-stabilized system is shown in Figure 2.1. Zirconium, tin, and hafnium act primarily as weak alpha stabilizers, but in some cases can be either neutral or weak beta stabilizers depending on the other alloying elements present. Vanadium, molybdenum, tantalum, niobium, chromium, silicon, copper, manganese, cobalt, iron, and hydrogen all act to stabilize the beta phase. Of these, vanadium, tantalum, niobium, and molybdenum are beta-isomorphous elements. Chromium, silicon, copper, manganese, cobalt, iron, and hydrogen are all eutectic formers. A schematic binary phase diagram of a beta-stabilized system is shown in Figure 3 (1, 7). Titanium alloys are classified as either alpha, near-alpha, alpha-beta, or (metastable) beta alloys, depending on the phases present at room temperature when the alloy is in its final form.

2.1.2 Alpha Alloys

Alpha alloys, either unalloyed titanium or binary alloys of titanium and aluminum, tin, or palladium, contain

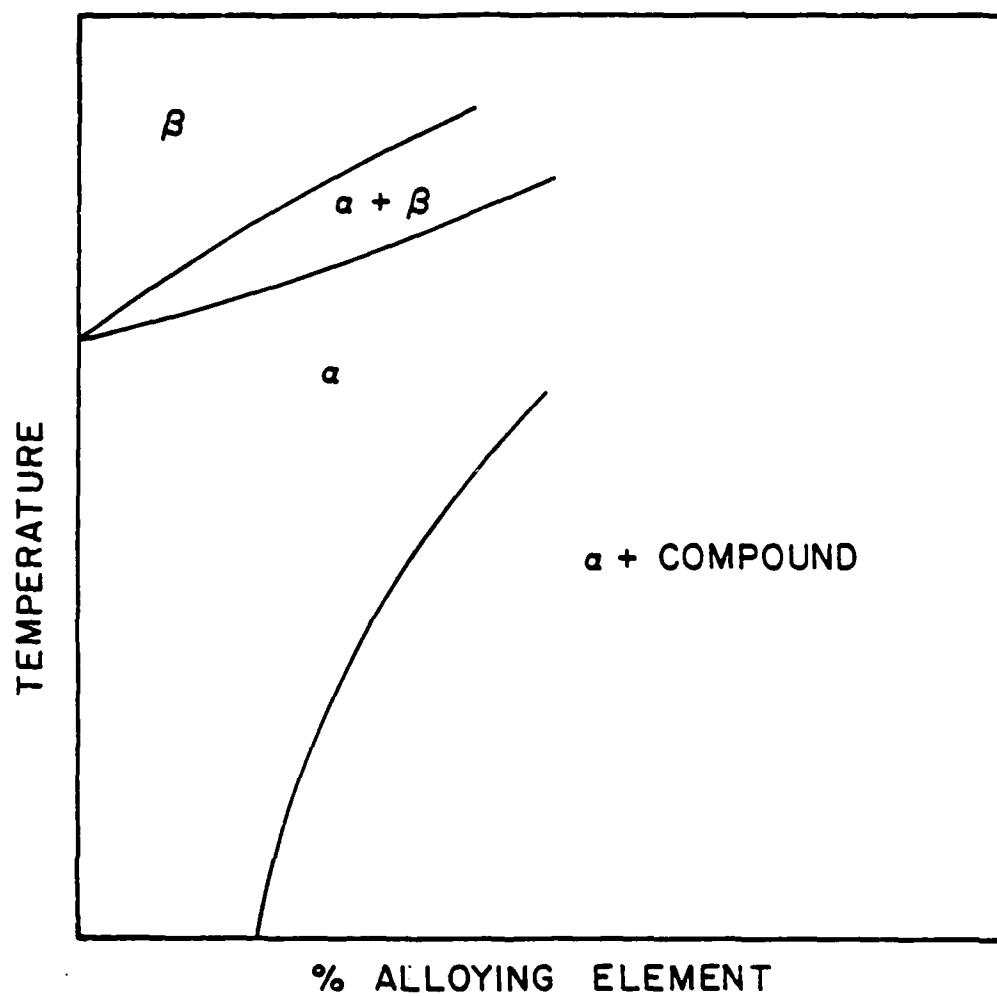


Figure 2.1 Schematic binary phase diagram for an alpha-stabilized titanium alloy system, showing elevation of the beta transus temperature with increasing alloy addition.

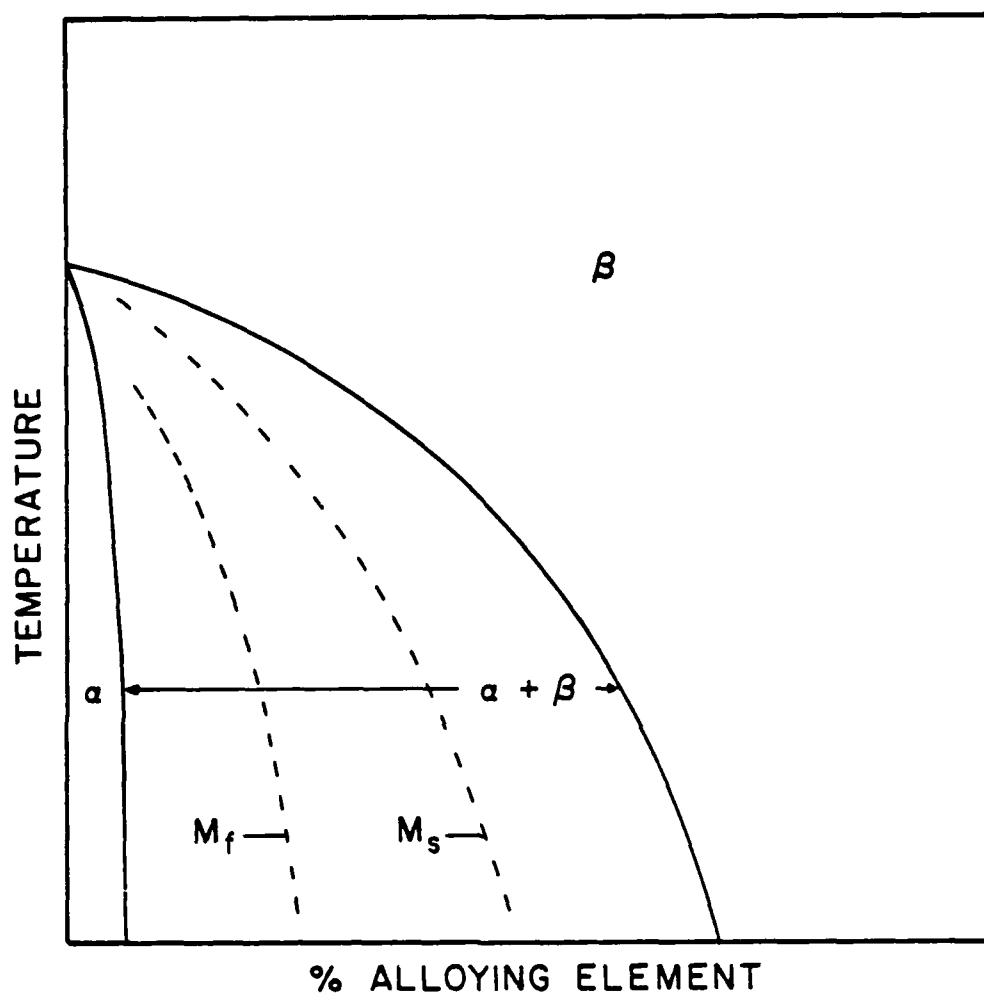


Figure 2.2 Schematic binary phase diagram for a beta-stabilized titanium alloy system, showing decreasing beta transus temperature with increasing alloy addition.

essentially no beta at room temperature. The phases present will be hcp alpha, hexagonal alpha' martensite which can be created by a sufficiently rapid cooling rate, and, at high aluminum or interstitial contents, ordered alpha 2 (Ti_3Al). Unalloyed titanium properties are controlled by the interstitial content, with additions of oxygen, carbon, and nitrogen increasing the strength of titanium while reducing the ductility. The strengthening effect of the interstitial elements is frequently expressed as an oxygen equivalent:

$$O_{eq} = \%O + 2(\%N) + 0.67(\%C)$$

where each 0.1% O equivalent increases the tensile strength of unalloyed titanium by approximately 17.5 ksi (1).

In other alpha alloys, aluminum is the primary addition because it both reduces the density and increases the strength of the alloy. The aluminum content is limited to approximately 5-6 atomic percent to avoid the formation of alpha 2, which can lead to severe embrittlement and reduced fatigue properties. When considering the formation of alpha 2, alpha-stabilizing elements are included in an aluminum equivalent:

$$Al_{eq} = \%Al + \%Sn/3 + \%Zr/6 + 10(\%O)$$

where the Al equivalent must be less than 9% to avoid the formation of alpha 2. This expression illustrates why tin

and zirconium are frequently added to alpha and alpha-beta alloys in place of aluminum or oxygen. Alpha alloys typically have tensile strengths from 50 ksi for relatively pure titanium to 125 ksi for Ti-5Al-2.5Sn, and ductilities of approximately 40%-50% reduction in area. These alloys are formable, weldable, perform well from cryogenic temperatures to approximately 550°C, and have good corrosion resistance. They are primarily used in the chemical, food, medical, and petroleum industries because of their corrosion resistance (1, 8).

2.1.3 Near-Alpha Alloys

Near-alpha alloys contain sufficient amounts of beta-stabilizing elements to retain a small amount of beta at room temperature, typically less than 10% (7). Two common near-alpha alloys are Ti-6211 and Ti-8Al-1Mo-1V (Ti-811). Near-alpha alloys have good strength and toughness, good corrosion resistance, high resistance to creep, and are weldable. Near-alpha alloys have tensile strengths in the range of 140 ksi, and ductilities of approximately 30% reduction in area. Typical applications for these alloys are aircraft engine components and airframes. The excellent salt-water corrosion resistance and stress corrosion cracking resistance of Ti-6211 has led to its use in marine applications (1,2). The deep-submergence vehicle used in

the recent exploration of the HMS Titanic, the Alvin, used Ti-6211 as the material for its hull (2).

2.1.4 Alpha-Beta Alloys

Alpha-beta alloys retain 10%-50% beta at room temperature. In addition to the phases present in near-alpha alloys, heavily stabilized alpha-beta alloys can contain an orthorhombic martensite, alpha". Ti-64, the most widely used titanium alloy, is an alpha-beta alloy. These alloys have higher strengths but inferior corrosion resistance than do alpha and near-alpha alloys, and are slightly heat-treatable. Both the strength and response to heat treatment of these alloys increases with increasing levels of beta stabilization, and the weldability and corrosion resistance decrease. Approximately 20% retained beta is usually considered to be the limit for weldability of alpha-beta alloys (7). These alloys have tensile strengths of approximately 140 ksi and about 30% reduction in area. Alpha-beta alloys continue to be the most commonly used alloys for structural applications in the aerospace industry, where they are used primarily for their high specific strength and stiffness (1, 2, 9, 10).

2.1.5 Metastable Beta Alloys

Metastable beta alloys, often called beta alloys, retain 100% beta when quenched to room temperature. These alloys have sufficient beta stabilizer content to suppress the martensite start temperature to below room temperature, shown schematically in Figure 3 (7, 11). Reported minimum solute levels for 100% beta retention with an ice water quench are 15 atomic % for vanadium, tantalum, and niobium, and 7 atomic % for molybdenum (7). After quenching, these alloys can be aged to precipitate various transition phases and/or alpha. The fine dispersion of second-phase particles produced by aging give these alloys very high strengths but limited ductility. In the solution treated and aged condition, tensile strengths of greater than 200 ksi are typical. Metastable beta alloys include Ti-13V-11Cr-3Al, Ti-8Mo-8V-2Fe-3Al, and Ti-11.5Mo-6Zr-4.5Sn. The first significant use of a metastable beta alloy was for airframe components in the Lockheed SR-71 "Blackbird" (11). Because of their formability in the "as-quenched" condition and very high strengths after aging, metastable beta alloys are now replacing alpha-beta alloys in structural aerospace applications (1, 10, 11).

2.2 Microstructures in Alpha-Beta Alloys

The factors used to define microstructures in near-alpha and alpha-beta alloys include the size and shape of the prior beta grain size, and the phases and morphologies present in the transformation structure. In addition to alloy content, these microstructures are controlled by the structure present prior to the beta to alpha transformation, and the rate at which the transformation occurs. These factors will be briefly discussed below. Because of the importance of the alpha-beta interface, the work describing the existence and characteristics of the interface phase will be reviewed as a separate sub-section.

2.2.1 Prior Beta Grain Shape

Two possible prior beta structures exist. Material that is beta-processed will have a prior beta grain structure which reflects the processing structure. For example, in a material that was hot rolled in the one-phase beta region, the prior beta grains will be elongated in the rolling direction. An equiaxed prior beta grain structure results from thermally cycling to temperatures above the beta transus, either as an annealing operation or as a result of an elevated-temperature fabrication process such as welding (2). Material that has been annealed at a temperature below the beta transus will contain a

combination of equiaxed alpha and primary alpha and beta which reflect the thermal history of the material (12).

2.2.2 Transformation Rate

The rate at which the beta to alpha transformation proceeds will determine the structure of the transformation products. Usually allotriomorphic alpha is present at the prior beta grain boundaries (2, 12). A very slow cool will result in the creation of a coarse Widmanstätten colony structure. As the cooling rate increases, the colony structure is replaced in the center of the prior beta grains by a fine Widmanstätten basketweave structure. Further increases in cooling rate refine and increase the amount of the basketweave structure. With sufficiently rapid cooling, the nucleation and growth transformation can be avoided, resulting in a structure consisting of alpha' martensite (1,2). These structures are created by the cooling rates usually seen in fabrication processes, for example, in the fusion and heat-affected zones of weldments (13). Examples of these structures are shown in Figure 2.3, micrographs of Ti-6Al-2Mo. These microstructures will be discussed in far more detail when the alloys used in this investigation are described.

A significant microstructural constituent in near-alpha alloys with high aluminum contents, for example Ti-811, is

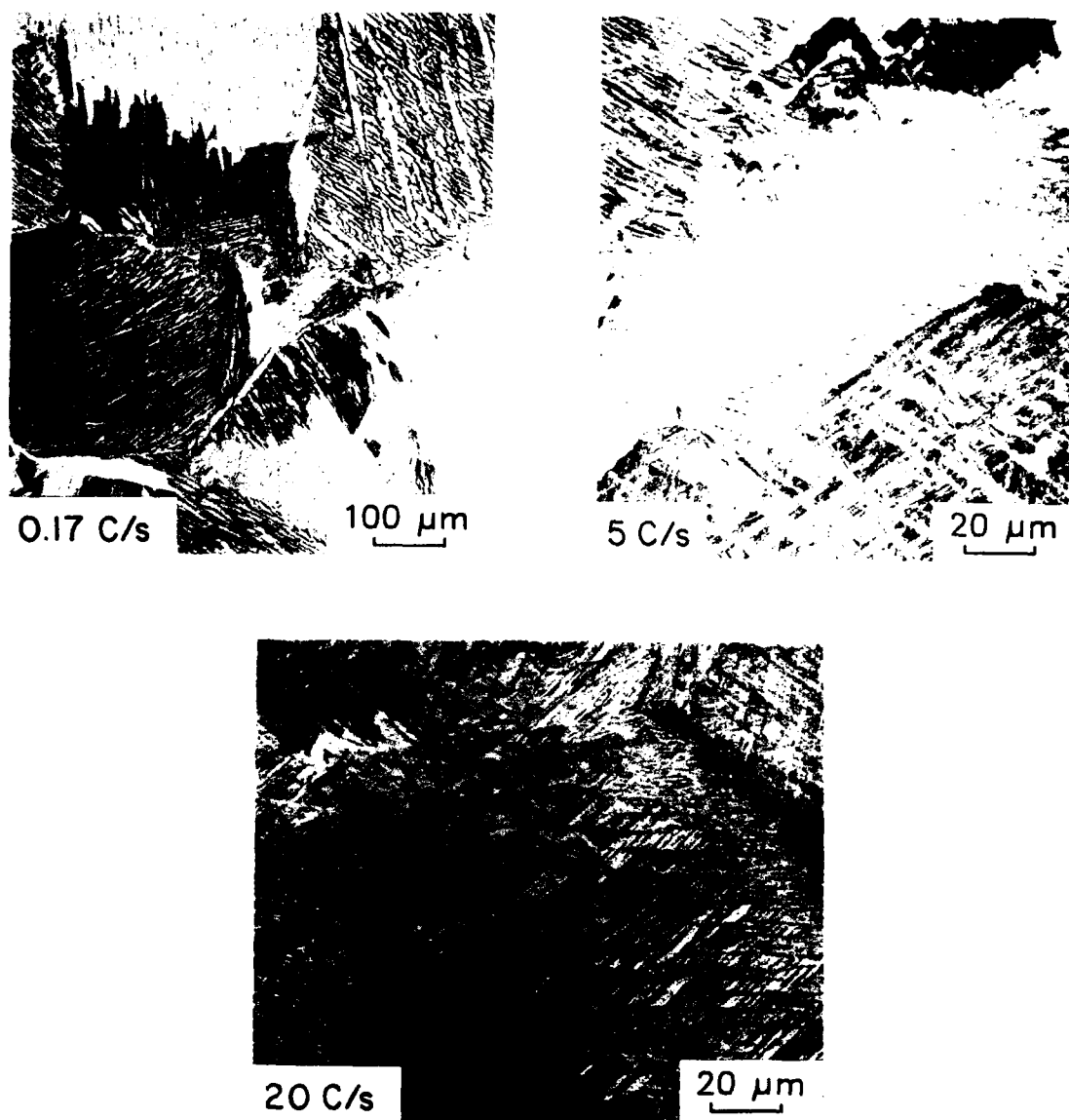


Figure 2.3 Micrographs of Ti-6Al-4V. As cooling rate increases, structure changes from Widmanstätten colonies (a), to basketweave alpha plus beta and martensite (c).

ordered alpha 2, or Ti_3Al . Alpha 2 appears during extended exposure to temperatures near $500^{\circ}C$ and occasionally in material which has been very slowly cooled. This phase is significant because it is associated with intense planar slip and deleterious effects on fatigue properties, ductility, and fracture toughness (1, 14). Alpha 2 has been observed in Ti-6211, but not under conditions associated with standard production or fabrication techniques. In alloys where alpha 2 does commonly occur, it is usually eliminated by the use of a duplex anneal. This consists of reheating the furnace-cooled material to high in the alpha plus beta phase field and air-cooling, creating a disordered alpha structure with enhanced ductility and impact resistance (2).

2.2.3 Alpha-Beta Interface Phase

Several researchers have noted the existence of a third phase at the alpha-beta interface in two-phase alloys (15-22). The interface phase is of particular interest in this investigation because the crack nucleation and propagation associated with the low-ductility failures occurs at the alpha-beta interface. Two distinct structures have been observed in the interface phase, fcc with either a striated or monolythic substructure, (15-19), and hcp with a striated substructure (16-19). Both phases occur in a wide range of

alloys.

The hcp interface phase has also been type 2 alpha. This phase is twin-related to type 1, or alpha which is itself crystallographically oriented with the parent beta phase. The type 2 alpha is twin-related to the type 1 alpha with either a $\{10\bar{1}2\}$ or $\{110\bar{1}\}$ twin plane. This structure has been observed in alpha-beta alloys which have been furnace or air cooled from the beta field, and in metastable beta alloys which have been aged. In both instances, the formation of the interface phase seems to be related to the precipitation of alpha from beta. The type 2 alpha is believed to be more thermodynamically stable than type 1 alpha (18).

Two alternate theories exist to explain the formation of the hcp interface phase. One, favored by Rhodes and Williams, is that the layer grows by nucleation and growth driven by a chemical potential difference (18). The second theory, favored by Margolin, et.al. (17), is that type 2 alpha results from mechanical twinning to relieve the stress produced by the lattice incompatibility of the transformation. This model is supported by the fact that the plane by which the two types of alpha are related changes as a function of alloy composition. The twinning model is also consistent with the observation that different

twinning modes occur in titanium depending on the direction of the stresses imposed on the hcp unit cell (15-18).

The fcc interface phase occasionally appears in near-alpha alloys as well, but is usually associated with slower cools than the hcp interface phase (15). The fcc interface phase has not been reported to occur under isothermal transformation conditions (14). Two theories exist for the growth of this phase as well. The first is that a compositional gradient in vanadium (or another slow-diffusing element) promotes the nucleation and growth of the fcc layer. The alternate theory is that the fcc layer grows in response to the strains created by a volumetric expansion involved in the beta to alpha transformation. This expansion puts the growing alpha in compression, promoting the growth of the more dense fcc layer (14,16).

More recent investigations of the interface phase have suggested that both the hcp and fcc versions are artifacts due to specimen preparation. This conclusion had been reported earlier in the case of the hcp interface phase, because it was only observed in thin foil specimens. Isaac and Hammond (23) have proposed that this is because type 2 alpha, which they agree forms to relieve the lattice incompatibility between the beta and alpha phases, can only form when the constraints imposed by bulk specimens are

relieved. Banerjee, Rhodes, and Williams (24) have investigated the effect of beta phase composition on the occurrence of both types of interface phase. These researchers have proposed that the relative hydrogen content of the material, which is affected by specimen type and preparation techniques, is the cause of the interface phase and controls what form of interface phase occurs.

2.3 Mechanical Property/Microstructure Correlations

This section will be divided into three parts. The first is a very general description of microstructure-property relationships in near-alpha alloys, and the second, the review expanded to alpha-beta alloys. The third subsection is a brief review of work done relating the microstructures and failure modes and mechanisms in alpha, near-alpha, and alpha-beta alloys.

2.3.1 Near-Alpha Alloys

In the absence of alpha 2, the room-temperature mechanical properties of near-alpha alloys are relatively insensitive to microstructural changes. For the same prior beta and alpha grain sizes, equiaxed alpha, Widmanstätten plus grain boundary alpha, and alpha' martensite all have essentially the same strength (25). The differences that do exist are, for the most part, attributable to grain

refinement. For example, α' is slightly stronger than either Widmanstätten or equiaxed α , 5%-10% in the case of Ti-6211, because of the grain refinement and higher dislocation density resulting from the displacive transformation. Also, for a given prior beta grain size, equiaxed microstructures will usually have slightly higher strengths than Widmanstätten microstructures. This is because the α grain size in an equiaxed structure is usually smaller than the Widmanstätten colony size in a Widmanstätten structure.

In addition to grain size strengthening, grain refinement results in shorter slip path lengths, reduced stress concentration at dislocation pile ups, and a reduced tendency to form microvoids. As a result, the ductility, resistance to fatigue crack initiation, and low cycle fatigue performance of equiaxed microstructures are better than those of Widmanstätten microstructures. Widmanstätten structures, however, will generally have greater fracture toughness, due to the more tortuous crack path created by the thick, randomly oriented α plates. Optimum microstructures can be created for particular applications by the use of thermal treatments designed to produce a combination of equiaxed α , coarse acicular α , and fine Widmanstätten α plus beta (15).

2.3.2 Alpha-Beta Alloys

The same general relationships between slip path length and tensile, fatigue, and fracture properties apply to alpha-beta alloys. However, the greater amount of beta retained makes alpha-beta alloys slightly stronger than alpha or near-alpha alloys. The bcc structure of beta has a large number of active slip systems. In the beta, dislocations can cross-slip and create dense dislocation tangles which restrict further dislocation motion. This permits the beta phase to be used as a strengthener when contained in an alpha matrix (27). Additionally, not only will more beta be retained at room temperature in more heavily stabilized alloys, the beta will be stronger than that retained in leaner alloys 1, 2). A second difference when compared to near-alpha alloys is the greater degree of variability available with alpha-beta alloys due to the increased beta-stabilizer content. One result of this is that alpha-beta alloys are somewhat heat-treatable. Depending on the temperature prior to quenching, either alpha' or metastable beta can be retained at room temperature, Figure 3. Either will be supersaturated in beta-stabilizing elements and can be aged to precipitate fine beta, alpha, or transition phase particles, resulting in an further increases in strength.

2.3.3 Microstructure-Failure Mode Relationships

The relationship between microstructure and fracture modes at room temperature has been the subject of many investigations (25-36). Both transgranular and intergranular fracture modes have been observed in near-alpha and alpha-beta alloys. As was noted earlier, equiaxed microstructures usually have greater tensile ductility and greater resistance to void nucleation. Widmanstätten plus grain boundary alpha microstructures, on the other hand, usually have greater fracture toughness and resistance to fatigue crack propagation.

Past investigations have shown that tensile failure of near-alpha and alpha-beta titanium alloys occurs by microvoid nucleation, followed by coalescence and/or growth. The fracture behavior of these alloys is usually analyzed in terms of slip character and slip path length (30, 31). These investigations generally have taken one of two approaches. The first is to attempt to derive an overall fracture criteria, either a critical stress or strain, based directly on microstructural considerations. The second approach is to examine the actual nucleation and growth of voids and to attempt to characterize these parameters with respect to the microstructures present. The following review will be divided along these lines.

2.3.3.1 Overall Fracture Models One area where investigators have had reasonable success with the development of overall fracture criteria is with alloys where the aluminum content is sufficiently high to cause the formation of alpha 2, Ti_3Al . Although alpha 2 is usually seen in alpha and lean alpha-beta alloys, investigators have reported it in aged Ti-64 (37) and Ti-6211 (38). When alpha 2 is present intense slip bands can form when the particles are sheared because of the local softening and continued dislocation motion on these planes. In this case, ductility and fracture mode are controlled by the planarity of slip and the slip path length (31, 39, 40).

Lutjering, et.al. (31) conducted investigations quantitatively relating the concepts of planarity of slip and slip path length to fracture strength and ductility. This investigation used Ti-8Al processed to create different alpha grain sizes and different levels of alpha 2 formation. The results of this study showed excellent correlation between observed mechanical properties and those predicted using a calculation of stress concentrations based on TEM observations of dislocation pileups and slip band spacing. It was found that a critical local stress was required for fracture, and that this stress was constant for all of the material investigated. The conclusion of this study was

that this critical stress could be reached by a combination of externally applied load and stress concentration due to microstructural considerations (31). A similar investigation was performed by Gysler, et.al. (41) on Ti-Mo alloys, metastable beta alloys into which a fine dispersion of ω had been introduced by aging. These alloys showed a similar dependence on planarity of slip and slip path length.

Although these investigations dealt with particle hardened systems which were extremely susceptible to planar slip, the overall approach is equally applicable to alpha-beta alloys provided their slip character is understood. One example of this is a relationship developed by Greenfield and Margolin (29). Based on an analysis of Ti-5.25Al-5.5V-0.9Fe-0.5Cu that had been solution treated, quenched, and aged to produce an equiaxed microstructure, the fracture strength along the tensile axis was predicted by the following expression:

$$\sigma_f = \sigma_o + K_d d^{-1/2} + K_\lambda \lambda^{-1/2} + K_D D^{-1/2}$$

σ_f = the fracture stress, corrected for necking

d = the equiaxed alpha traverse particle diameter

λ = the mean free path between alpha particles

D = beta matrix grain diameter

σ_o , K_d , K_D , K_λ are constants.

2.3.3.2 Void Nucleation Several investigations have been made of void nucleation and growth and how they relate to microstructural considerations (26-36). One model for the nucleation of microvoids, based on an earlier single phase model by Cotrell (42), has been proposed by Greenfield and Margolin (28). They found that in equiaxed alpha microstructures, voids nucleated preferentially on equiaxed alpha/aged beta interfaces. In Widmanstatten plus grain boundary alpha structures, the voids nucleated only on one side of the grain boundary alpha film. In both microstructures, the result was intergranular failure by microvoid coalescence. Based on these observations and electron microscopy of the alpha/beta interfaces in strained samples, Greenfield and Margolin proposed that slip occurs preferentially in the softer alpha phase, essentially on one slip system. At a crystallographically oriented alpha/beta interface, a parallel slip system in the beta can be activated and slip is transferred across the interface. This leads to continuous slip lines passing from the alpha to the beta phases. However, at a non-oriented interface, they observed that the slip lines stop, which suggests a dislocation pile up. The result of this pile up is high local stresses and void nucleation.

Greenfield and Margolin (28) pointed out that their

model was consistent with microstructural observations. In the equiaxed microstructures, the recrystallized alpha has no orientation relation with the beta and all alpha/beta interfaces are equally probable for void nucleation. Dislocation motion is blocked at the alpha grain boundaries, either alpha/alpha boundaries, or alpha/aged beta boundaries. The slip path length in these structures is determined by the alpha grain size. In the Widmanstatten structures, individual alpha plates are surrounded by beta of one orientation and have the orientation relation on both sides. This allows slip to pass from the alpha to the beta within a Widmanstatten colony and dislocations are blocked only at colony boundaries. The slip path length in these microstructures is thus dictated by the Widmanstatten colony size. In alpha' martensite structures, no orientation relationship exists between the alpha' and the beta. In this case, the slip path length is reduced to either the thickness of the grain boundary alpha film, or the width of an alpha' platelet.

Void nucleation at alpha/transformed beta interfaces have been found by other investigators as well. However, void nucleation has also been reported at locations other than alpha/beta interfaces. Margolin and Mahajan (32), in a study of aged Ti-64 and a review of previous investigations,

found that in equiaxed structures, void nucleation occurred both at alpha/aged beta interfaces and within the equiaxed particles. Within the particles, the voids were often, but not always associated with subboundaries. In Widmanstätten plus grain boundary alpha structures, nucleation was found to occur at the grain boundary alpha/beta interfaces, at grain boundary alpha/alpha' interfaces, and within the Widmanstätten alpha platelets where the voids were parallel to the twin boundaries within the plate. Additionally, voids were also found at alpha'/beta interfaces and within the alpha' particles. In an overview of microstructural effects on mechanical properties, Margolin, et.al. (43) reported these nucleation sites and also noted void nucleation at slip band intersections.

In spite of the variety of the void nucleation sites observed, the review of Margolin, et. al. (43) did show that in most cases, void nucleation occurred on only one side of an alpha particle, supporting the model of Greenfield and Margolin (28). Additional support for the Greenfield and Margolin model was reported by Baselack and Mahajan (44). These investigators found void nucleation exclusively at grain boundary alpha/matrix interfaces and showed slip lines continuous on one side of the grain boundary alpha film and being blocked at the other.

The results of these studies show that void nucleation seems to be associated with crystallographic inhomogeneities of some sort, but no clear dependence exists between slip path length and void nucleation. In microstructures where the slip path is reduced to the width of an alpha' lath or to the diameter of a sub-grain in an equiaxed particle, void nucleation still occurs at these sites in addition to sites associated with longer slip paths (25, 44, 45). It is possible that the different nature of the various interfaces overshadows a significant slip path length effect, but this has not been shown.

2.3.3.3 Void Growth Void growth and the final fracture characteristics have also been extensively studied. Although Margolin and Greenfield (29) found that the fracture strength of Ti-5.25Al-5.5V-0.9Fe-0.5Cu was controlled by void nucleation, this contrasts with the results of most other investigators. It is usually reported that void growth rather than void nucleation is the cause of different tensile ductility and fracture characteristics (29, 37-46). Further, it is usually reported that growth of existing voids, rather than continued void nucleation and coalescence is the cause of eventual fracture (32, 43, 45). This is shown by a linear, rather than accelerating, relationship between applied strain and the length of the

longest void (32, 43-47). In most cases, the critical event for fracture is described as the growth of the longest void to a point where a criteria based on void length and stress level is reached. A relationship is usually developed between critical fracture strength σ_f and the length of the longest void, L_f (32, 43-47). One example of this, reported by Margolin and Mahajan (32), is:

$$\sigma_f = \sigma_0 + KL_f^{-1/2}$$

Attempts to relate the growth rate of the longest void (G_l) to microstructural considerations have resulted in conflicting evidence. In some instances, G_l was found to increase with increasing prior beta grain size and grain boundary alpha thickness (32, 44), while in others it was not (44). In other investigations, a microstructural dependence was found in Widmanstätten structures, but not in equiaxed structures (32).

The mechanism of crack growth and eventual fracture in titanium alloys is not well understood. Both transgranular and intergranular fracture have been reported in a wide range of alloys and microstructures. Greenfield and Margolin (28) found that the failures in their Widmanstätten microstructures were primarily intergranular with respect to the prior beta grains. They observed that once nucleated, the cracks propagated within the alpha along the grain

boundary alpha/beta interface. Other investigators have observed similar behavior (19, 29, 30, 32). Growth of voids along the grain boundary alpha/matrix interface is usually explained in terms of local plastic flow at the advancing crack tip (29, 30). Gerberich (30) has described the crack growth as being similar to that seen in elastic fracture. He attributed cracking adjacent to the alpha/beta interface to constraint of the alpha phase which results in triaxiality of stress, a locally higher yield stress for the alpha, and easy crack propagation. According to this model, as the grain boundary alpha thickness increases the fracture toughness would be expected to increase due to the lesser constraint of the alpha film and the attendant reduction in void growth. A similar mechanism was proposed in one investigation of Margolin and Greenfield (28). In an earlier investigation however (29), these investigators attributed fracture adjacent to the alpha/beta interface to a breakdown of compatibility at the interface, reduced constraint of the alpha at the advancing crack tip, and crack growth by localized plastic flow. A third mechanism was proposed by Mahajan and Margolin (34) relating the growth of voids to the elastic discontinuity at the interface. Because of this discontinuity, the stress is highest at the alpha/beta interface and decreases with

distance from the boundary. If the crack moves into the softer alpha phase, the stress available to propagate the crack is diminished because of the diminished distance to the interface.

Transgranular crack propagation has been observed in similar alloys and microstructures by several investigators (32-33). In a study on Ti-4.5Al-5Mo-1.5Cr (CORONA 5), Baselack and Mahajan (33) found that Widmanstätten plus grain boundary microstructures fracture by both intergranular and transgranular crack initiation and propagation. Also, both modes were seen to occur either with extensive plastic deformation or as interface separation with little or no deformation. The level of deformation observed depended on the orientation of the applied stress with respect to the crack, but the fracture mode did not. The low-deformation cracks were proposed to nucleate and grow as described in the Greenfield model (28) and the extensive deformation cases were attributed to shear-induced interface sliding (33).

Mahajan and Baselack (27) noted that two alloys with similar microstructures but different slip accommodation characteristics displayed identical void nucleation behavior. Both Ti-6246 and Ti-662 showed void nucleation exclusively at the grain boundary alpha/beta interface as

predicted by the Greenfield model (28). However, in Ti-6246, the cracks propagated along the interface, and in Ti-662, the failure was transgranular. Also, slip lines appeared to be blocked by alpha/beta interfaces in Ti-6246 but were not in the Ti-662. This seems to contradict the Greenfield and Margolin void nucleation model and suggests that slip transferral from alpha to beta is significant in crack growth but that void nucleation is controlled by another mechanism (27).

2.3.3.4 Summary The bulk of the work to date suggests that the deformation characteristics of titanium alloys may be thought of in terms of slip character and slip path length, but these concepts only apply well to systems which show gross planar slip. In other alloys, there seems to exist a general correlation, but other factors can contribute to and even dominate the mechanical behavior. The model for void nucleation and growth proposed by Greenfield and Margolin (28) appears to be a good starting point for a consideration of the behavior of these alloys. In this model, the nucleation of microvoids requires an interface which blocks dislocations. In the case of Widmanstätten microstructures, void nucleation often occurs at a non-Burgers-related grain boundary alpha/matrix interface and is associated with long slip path lengths.

On the other hand, when void nucleation is seen at other types of interfaces, no dependence on slip path length is observed.

Void growth, rather than nucleation, is usually considered to be the controlling factor in fracture ductility. Both intergranular and transgranular void growth and fracture have been reported. In Widmanstätten microstructures, void growth is usually within the grain boundary alpha film and adjacent to the non-Burgers-related interface. This has been associated with slip path length, constraint of the alpha film, and elastic incompatibility at the interface. However, transgranular fracture has also been observed and both modes have been observed in the alloys used in this investigation. One possible explanation for this behavior is that the limited number of slip systems available in the alpha phase make the orientation of the alpha film with respect to the applied stress the critical factor.

ELEVATED TEMPERATURE BEHAVIOR AND MODELS

This section consists of three parts. The first is a review of work specifically addressing the high temperature behavior of near-alpha and alpha-beta titanium alloys. This is followed by a discussion of the two models which have been proposed to explain this behavior. The third section is the presentation of the lattice incompatibility model, the model around which this investigation has been developed.

3.1 Review of Work To Date

The results of six investigations, or groups of investigations, are reviewed in this section. Each study will be discussed individually, then general conclusions will be made based on the data taken as a whole.

3.1.1 Lewis and Caplan

Lewis and Caplan investigated the hot ductility behavior of several titanium alloys. The results of this investigation are presented in Figure 1.1 (6). Three of the alloys tested, Ti-64, Ti-6211, and Ti-6Al, failed intergranularly with a severe reduction in ductility when tested at approximately 800°C. Ti-3Al-2.5V had only a moderate loss in ductility and unalloyed titanium had essentially none. The ductility loss was found to occur on

cooling following a thermal excursion into the beta region. When the material was tested on heating following an excursion into the beta region, the ductility was also reduced compared to that of the original material, but not as severely as during cooling in the initial cycle. This indicated that either the ductility loss is associated with the dynamic cooling conditions or that the material is irreversibly conditioned during a thermal cycle into the beta region. Lewis and Caplan found no evidence of second phase particles on the fracture surfaces of samples tested in situ at room temperature and 77°K, but the concentration of sulfur present on the fracture surfaces was found to be 300 times the bulk concentration (6).

In other work, Lewis (49) attempted to characterize the hot ductility dip in Ti-6211 with respect to strain rate, cooling rate, and microstructure. This investigation showed that the hot ductility dip existed within a particular window of time-temperature space and corresponded with the beta to alpha transformation. The results of this investigation are shown in Figure 3.1. In this figure, the time-temperature ductility map is superimposed on the continuous cooling transformation (CCT) diagram of Gordine (50). The regions of various hot ductility behavior can be seen to correspond with the beta to alpha transformation.

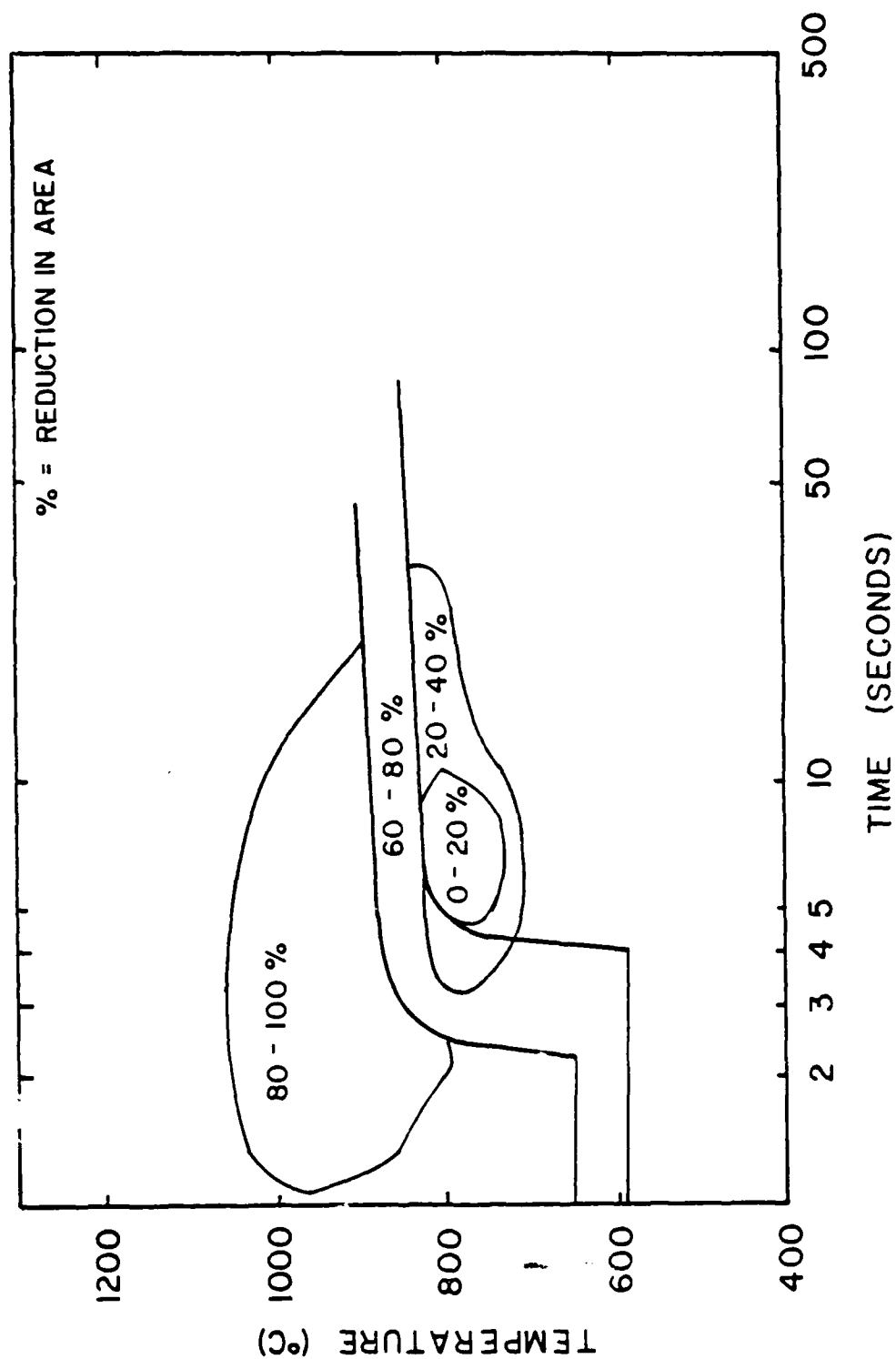


Figure 3.1 Ti-6211 ductility map of Lewis (49) superimposed on the CCT diagram of Gordine (50), showing minimum ductility region just below the beta to alpha transformation.

In all cases, the hot ductility dip was not affected by changes in strain rate over the range studied, 1.2 s^{-1} to 25 s^{-1} .

Lewis (49) found that at temperatures above the beta to alpha start temperature, the failure mode was transgranular ductile rupture, preceded by a large amount of plastic flow. At temperatures within the transformation, failure occurred by a mixture of low-ductility intergranular and high-ductility transgranular mechanisms. The ductility decreased with decreasing temperature and increasing cooling rate, corresponding with increasing amounts of alpha phase. Also, the net section stress decreased with decreasing temperature in the single phase beta region but increased with decreasing temperature in the alpha plus beta region. This is shown in Figure 3.2 (6). Lewis interpreted this to indicate that the alpha phase is both stronger and more ductile than the beta phase at temperatures within the transformation.

The lowest ductility observed by Lewis (49) was in rapidly cooled samples tested immediately below the beta to alpha transformation finish. Failure of these samples occurred by microvoid nucleation and coalescence at the grain-boundary alpha/transformed beta interface. Two possible explanations were given for the low ductility of

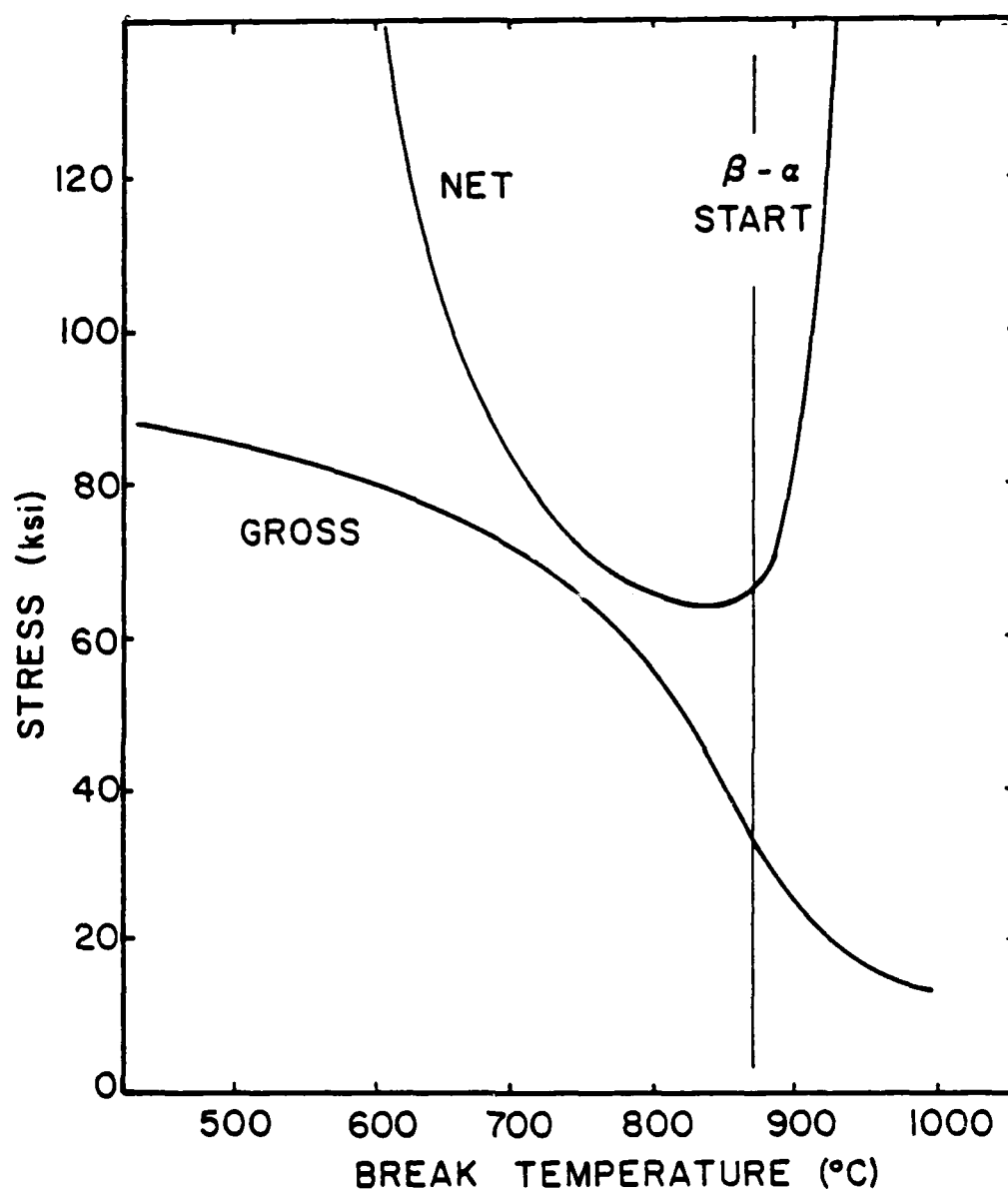


Figure 3.2 Gross and net fracture stress as a function of temperature for tensile tests of Ti-6211 (6). Net fracture stress increases with amount of alpha phase.

this interface. The first was the segregation of alloying elements to either side of this interface, altering the local flow properties. The second possible cause discussed was coating and weakening of the interface by impurity segregation.

It is important to note that Lewis based his interpretations on the Gordine CCT diagram for Ti-6211 (50). More recent work has established a slightly different CCT diagram for this alloy in which the beta to alpha transformation occurs at lower temperatures (13, 51). In Figure 3.3, the ductility map developed by Lewis (49) is superimposed on the more recent CCT diagram. Obviously, an interpretation of the test results based on this diagram would result in different conclusions. The region of lowest ductility is now shown to fall much closer to the beta to alpha transformation finish. However, caution must be exercised in the application of either diagram. CCT diagrams are developed using a particular set of cooling curves and only strictly apply to processes using identical cooling curves. With any other thermal profiles, the time at temperature, hence the nucleation behavior, will be different.

Experimental evidence has shown that the lower CCT diagram more accurately predicts phase stability over the

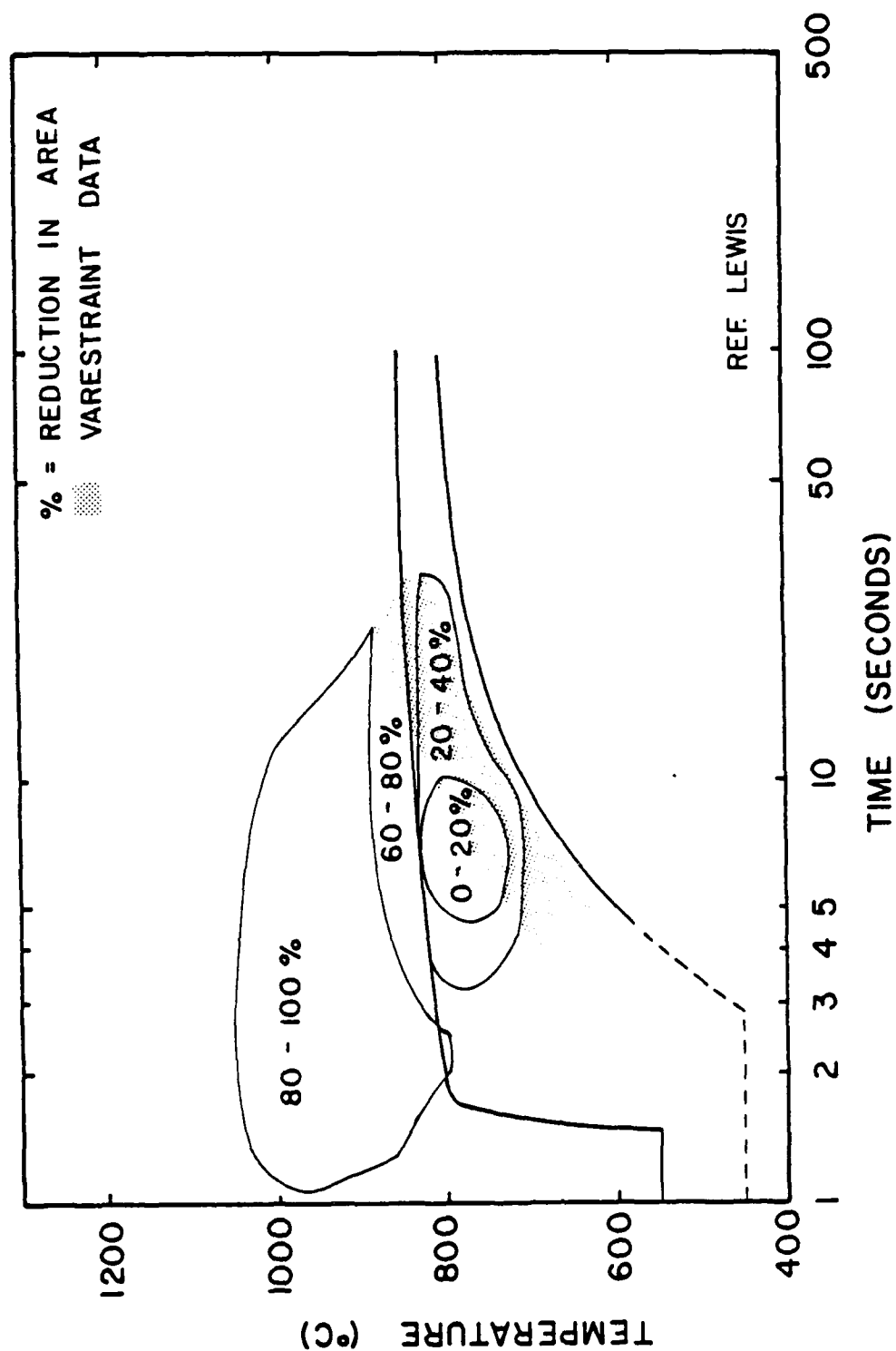


Figure 3.3 Lewis (49) ductility map and vareststraint cracking temperatures (63) for Ti-6211 superimposed on the CCT diagram of Damkroger (13). Minimum ductility occurs near the beta to alpha transformation finish.

range of cooling rates seen in GTA and GMA welding processes (13). The cooling profile used in the Lewis study, a simulated GTAW cooling cycle, falls within this range. On the other hand, Lewis made microstructural observations of samples which failed at 848°C and found heavily deformed transformation products (49). This indicates that these phases were present at 848°C, above the beta to alpha start temperature in the more recent diagram. A possible explanation for this discrepancy is that the samples in the Lewis study, tested using the Gleeble facility at DWTNSRDC-Annapolis, showed evidence of varying and occasionally heavy interstitial contamination (52). Because oxygen, nitrogen, and carbon are all potent alpha stabilizers, high concentrations of these elements would raise the transformation temperature (1, 53). Oxygen contamination is also a possible reason for the difference between the two CCT diagrams. This discrepancy serves to point out both the importance of consistently good atmospheric control when working with titanium and the risks involved when attempting to use data from other studies.

3.1.2 Starke, et .al.

Starke and his co-workers investigated the susceptibility of Ti-6211 to the hot ductility dip on the basis of microstructural variables (55). The goal of

this investigation was to determine whether the hot ductility dip occurred as a result of a given microstructural condition or as a result of non-equilibrium effects associated with a particular thermal cycle. The variables studied were beta grain size and shape, alpha morphology, and intragranular structure. Tensile tests were run at room temperature, 500°C and 800°C, immediately following a slow heating cycle to these temperatures. It was concluded that if the prior beta grains were equiaxed, any transformation structure other than equiaxed alpha was susceptible to the high temperature ductility loss. Also, it was found that this behavior was not dependent on either the prior beta grain size or the scale of the transformation structure. The results of this investigation results are presented in Table 3.1.

In the Starke (55) studies, the effect of alpha phase morphology was first investigated by testing a sample with a structure of equiaxed alpha with retained beta at the grain boundary triple points, sample E-1. This structure showed high ductility at all test temperatures, implying that a Widmanstatten or martensite plus grain-boundary alpha structure is required to cause reduced hot ductility.

The effects of prior beta grain shape and intragranular slip path length were then investigated. The as-received

Table 3.1

Results of Starke, et. al. (12)

Sample	Microstructure	Temperature	%RA
W-1	Widmanstatten alpha-beta plus grain boundary alpha. Elongated prior beta grains	RT	20
		500	24
		800	62
W-2	Widmanstatten alpha-beta plus grain boundary alpha. Equiaxed prior beta grains	RT	28
		500	23
		800	22
W-4	Widmanstatten alpha, beta transformed to martensite. Elongated prior beta grains	RT	28
		500	27
		800	45
W-5	Martensite. Equiaxed prior beta grains	RT	22
		500	23
		800	23
W-6	Martensite. Large equiaxed prior beta grains.	RT	-
		500	-
		800	21
G-1	Martensite. Equiaxed prior beta grains	RT	18
		500	24
		800	17
E-1	Equiaxed alpha with beta at the grain boundary triple points	RT	-
		500	40
		800	-

plate had a grain-boundary alpha plus Widmanstatten structure in elongated prior beta grains, sample W-1. This material failed by transgranular ductile rupture at all test temperatures. In samples thermally cycled to above the beta transus and air-cooled, the structure is one of Widmanstatten plus grain boundary alpha or alpha', but now within equiaxed prior beta grains, samples G-1 and W-2. These samples, including the "Gleeble" cycled sample, (thermally cycled as in the Lewis and Caplan (6) study, then tested on reheating), all failed intergranularly when tested at 800°C, but transgranularly at the lower test temperatures. Other samples were cycled to a temperature high in the alpha plus beta range and quenched to transform the beta between Widmanstatten platelets to martensite, samples W-3 and W-4. Because martensite platelets have no orientation relationship with the surrounding alpha, the alpha/alpha' interfaces act as a barrier to slip. In these structures continuous slip paths were limited to the width of an individual alpha platelet. These samples behaved identically to the previous set, indicating that the loss of ductility is independent of slip path length.

Starke and his co-workers also addressed the possibility that impurity segregation to the prior beta grain boundaries was contributing to the hot ductility dip.

It was pointed out that intergranular fracture associated with grain-boundary embrittlement results in a smooth fracture surface rather than the dimpled fracture associated with the ductility dip. A thermally cycled sample was tested at 800°C following a hold time of 30 minutes. The failure was intergranular, but occurred with more ductility than the samples tested without a hold time. This implies that equilibrium partitioning of impurities to the grain boundary alpha/transformed beta interface was not a cause of the ductility dip.

In the Starke investigation, the ductility of a previously created microstructure was measured on heating. It was assumed that the behavior seen resulted from the same mechanism as the hot ductility dip seen on cooling in a rapid thermal cycle. This follows the premise that an irreversible conditioning process occurs when a sample is thermally cycled to above the beta transus. Starke et. al. (55) proposed that the conditioning process was the creation of a specific microstructural condition, grain boundary alpha plus transformed beta within equiaxed prior beta grains.

3.1.3 Inouye and David

In an investigation of room temperature impact strength, David and Inouye (57) found that the impact

strength of Ti-6211 welds was drastically reduced by trace quantities of boron present in the filler wire. Boron-rich precipitates were observed on the fracture surfaces of specimens thermally cycled to above the beta transus, cooled, and broken at room temperature. It was not stated whether these precipitates were believed to act as crack initiation sites or simply indicated segregation of boron to the grain boundaries. Further tests showed that the impact strength of Ti-6211 Charpy specimens machined from as-cast ingots could be reduced from 40 ft-lbs to 15 ft-lbs by the addition of 50 ppm boron. These investigators postulated that the conditioning process associated with the hot ductility dip may be a boron segregation to the beta grain boundaries during thermal cycling (58). No explanation was given for the observation that the ductility of Ti-6211 is increased by further cooling below the hot ductility dip region.

Inouye and David (51) also generated a partial CCT diagram for Ti-6211. The transformation start and finish points for this diagram lie between those reported by Gordine (50) and Damkroger (13). This is further evidence that caution must be used in the application of any CCT diagram. The procedures used by Inouye and David (51) in the development of their diagram were not discussed.

3.1.4 Ushkov

A study similar to that of Starke, et. al (55) was made on the hot ductility of several titanium alloys by Ushkov (59). The results are presented in Figure 3.4. Both coarse and fine-grained specimens were tested, with the coarse-grained specimens showing a more severe ductility loss than fine-grained specimens of the same composition. In general, all specimens showed a reduction in ductility in the range of 600°C to 800°C. However, the coarse-grained specimens showed a severe and equal loss of ductility for all alloys. In the fine-grained material, the ductility loss was a function of alloy content. In terms of alloy content, the most severe ductility losses were associated with the presence of 5%-6% Al and 2%-4% other additions. Ti-8Sn and Ti-6Al did not show a ductility loss in the fine-grained condition and were not included in the coarse-grained condition. No speculations were made on the role of alloy content on the extent or severity of the ductility dip.

The mechanism of deformation and failure were analyzed by metallographic analysis of voids in samples of Ti-6Al deformed under differing conditions. It was found that at high temperatures, void formation was observed at grain boundaries and slip band intersections after only 5%-6%

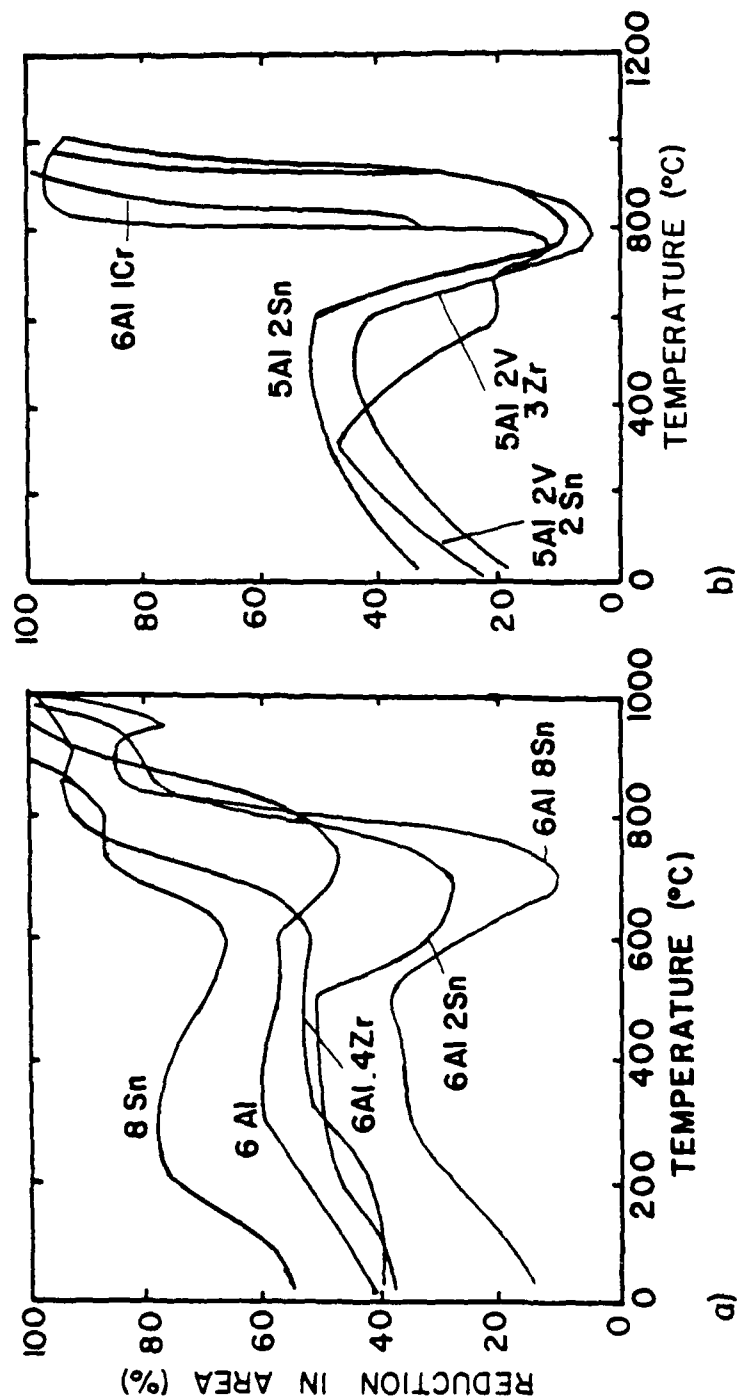


Figure 3.4 Ductility versus temperature for several titanium alloys (59) showing severe ductility loss for Ti-Al-Sn alloys in fine grained material (a), and all coarse grained material (b).

deformation. These same samples did not fail until almost 100% reduction in area. In samples tested at lower temperatures, void formation was not detected until immediately prior to fracture and fracture occurred at much lower deformation levels. No void formation was detected at any deformation levels in samples tested at temperatures within the beta region. The effect of strain rate was investigated as well, the strain rate being varied from 3×10^{-5} /s to 5/s. It was found that the rate and extent of void formation were increased by increases in strain rate. This was interpreted as indicating that void nucleation was affected more strongly by stress level than amount of strain and that vacancy condensation was not responsible for the nucleation of voids. Bi-axial tension and torsion tests also resulted in the nucleation of voids, indicating that shear as well as tensile stresses caused void formation (59).

The results of the microstructural analysis in the Ushkov (59) investigation are in contrast to those of Starke, et. al. (55). Ushkov found that when the Ti-6Al specimens were modified to produce either a martensitic structure or a refinement of the alpha grain size, the ductility at 800°C was significantly increased. In this case, the refined microstructure resulted in a

homogenization of the deformation and a reduced tendency to form the intense slip bands associated with void formation.

3.1.5 Krishnamohanrao, Kutumbarao, and Rao

These investigators combined data from the literature and their own work to create failure maps for several titanium alloys (60, 61). These fracture mechanism maps are binary plots which identify the regions of stress and temperature in which a particular failure mechanism is dominant. The maps plot the normalized tensile stress σ/E (where σ is the nominal applied stress in creep tests or UTS in tensile tests and E is Young's modulus) vs the homologous temperature T/T_m . At low temperatures and high stresses, the maps represent tensile tests. Above a certain point (presumably a critical temperature but this was not discussed) the mode of testing was changed to stress-controlled creep testing. As is usually the case when data is compiled from several sources, the starting materials and microstructures, as well as the test procedures used, varied widely.

Examples of fracture maps for commercial-purity titanium and Ti-6Al-4V are shown in Figure 3.5. The maps for all of the alloys are similar and contain several regions. At high stresses, failure is by dynamic fracture. At slightly lower stress levels and temperatures below

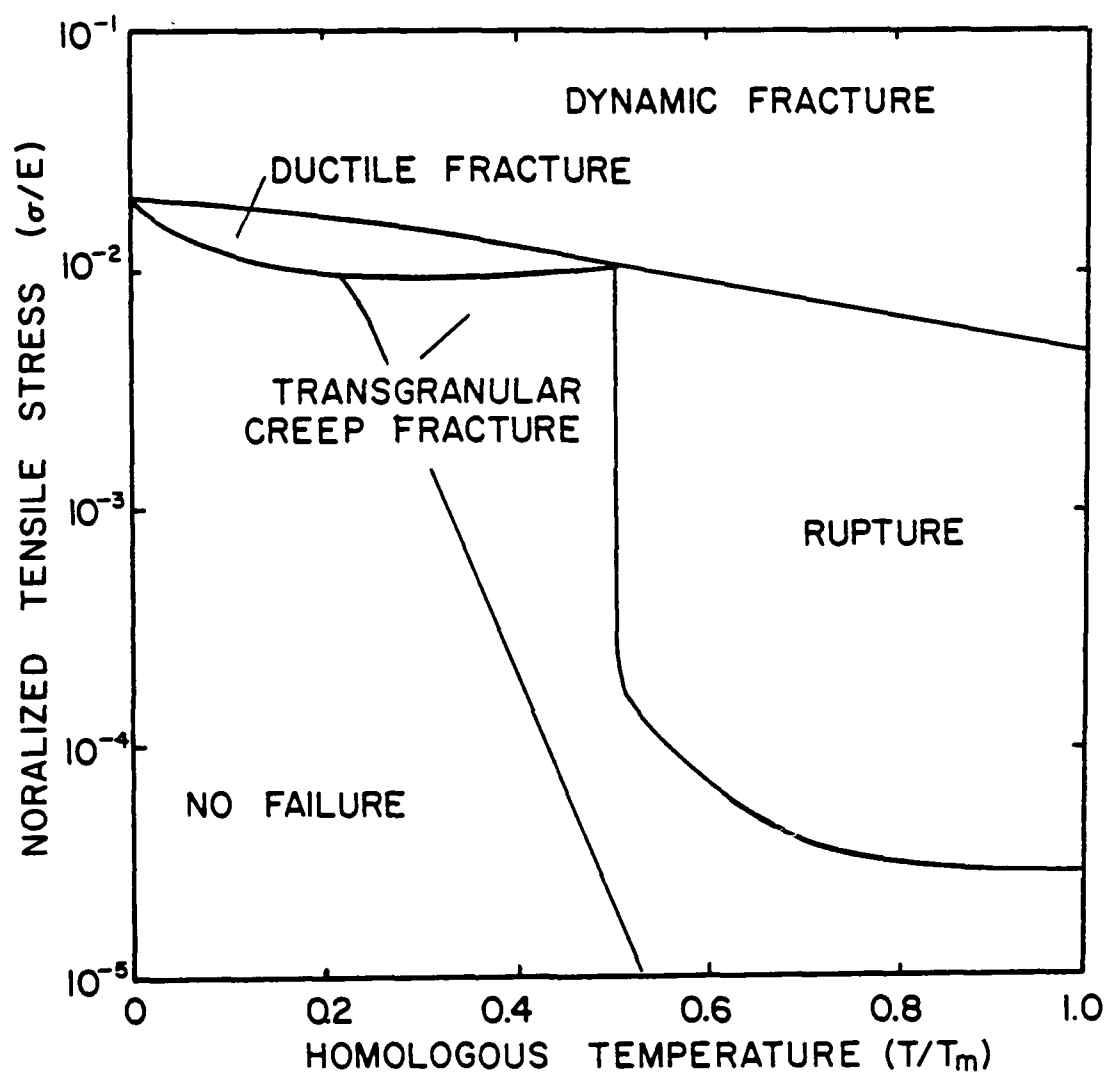


Figure 3.5(a) Fracture mechanism map for Ti-6Al-4V (60, 61). High temperature ductility loss failures occur at the intersection of the regions labelled ductile fracture, dynamic fracture, and rupture.

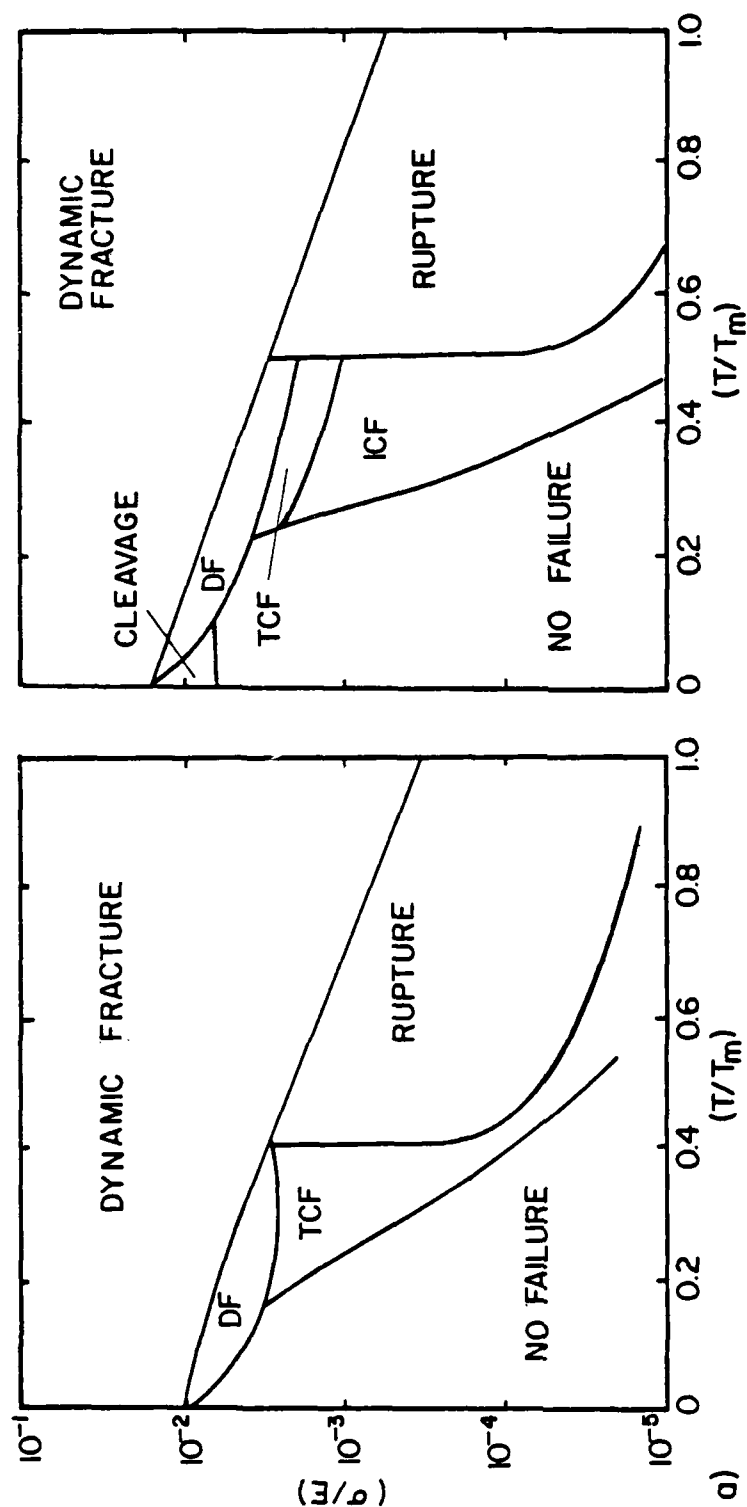


Figure 3.5 Fracture mechanism maps for iodide (b) and commercial purity (c) titanium (60, 61). Note that the map for commercial purity titanium (c) contains cleavage and intergranular creep failure regions.

$0.5T_m$, the failure mechanism was identified as ductile fracture, characterized by a traditional "cup and cone" fracture surface appearance. At still lower stresses and temperatures in the range of $0.3-0.5T_m$, the failures were by either intergranular or transgranular creep failure, and at temperatures above $0.5T_m$, the samples failed by ductile rupture. In some alloys, commercial-purity titanium for example, the region of ductile fracture does not extend to the lowest test temperatures. In these cases, a cleavage failure region is also identified (60,61).

The stress and temperature range used for preliminary ductility testing of Ti-6Al-4V is superimposed on the ductility map for this alloy. As can be seen, the testing of Ti-64 was done primarily in the dynamic fracture range, with some of the weakest specimens being in the rupture region. This is in contrast with the appearance of the fracture surfaces. Only the specimens which failed at points within the rupture region appear as predicted by the fracture map. The samples tested within the minimum ductility region have an appearance similar to that of those in the intergranular creep rupture region. At lower temperatures, the fracture appearance most closely resembles those in the ductile fracture region. This sequence of changing fracture surface appearance with temperature is as

predicted by the fracture map but to occurs at stress levels which are higher than predicted. Perhaps this discrepancy is due to the relatively low strain rate used in the testing which produced the failure mechanism maps, 3×10^{-5} /s. This contrasts with the results of Ushkov (59) which showed that very low strain rates could suppress the formation of voids and result in very high ductility. This suggests that perhaps the strain rate used by Rao, et.al. (60,61) was too low to highlight the existence of the low ductility region.

3.1.6 CSM Welding Research

The weld cracking susceptibility of Ti-6211 and Ti-64 has been investigated using the Varestraint test (13, 62-66). In this test, a constant augmented strain is imposed on a section of weldment which varies in temperature from just below the liquidus to some much lower temperature. Following testing, the samples were examined and the extent and location of cracking noted. The location of the cracking, combined with thermal analysis of the weldments, were then used to determine the thermal history of the cracked region and the critical temperature of cracking (63).

It was determined that Ti-64 was not susceptible to cracking in either GTA or GMA welding. This was also found with Ti-6Al-2V, and quaternary alloys of Ti-6Al-2V plus 2,

4, and 6 Zr. In Ti-6211, cracking was observed in both the fusion and heat-affected zones of GTA weldments and on the fusion line of GMA weldments. This cracking is shown in Figure 3.6 (63). In all cases, the cracking occurred by ductile rupture along the prior beta grains, identical to that seen in the hot ductility dip failures of Lewis and Caplan (6). Fractographs of the weld crack surfaces are shown in Figure 3.7. It was found that the cracking temperature increased as the heat input increased and the cooling rate decreased. When plotted on the CCT diagram of Damkroger (13), the locus of points which define the restraint cracking falls within the beta to alpha transformation, near the transformation finish, and in the same temperature range as the hot ductility dip (66). This was shown in Figure 3.3 (49,66). This suggests that the transformation is related to the loss of ductility.

In all cases, the microstructures in the region of cracking consisted of Widmanstätten plus grain boundary alpha and alpha' in an equiaxed prior beta grain structure. This microstructure, shown in Figure 3.8, is similar to those seen by Lewis and Caplan (6). The large lenticular patches which appear within the Widmanstätten matrix in Ti-6211 have been identified by Lewis and Williams as alpha' martensite. In comparison, Ti-64, which showed no tendency

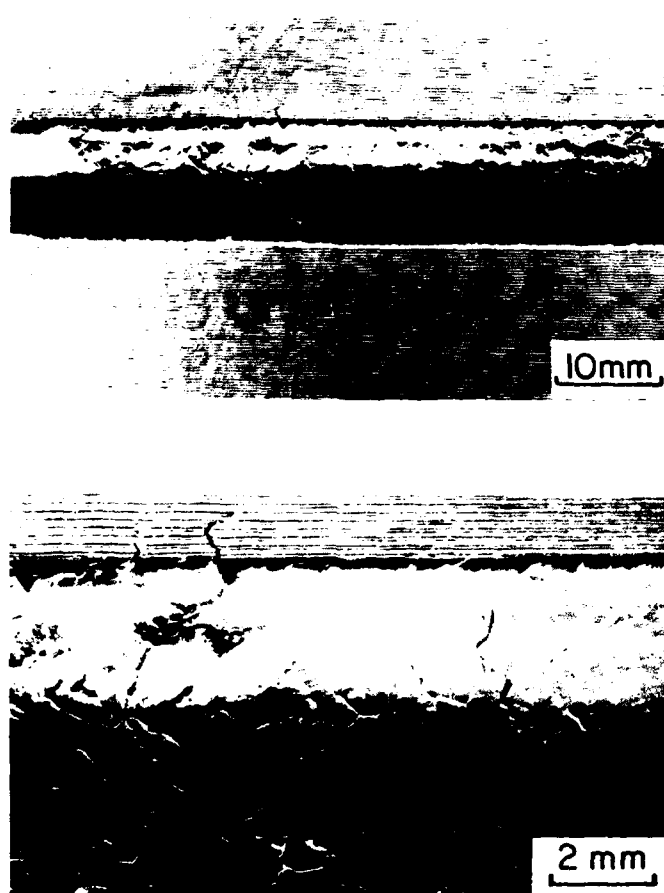


Figure 3.6 Varcstraint weld cracks in autogenous GTA weldments of Ti-6211 (63). Both fusion zone and heat-affected zone cracking can be seen.

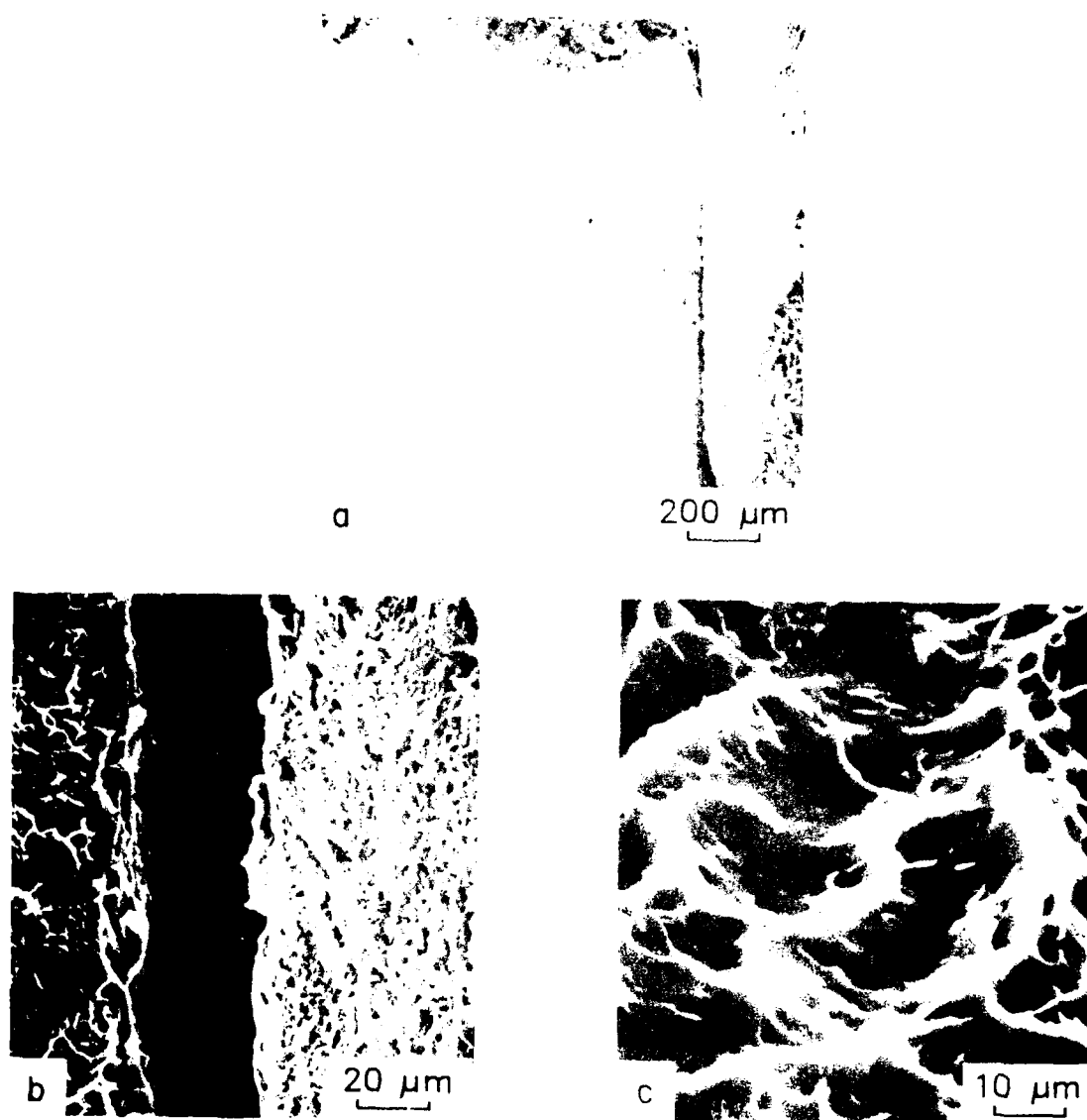


Figure 3.7 Fractographs of varestraint weld cracks in a Ti-6211 GTA weldment (63). Cracking is macroscopically brittle (a), but occurs by localized ductile rupture (c).

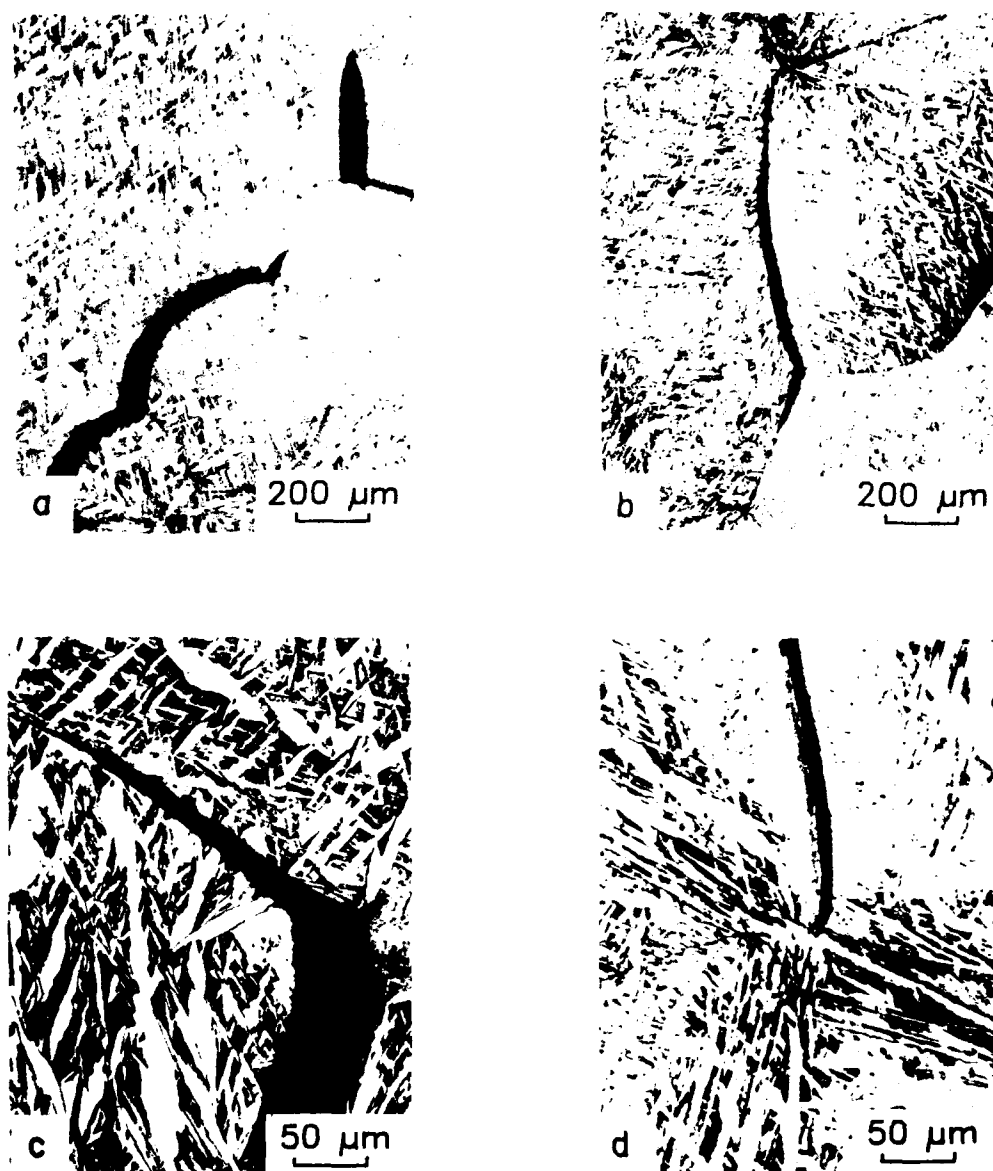


Figure 3.8 Optical micrographs of fusion zone (a, c) and heat-affected zone (b, d) regions in a Ti-6211 GTA weldment showing coarse, lenticular alpha prime martensite (63).

to crack, has a much finer structure, Figure 3.9. The Ti-64 microstructure also contains normal, fine, α' martensite, and has a thicker grain boundary α film than does Ti-6211. A similar observation was made regarding the apparent microstructural dependence of the ductility loss during a study of GMA weld restraint cracking (66). In the GMA welds, cracking occurred at the fusion line at the root of the last bead deposited. The weld bead crown however, which was subjected to the highest strain, did not crack. The microstructure at the bead crown had significantly finer transformation products within the equiaxed prior beta grains as a result of a higher cooling rate.

The effects of oxygen and nitrogen contamination were also investigated. These results are presented in Figure 3.10 (63,64). It can be seen that both fusion zone and heat-affected zone cracking increase with oxygen and nitrogen content up to approximately 0.15% nitrogen or 0.2% oxygen. Beyond these levels, cracking fell to essentially zero. This was attributed to the change in prior beta grain shape from equiaxed to elongated and the refinement of the Widmanstätten structure.

Four main conclusions can be drawn from the CSM welding research. The first is that the weld cracking seen in

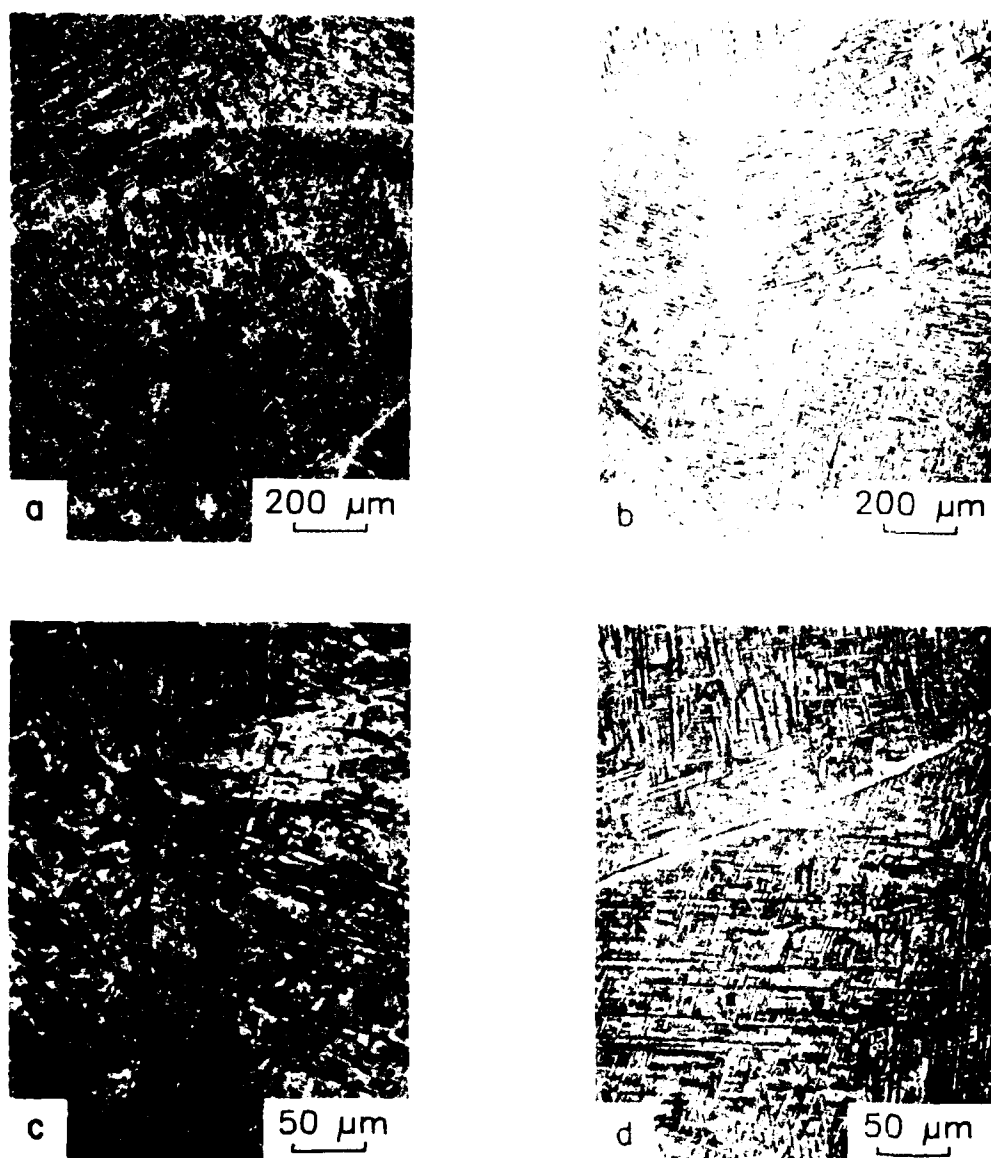


Figure 3.9 Optical micrographs of fusion zone (a, c) and heat-affected zone (b, d) regions in a Ti-6Al-4V GTA weldment showing fine Widmanstatten alpha plus beta and grain boundary alpha (63).

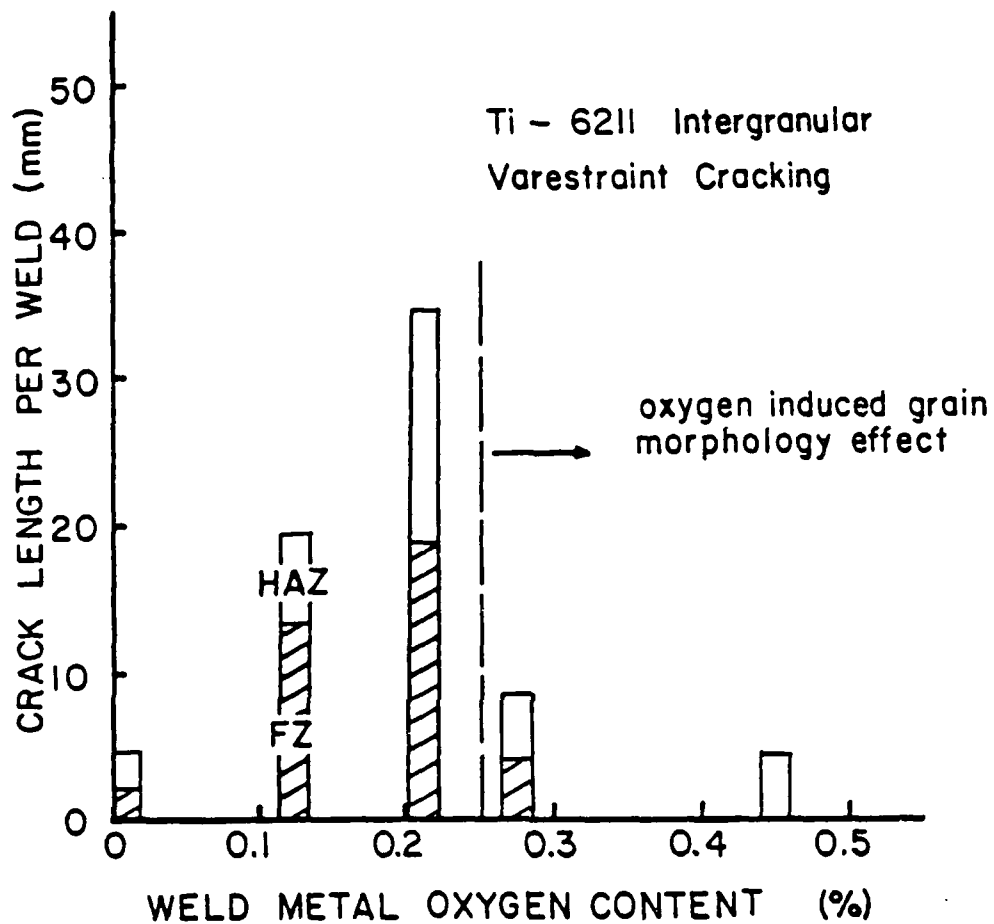


Figure 3.10(a) Effect of weld metal oxygen content on varestraint weld cracking in Ti-6211 (64). Cracking increases with oxygen content up to 0.2% then decreases due to a change in grain morphology.

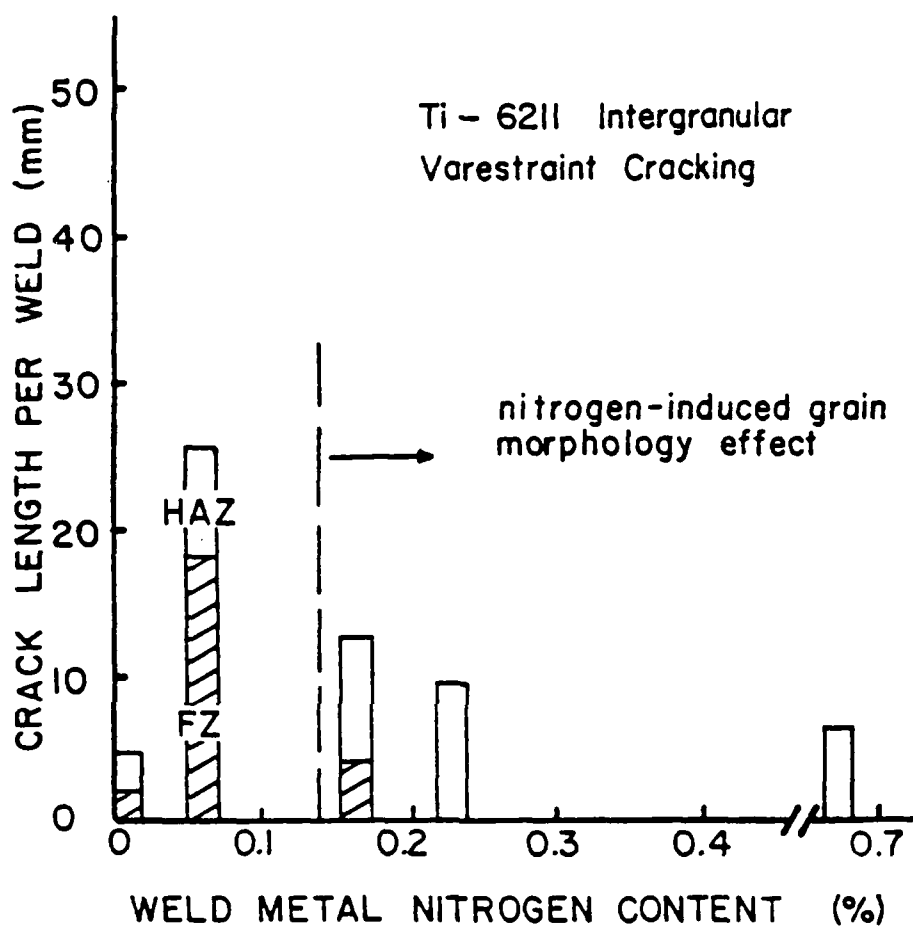


Figure 3.10(b) Effect of weld metal nitrogen content on varestraint weld cracking in Ti-6211 (64). Cracking increases up to 0.1%.

varestraint testing appears to be the same phenomenon as the hot ductility dip (6). The second is that the loss of ductility is associated with the beta to alpha transformation. Third, the cracking is related to a particular room temperature microstructure hence combination of alloy content and transformation rate. The fourth observation is that small amounts of oxygen and nitrogen contamination increase the cracking susceptibility of Ti-6211 (64).

3.1.7 Summary of High-Temperature Studies

A few general conclusions can be made regarding the high-temperature investigations which have been conducted to date. The first is that the hot ductility dip and the occurrence of weld cracking seem to be different manifestations of the same phenomenon, a general loss of ductility in the temperature range of the beta to alpha transformation finish. The ductility loss is a function of alloy content and seems to be tied to the presence of 5-6% Al and 2-3% other alloy elements. In terms of specific elements, Sn and the Nb+Ta+Mo combination in Ti-6211 lead to severe ductility losses. A specific combination of heat treatment and alloy content appear to be responsible, one which produces a relatively coarse Widmanstätten plus grain boundary alpha transformation structure within equiaxed

prior beta grains. The ductility loss is also particularly severe in the case of large prior beta grains. These microstructural conditions are relaxed in the case of Ti-6211 where virtually all transformation structures seem equally susceptible to the ductility loss. Similarly, Ti-Al-Sn ternary alloys also seem susceptible to the ductility loss regardless of microstructural considerations.

3.2 Analysis of Existing Models

Two models have been specifically proposed to explain the high temperature ductility loss in alpha-beta titanium alloys. In the following section, these models will be discussed individually and summarized with respect to the body of data regarding the high temperature ductility loss.

3.2.1 Solute Partitioning Model

The solute partitioning model, proposed by Lewis (6) and presented schematically in Figure 3.11, states that the underlying cause of the hot ductility dip is the solute partitioning which occurs during the beta to alpha transformation. Lewis (6, 49) has proposed that the element partitioning is sulfur, and Inouye and David (57) have suggested that it is boron. In this model, as the material transforms the alpha is believed to reject impurities which then coat the advancing interface. If the material is

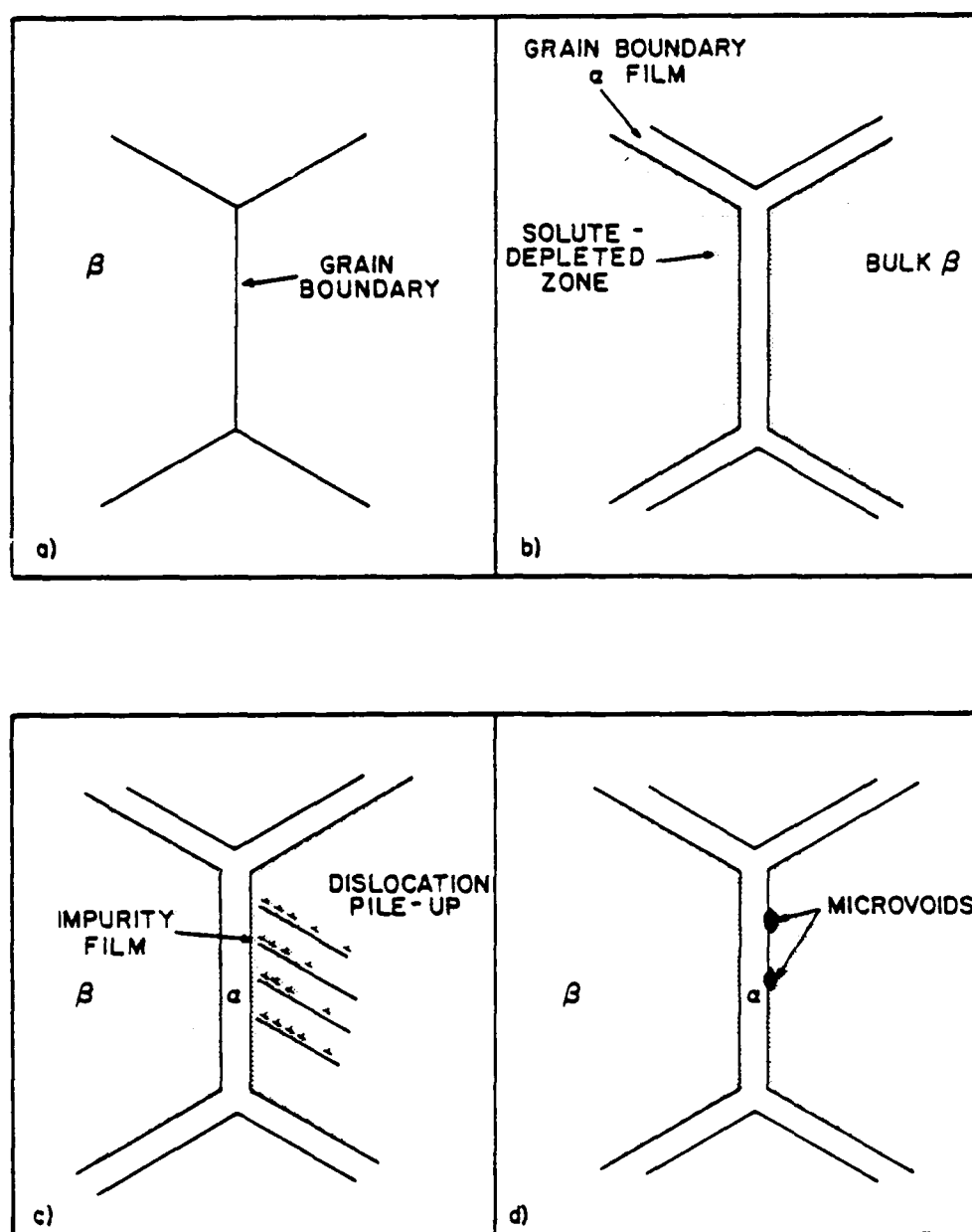


Figure 3.11 Schematic of the solute partitioning model (6). Strain is concentrated in a solute-depleted zone adjacent to the grain boundary α film (b) and blocked at an impurity-coated α/β interface (c), causing microvoid nucleation (d).

strained at this point in the transformation, slip is concentrated in the weaker beta matrix. The slip paths terminate at the alpha/beta interface because the impurity film prevents the slip from being transferred from the beta to the alpha. This results in dislocation pile-ups, localized stress concentration, and void nucleation at the alpha/beta interface. In this model, the slip concentration may be aided by a weakened solute-depleted zone near the interface (67).

The failures associated with the high temperature ductility loss are not typical of grain boundary embrittlement failures. Unlike grain boundary embrittlement, testing within a specific temperature range is required to achieve the high temperature ductility loss. Further evidence is the appearance of the fracture surfaces of the hot ductility dip samples, which are dimpled rather than smooth (55). However, the solute partitioning model maintains that the impurity film is the controlling feature. Without this film, slip in the beta phase would simply pass to the alpha phase. In the solute partitioning model, the behavior of different alloys is predicted because of changes in the solubility of these alloys for impurities (67).

A second difficulty with the solute partitioning model is its failure to explain the observed effect of cooling

rate on the hot ductility dip behavior. In rapidly cooled Ti-6211 welds, vareststraint cracking was suppressed (66). These welds had a Widmanstatten plus grain boundary alpha or alpha' structure at room temperature. Therefore, any non-equilibrium solute build-up associated with the formation and movement of an allotriomorphic alpha interface must have existed in these welds, yet they did not crack. One possible way to interpret this within the solute partitioning model is to instead say that the ductility dip results from an equilibrium partitioning of the impurities to the interface. However, Starke et. al. (55) found that ductility was increased in samples held at the test temperature prior to testing. A third problem with the solute partitioning model is that rejection of impurities by the advancing alpha interface has not been demonstrated (68).

It is apparent that a strain concentration mechanism is necessary to create the loss in high temperature ductility. This point is not directly contested by the proponents of the solute partitioning model. This model simply states that, while a strain concentration is necessary, it will not cause the ductility dip without the presence of an impurity film (67).

3.2.2 Differential Strength Model

The differential strength model, developed by Starke, et. al. (55), is schematically represented in Figure 3.12. In this model the critical condition is the existence of a grain boundary alpha film and an equiaxed prior beta grain structure. During the beta to alpha transformation, allotriomorphic alpha is nucleated and grows at the boundary between two beta grains. Because these grains have different orientations, the alpha will generally have the Burgers relationship with only one of the beta grains. This model proposes that a Burgers related alpha/beta interface will permit the transfer of slip between the two phases, but a non-Burgers related interface will not. In contrast to the work of Lewis and Caplan, (6, Figure 3.2) this model also maintains that the grain-boundary alpha film is weaker at 800°C than the transformed beta grain itself. When loaded, the strain is concentrated in the weaker grain boundary alpha and blocked at a non-Burgers related alpha/beta or alpha/matrix interface. This results in dislocation pile-ups, stress concentration, and void nucleation. This mechanism is similar to that proposed for two-phase titanium alloys at room temperature by Greenfield and Margolin (28). In the differential strength model, a grain boundary alpha film is required to provide the strain

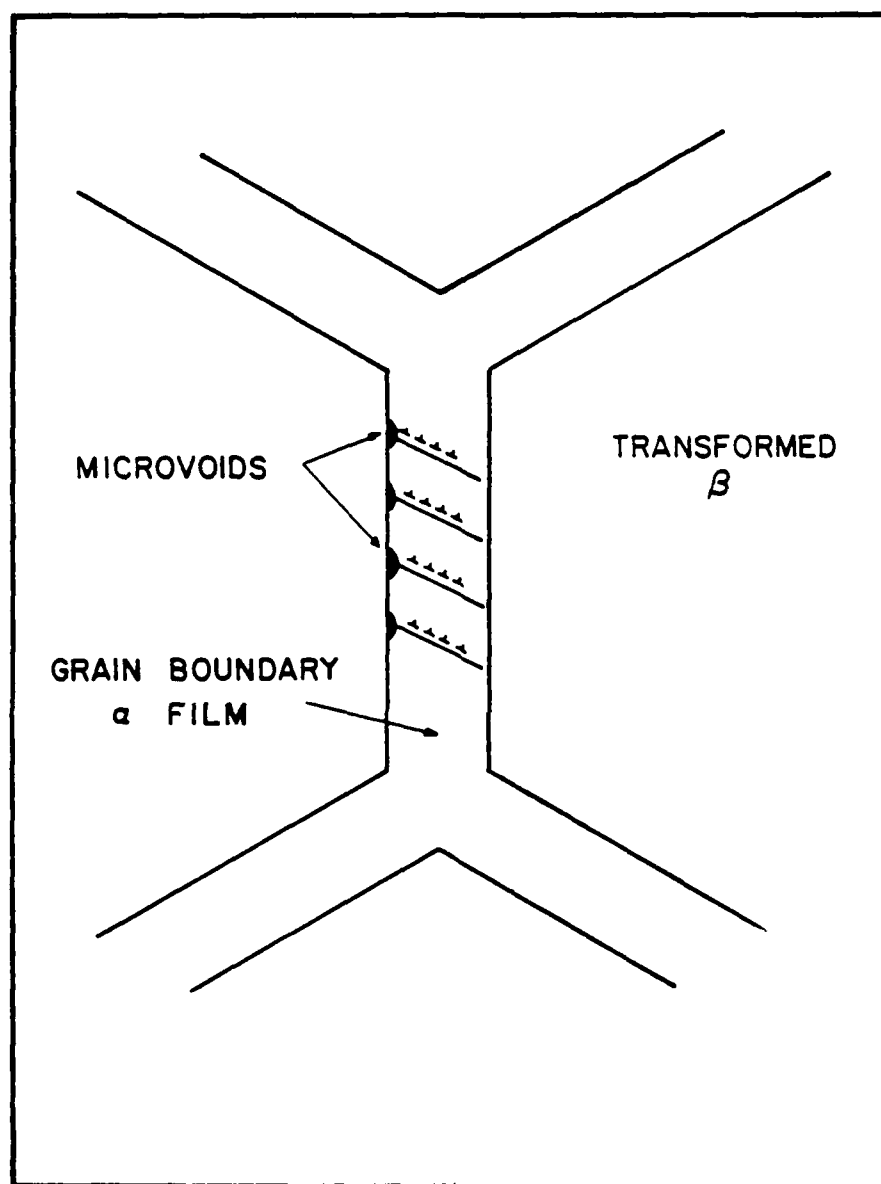


Figure 3.12 Schematic of the differential strength model (55). Strain is concentrated in the weaker grain boundary alpha film and blocked at an alpha/beta interface, causing void nucleation.

concentration adjacent to a non-Burgers related interface. Equiaxed prior beta grains are necessary to insure that a grain boundary film will be favorably oriented for slip (54-56).

The differential strength model directly addresses only the case of a grain boundary alpha film coexisting with beta or a transformed beta matrix, and isothermal testing of a stable microstructure. However, the insensitivity to transformation structure observed by Starke, et. al. (55) was taken as an indication that the results would be the same for testing on cooling during a rapid thermal cycle. In the development of the differential strength model, the alloy to alloy variation of the ductility dip is not specifically discussed. It is implied that changes in alpha and beta compositions are believed to alter the strengths and perhaps slip systems of the two phases, hence, the extent of strain localization (69).

Difficulties arise with the differential strength model as well. It has been shown that the severity and temperature of the ductility loss are functions of cooling rate (49,62-66). In particular, the ductility dip is substantially ameliorated in samples either cooled very rapidly or held at the test temperature prior to testing. In both cases, the kinetics of the beta to alpha

transformation and thus the transformation structures were altered. It is possible that the scope of the Starke investigation (55) was too narrow to discover these differences. Similarly, in samples tested on heating in a second thermal cycle, the loss of ductility was not as severe as that seen on cooling in the initial thermal cycle (6, 55). This suggests that the dynamic conditions of the rapid thermal cycle at least accentuate the loss of ductility.

The most severe shortcoming of the differential strength model is its failure to adequately explain the observed alloy dependence of the hot ductility dip. This model is contingent on the strength of the transformed beta being greater than the grain boundary alpha. This conflicts with the results of Lewis and Caplan on alloys other than Ti-6211 (6, Figure 1.1). Lewis and Caplan found that Ti-6Al, an alpha alloy, had a significant loss of high temperature ductility, but unalloyed titanium did not. This indicates that the addition of aluminum, which partitions to and strengthens the grain boundary alpha film, is associated with the hot ductility dip (1, 6). This is the opposite of the relationship required in the differential strength model. Similarly, in welds deliberately contaminated with oxygen and nitrogen, also effective alpha strengtheners,

weld cracking was increased (63, 64).

3.2.3 Summary of Existing Models

Strain localization is a central feature of both models. The solute partitioning model states that it occurs in a weaker beta phase and in impurity film prevents it from being transferred to the alpha phase. The differential strength model maintains that it occurs in a weaker grain boundary alpha film and that a non-Burgers-related alpha/beta interface causes dislocation pile-ups and void nucleation. In the differential strength model, the irreversible conditioning is believed to be the creation of a susceptible microstructure. Any sample possessing this microstructure, grain boundary alpha surrounding equiaxed prior beta grains, is susceptible to low-ductility intergranular failure when tested at the critical temperature. In the solute partitioning model, the conditioning is the coating of the grain boundary alpha/beta interface with an impurity film. Once this film is created, the sample will display a ductility loss, the severity of which is controlled by the extent of strain localization.

It is apparent then that the existing models for the hot ductility dip in titanium alloys cannot be viewed as definitive. It is the purpose of this thesis to propose an alternative model and to evaluate this model within the

context of a general investigation of the high temperature ductility of alpha-beta titanium alloys.

3.3 Lattice Incompatibility Model

The lattice incompatibility model was initially conceived by B.B. Rath of the Naval Research Laboratory (70). This model proposes that the major cause of the hot ductility dip is the lattice incompatibility associated with the beta to alpha transformation. As the material cools, the beta to alpha transformation begins at the beta grain boundaries, creating a grain boundary alpha film followed by Widmanstatten colonies. This situation exists over a narrow temperature range prior to the transformation of the bulk beta grain. Because the close-packed hcp alpha is more dense than the bcc beta, the transformation results in a volumetric contraction. This is shown in Figure 3.13, a plot of relative dilation versus temperature for Ti-6211 cooled at 4°C/s. The result of this contraction is that a tensile stress is imposed on the grain boundary alpha region and advancing alpha/beta interface. This state exists until the bulk grain transforms. The lattice incompatibility model proposes that this stress is related to the high temperature ductility loss sometimes seen in titanium alloys (28). The lattice incompatibility model is shown schematically in Figure 3.14.

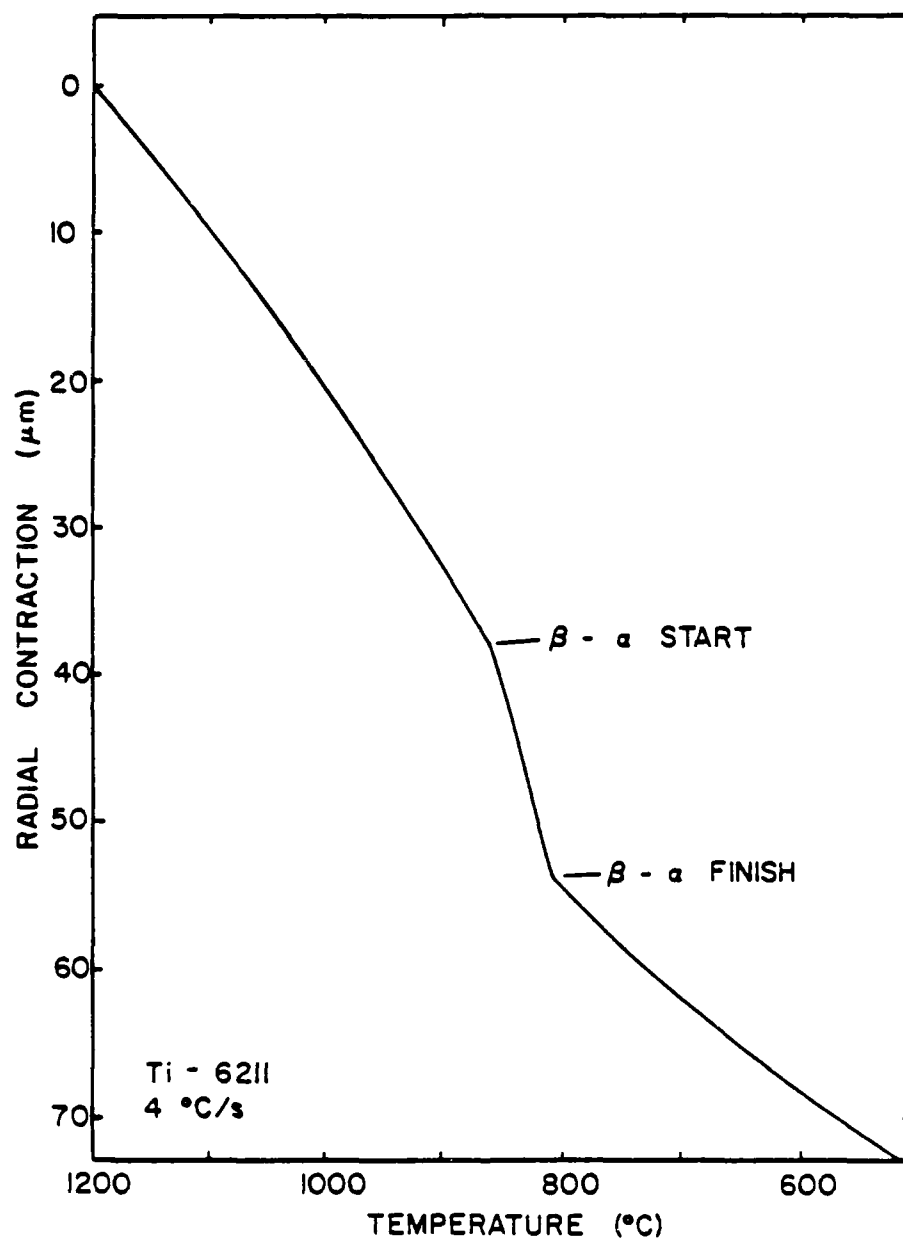


Figure 3.13 Ti-6211 dilatometric curve showing contraction which occurs during the beta to alpha transformation.

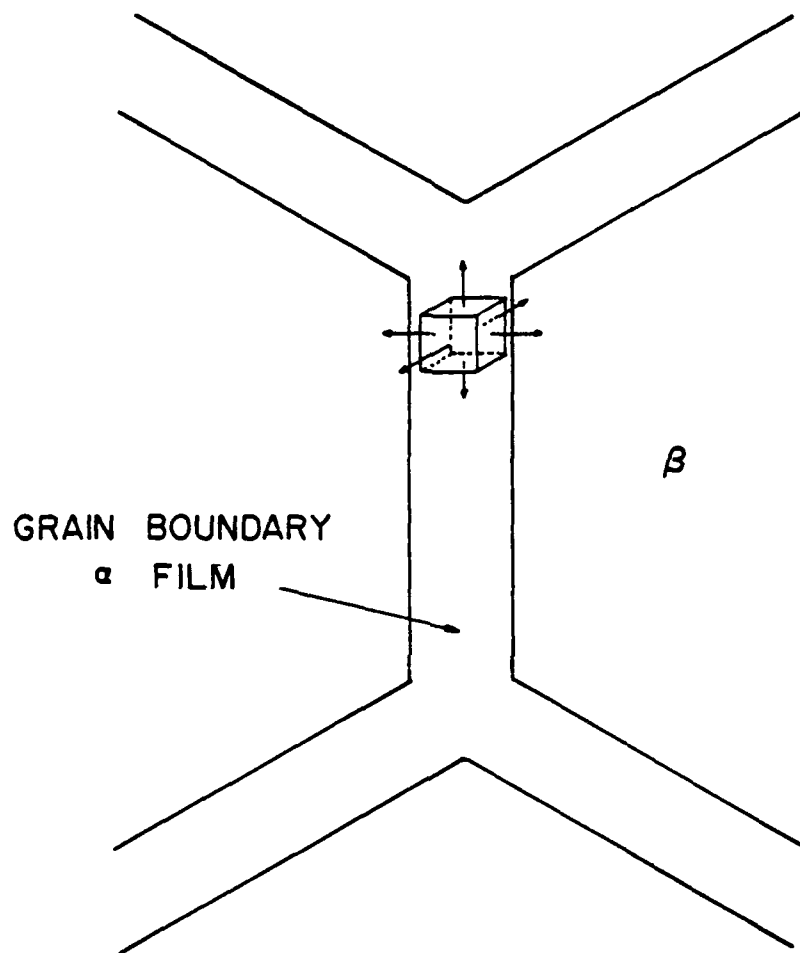


Figure 3.14 Schematic of the lattice incompatibility model (70). The lattice incompatibility imposes a tensile stress on the constrained alpha film which contributes to the local stress state and causes failure within the alpha film.

With the lattice incompatibility model, the varying susceptibility of different alloys is predicted. The specific alloy additions alter the lattice parameters of the alpha and beta phases, affecting the transformation stress. Data on element partitioning and lattice parameter effects in titanium alloys is limited. However, the general observations that can be made based on the existing data tend to support the lattice incompatibility model. Pearson (71) published a compilation of the lattice parameters of several binary systems. The data for binary alloys based on titanium is shown in Figure 3.15. This figure shows that aluminum reduces the lattice parameters of the alpha phase. Because aluminum partitions to the alpha phase, the effect of aluminum is to increase the relative contraction and accentuate the tensile stress developed during the transformation. This is consistent with the data of Lewis and Caplan (6) which shows that a minimum amount of aluminum is necessary to cause the ductility loss.

Figure 3.15 also shows the effects of several beta stabilizing elements on the lattice parameters of the beta phase. Vanadium and molybdenum contract the beta lattice while niobium and tantalum either slightly enlarge the lattice or have no effect. This also consistent with the observed alloy variations. Lewis and Caplan (6) and Hayduk,

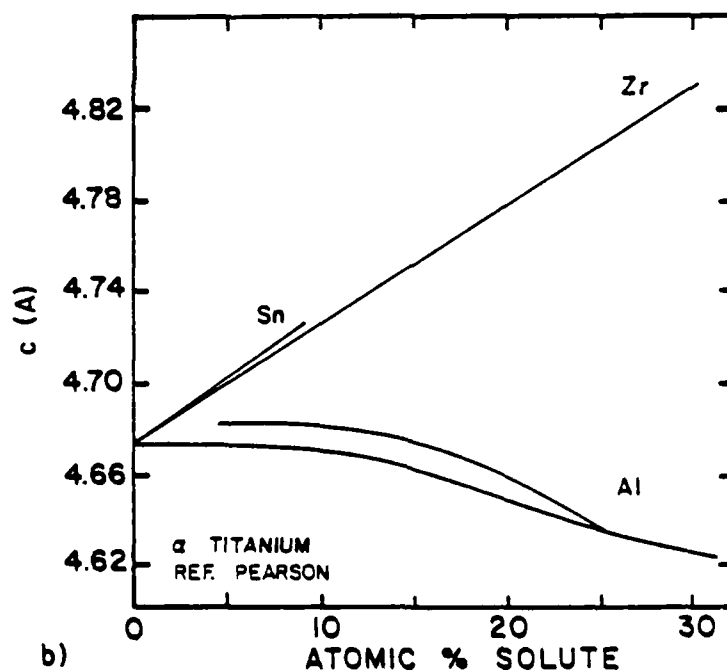
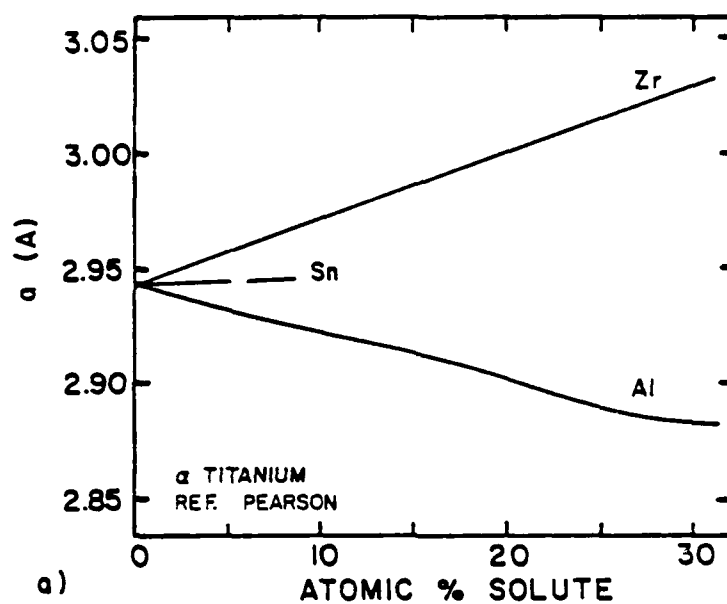


Figure 3.15(a) Lattice parameter effects of binary additions to alpha titanium (71). The addition of aluminum reduces both the a (a) and c (b) parameters.

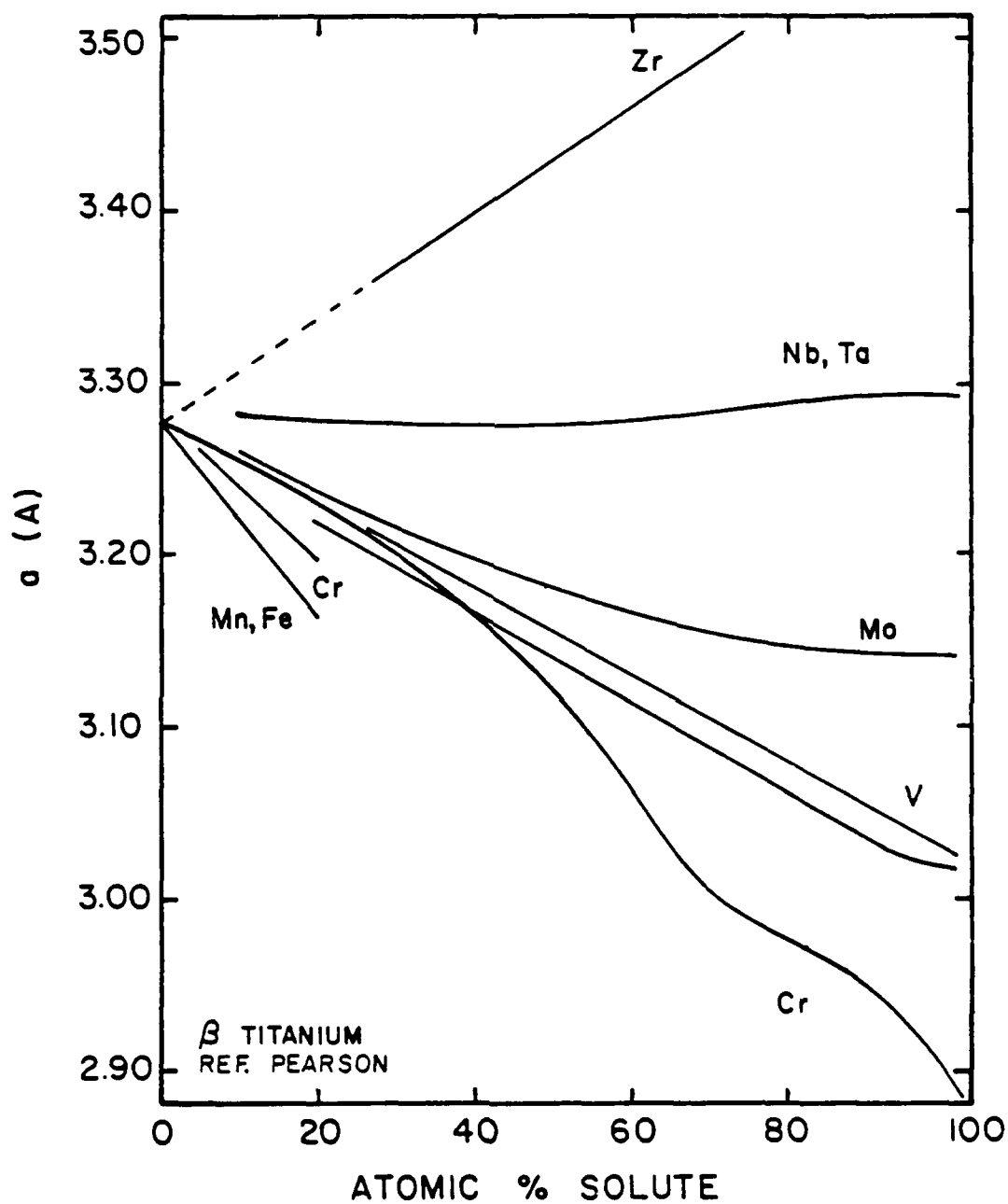


Figure 3.15(b) Effects of various elements on the lattice parameter of beta titanium (71). Vanadium and molybdenum contract the beta lattice but niobium and tantalum have little effect.

et. al. (63, 64) found that Ti-64 is far less susceptible to the ductility loss and to vareststraint weld cracking than is Ti-6211.

The lattice incompatibility model is also consistent with the observed effect of cooling rate on minimum ductility temperature, an effect seen in both Gleeble and Vareststraint testing (49, 63-66). If the critical event is the development of stress during the beta to alpha transformation, the region of minimum ductility for any given alloy should be related to the beta to alpha transformation. This was shown in Figure 3.3, a plot of minimum ductility temperatures and vareststraint cracking temperatures superimposed on the Ti-6211 CCT diagram of Damkroger.

Similarly, the lattice incompatibility model explains why the ductility dip may be reduced by rapid cooling. For a given alloy, the amount of transformation at the prior grain boundaries, hence the amount of transformation stress developed, is reduced as the cooling rate is increased. An additional consideration is that as the cooling rate is increased, the transformation temperature is reduced. If the materials' response to the transformation stress requires plastic deformation, it will be reduced if the transformation occurs at lower temperatures.

There are several possible mechanisms by which the tensile stress developed during the beta to alpha transformation may contribute to the ductility loss. The simplest explanation is a superposition of the transformation stress and an applied stress. Because both stresses will be a maximum at the grain boundary alpha/matrix interface, the result is void nucleation at this interface. A corollary to this is to assume that the transformation stress increases the triaxiality of the local applied stress state in the interface region. This also results in increased void nucleation and growth, effects which have been documented in Ti-64 (59, 72). In this case, the temperature dependence of the ductility loss represents a situation which meets two conditions. The first is that the applied stress is concentrated at the interface and the second is that the bulk strength of the material is low enough for the residual stress in the grain boundary region to be a significant portion of the local fracture strength.

A second possible way in which the transformation stress may contribute to the hot ductility dip is by the accommodation of this stress by local plastic flow. One result of this plastic flow could be the direct nucleation of microvoids. This explanation is also consistent with the observed temperature dependence. The criteria here is

again a situation where the deformation characteristics concentrate stress at the interface and where the bulk material strength is low enough for the pre-existing void nuclei to significantly contribute to the fracture.

Plastic flow caused by the transformation stress could also create regions of high dislocation density near the interface. This substructure then interacts with dislocations moving in response to an applied stress to nucleate voids. Support for this mechanism exists in that dislocation substructures have been seen in the interface phase, which forms under conditions similar to those associated with the hot ductility dip (15-18). This idea has also been discussed in other systems and is sometimes referred to as one type of geometrically required dislocation density. A dislocation substructure would also be affected by transformation rate and the elastic properties of the two phases.

A third possible result of the transformation stress is the creation of an excess concentration of vacancies which condense to form microvoids. The excess quantity of vacancies could result from the rapid generation and climb of dislocations caused by the incompatibility at the interface. One such mechanism is the grain boundary source model of Price and Hirth (73), where the grain boundaries

act as a continuous source of screw dislocations. At high temperatures, the excess vacancies could rapidly diffuse along the interface and coalesce into large vacancy complexes, and eventually, microvoids. This type of condensation process was shown to occur in copper at 400°C - 500°C by Hull and Rimmer (74).

Regardless of their specifics, all of these mechanisms share the basic premise of the lattice incompatibility model. This premise is that the extent of the ductility loss can be related to the extent of the lattice incompatibility between the beta and alpha phases. This model and investigation are based on a simple volumetric interpretation of lattice incompatibility. Ideally, the effect of the alpha c/a ratio on lattice incompatibility and transformation stress would also be investigated. Similarly, lattice parameter gradients resulting from non-equilibrium partitioning would be considered as well.

The lattice incompatibility concept requires that three criteria be met to cause the high temperature ductility loss. The first is that the alloy be of a susceptible composition. The magnitude of the volumetric contraction is controlled by the composition of the alpha and beta phases. Second, the beta to alpha transformation must be traversed at an acceptable cooling rate to insure that the grain

boundary alpha plus beta microstructure exists at some point. The third criteria is that the transformation occur at a sufficiently high temperature to allow either local plastic deformation, void nucleation, or vacancy diffusion and condensation to take place. If these criteria are met and the material is tested within the critical temperature range, the lattice incompatibility model predicts that low ductility will result.

EXPERIMENTAL PROCEDURE

This investigation was designed to evaluate the lattice incompatibility model of Rath (4) within the context of an overall investigation of the high temperature ductility of alpha-beta titanium alloys. Specifically, the experimental procedure consisted of four sections. The first section, a series of initial screening tests, was used to establish that the high-temperature ductility loss reported by Lewis and Caplan (6, 49) could be duplicated using the CSM Gleeble test facility. These tests were also used to develop a hot ductility testing procedure. The second section of the investigation was the development of CCT diagrams for each of the model alloys and an analysis of their microstructures with respect to phase stability and transformation kinetics. The third section was the calculation of the beta to alpha lattice incompatibility of each alloy based on high-temperature lattice parameter measurements and radial dilatometry. The final step of the experimental procedure was high temperature tensile testing of six specific alloys. The results of these tests were combined to characterize the high temperature deformation behavior of alpha-beta titanium alloys with respect to alloy content, lattice incompatibility, and transformed microstructure.

4.1 Initial Screening Tests

The alloys used in the initial testing were Ti-6211, Ti-64, and Ti-6Al-2V-2Zr. The compositions of these alloys are included in Table 4.1. Hot ductility tests were run using the Gleeble 1500 thermal mechanical testing facility. This consisted of tensile testing, on cooling, samples which had been thermally cycled to above the beta transus. A procedure was chosen which consisted of:

- 1) heating to 1200°C in two minutes at a constant rate
- 2) holding for 5 minutes at 1200°C
- 3) cooling at 10°C/s to the test temperature and testing upon reaching the test temperature.

Prior to the selection of this procedure, several aspects of the test technique were evaluated. Two parameters which were examined were annealing time and temperature, and effective strain rate.

4.1.1 Annealing Time and Temperature

The annealing time and temperature control the prior beta grain size, which has been shown to influence high temperature ductility (59). Five minutes at 1200°C was found to be long enough to insure complete transformation to beta and to provide a consistent prior beta grain size of approximately 0.3 mm. In some cases, other combinations of annealing time and temperature were used. These will be

Table 4.1

Compositions of Materials Used

Alloy	Composition in Weight Percent					
	Al	V	O	H	N	Fe
CP Ti (1)			0.1	0.002	0.11	0.09
Ti-6Al (2)	5.89					
Ti-6Al-2V (2)	5.91	1.98				
(3)	5.42	2.05	0.126	0.003		0.04
(4)	6.05	2.03	0.107	0.001		
Ti-6Al-4V (1)	6.10	4.20	0.200	0.009	0.02	0.02
(5)	6.00	4.10	0.200	0.007	0.02	0.18
(2)	5.98	4.02				0.04
Ti-6Al-6V (2)	5.96	5.82				0.09
(3)	5.91	6.09	0.095	0.002		0.06
(4)	5.76	5.93	0.116	0.003		0.05
	Al	Mo	O	H	N	Fe
Ti-6Al-2Mo (2)	5.83	1.80				0.01
Ti-6Al-4Mo (2)	5.83	4.01				0.04
Ti-6Al-6Mo (2)	5.86	6.39				0.02

Table 4.1 (cont.)

Alloy	Composition in Weight Percent							
	Al	Nb		O	H	N	Fe	
<hr/>								
Ti-6Al-2Nb								
(2)	6.23	2.14					0.01	
Ti-6Al-6Nb								
(2)	6.03	6.38					0.02	
Ti-6Al-4Nb								
(2)	6.06	4.32					0.02	
(3)	6.36	4.06		0.093	0.001		0.04	
(4)	6.25	3.93		0.040	0.003		0.04	
<hr/>								
	Al	Mo	Ta	Nb	O	H	N	Fe
<hr/>								
Ti-6211								
(1)	5.7	0.68	1.0	2.1	0.068	0.010	0.004	0.04
(6)	6.0	0.81	0.9	1.9	0.071	0.009	0.005	0.09
(7)	5.9	0.60	0.9	2.0	0.056	0.011	0.008	0.09
<hr/>								
	Al		V	Nb	O	H	N	Fe
<hr/>								
Ti-6Al-2V-2NB								
(3)	5.69		1.92	1.70	0.103	0.006		0.06
(4)	5.67		2.13	1.92	0.109	0.004		0.11

Table 4.1 (cont.)

Sources of Material Used
(as Noted Above)

- (1) 0.25 in. diameter rod supplied by Astro Metallurgical,
1st batch
- (2) 250g buttons supplied by TIMET
- (3) 0.5 in. diameter rod supplied by TIMET, ingot top
- (4) 0.5 in. diameter rod supplied by TIMET, ingot bottom
- (5) 0.25 in. diameter rod supplied by Astro Metallurgical,
2nd batch
- (6) 0.5 in. thick plate supplied by RMI, Hayduk thesis
material (H)
- (7) 0.5 in. thick plate supplied by RMI, last material
-no varestraint cracking (N)

noted in the discussion of the hot ductility test results.

4.1.2 Effective Strain Rate

The selection of effective strain rate was important to insure that the tensile testing was carried out under isothermal conditions and to insure sample to sample consistency. Because the Gleeble is a closed-loop (feedback-controlled) system, the actual tensile testing had to be done with the heat turned off. Too low a strain rate allowed the sample to cool prior to fracture but too high a strain rate resulted in excessive adiabatic heating of the sample. This problem, manifested as the inability to accurately control the specimen temperature during tensile testing, can be seen in the Gleeble test results of Lewis (49). Because of this, the results of his ductility mapping are confused by the uncertainty of exactly what microstructure was being testing in any given situation.

Several factors combine to determine the effective strain rate in a Gleeble specimen, including sample configuration and material, test temperature and longitudinal thermal gradient, and programmed crosshead displacement rate. The specimens used in the initial screening tests were 6.3 mm diameter rods, approximately 10 cm long and threaded on both ends. When loaded in the Gleeble test system, this sample configuration resulted in a

free span of approximately 2 cm, as shown in Figure 4.1.

The specimen is clamped between water cooled copper jaws and resistance heated by passing a current through the sample. Specimen temperature is monitored by a 0.010" diameter thermocouple spot welded to the specimen surface at the center of the free span. Type R (Pt versus Pt-13%Rh) thermocouples were used. The programmed temperature is maintained at the specimen cross-section to which the thermocouple is mounted. This, combined with the water cooled jaws, creates a longitudinal thermal gradient in the sample, shown in Figure 4.2. Because of this gradient, the deformation is concentrated in an effective gauge length, a small portion of material at the specimen center. The longitudinal thermal gradient has been extensively characterized by Duffers Scientific, Inc., the manufacturer of the Gleeble (75). They have found that for a wide range of test temperatures, the effective gauge length is the portion of the sample at a temperature higher than approximately 90% of the peak temperature. Duffers has reported that for most situations, "carbon steel" has an effective gauge length of approximately 25% of the free span. For "stainless steel", which has a thermal conductivity nearer to that of titanium, they reported that the effective gauge length is about 33% of the free span.

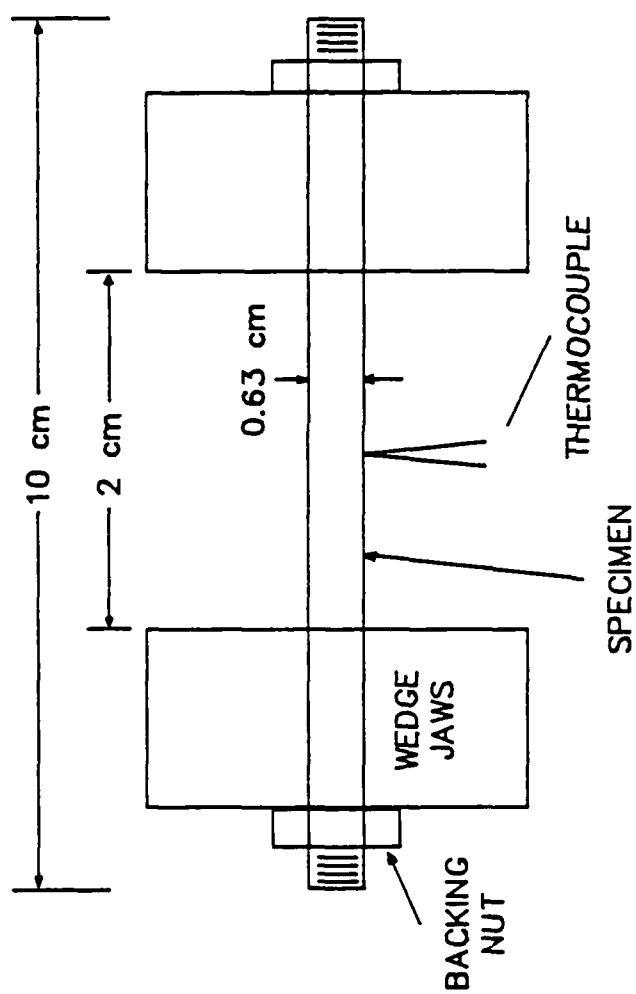


Figure 4.1 Gleeble specimen configuration for smooth specimens (no reduced section).

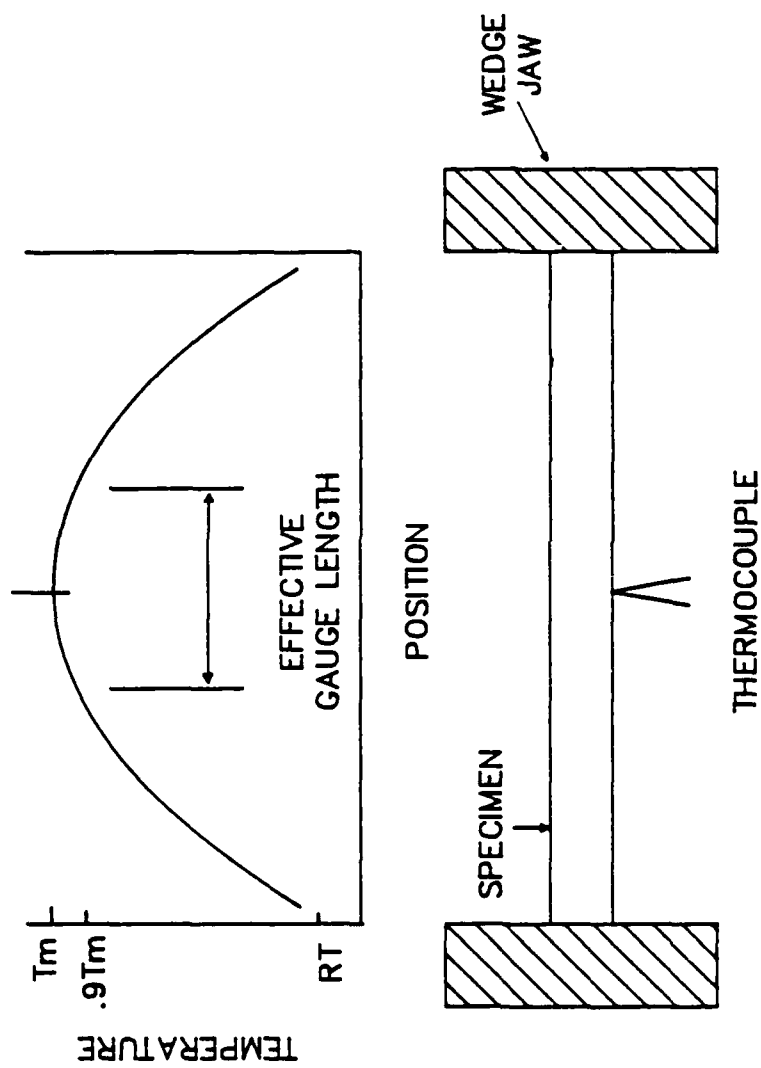


Figure 4.2 Schematic of the thermal gradient in gleeble specimens tested at elevated temperature. The effective gauge length is the length of sample at a temperature greater than 90% of the maximum temperature.

This value, 33% of the free span, was used by Lewis in the calculation of his effective strain rates (49). This value also agrees with examination of failed specimens. In samples that failed at temperatures above room temperature, the deformation was contained in the center 1/3 of the free span. Based on this, the effective gauge length for constant diameter titanium rods with a 15mm - 25mm free span was defined as the center 33% of the free span. However, if the sample has a substantially longer or shorter free span the effective gauge length will change. Also, if the sample contains a reduced section, the effective gauge length will be a portion of the reduced length which is larger than 33%.

Crosshead displacement rates from 0.01 cm/s to 10 cm/s were used. This led to effective strain rates of approximately 0.0015 s^{-1} to 15 s^{-1} . The ductility behavior was not observed to change over this range of strain rates. This agrees with the results of Lewis (49). Therefore, it was determined that changes in specimen geometry would not greatly affect the results of the hot ductility testing. A crosshead displacement rate of 1 cm/s was chosen for the remainder of the investigation. This value was selected as best minimizing both sample cooling and adiabatic heating.

4.1.3 Results of Initial Screening Tests

The initial screening tests showed that the hot ductility dip reported by Lewis and Caplan (6) could be reproduced using the CSM Gleeble facility. Ductility, measured as reduction in area, is shown as a function of temperature for Ti-6211, Ti-64, and Ti-6Al-2V-2Zr in Figure 4.3. When tensile tested during cooling at 10°C/s , Ti-6211 was found to have a large ductility loss, Ti-64 a small loss, and Ti-6Al-2V-2Zr a moderate loss.

4.2 CCT Diagram Development

Partial CCT diagrams, covering the range of cooling rates used in the hot ductility mapping, were developed for several model alpha-beta alloys. The alloys studied in this and the following sections of the experimental procedure are listed in Table 4.2. Prior work (6, 59) has shown that the high temperature ductility loss is associated with the presence of 5%-6% aluminum in combination with a beta stabilizer. Therefore, the alloy matrix was based on Ti-6Al. Vanadium, molybdenum, and niobium each affect the beta lattice parameters differently, Figure 3.15, so these elements were chosen as ternary additions to evaluate the lattice incompatibility effect. These elements also differ in their effect on phase stability, and ranked in terms of decreasing beta stabilization, have the order: vanadium,

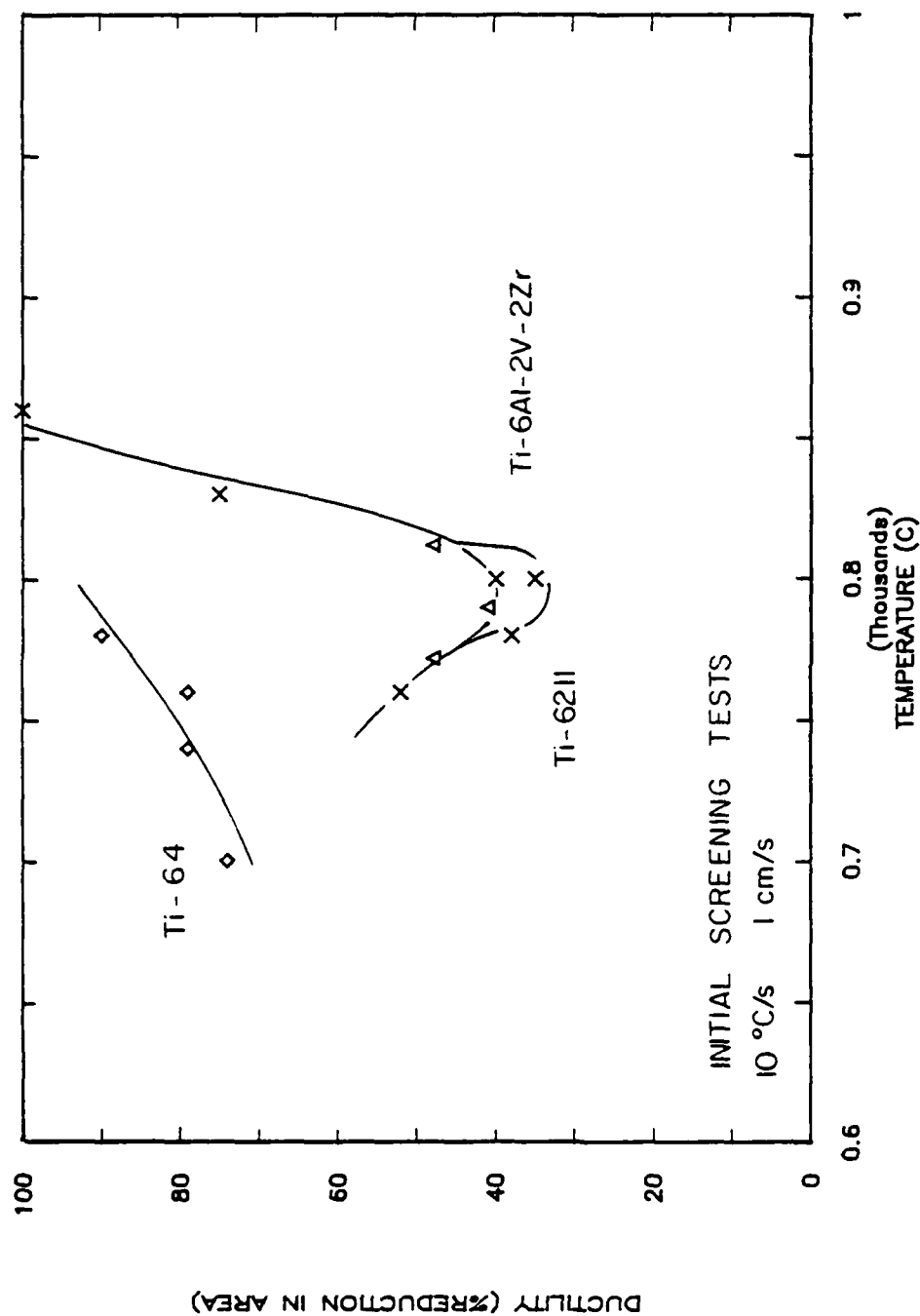


Figure 4.3 Ductility versus temperature for three alloys, cooled at 10 °C/s. Ti-6211 and Ti-6Al-2V-2Zr show a large ductility loss, Ti-6Al-4V, essentially none.

Table 4.2

Matrix of Alloys Tested

Alloy	Tests Performed		
	CCT	Lattice Parameters	Hot Ductility
unalloyed titanium	x	x	x
Ti-6Al	x	x	x
Ti-6Al-2V	x	x	x
4V	x	x	x
6V	x	x	x
Ti-6Al-2Mo	x	x	
4Mo	x	x	
6Mo	x	x	
Ti-6Al-2Nb	x	x	
4Nb	x	x	x
6Nb	x	x	
Ti-6211	x	x	x
Ti-6Al-2V-2Nb	x	x	x

niobium, and molybdenum (7,76-78). In the absence of information regarding the effect of these elements on the kinetics of the beta to alpha transformation, it was hoped that these alloys would also provide a wide range of microstructures. Other alloys investigated included unalloyed titanium (CP Ti), Ti-6Al-2Nb-1Ta-0.8Mo (Ti-6211), and a series of Ti-6Al-2V-Zr quaternary alloys. These alloys were included primarily because of their ready availability and technological importance.

The purpose of the initial alloy matrix was twofold. First, it was used to document the transformation behavior and the lattice incompatibility of these specific alloys. This allowed specific alloys to be chosen for hot ductility testing which, on the basis of the lattice incompatibility model, were expected to display a given type of hot ductility behavior. The second purpose of the alloy matrix was to provide a data base from which to predict the transformation behavior and to estimate the lattice incompatibility of alloys not specifically included in the matrix, but containing the same alloying elements.

The alloys in the initial matrix were obtained from several sources, with commercially available material being used whenever possible. Several alloys were fabricated at the Naval Research Laboratory in the form of small ingots,

or buttons. These ingots were triple-arc-remelted in a purified argon atmosphere, then beta-worked and beta annealed in air. The final ingots were ground to remove the interstitial-contaminated layer, pickled in a mild version of Kroll's reagent, and analyzed for content of the major alloying elements using wavelength-dispersive-spectroscopy. The hardness of these buttons was also tested as a screen for excessive interstitial content (79). Additional 250 gram ingots were provided by TIMET, supplied in the hot-rolled condition. These ingots were homogenized for 6 hours at 1100°C , cold-rolled 15%, and recrystallized for 30 seconds at 1000°C to produce a prior beta grain size of approximately 0.1 - 0.5 mm. The bulk of the Ti-64 and Ti-6211 used in this investigation, and the CP Ti, were supplied by Astro Metallurgical in the form of beta-worked 0.25 in. diameter rod. Additional Ti-64 and Ti-6211 were supplied by TIMET and RMI in the form of either beta-worked plate or alpha-beta worked plate. The compositions of all materials are given in Table 4.1.

The CCT diagrams were developed for these alloys using radial dilatometry and the Gleeble 1500 thermal mechanical testing system. The sample and dilatometer configurations are shown in Figures 4.1 and 4.4. The samples were thermally cycled as described in the initial hot ductility

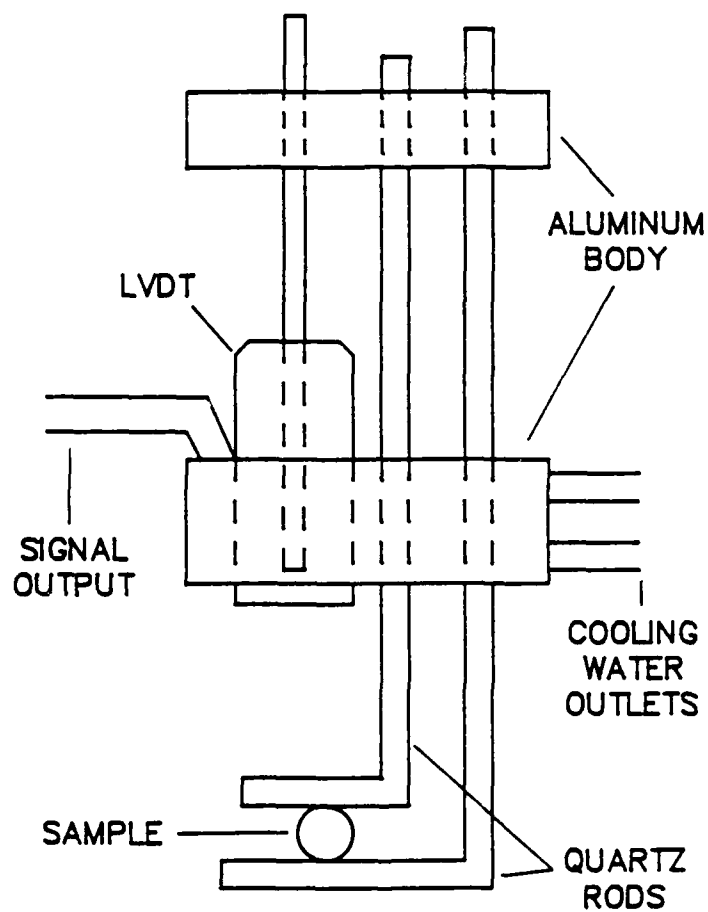


Figure 4.4 Gleeble radial dilatometry fixture. Sample is clamped between two quartz rods, the relative positions of which are measured by an LVDT.

testing and cooled at constant rates varying between 0.17°C/s and 100°C/s . Constant cooling rates were selected for their consistency, repeatability, and ease of programming. The transformation start and finish temperatures were detected by a slope change in the radial dilation when plotted against temperature, Figure 3.13, and verified by metallographic examination. When cooling rates of 50°C/s or higher were used, the conductive cooling through the jaws in the Gleeble was not adequate to prevent a slight thermal arrest during the transformation. In some instances, this could be prevented by flooding the specimen surface (and inside surface of tubular specimens) with helium. However, in cases where a thermal arrest did occur, only a transformation start was recorded. At the highest cooling rates used, helium quenching was combined with a very short specimen free span. The dilatometry fixture could not be used in these cases so the transformation start was detected by the start of the thermal arrest, and no transformation finish temperature was noted. Figure 4.5 shows the CCT diagram developed for Ti-6211.

It is important to again note that caution must be used when attempting to apply a CCT curve to any situation other than the one under which it was developed. In the case of this study, the cooling cycles and specimen geometries used

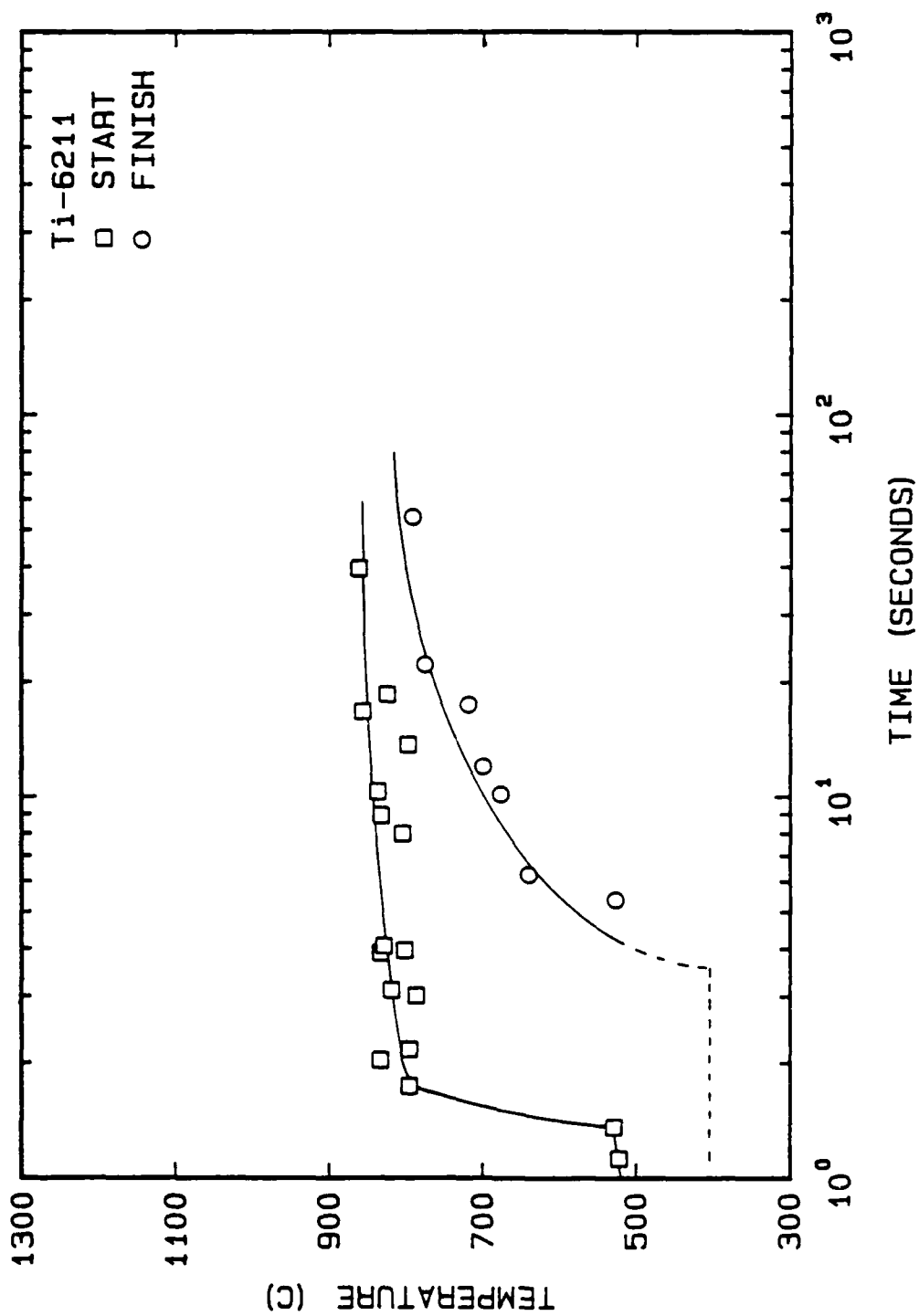


Figure 4.5 Continuous cooling transformation (CCT) diagram for Ti-6211 (13).

In the CCT diagram development were identical to those used in the hot ductility studies and the dilatometry/thermal expansion coefficient determination.

The feasibility of using neutron diffraction to make in-situ measurements of transformation kinetics was examined. Preliminary work was done in this area using the facility at the Danish National Laboratory at Risø. The procedure used was to monitor the diffracted intensity of the beta phase as it diminished during the transformation. The experimental setup was not sufficiently developed to obtain data which could be used to accurately fit kinetic equations. However, the potential of the technique was demonstrated and the transformation start and finish points measured agreed reasonably well with those obtained dilatometrically. A report of the neutron diffraction transformation kinetics measurements is included as Appendix A.

4.3 Lattice Incompatibility Measurements

The investigation of the lattice incompatibility model required that the correspondence between lattice incompatibility and hot ductility dip susceptibility be established. Ideally, this required that the lattice parameters of both phases be known during the beta to alpha transformation. Unfortunately, the measurement of

diffraction peak positions several times a second during continuous cooling conditions was not possible with the available experimental facilities. In lieu of this, the lattice incompatibility was determined by combining two techniques, lattice parameter measurements made using high-temperature wavelength-dispersive x-ray diffraction and radial dilatometry. Each of these tests will first be discussed individually, and then with respect to the procedure for the calculation of lattice incompatibility values.

Although not used in this investigation, lattice parameter measurements were also made using energy-dispersive spectroscopy at the Synchrotron Radiation Facility at Stanford University, and using neutron diffraction at the Danish National Laboratory at Risø. These results are presented in Appendix B.

4.3.1 X-Ray Diffraction

The equilibrium lattice parameters of the alpha and beta phases of the model alloys were measured at CSM using three facilities. The room temperature lattice parameters were measured using the room temperature diffractometers in both the Metallurgical Engineering and Physics departments. The Metallurgical Department facility uses a Philips XRG 3100 generator, a scintillation detector, and output to a

chart recorder. The Physics Department system uses a Rigaku Rotaflex RU-200 Rotating Anode generator, a scintillation detector, and is controlled via a Rigaku MCD Control/Data Processing Unit. Again, output is to a strip-chart recorder. The high temperature measurements were made on the Metallurgical Engineering Department high temperature diffraction system. This system consists of a Philips XRG 3000 generator and a proportional counter, with Philips/Carpenter electronics and output to a strip chart recorder. A Philips/MRC high vacuum, high temperature specimen chamber was used after being modified to meet the particular requirements of this investigation (discussed later). Cu K_α radiation was used in all cases. Because low-angle peaks were used, the K-alpha and K-alpha II doublets could not be resolved. Therefore, a weighted average of their wavelengths, 1.54184 Å, was used as the wavelength of radiation (80). The strip-chart recorder traces were evaluated manually and the peak positions were taken to be the peak center at half-maximum intensity.

Specimens were prepared by mechanically grinding to a 600 grit finish, pickling in a solution of 2% HF, 30% HNO_3 , and 68% H_2O , and rinsing in methanol. Room-temperature measurements used bulk specimens of several different sizes and geometries. Two commonly used sizes were 20mm X 20mm X

4mm, and 35mm X 6mm X 4mm.

For the high temperature testing, the Philips/MRC specimen chamber was modified to meet the requirements of this investigation. The specific requirements of this investigation, combined with the limitations of the existing equipment, were unusual enough to prevent the use of established experimental techniques (81). Obviously, the specimen had to be kept flat and held in place in the focussing circle. However, because the experimental setup used a horizontal goniometer, the specimen had to be held vertically. Above room temperature, the irradiated area of the specimen also had to be maintained at a constant, known temperature, and be kept free of interstitial contamination. The final requirement was that no material other than the sample be in the irradiated area.

Three sample configurations were developed to meet these requirements, and are shown in Figure 4.6. The bulk of the data was obtained using the configuration shown in Figure 4.6(c) and Figure 4.7. This final specimen configuration was a plate, 35mm X 6mm X 1mm, with a 3mm hole in one end and a 1mm hole in the other end. The sample spanned water cooled supports and was resistively heated. One end of the specimen was clamped to the support and the other end was held in place by a spring which was pre-loaded

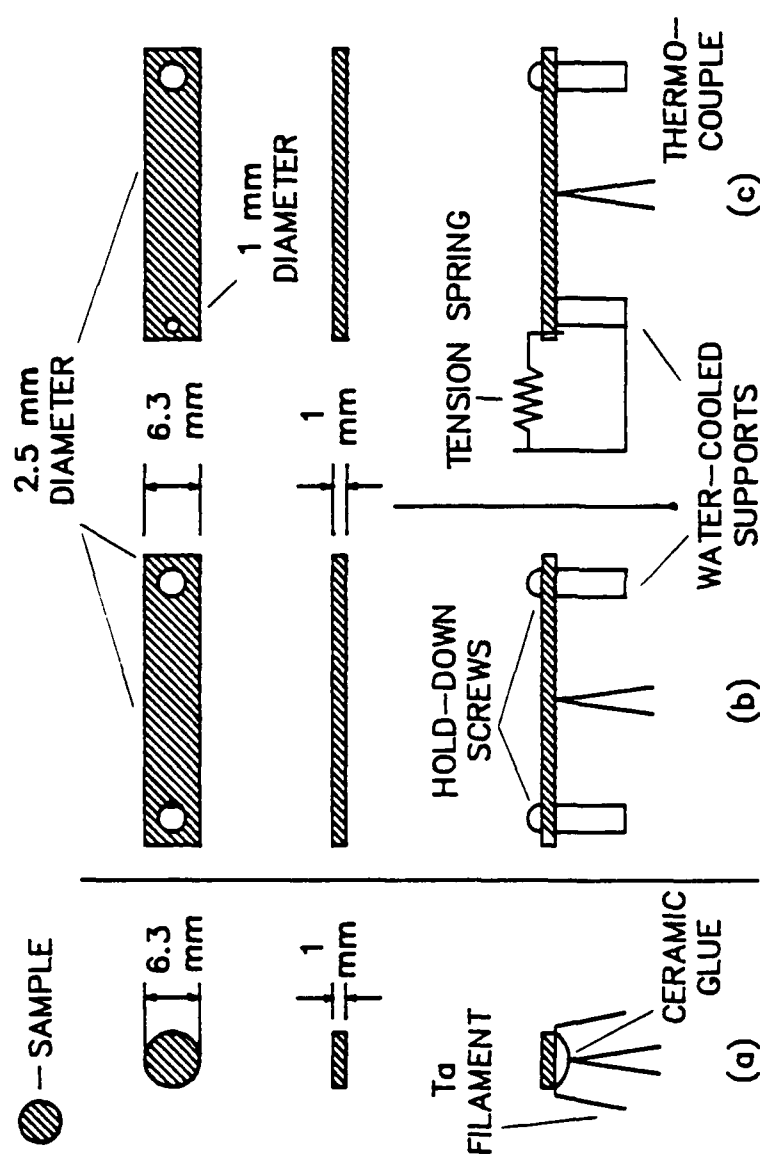


Figure 4.6 High-temperature x-ray diffraction specimen configurations. Geometries include discs glued to a tantalum filament (a), and direct resistance heated plates, either clamped (b), or spring loaded (c).

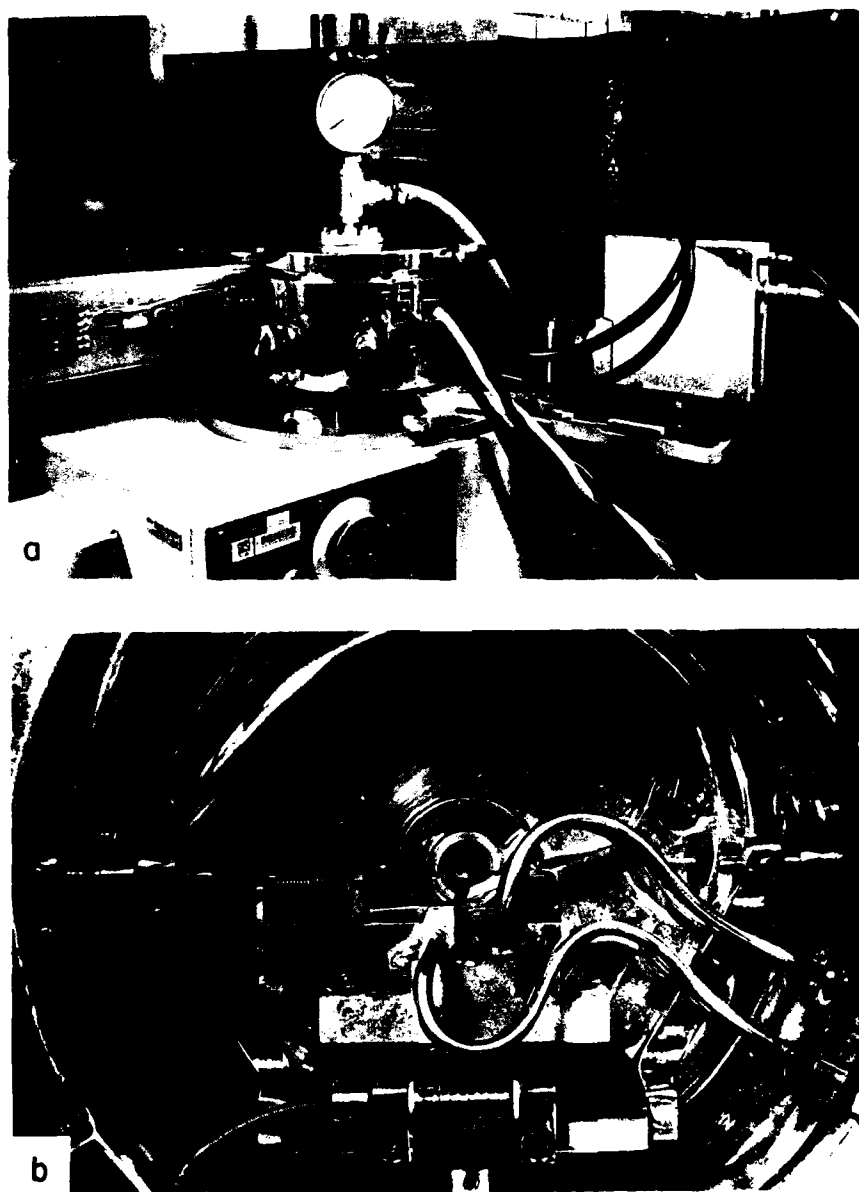


Figure 4.7 High-temperature x-ray sample, holder, and chamber assembly.

so that it exerted a tensile load on the specimen. Because of the large volumetric expansion that occurs when alpha transforms to beta, this tensile loading was needed to keep the specimen relatively flat and in the focussing circle for beta measurements. A 0.010 in. diameter thermocouple spot-welded to the underside of the specimen surface was used to monitor the specimen temperature. Both type K (Chromel-Alumel) and type R (Pt versus Pt-13%Rh) thermocouples were used with a reference junction maintained at approximately room temperature. The thermocouple output was then adjusted to reflect the use of a room-temperature reference junction rather than 0°C. All high-temperature lattice parameter measurements were made in flowing high-purity helium. Specimen appearance was used as a method of monitoring the extent of interstitial contamination, and data from samples which showed evidence of extensive contamination was discarded. The high-temperature specimen and chamber configuration is shown in Figure 4.7.

To maximize the accuracy of the lattice parameter measurements, it was necessary to compensate for errors inherent in the x-ray diffraction procedure. The steps taken to minimize interstitial contamination have already been discussed. Additionally, two particular sources of error were addressed in the procedures developed for processing

the x-ray diffraction data. These are gross misalignment of the specimen due to incorrect specimen loading, and the systematic errors inherent in mechanical diffractometry in general.

4.3.1.1 Misalignment Due to Specimen Loading The alignment of the high temperature diffractometer varied somewhat from sample to sample because of the manual nature of the specimen loading and alignment procedures. Therefore, the diffraction peak positions measured in either of the room-temperature diffractometers, which were far more reproducible, were used as standard values. These values are given in Table 4.3. The high temperature diffraction peak positions for each sample were then normalized to these standard values. This was done by duplicating the room temperature runs with the high temperature diffractometer and comparing the individual peak positions from the two data sets to obtain a correction factor for each peak. This correction factor was then applied to all high temperature measurements of that particular (hkl) diffraction peak position in that sample. This procedure is illustrated in Table 4.4. For the beta phase, room temperature diffraction peaks were usually not available for direct comparison. In these cases, the correction factor for the beta peaks was obtained by interpolation between the correction factors of

Table 4.3

Standard Values for Room Temperature Diffraction Peaks

 $(\lambda = 1.54184 \text{ \AA})$

Alloy	2 θ ($^{\circ}$) for listed hkl reflections							
	010	002	011	012	110	103	112	201
Ti	35.39	38.38	40.44	53.25	63.44	70.67	76.72	77.40
Ti-6Al	35.44	38.59	40.46	53.19	63.48		76.77	78.08
Ti-6Al-2V	35.46	38.56	40.50	53.41	63.60	71.11	76.93	78.17
Ti-6Al-4V	35.45	38.53	40.48	53.34	63.59	71.04	76.85	78.16
Ti-6Al-6V	35.46	38.60	40.57	53.43	63.77	71.20	77.02	78.30
Ti-6Al-2Mo	35.20	38.43	40.25	53.18	63.26	70.89	76.53	77.84
Ti-6Al-4Mo	35.35	38.41	40.42	53.22	63.41	70.95	76.77	78.01
Ti-6Al-6Mo	35.42	38.63	40.48	53.33	63.60	71.08	76.88	78.14
Ti-6Al-2Nb	35.25	38.43	40.24	53.15	63.29	70.79	76.49	77.79
Ti-6Al-4Nb	35.30		40.41	53.20	63.36	70.88	76.68	77.93

Table 4.3 (cont.)

Alloy	2 θ ($^{\circ}$) for listed hkl reflections						
	010	002	011	012	110	103	112
<hr/>							
Ti-6Al-6Nb							
	35.32	38.40	40.40	53.30	63.41	70.89	76.81
Ti-6211							
	35.32	38.47	40.37	53.18	63.28	70.85	76.60
Ti-6Al-2V-2Nb							
	35.35	38.46	40.43	53.26	63.51	71.02	76.82

Table 4.4

Example of Diffraction Peak Correction Procedure

(Shown for Ti-6Al-2Nb)

Temperature	hkl	2 θ	2 θ Standard	Correction	2 θ Corrected
RT	010	35.39	35.25	-0.19	35.25
	002	38.54	38.43	-0.11	38.43
	011	40.46	40.24	-0.22	40.24
	012	53.30	53.15	-0.15	53.15
	110	63.50	63.29	-0.21	63.29
	112	76.77	76.49	-0.28	76.49
	201	78.03	77.79	-0.24	77.79
250°C	010	35.31		-0.19	35.17
	002	38.42		-0.11	38.31
	011	40.37		-0.22	40.15
	012	53.15		-0.15	53.00
	110	63.33		-0.21	63.12
	112	76.51		-0.28	76.23
500°C	010	35.19		-0.19	35.05
	002	37.31		-0.11	38.20
	011	40.22		-0.22	40.00
	012	53.00		-0.15	52.85
	110	63.16		-0.21	62.95
	112	76.34		-0.28	76.06
	201	77.56		-0.24	77.32

surrounding alpha phase peaks.

4.3.1.2 Systematic Errors A second source of error in lattice parameter calculation based on x-ray diffraction is the error in measurement of the peak positions themselves. Based on Bragg's law, $n\lambda = 2d\sin(\theta)$, the effect that an error in peak position measurement, $\Delta\theta$, has on calculated plane spacing, Δd , can be expressed as a function of θ , $d(d)/d = -\cot(\theta) d\theta$. Ideally, diffraction peaks occurring near $2\theta = 180^\circ$ would be used because $-\cot(\theta) = 0$ at $2\theta = 180^\circ$ so an error in measured peak position near $2\theta = 180^\circ$ results in the smallest possible error in calculated d spacing. In this investigation, most higher index peaks were not intense enough to use. This forced the use of peaks which, with weighted Cu K α radiation, $\lambda = 1.54184\text{\AA}$, had 2θ values between 30° and 80° . Fortunately, the combination of careful experimental technique and the extrapolation of calculated lattice parameters against a specific function of θ to $2\theta=180^\circ$ should theoretically result in lattice parameters with an accuracy of approximately 0.001 \AA (80, 82).

The function of θ selected to use in the extrapolation of calculated lattice parameters to $2\theta=180^\circ$ depends on the type of apparatus used, or more correctly, on the errors inherent in the chosen apparatus. These errors are

thoroughly discussed in references 80-84. In this investigation, an extrapolation parameter of $\cos^2\theta/\sin\theta$ was used. This parameter was combined with Cohen's method (83-85) of least squares fitting to calculate lattice parameters. When presented in the Results and Discussion section, data processed in this manner will be labelled with the suffix "ANG". For comparison, a second data processing method was used which averaged all of the possible lattice parameter combinations calculated from a set of diffraction peaks. Data processed in this manner will be labelled with the suffix "MUL". A discussion of the development of these data processing methods is included as Appendix C. This appendix also includes BASIC computer programs written to implement these data processing methods. The effect that the choice of data processing method can have on calculated parameters is addressed in Appendix D, a discussion of the errors involved in the lattice incompatibility measurements in general. To facilitate the direct comparison of the alpha and beta lattices, the lattice parameters of each phase were used to compute the volume of a 2-atom cell.

4.3.2 Lattice Incompatibility Calculation

The hot ductility dip is associated with dynamic cooling conditions where the transformation takes place at temperatures below the equilibrium transformation

temperatures. Hence, some method of approximating the lattice parameter of the non-equilibrium beta phase which is retained at a given cooling rate was required. This was accomplished by combining the equilibrium lattice parameter measurements with radial dilatometry at the desired cooling rates. The specifics of Gleeble dilatometry were discussed earlier and the experimental apparatus is shown in Figure 4.4. Figure 4.8 shows a Gleeble dilatometry curve for Ti-6211 held at 1200°C for five minutes and cooled at 10°C/s. This curve can be used, for these specific conditions, to relate the size of the sample at any temperature to the size of the sample at 1200°C. Because the volume/atom of the beta phase existing at 1200°C is known from the lattice parameter measurements, the dilatometry data can be used to calculate the size of the beta lattice at any temperature, provided it is cooled from 1200°C at 10°C/s. Examples of this calculation are shown in Figure 4.8.

In this investigation, lattice incompatibility was defined as a bulk volumetric contraction. This contraction was measured between the non-equilibrium retained beta phase and either the equilibrium alpha phase, or the equilibrium alpha-beta mixture, at the beta to alpha transformation start temperature. This procedure is shown schematically in Figure 4.9. In this figure, the incompatibility between the

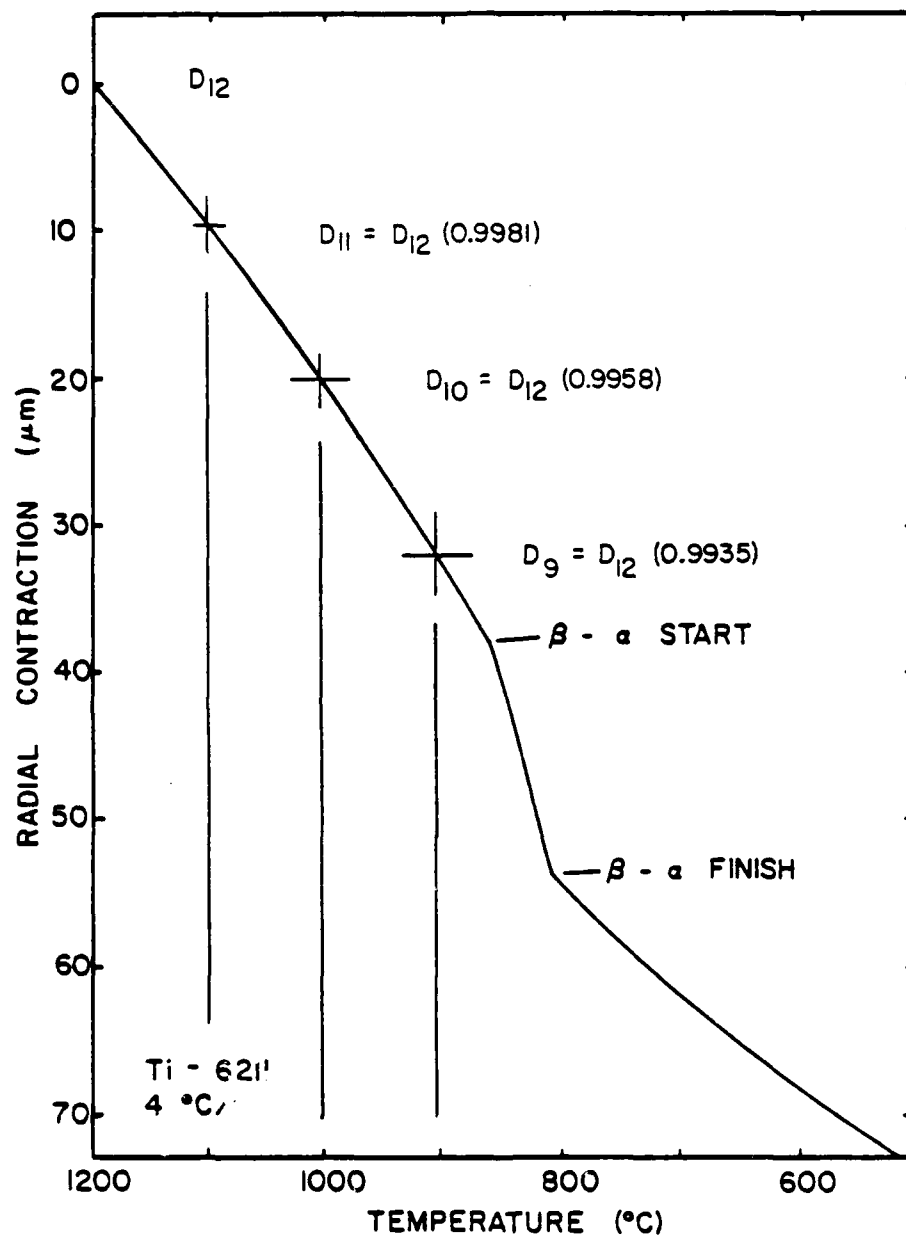


Figure 4.8 Ti-6211 dilatometry curve, including calculations which show the size of the beta phase at any temperature, relative to its size at 1200 $^{\circ}\text{C}$.

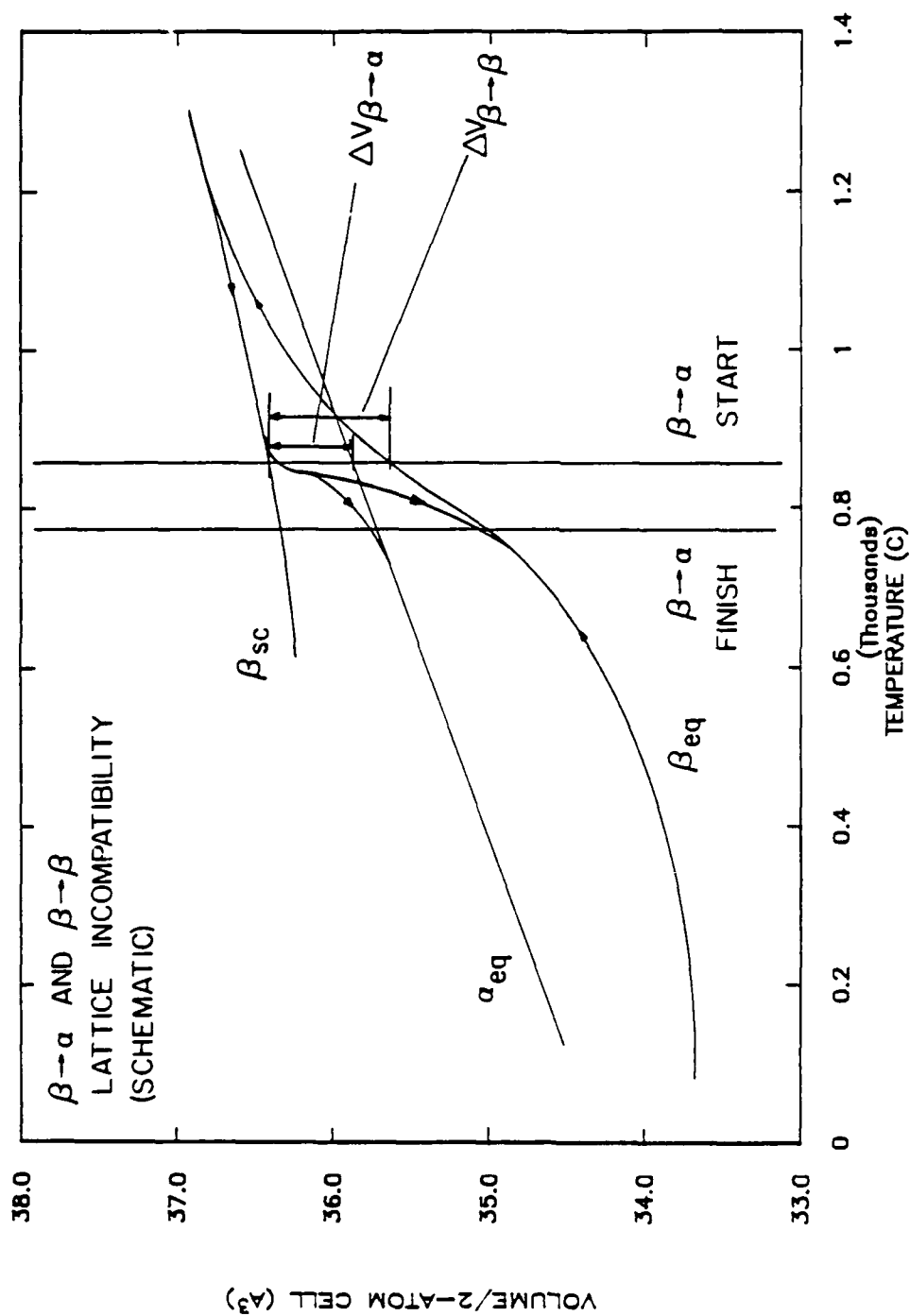


Figure 4.9 Schematic illustrating the measurement of beta to alpha and beta to beta lattice incompatibility.

retained beta and equilibrium alpha is labelled ΔV_{α} . The incompatibility between the retained beta and an equilibrium alpha-beta mixture is calculated as a weighted sum of the two individual incompatibility values, ΔV_{α} and ΔV_{β} . In the Results and Discussion section, the weighted sum will be referred to as $\Delta V_{\alpha\beta}$. In either case, incompatibility is expressed as a percent contraction of the retained beta phase.

4.4 Hot Ductility Testing

Hot ductility testing was done using the Gleeble 1500 thermal-mechanical testing system. Six alloys were selected for this testing: Ti-6Al-2V (V2), Ti-6Al-4V (Ti-64 or V4), Ti-6Al-6V (V6), Ti-6Al-4Nb (N4), and Ti-6Al-2V-2Nb (622). These alloys were chosen to independently vary transformed microstructure and lattice incompatibility, and to give a broad range of both. In particular, the niobium containing alloys were chosen as a result of the lattice parameter measurements. These measurements suggested that niobium was the major contributor to the low ductility of Ti-6211 because it expands the beta lattice without a corresponding expansion of the alpha phase. The material used in the hot ductility testing was supplied by TIMET in the form of beta worked 0.5 in. diameter rod. These rods were cut to length and ground to produce 11.1 mm diameter Gleeble specimens.

The compositions of these ingots are included in Table 4.1.

The procedure used in the hot ductility tests was discussed earlier and the standard sample configuration is shown in Figure 4.1. In addition to the geometry shown in Figure 4.1, sample configurations included free spans from 10mm to 30mm and diameters from 4mm to 11mm in smooth samples, and from 3mm to 6mm in samples with a reduced section. The length of the reduced section varied from 5mm to 19mm, but was usually sized to approximate the free span of the specimen.

As discussed earlier, the standard thermal cycle used was 2 minutes to 1200°C, 5 minutes at 1200°C, and cooling at a constant rate to the test temperature. Tests were also performed on Ti-6211 and Ti-6Al-2V using different annealing times and temperatures to investigate the effect of prior beta grain size on hot ductility. Cooling rates between 0.17°C/s and 50°C/s were used. The specific cooling rates used with each material were chosen to insure that a wide range of microstructures was being tested for each alloy. The cooling rates used for each alloy are listed in Table 4.5.

Ductility was determined for these specimens as percent reduction in area. Measurements of the samples initial diameter were made using a micrometer, and of the final

Table 4.5

Cooling Rates Used in Hot Ductility Testing

Alloy	Cooling Rates ($^{\circ}\text{C/s}$)
unalloyed titanium	10
Ti-6Al	10
Ti-6Al-2V (1)	0.17, 1, 10, 50
-4V	0.17, 1, 5, 10, 20
-6V	0.17, 0.5, 1, 2, 10
Ti-6211 (2)	0.17, 5, 10, 50
Ti-6Al-2V-2Nb	0.17, 1, 10, 20
Ti-6Al-4Nb	0.17, 1, 10, 20, 50

(1) 10 $^{\circ}\text{C/s}$ tests run using beta anneals of 5 minutes/1200 $^{\circ}\text{C}$, 5 minutes/11 $^{\circ}\text{C}$, 5 minutes/1300 $^{\circ}\text{C}$, and 10 minutes/1300 $^{\circ}\text{C}$.

(2) duplicate sets of tests run with beta anneals of 5 minutes/1200 $^{\circ}\text{C}$ and 5 minutes 1100 $^{\circ}\text{C}$.

area, using either a travelling microscope or calipers. In all cases, the values used to calculate reduction in area were the average of several readings. In the case of the failed specimens, the diameters of both sections were measured. Additionally, qualitative comparisons of the fracture surfaces were made using optical fractography and scanning electron microscopy. The percent elongation between the point of maximum load and failure was used as an additional measure of ductility for some specimens. Ultimate tensile strength was also determined in each test.

4.5 Microstructural Analysis

Microstructural analysis was used to support several aspects of this investigation. During the development of the CCT diagrams, the microstructures produced at several cooling rates were used to identify the transformation or transformations which had occurred. These microstructures then made it possible to choose cooling rates which would produce a similar range of microstructures in each of the alloys investigated. Metallographic analysis was also used to characterize the transformed microstructures with respect to several microstructural aspects believed to contribute to the materials deformation behavior. For example, the amount and width of the Widmanstatten colonies occurring at the prior beta grain boundaries were measured.

Standard metallographic sample preparation procedures were employed (86). Gleeble samples were sectioned both transversely and longitudinally. These samples were rough ground on silicon carbide paper through 600 grit, then polished with 6 micron diamond paste and 1 and 0.05 micron alumina slurries. Kroll's reagent was used throughout as an etchant. Longitudinal sections of failed Gleeble specimens were nickel plated prior to sectioning to protect the fracture surface, then prepared in a similar manner. In addition to optical microscopy, fractography was performed on selected Gleeble specimens using a JEOL 840 scanning electron microscope. Fractography samples were cleaned in methanol and no surface preparation was used.

RESULTS AND DISCUSSION

The results and discussion will be divided into four main sections. The first will be a discussion of the phase stability of the model alloys, within the context of their relationship to each other and to commercially available alpha-beta alloys. This subsection will present the partial CCT diagrams and microstructures produced at several cooling rates for the alloys investigated. The individual alloying elements will be evaluated with respect to equilibrium phase stability and the kinetics of the beta to alpha phase transformation. A theoretical model for the beta to alpha transformation will be developed and qualitatively evaluated.

The second subsection will present the results of the lattice incompatibility testing. The lattice incompatibility of each alloy will be evaluated in two ways, each based on a particular assumption of stress development during the transformation. The alloying elements will be evaluated with respect to their effect on alpha phase volume, beta phase volume, coefficient of thermal expansion, and the resulting lattice incompatibility.

The third section will report the results of the hot ductility testing. The ductility and strength of several of

the model alloys will be related to test temperature and cooling rate. These results will be discussed with respect to alloy content, lattice incompatibility, and transformed microstructure. Based on the results, conclusions will be drawn concerning the validity of the lattice incompatibility model and any other affects which appear to be contributing to the ductility loss.

The final section will combine the results of the previous three sections to analyze the hot deformation characteristics of these titanium alloys. The overall deformation of the material will be described and the causes for the high temperature ductility loss discussed.

5.1 Phase Stability and Transformation Kinetics

Previous investigations (49, 62-66) have shown that with similar welding parameters or identical Gleeble thermal cycles, different alloys show drastically different susceptibilities to the high temperature ductility loss. It has also been shown that, for a single alloy, the extent of the ductility loss depends on both the specific thermal cycle used and the temperature of testing. Therefore, one possible explanation for the alloy to alloy variation in ductility loss susceptibility is that, for a single thermal cycle, different microstructures are being tested in the various alloys. This possibility was investigated by

evaluating the model alloys in terms of their phase stability and transformation kinetics.

The phase stability and transformation kinetics of the alloys in the initial matrix were characterized by development of CCT diagrams and microstructural analysis. The results of this work, presented in the five following sub-sections, were used to provide a base from which to select alloys and cooling rates for hot ductility testing, and to gain an understanding of the transformations and transformation mechanisms which occur in alpha-beta titanium in general. The CCT diagrams developed and the microstructures produced will be presented and discussed in the first two sub-sections. The third sub-section contains a description of the overall transformation mechanism. The results of these studies were then used to develop a model which quantitatively describes the transformations in these alloys. This model can be used to predict the microstructural changes that result from changes in several system variables. This model is presented in the fourth sub-section. The fifth sub-section is a discussion of a microstructural anomaly which sometimes appears in near-alpha titanium alloys, "rabbit ears" martensite.

5.1.1 CCT Diagrams

Partial continuous-cooling-transformation (CCT) diagrams were developed for each of the model alloys using cooling rates from 0.167°C/s to 50°C/s . This range of cooling rates and the microstructures produced roughly approximate those associated with the high temperature ductility loss. These partial CCT diagrams are shown in Figures 5.1-5.13, the data are tabulated in Table 5.1, and example microstructures are shown in Figure 5.14. The remainder of the micrographs associated with these CCT diagrams are compiled under separate cover (87).

The results shown in Figures 5.1-5.13 and Table 5.1 can be explained by examination of the binary phase equilibria of the components systems and a consideration of the kinetics of the pertinent transformations. As a point of reference, psuedo-binary diagrams for these systems shown in Figure 5.15 (76-78, 87). These diagrams were generated by a simple superposition of the phase fields of the respective binary diagrams on that of Ti-6Al, Figure 5.16 (88). The equilibrium beta transus temperatures in these figures can be compared with the beta to alpha transformation start temperatures given in Table 5.1. This comparison verifies that the transformation kinetics of the alloys studied cannot be predicted soley on the basis of their equilibrium

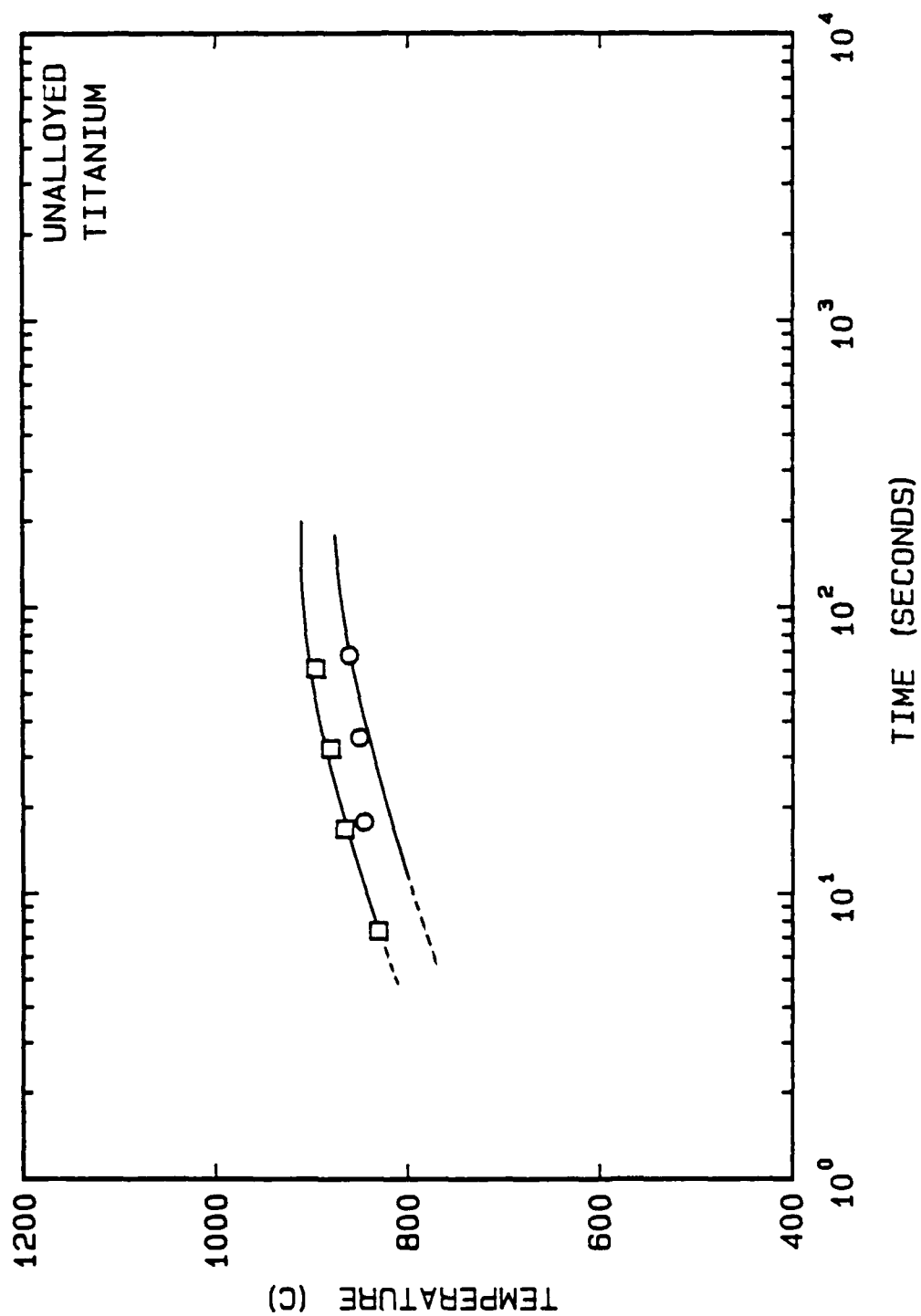


Figure 5.1 Partial CCT diagram for Grade 2 unalloyed titanium for the range of cooling rates between 10°C/s and 50°C/s.

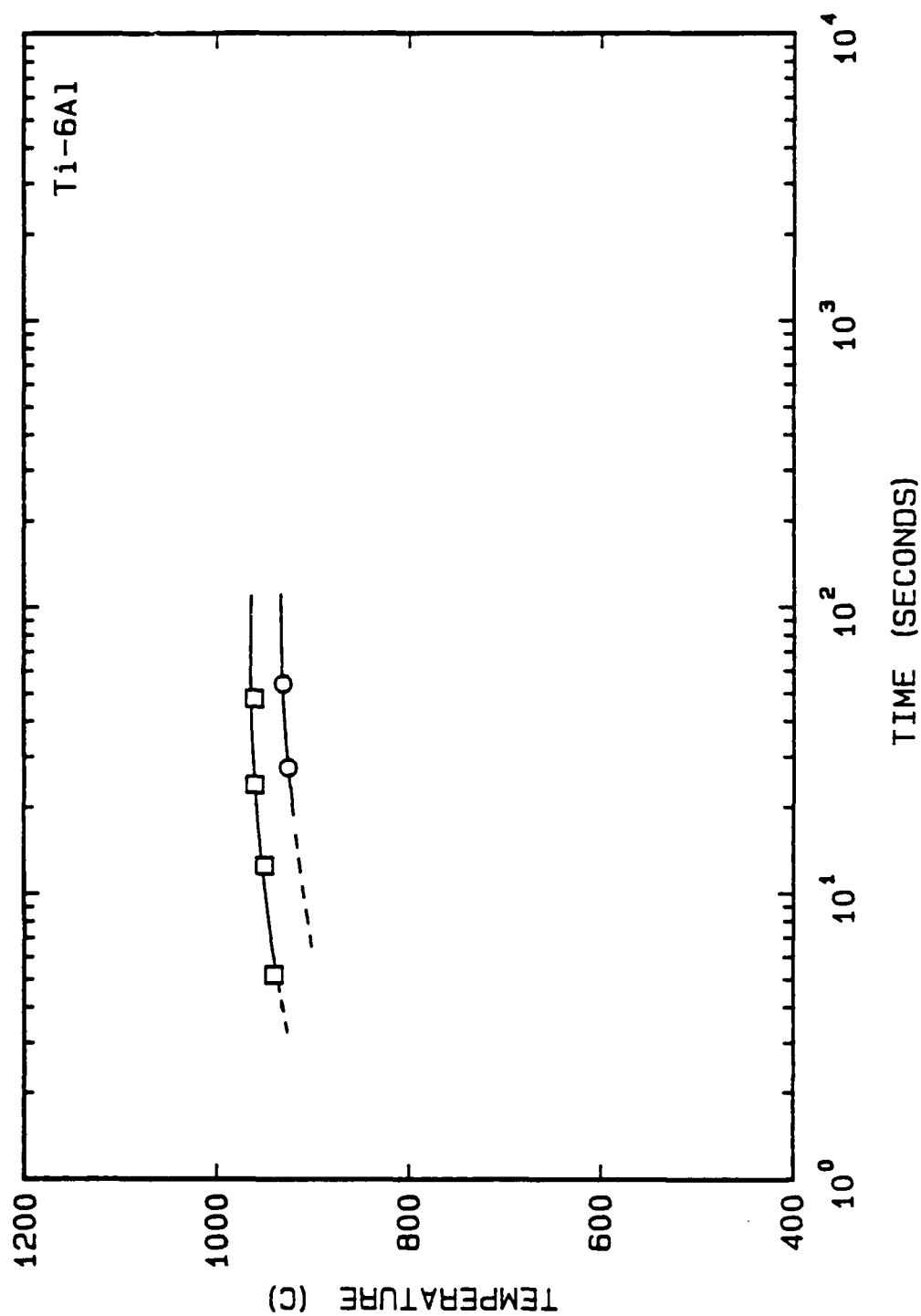


Figure 5.2 Partial CCT diagram for Ti-6Al for the range of cooling rates between 1 C/s and 50 C/s.

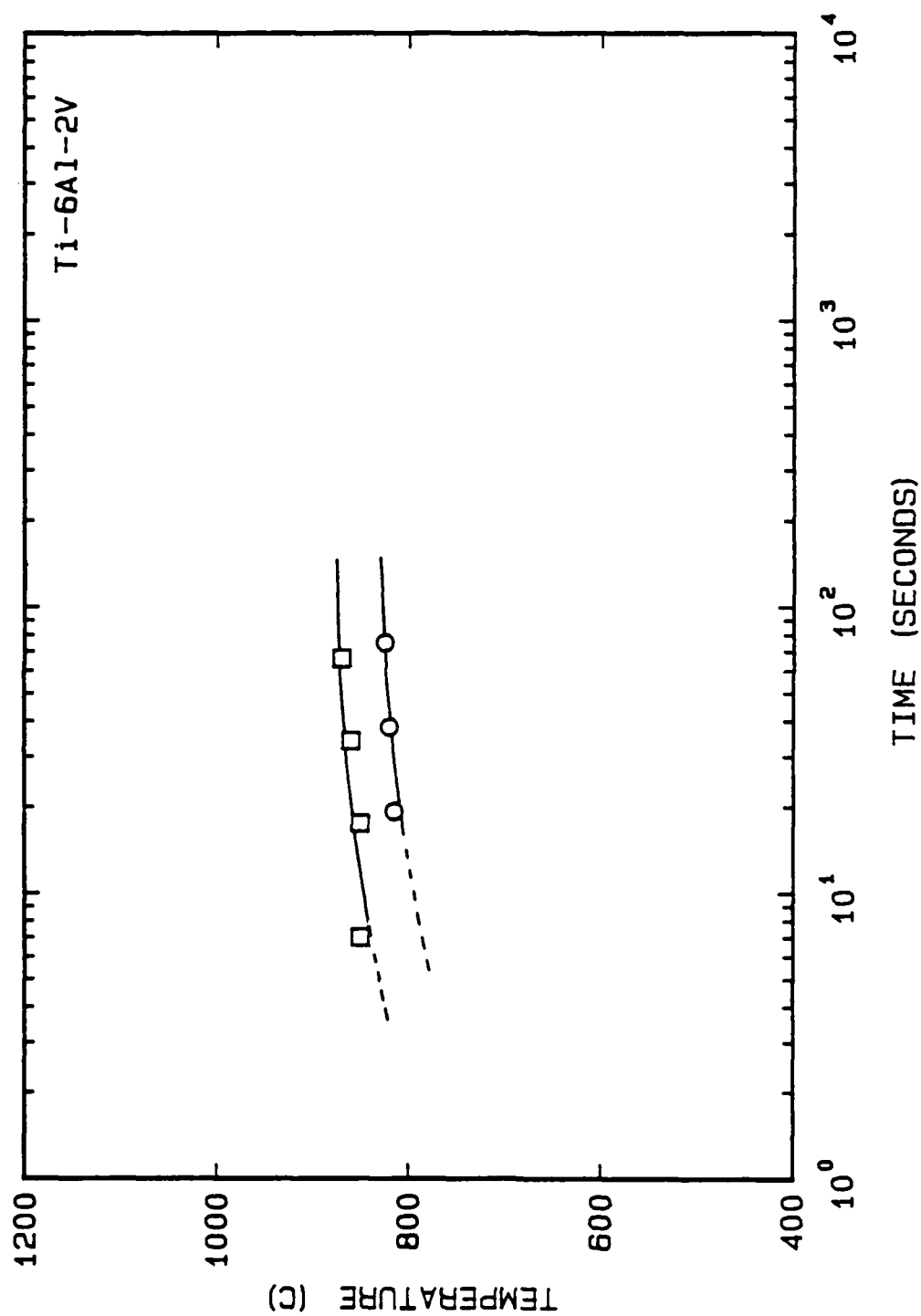


Figure 5.3 Partial CCT diagram for Ti-6Al-2V for the range of cooling rates between 1°C/s and 50°C/s .

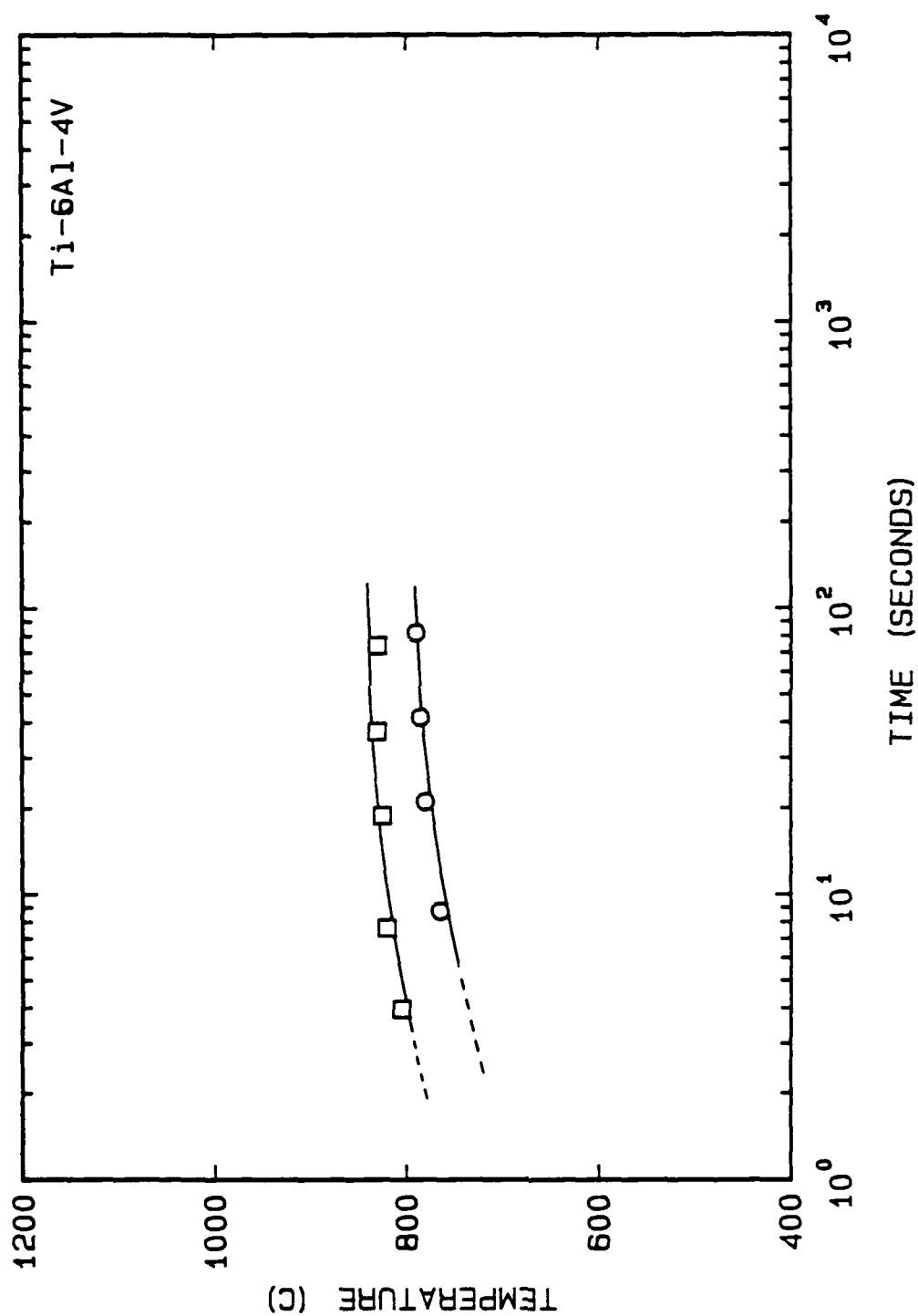


Figure 5.4 Partial CCT diagram for Ti-6Al-4V for the range of cooling rates between 1°C/s and 50°C/s.

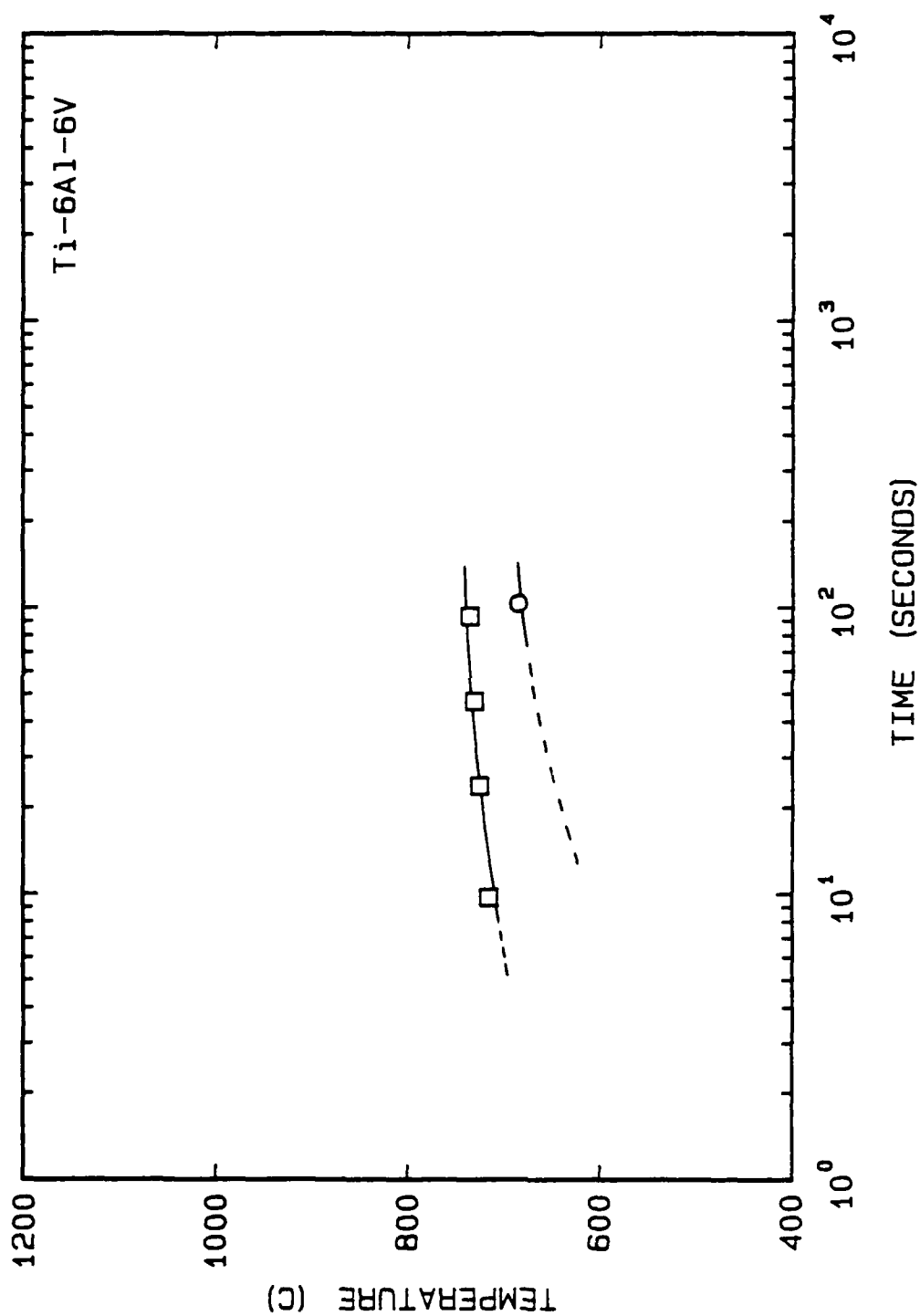


Figure 5.5 Partial CCT diagram for Ti-6Al-6V for the range of cooling rates between 1°C/s and 50°C/s.

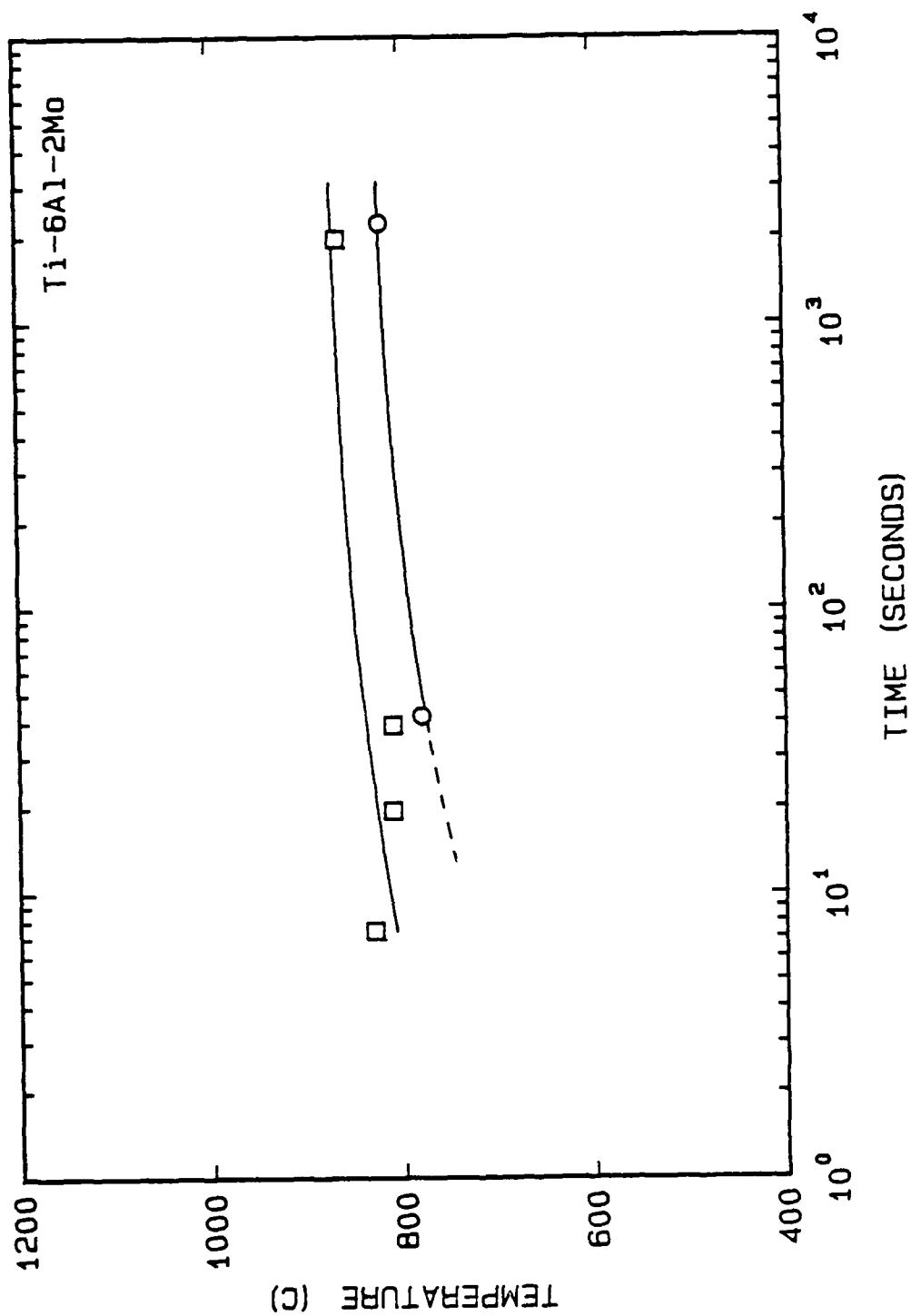


Figure 5.6 Partial CCT diagram for Ti-6Al-2Mo for the range of cooling rates between 0.17°C/s and 50°C/s.

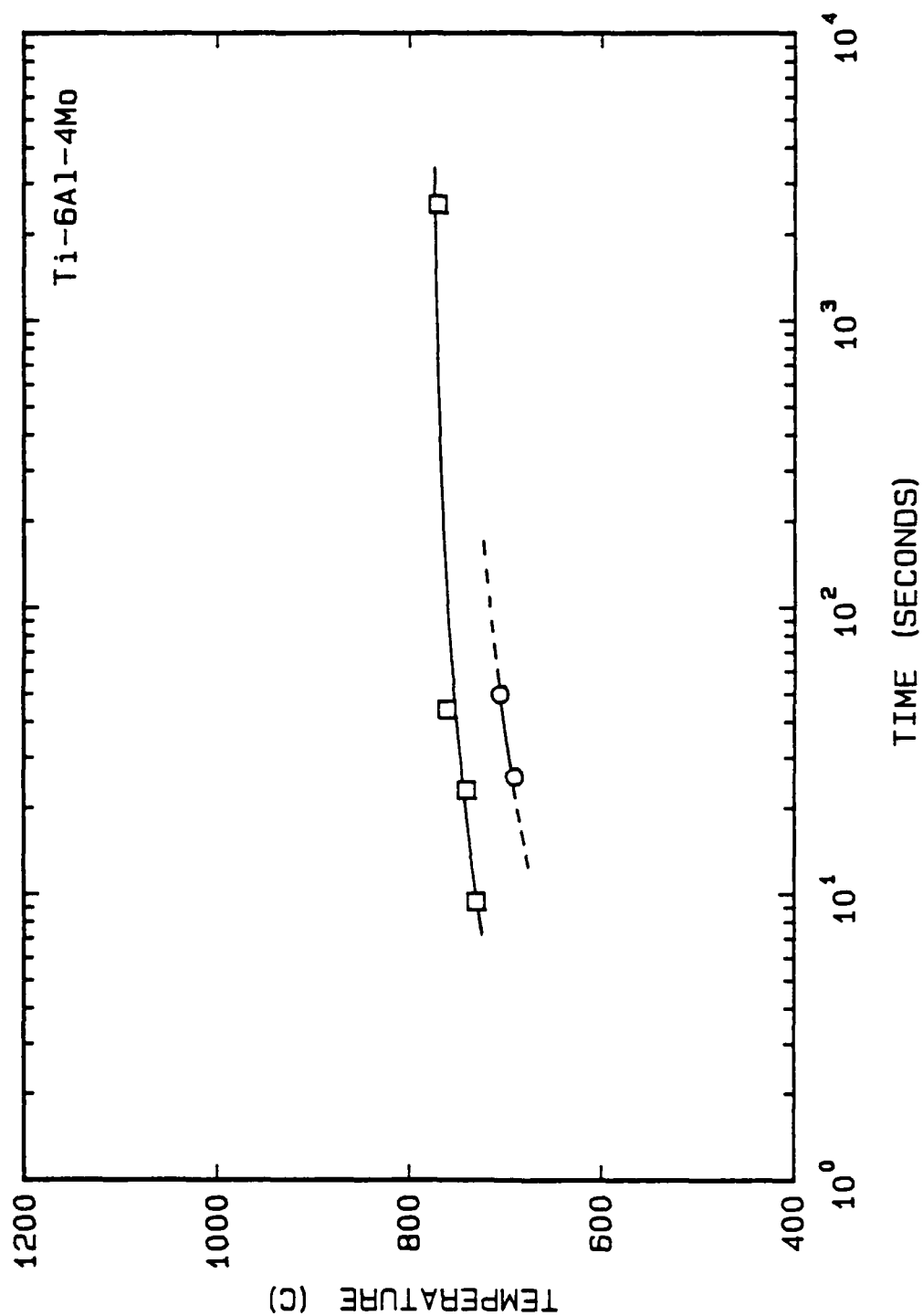


Figure 5.7 Partial CCT diagram for Ti-6Al-4Mo for the range of cooling rates between 0.17°C/s and 50°C/s .

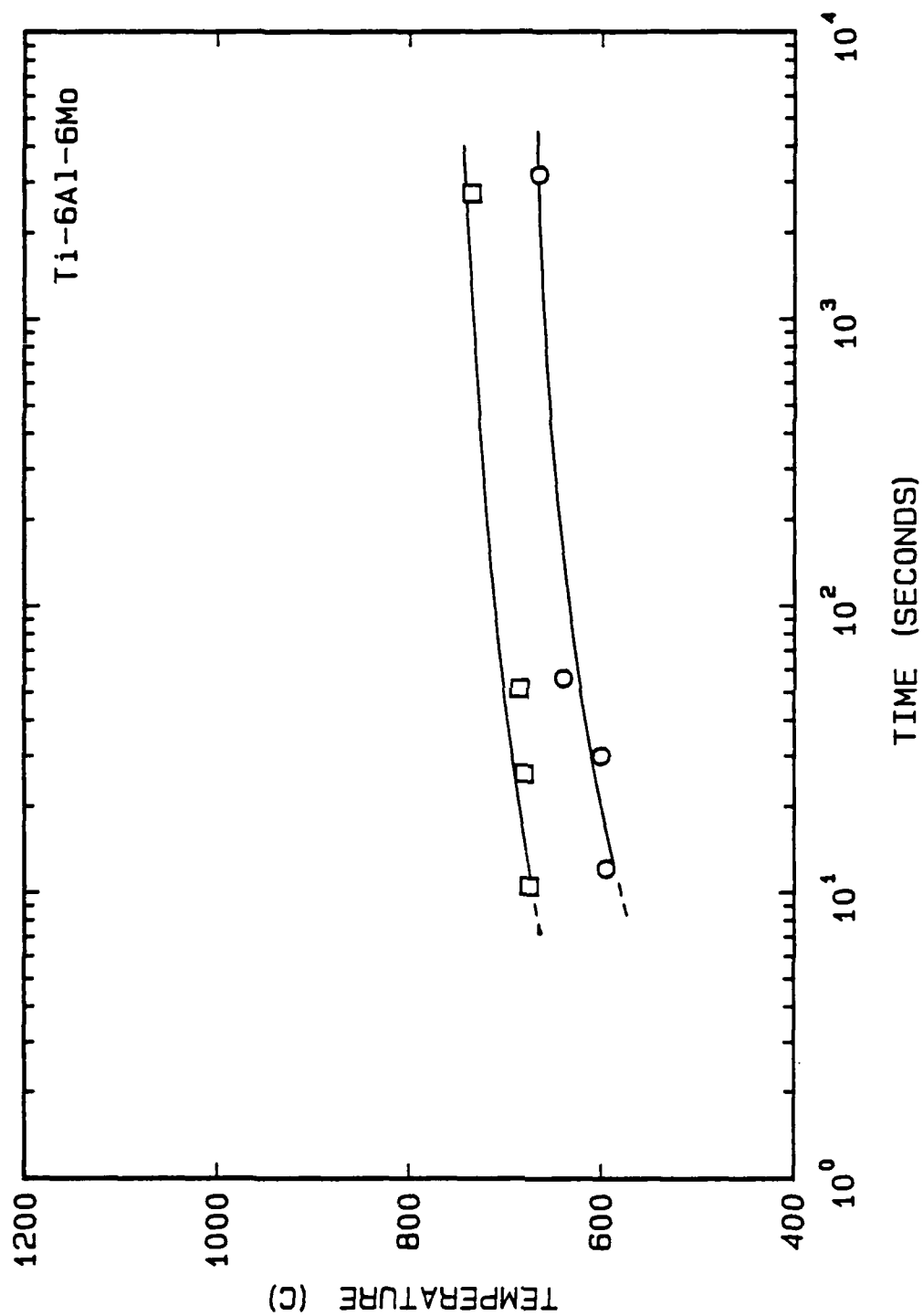


Figure 5.8 Partial CCT diagram for Ti-6Al-6Mo for the range of cooling rates between 0.17°C/s and 50°C/s.

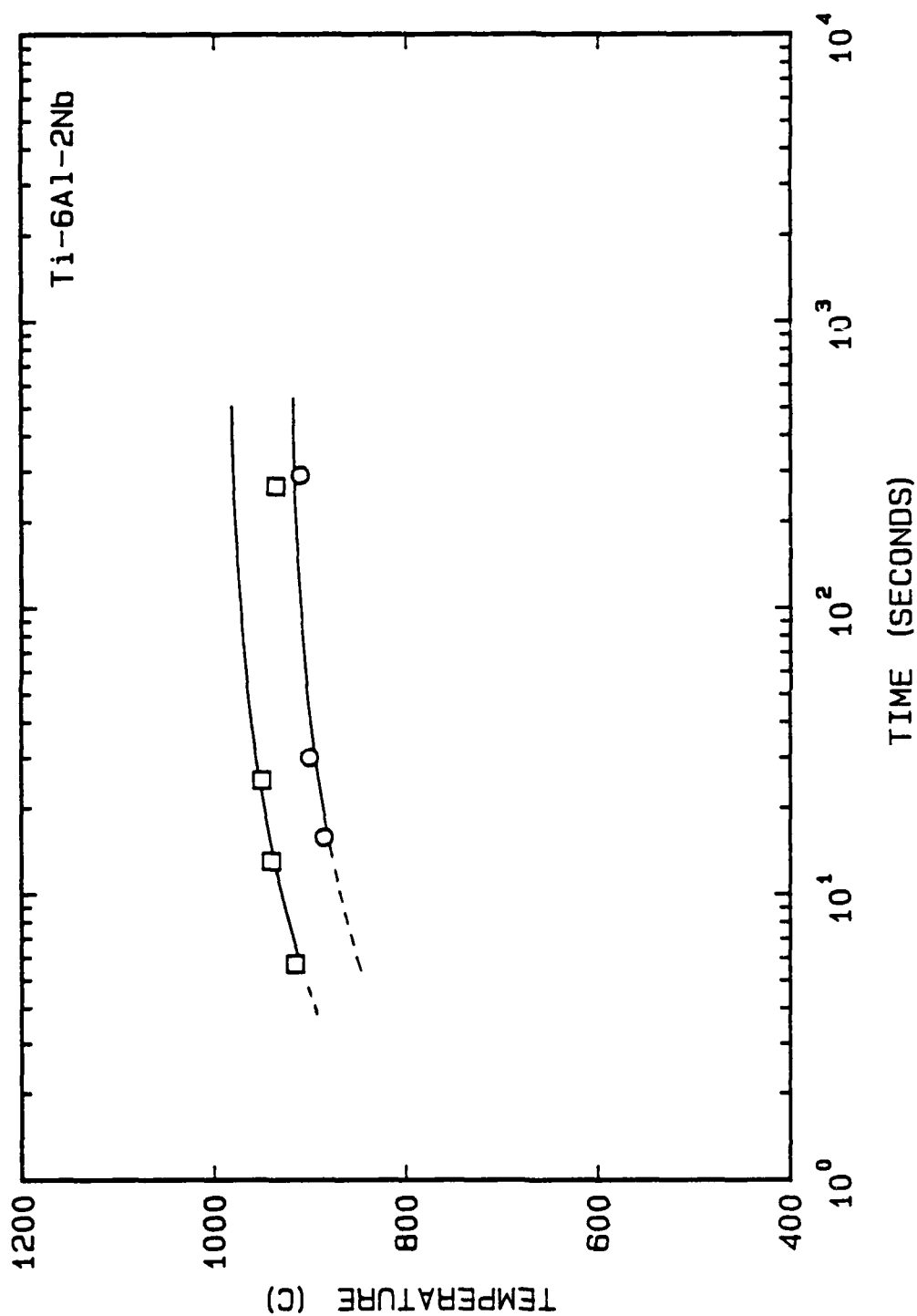


Figure 5.9 Partial CCT diagram for Ti-6Al-2Nb for the range of cooling rates between 1°C/s and 50°C/s.

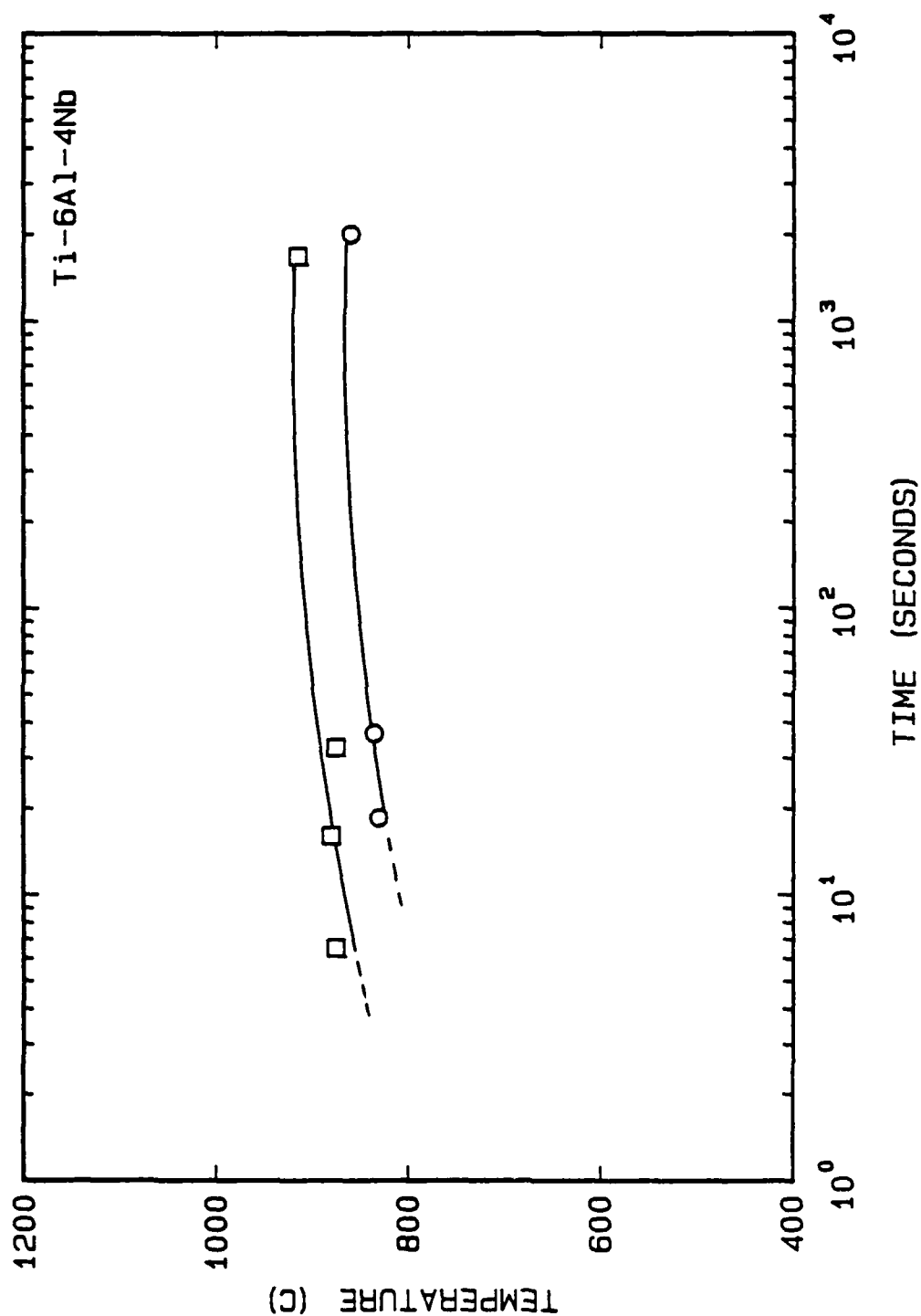


Figure 5.10 Partial CCT diagram for Ti-6Al-4Nb for the range of cooling rates between 0.17°C/s and 50°C/s.

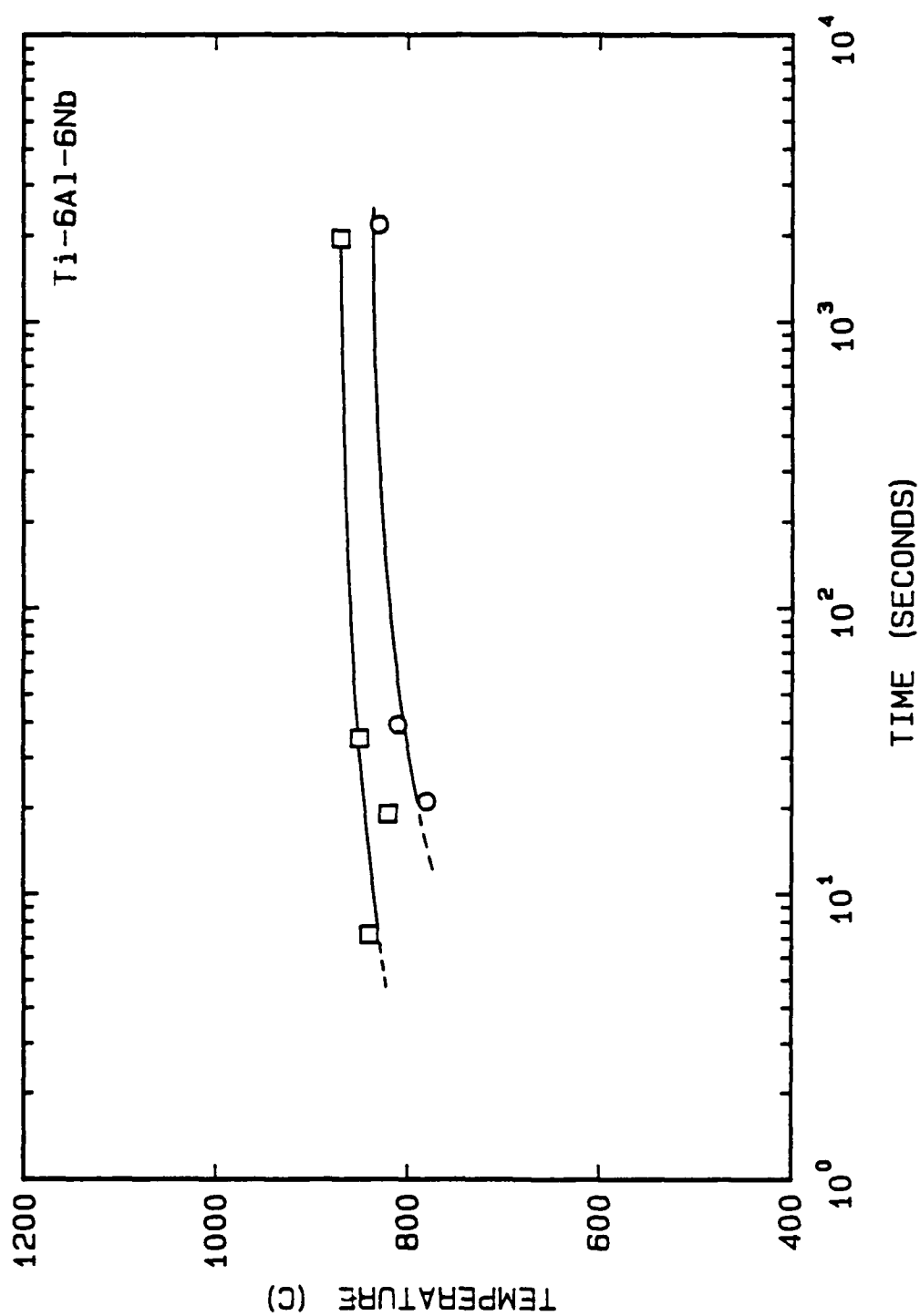


Figure 5.11 Partial CCT diagram for Ti-6Al-6Nb for the range of cooling rates between 0.17°C/s and 50°C/s.

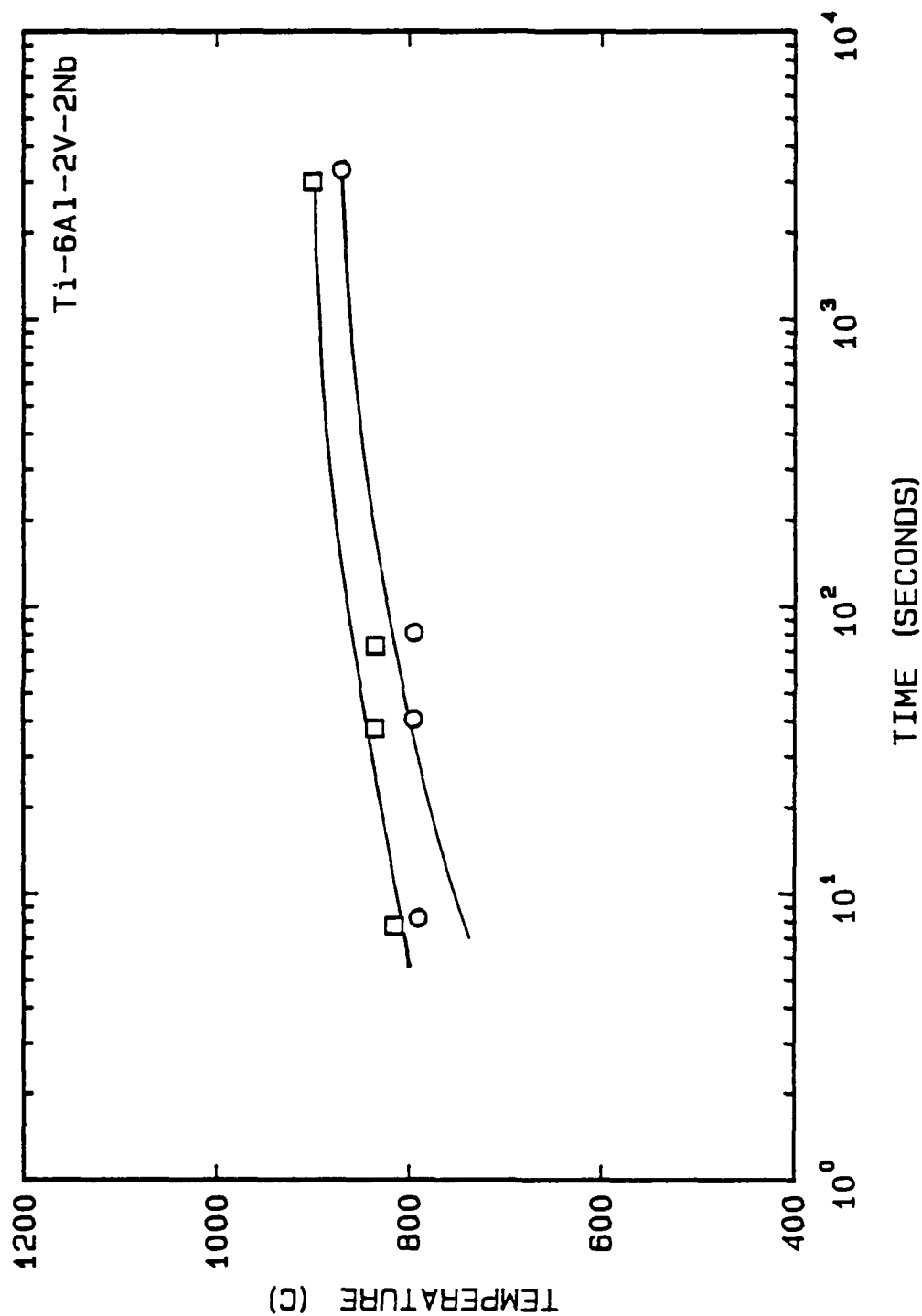


Figure 5.12 Partial CCT diagram for Ti-6Al-2V-2Nb for the range of cooling rates between 0.17°C/s and 50°C/s.

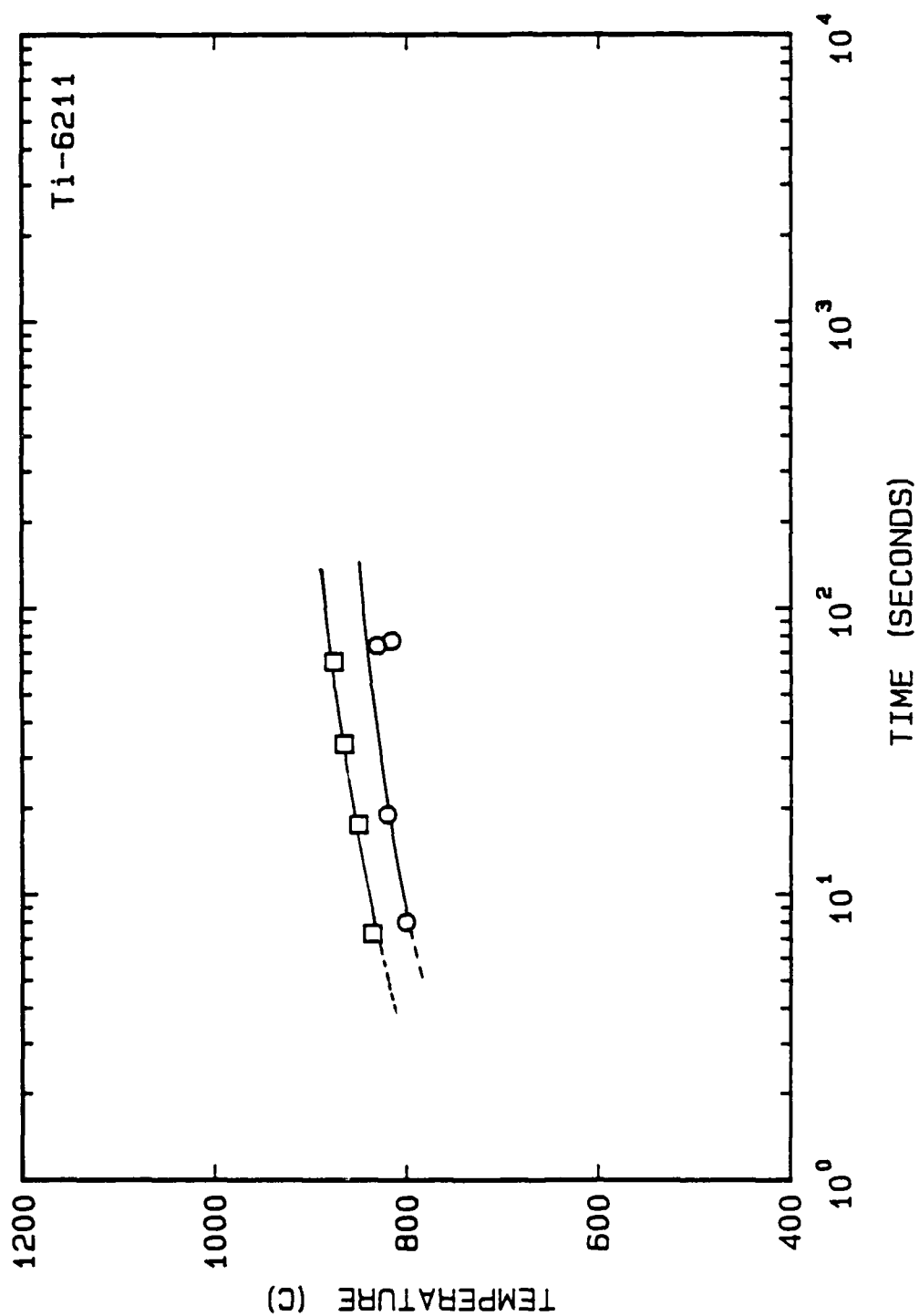


Figure 5.13 Partial CCT diagram for Ti-6211 for the range of cooling rates between 1°C/s and 50°C/s.

Table 5.1

Beta to Alpha Transformation Start and Finish Temperatures
for Several Alloys and Cooling Rates

Alloy	Cooling Rate ($^{\circ}\text{C/s}$)	T_s ($^{\circ}\text{C}$)	T_f ($^{\circ}\text{C}$)
unalloyed titanium	50	830	-
	20	865	845
	10	880	850
	5	895	860
Ti-6Al	50	940	-
	20	950	-
	10	960	925
	5	960	930
Ti-6Al-2V	50	850	-
	20	850	815
	10	860	820
	5	870	825
Ti-6Al-4V	100	805	-
	50	820	765
	20	825	780
	10	830	785
	5	830	790
Ti-6Al-6V	50	715	-
	20	725	-
	10	730	-
	5	735	685
Ti-6Al-2V-2Nb	50	815	790
	10	835	795
	5	835	795
	0.1	900	870

Table 5.1 (cont.)

Alloy	Cooling Rate ($^{\circ}\text{C/s}$)	T_s ($^{\circ}\text{C}$)	T_f ($^{\circ}\text{C}$)
Ti-6211	50	835	800
	20	850	820
	10	865	815
	5	875	830
Ti-6Al-2Nb	50	915	-
	20	940	885
	10	950	900
	1	935	910
Ti-6Al-4Nb	50	875	-
	20	880	830
	10	875	835
	0.17	915	860
Ti-6Al-6Nb	50	840	-
	20	820	780
	10	850	810
	0.17	870	830
Ti-6Al-2Mo	50	830	-
	20	810	-
	10	810	780
	0.17	865	820
Ti-6Al-4Mo	50	730	-
	20	740	690
	10	760	705
	0.17	770	-
Ti-6Al-6Mo	50	675	595
	20	680	600
	10	685	640
	0.17	735	665

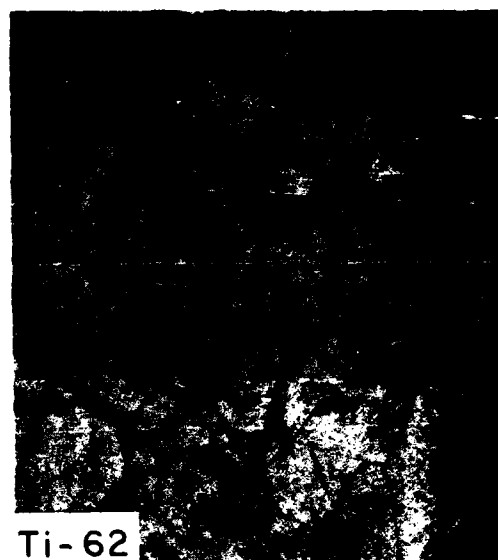


Figure 5.14 Optical micrographs of Ti-6Al-2V, Ti-6Al-4V, Ti-6Al-6V, and Ti-6211, cooled at 10°C/s. Note increasing refinement of structure with increasing vanadium addition.

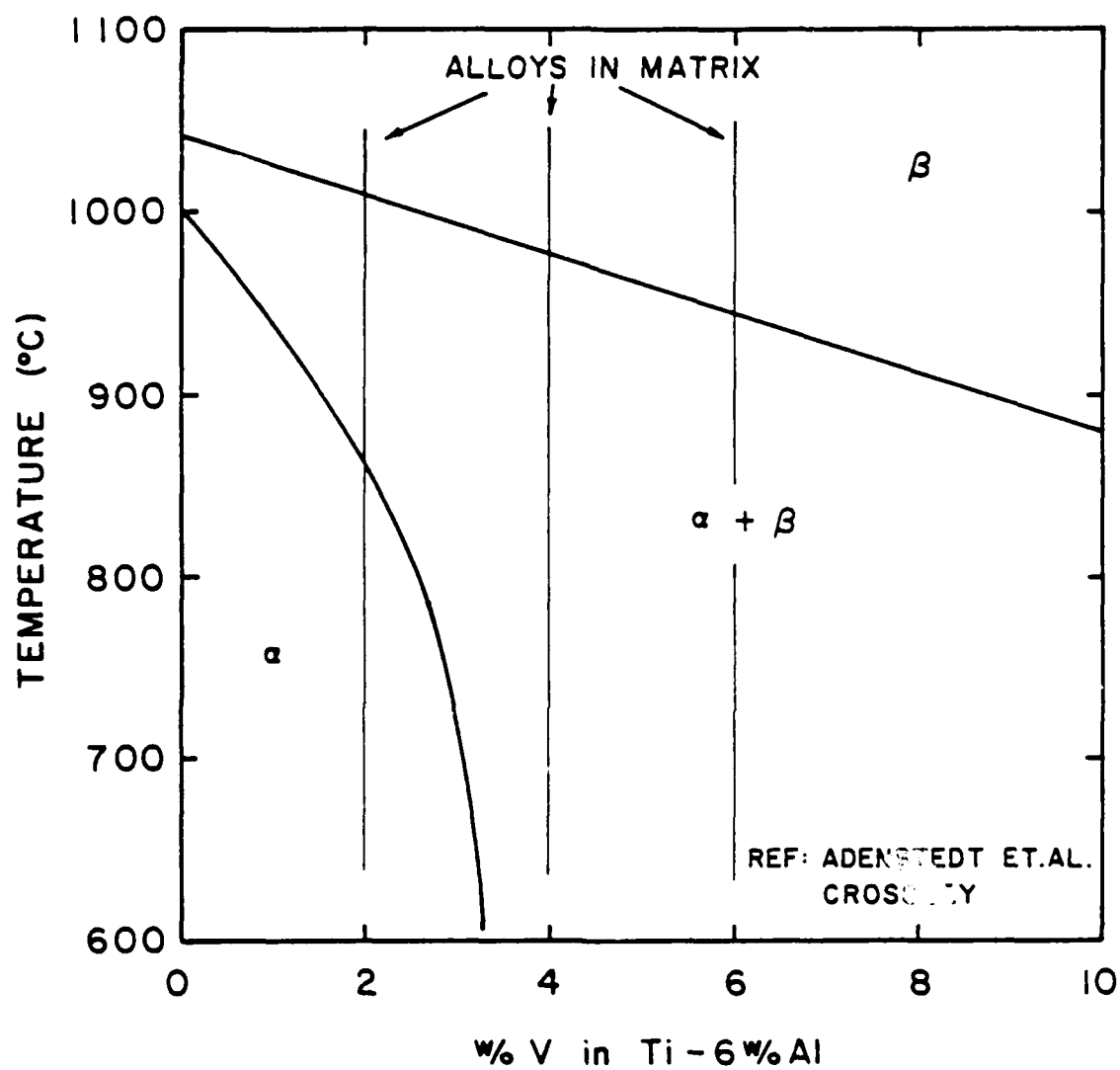


Figure 5.15(a) Psuedo-binary phase diagram for the system Ti-6Al-V.

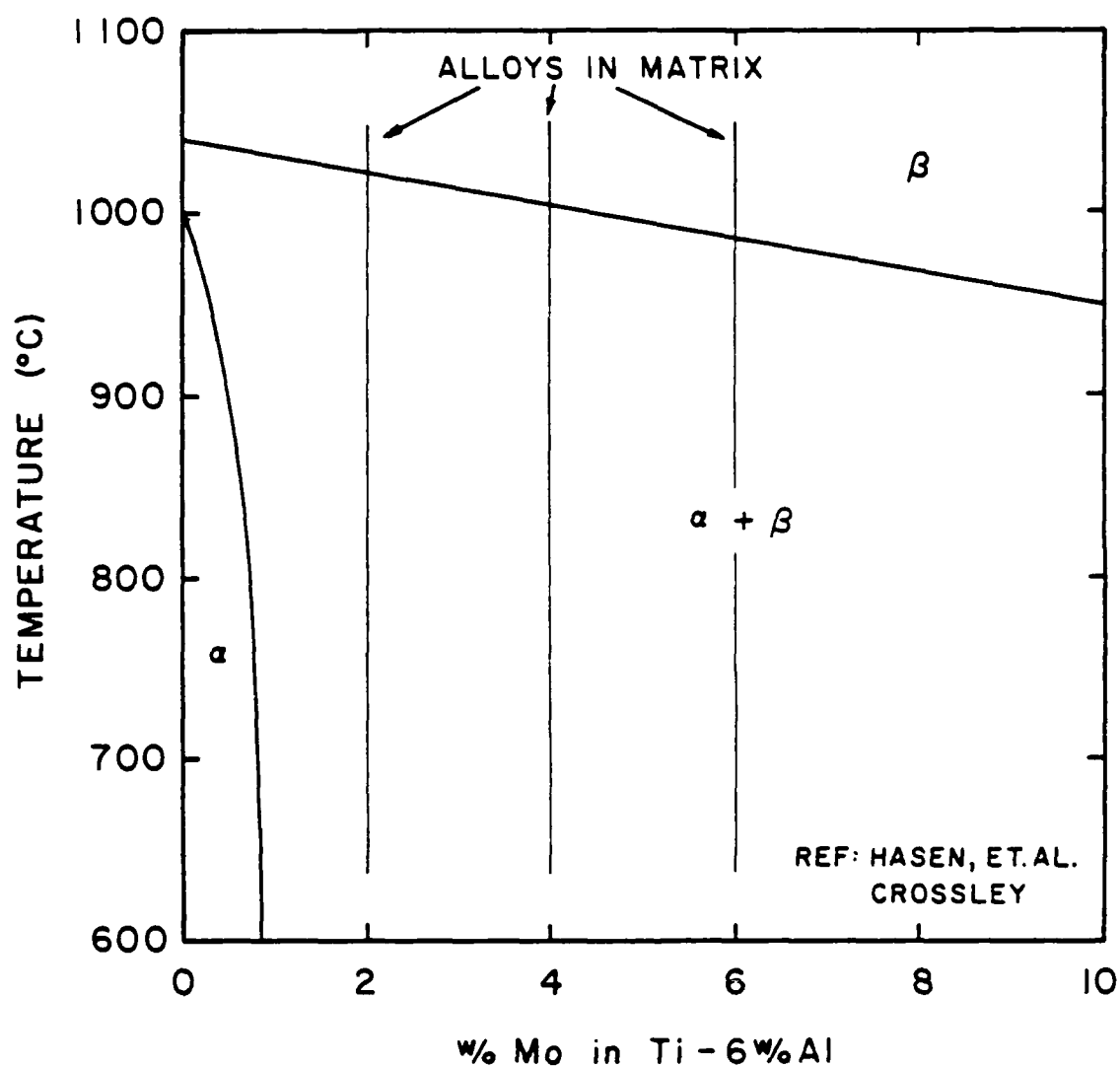


Figure 5.15(b) Psuedo-binary phase diagram for the system Ti-6Al-Mo.

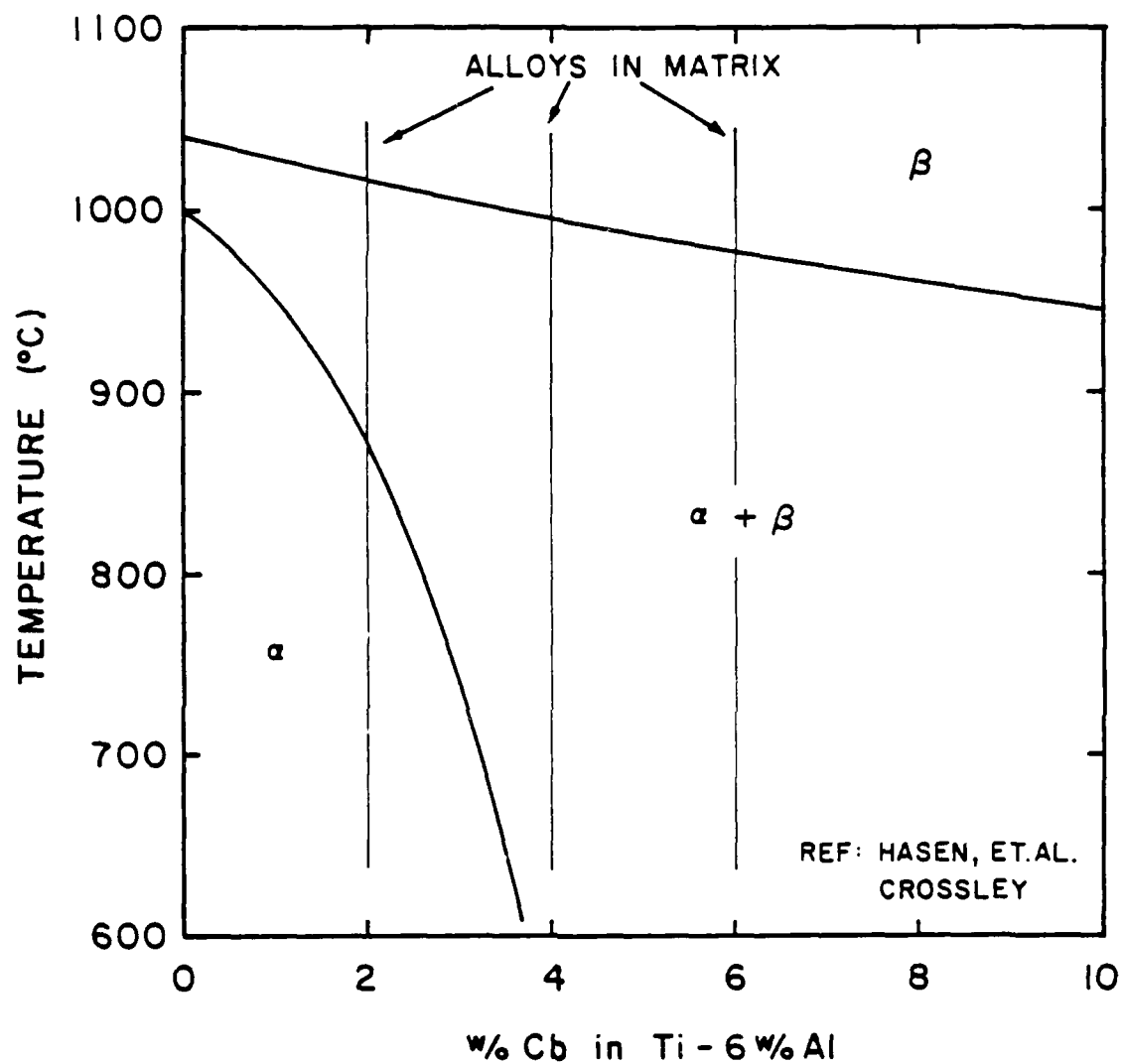


Figure 5.15(c) Psuedo-binary phase diagram for the system Ti-6Al-Nb.

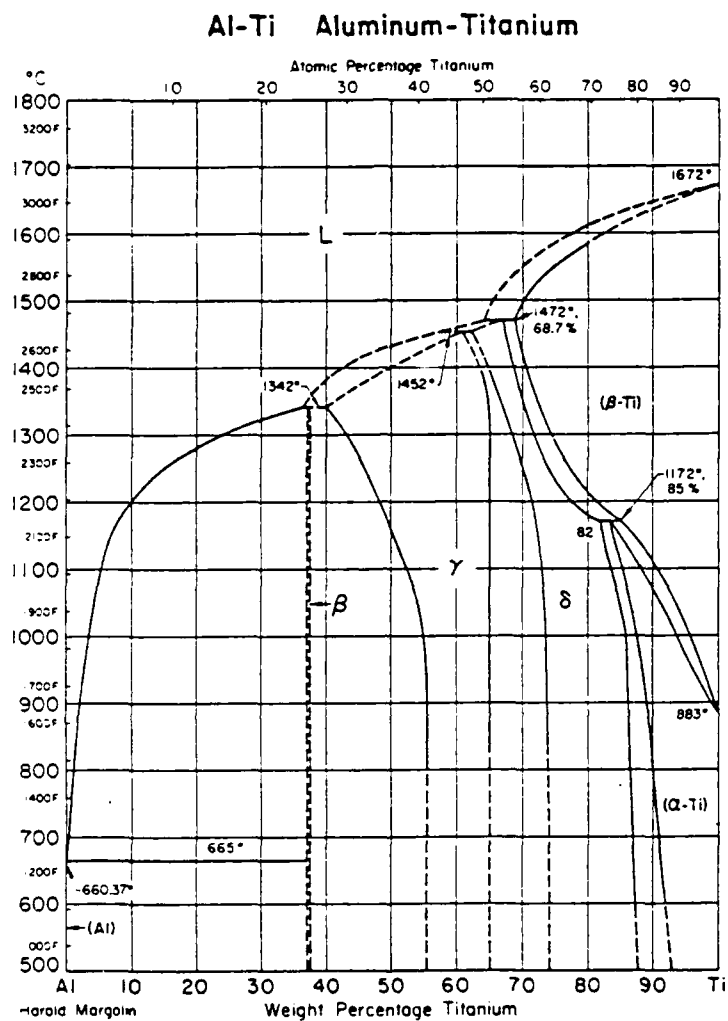


Figure 5.16 Titanium-aluminum binary phase diagram (88).

phase stability. The differences between the two sets of temperatures provide a base from which to begin a discussion of the transformation kinetics of these alloy systems. First, the effect of the addition of aluminum to titanium will be considered, followed by the further addition of beta stabilizer elements.

5.1.1.1 Aluminum Additions Figure 5.1 shows the partial CCT diagram for CP Ti. At a cooling rate of 10°C/s , the beta to alpha transformation start temperature is 880°C . The addition of 6% aluminum, Figure 5.2, raise this temperature to 960°C . These temperatures can be compared with equilibrium beta transus temperatures of 883°C and 1040°C respectively, a comparison which points out two things. First, the difference in equilibrium temperatures is much larger than that between beta to alpha transformation start temperatures. The second is that at 10°C/s , unalloyed titanium transforms at essentially zero undercooling but Ti-6Al requires a substantial amount of undercooling for the transformation to begin. This difference in behavior reflects the difference in transformation mechanisms between the two alloys. In the case of unalloyed titanium, the transformation is interface-controlled and can proceed with virtually no undercooling. The addition of aluminum, however, results in a

transformation which is controlled by long-range diffusion. As a result, substantial undercooling is required for the transformation to occur during rapid continuous cooling.

5.1.1.2 Addition of Beta Stabilizer Elements The further addition of one of the beta stabilizer elements lowers both the equilibrium and continuous cooling transformation temperatures. Based on the equilibrium beta transus temperatures shown in Figure 5.15, vanadium would be expected to have the greatest lowering effect on the transformation temperature, niobium the next most severe, and molybdenum the least. Figures 5.3, 5.6, and 5.9 show that this is not as predicted. At 10°C/s , Ti-6Al-2V, Ti-6Al-Nb, and Ti-6Al-2Mo have beta to alpha transformation start temperatures of 860°C , 950°C , 810°C , respectively.

When comparing different systems however, a second aspect of phase equilibria must be considered, the partitioning of the specific alloy elements. In binary alloys, molybdenum partitions far more strongly to the beta phase than do either vanadium or niobium (76-78). It has been shown (7) that the stability of the beta phase in binary titanium alloys can be characterized in terms of the electron/atom ratio, regardless of specific alloy content. This is consistent with the appearance of the phase diagrams (76-78) because molybdenum makes a larger electron

contribution than do either vanadium or niobium. It is reasonable to assume that electron/atom ratio can be used to describe beta phase stability in ternary alloys based on Ti-6Al. Thus, the beta stabilizer elements can be ranked in order of increasing extent of partitioning: vanadium, niobium, and molybdenum. In a transformation controlled by the diffusion of the beta stabilizer element, this relative order would be expected to apply to the relative levels of undercooling required to begin transformation, all else being equal.

In addition to the equilibrium effects discussed above, the effects of the alloying elements on the kinetics of the transformation must be considered, specifically the diffusion of the beta stabilizer element. Based on published (89, 90) values for D_0 and Q (in the expression $D_T = D_0 e^{-Q/RT}$) and the pseudo-binary diagrams in Figure 5.15, the diffusivities of niobium, vanadium, and molybdenum in beta titanium at the beta transus temperature can be calculated. These values are $1.01 \times 10^{-9} \text{ cm}^2/\text{s}$, $9.65 \times 10^{-10} \text{ cm}^2/\text{s}$, and $4.04 \times 10^{-10} \text{ cm}^2/\text{s}$, for Ti-6Al-2Nb, Ti-6Al-2V, and Ti-6Al-2Mo, respectively. Thus, the diffusivity of molybdenum is much lower than either niobium or vanadium. So, in addition to the greater extent of partitioning, the transformations in the molybdenum containing alloys are

further retarded by the relatively slow diffusion of molybdenum.

Based on the above consideration of equilibrium and kinetic effects, the relative positions of the CCT diagrams shown in Figures 5.1-5.13 can be rationalized as follows. The greater partitioning and slow diffusion of molybdenum cause the transformations in the molybdenum containing alloys to occur at much greater undercooling than either of the other systems, in spite of the equilibrium beta transus temperatures. On the other hand, the diffusivities of niobium and vanadium are very similar. The difference between these two systems can be explained by consideration of the equilibrium contributions. Based on the assumption of a constant electron/atom ratio in the alpha phase, vanadium would be expected to partition slightly more strongly to the beta phase (7). Also, because of its lower atomic weight, the vanadium alloys contain approximately twice as much beta stabilizer than do the niobium alloys, when the alloy contents are expressed in terms of atomic percent. This greater partitioning, combined with lower beta transus temperatures, cause the beta to alpha transformation to be suppressed to a greater degree in the vanadium system.

5.1.2 Discussion of Microstructures

All of the alloys tested with the exception of CP Ti and Ti-6Al can be classified as near-alpha or alpha-beta alloys. The microstructures observed contained alpha, beta, and in the case of very rapid cooling, alpha prime martensite. Equilibrium considerations such as the relative partitioning of the alloy elements discussed in the previous section will affect the relative stability of the beta and alpha phases, as well as any non-equilibrium phases which exist. However, the microstructures are primarily controlled by the relationship between the kinetics of the beta to alpha transformation and the cooling rate. In the following two sub-sections, the microstructures will be discussed with respect to first cooling rate, then alloy content.

5.1.2.1 Cooling Rate Effects Microstructures produced in Ti-6211, Ti-6Al-2V and Ti-6Al-6V at a range of cooling rates are shown in Figures 5.17-5.19. These microstructures contain examples of the specific microconstituents that will be referred to throughout the remainder of this investigation. These microconstituents are a grain boundary allotriomorph, or film, coarse Widmanstätten colonies, fine basketweave Widmanstätten alpha plus beta, and alpha prime martensite. The microstructures in these figures (and

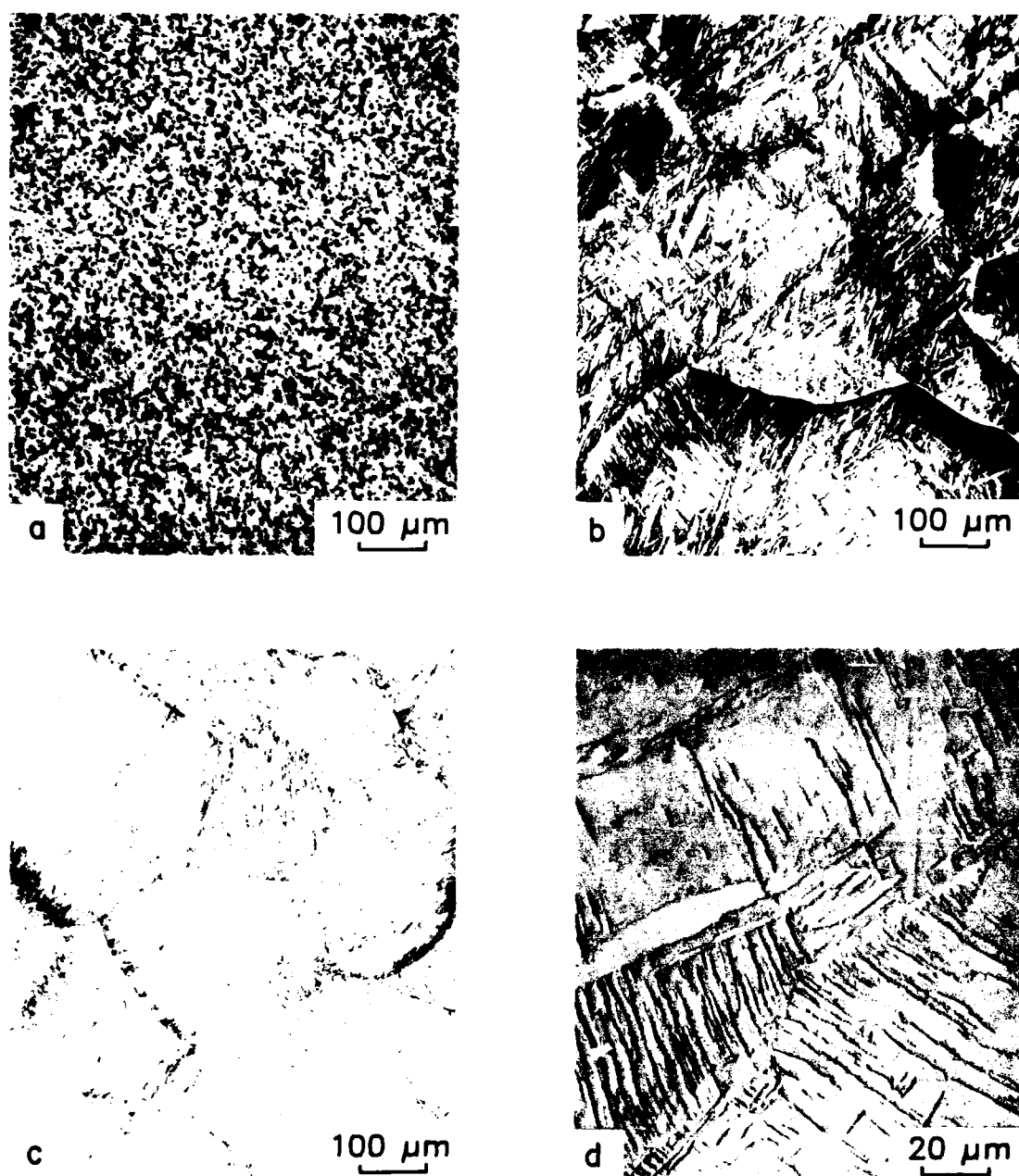


Figure 5.17 Optical micrographs of Ti-6211. As-received material (a) is equiaxed alpha plus beta. Cooling at 20 °C/s (b) or 50 °C/s (c) produces coarse, lenticular martensite, 250 °C/s, fine alpha prime martensite (d).

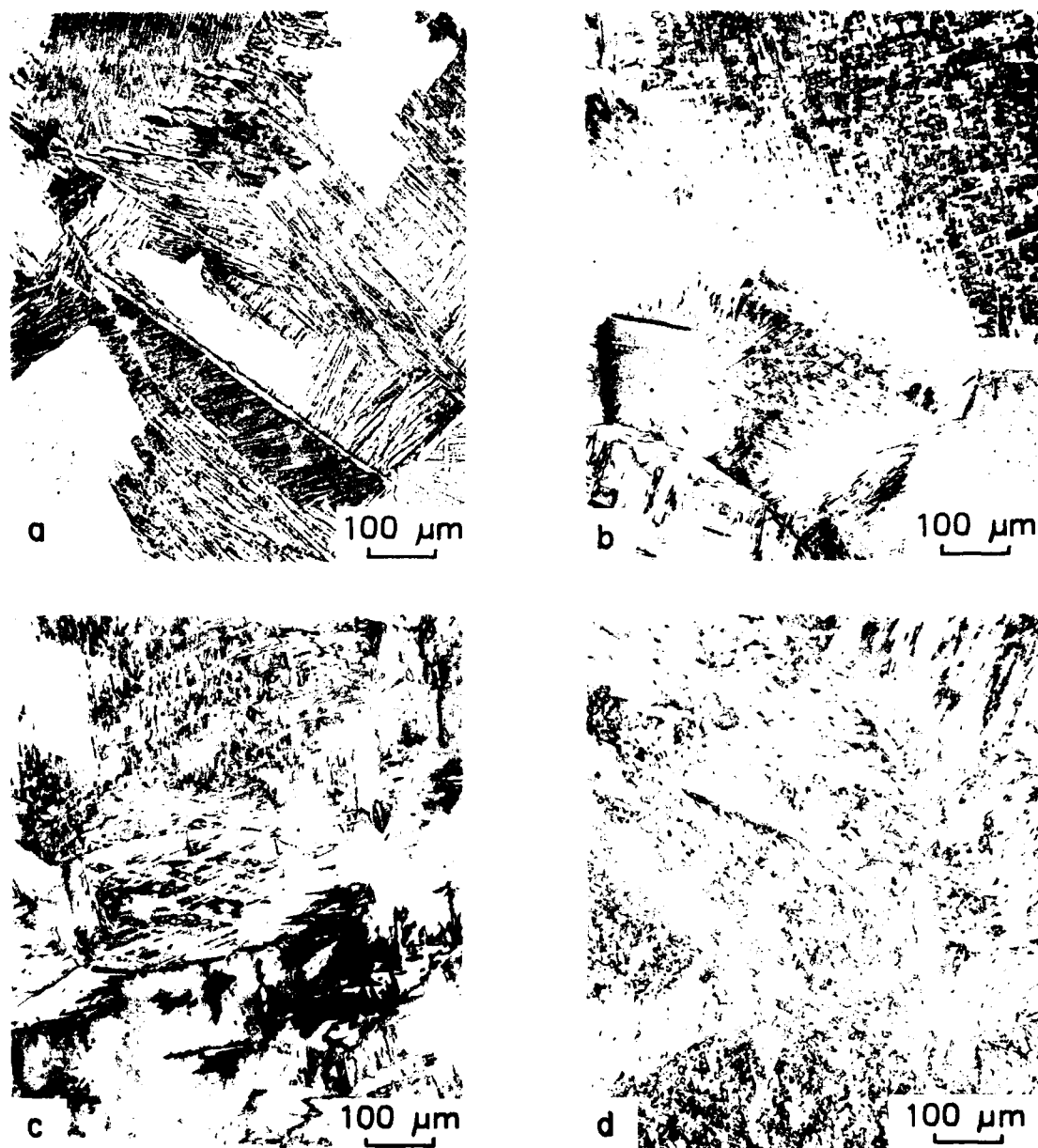


Figure 5.18 Optical micrographs of Ti-6Al-2V cooled at (a-d), 0.17°C/s , 10°C/s , 50°C/s , and 100°C/s . As cooling rate increases, lamellar structure (a) is replaced by fine basketweave structure (d).

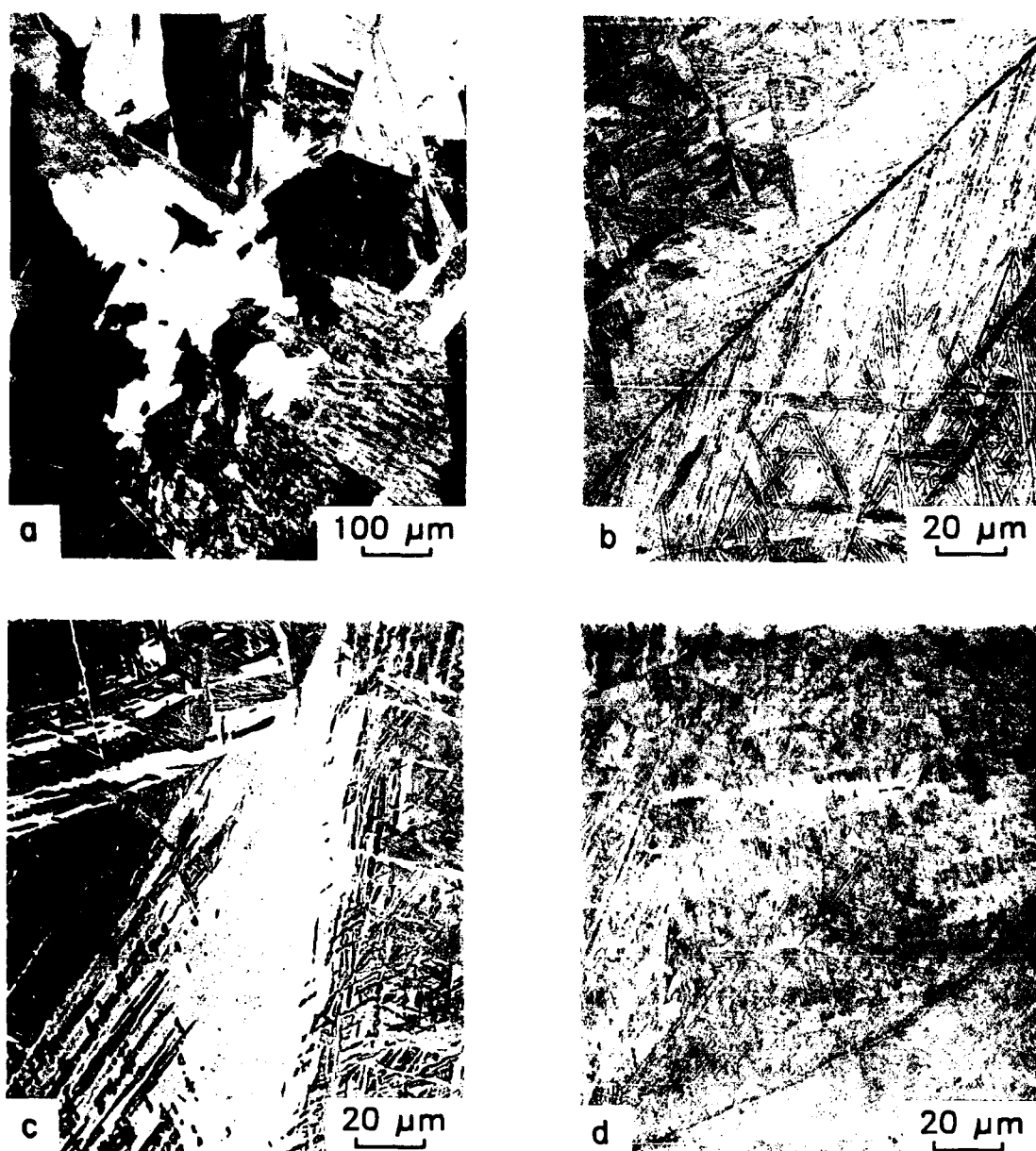


Figure 5.19 Optical micrographs of Ti-6Al-6V cooled at (a-d), 0.17°C/s , 1°C/s , 2°C/s , and 5°C/s . As cooling rate increases, lamellar structure (a) is replaced by fine basketweave structure (d).

throughout this investigation) show the general relationship between microstructure and cooling rate that is always seen in alpha-beta titanium alloys (91). As the material cools through the beta to alpha transformation, allotriomorphic alpha nucleates and grows at the beta grain boundaries. If the transformation continues under nearly equilibrium conditions, the resultant microstructure will be coarse equiaxed alpha with retained beta at the grain boundary triple points, Figure 5.17(a). Transformation during continuous cooling conditions but at a very slow cooling rate will create a microstructure consisting of alpha allotriomorphs at the prior beta grain boundaries and coarse Widmanstatten colonies, Figures 5.18(a) and 5.19(a). As the cooling rate increases further, the Widmanstatten colony structure is increasingly replaced at the center of the prior beta grains by fine basketweave Widmanstatten alpha plus beta, apparently nucleated intragranularly, Figures 5.17-5.19(a-c). With sufficiently rapid cooling, the nucleation and growth transformation can be avoided, producing a structure consisting of alpha prime martensite, Figures 5.17-5.19(d). In comparison, the range of structures created by the cooling rates usually seen in fabrication processes, for example, in the fusion and heat-affected zones of weldments, vary from grain boundary alpha

plus coarse Widmanstätten alpha plus beta to alpha prime martensite (62-66).

5.1.2.2 Alloy Effects Figures 5.14 and 5.17-5.19 illustrate the interdependence of cooling rate and alloy content in determining the transformed microstructures in these alloys. When cooled at the same rate, the transformation structure in Ti-6Al-2V is much coarser and contains more of the Widmanstätten colony structure than do the microstructures of either Ti-6Al-4V or Ti-6Al-6V, Figure 5.14. Comparison of the microstructures in Figure 5.14 with those in Figures 5.18 and 5.19 show that a similar microstructural trend can be produced by either changes in vanadium content or cooling rate. Specifically, the fine basketweave structure is favored by high cooling rates and the addition of vanadium. The colony microstructure is favored by low cooling rates and a low vanadium content. Although not shown, similar relationships were observed in the Ti-6Al-Mo and Ti-6Al-Nb systems.

5.1.3 Overall Transformation Mechanism

The microstructures observed in this investigation contain alpha prime martensite and three distinct microconstituents which are products of nucleation and growth. These microconstituents are a grain boundary alpha

film, coarse Widmanstätten colonies, and fine basketweave Widmanstätten alpha plus beta. The existence of these three distinct structures suggests that during continuous cooling, the beta to alpha transformation consists of three competing processes, the relative rates of which change with cooling rate and alloy content.

The transformation begins near the equilibrium temperature with site saturation nucleation at the beta grain boundaries, followed by the growth of a plane front allotriomorph. Eventually constitutional supercooling causes a breakdown of the planar interface and the formation of the Widmanstätten colonies. The colonies form by growth of an existing alpha allotriomorph and thus, require no nucleation. The growth of the colonies is controlled by the diffusion of the beta stabilizer element. Therefore, the colony structure will be favored in alloys with high-diffusivity beta stabilizers and high beta to alpha transformation temperatures. For an individual alloy system, the colony structure will be favored by situations where the transformation occurs at small undercooling, in lean alloys and at slow cooling rates. The micrographs in Figures 5.14, 5.18, and 5.19 show these trends.

As the transformation proceeds during continuous cooling, the colonies grow inward toward the beta grain

center until a point is reached where it is energetically more favorable for the remainder of the grain to transform to the fine basketweave structure. The basketweave structure begins to form when continuous cooling reduces the temperature to the point where intragranular nucleation within the beta grain is possible. The growth of these nuclei then occurs on a much finer scale due both the continuous nucleation and also to the low temperature and short diffusion distances. Because the formation of the basketweave microconstituent contains both nucleation and growth, it will be favored (as opposed to the colony microconstituent) in alloys with slower diffusing beta stabilizer elements and lower beta to alpha transformation temperatures. Within an individual alloy system, the basketweave microconstituent will be favored by richer alloys and higher cooling rates. These trends are seen in the microstructures contained in Figures 5.14 and 5.17-5.19.

Throughout the preceding discussion, the assumption has been made that the the velocity of the alpha/beta interface, hence the growth of the alpha phase, is controlled by the diffusion of the beta stabilizing element rather than by the diffusion of aluminum. In the absence of data regarding the diffusivity of aluminum in beta titanium, this assumption can be supported by a consideration of the

equilibrium phase diagrams shown in Figures 5.15 and 5.16. A comparison of these figures shows that the alpha + beta two-phase field is much larger in the case of the beta stabilized systems. This indicates that the extent of partitioning during the transformation is much greater for the beta stabilizing elements than for aluminum. Examination of Figure 5.20, the ternary Ti-Al-V diagram of Farrar and Margolin (92), supports this. Figure 5.20 contains 1000°C, 900°C, and 800°C isothermal sections of this diagram. In each section, the position of Ti-6Al-4V is indicated. At 1000°C, the material is all beta, hence the beta contains 4% vanadium. At 900°C, the beta composition is 5Al-8V and the alpha composition is 6Al-1V. At 800°C, near the beta to alpha transformation finish for the cooling rates in this investigation, the beta composition is 4Al-14V and the alpha composition is 6Al-2V.

The greater partitioning of beta stabilizing elements has been shown experimentally as well. Mahajan, et.al. (93) measured the composition of alpha and beta in a Widmanstatten colony structure produced in slowly cooled Ti-6Al-2Sn-4Zr-6Mo. These investigators found that the composition of the beta phase was approximately 15Mo-2Al, and of the alpha phase, approximately 1Mo-5Al.

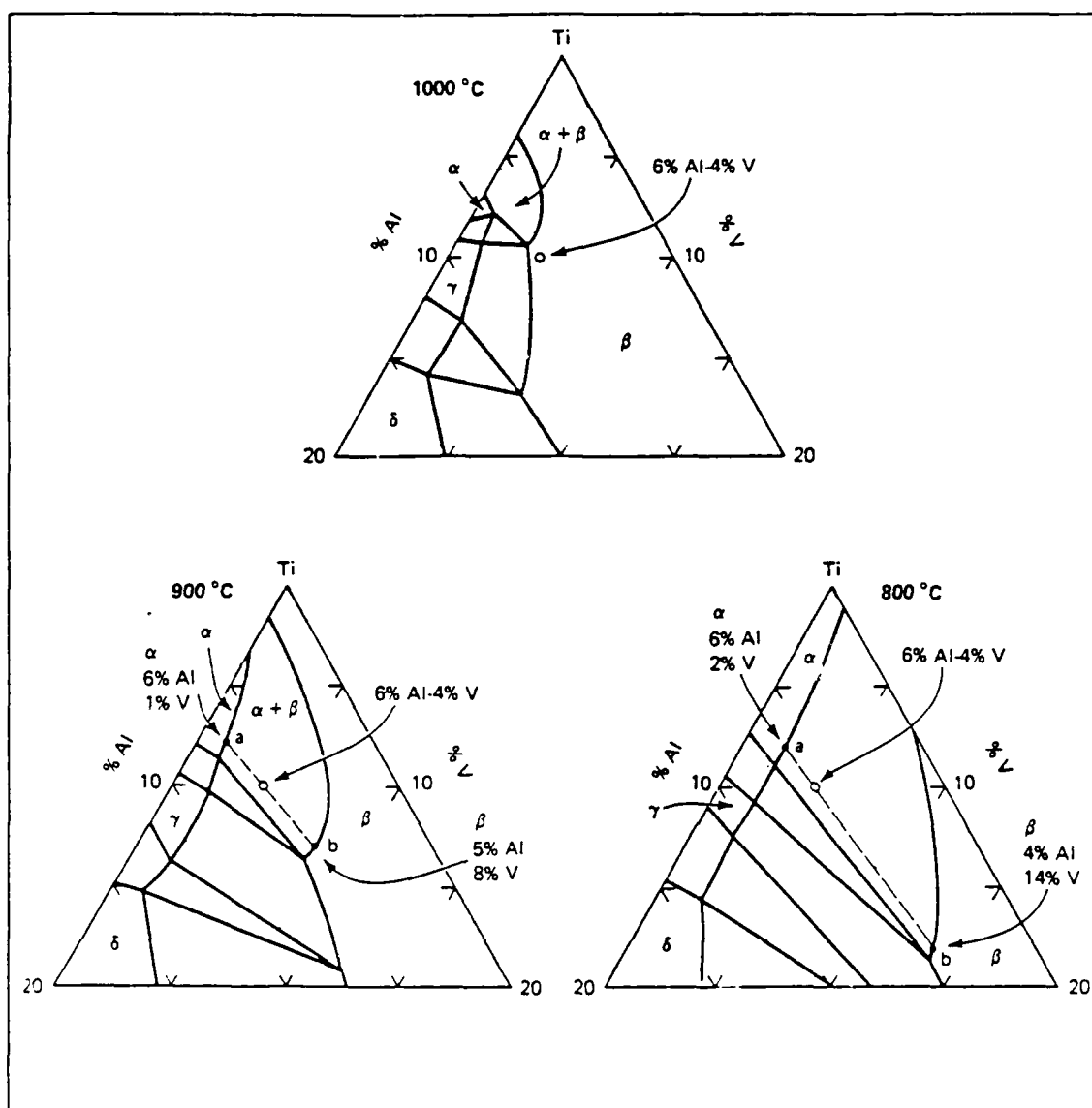


Figure 5.20 800°C, 900°C, and 1000°C isothermal sections of the titanium-aluminum-vanadium ternary phase diagram of Farrar and Margolin (92).

5.1.4 Transformation Kinetics Modelling

Several attempts have been made to model the kinetics of continuous cooling transformations (94-103). The most common approach has been to convert the isothermal equations developed by Avrami (104-106) or Johnson and Mehl (107) to continuous cooling using the Scheil (108) additivity principle. Usually, the development of these models has been to test the limits of applicability of the additivity concept. A good example of this type of investigation is the modelling of the austenite to ferrite plus pearlite transformation(s) in ferrous alloys done by Hawbolt, et. al. (100). These investigators found that the additivity principle could be successfully applied only after the inclusion of a separate incubation time prior to the transformation start. However, Umemoto, et. al. developed a successful model for similar systems using only the additivity principle, without the incorporation of an incubation.

In this investigation, the applicability limits of the additivity principle are further tested. While past investigations (100, 101) have modelled systems containing more one than one transformation, the individual transformations have each existed over a different temperature range. None have modelled transformations which

compete within a given temperature range. In this investigation, the formation of the grain boundary alpha film, the Widmanstatten colonies, and the basketweave alpha plus beta all occur over the same temperature range and are all referenced to the same equilibrium temperature. Therefore, the success of this model not only extends the limits of applicability of the additivity principle, but also validates the assumed overall transformation mechanism.

With the model developed in this study, it is the kinetics of the individual transformations which dictate their rates, and thus the microstructures formed, in a given situation. Because of this, once this model is developed, it can be used to predict the effects of system changes on transformation kinetics and microstructures, based on changes in fundamental quantities. Examples of such predictions are included.

In the sub-sections that follow, the isothermal kinetics of each transformation will be modelled individually, using the equations of Avrami (104-106) and Johnson and Mehl (107). These isothermal equations will then be modified to describe continuous cooling conditions using the additivity principle and combined into an expression to describe the overall transformation kinetics. The model will then be calibrated to fit, in a general

sense, the transformation temperatures and microstructures produced in Ti-6Al-4V. Following this, the effects of several system changes will be investigated.

5.1.4.1 Growth of Widmanstatten Colonies Using the assumptions of site saturation and one dimensional growth, the formation of the Widmanstatten colony structure can be described by the following equation:

$$X = 1 - \exp(-A I_0 G t) \quad 5.1$$

where: X = volume fraction transformed

$A = 2\pi d^2$, twice the area of the plates

I_0 = number of plates per volume

G = interface velocity, dx/dt

t = time

In the above analysis, it is assumed that the sideplates are cylindrical and grow by lengthening only, and that G is constant at any temperature.

5.1.4.2 Grain Boundary Allotriomorph The colony structure results from the breakdown of a planar transformation front due to constitutional supercooling. This situation was modelled as the colony structure growing off a grain boundary allotriomorph which was itself growing to a maximum of 2 volume percent of the final transformed structure. (The value of 2 volume percent was determined by

metallographic observation of microstructures produced in several alpha-beta titanium alloys over a wide range of cooling rates.) The volume percent transformed of the allotriomorph was used as the nucleation event for the colony growth. The formation of the grain boundary allotriomorph itself was modelled as having continuous nucleation and one-dimensional growth by movement of a planar interface. The isothermal equation for this transformation is:

$$X = 0.02(1 - \exp(-AIGt^2))$$

where: X = volume fraction transformed

A = number of nucleation sites per volume

(related to $2S_v$, twice the boundary area per volume)

I = nucleation rate, nuclei per time

G = interface velocity, dx/dt

t = time

In this case, I is constant at any temperature but G is proportional to $t^{-1/2}$.

5.1.4.3 Basketweave Structure The nucleation and growth of the Widmanstätten basketweave alpha plus beta structure can be modelled in a similar fashion.

$$X = 1 - \exp(-BIGt^2) \quad 5.2$$

where: X = volume fraction transformed

$B = \pi d^2/4$, the area of the Plates

I = nucleation rate, nuclei per volume per time

G = interface velocity, dx/dt

t = time

In this case, it is assumed that growth occurs by lengthening of a cylindrical particle and that I and G , while both functions of undercooling, are constants at any temperature.

5.1.4.4 Application of the Additivity Principle The Scheil (108) additivity principle models continuous cooling as a series of small isothermal steps. At each step, the time spent is a portion of the time required, at that temperature, to achieve a given amount of transformation. When the fractions add up to 1, the given amount of transformation has been achieved. Mathematically:

$$1 = \sum (t_T/\tau_T) \quad 5.3$$

where: X_0 = volume percent transformed

t_T = time spent at temperature T

τ_T = time for X_0 volume percent transformation at T

Or, in integral form:

$$1 = \int (dt/\tau)$$

$$\text{or: } 1 = \int (dt/dT)(dT/\tau)$$

$$\text{or: } 1 = \int (dt/dX)(dT/\tau)$$

Development and early evaluations of the additivity concept were performed by several investigators, usually for the purpose of converting isothermal (TTT) diagrams to continuous cooling (CCT) diagrams (96-103). Avrami (95) proposed that the additivity principle was valid for transformations where nucleation rate was proportional to growth and called these situations "isokinetic" transformations. Cahn (96) expanded the applicability of the additivity concept to include all transformations where $dX/dt = a$ function of X and T only. Cahn also pointed out that reactions involving two time-temperatures parameters, nucleation and growth, will generally not be additive. However, in certain instances, such as site saturation nucleation where the transformation proceeds by growth only, only one time-temperature parameter is involved and the reaction is additive. Another example is a situation where $I \propto G$, reducing these two parameters to one, the Avrami isokinetic assumption. Kuban, et. al. (97) further extended the applicability of the additivity principle in a study of the austenite to pearlite transformation in a 1080 plain

carbon steel. This study showed that the additivity principle was applicable whenever a criteria of "effective site saturation" was met. This criteria was described as a situation where "...the nuclei formed in the initial stages of the transformation dominate the subsequent transformation kinetics" (97). By comparison of predicted and measured results, Kuban, et. al. found that this criteria was met when the first 20% of the transformation product grew to account for between 50% and 85% of the volume transformed at a total of 90% transformed. The actual percentage required for successful application of the additivity depended on the choice of a specific Avrami form for the original isothermal equation.

Bypassing for now the problems with the additivity concept and following a procedure similar to that of Umemoto (102), equation (5.3) can be used to convert the isothermal kinetic expressions (5.1) and (5.2) to continuous cooling expressions. First note that equation (5.3) can be re-written as follows:

$$1 = \sum [(\Delta T/Q)(1/\tau)] \quad 5.4$$

where: Q = cooling rate ($\Delta t/\Delta t$)

and: ΔT = temperature step (not undercooling)

Equations (5.1) and (5.2) can each be converted to apply to continuous cooling by combination with the

additivity concept. However, because two competing transformations will be combined, they must each be corrected for the impingement of the competing transformation product as well as their own impingement. This is done by using the unimpinged isothermal equations for the additivity procedure and later making the necessary corrections. If not corrected for self-impingement, equations (5.1) and (5.2) are:

$$X = AI_0 Gt \quad 5.1$$

$$X = BIGt^2 \quad 5.2$$

Assuming for now that A , I_0 , and G are not functions of t , and solving for t in equation (5.1):

$$t = X/AI_0 G$$

$$\text{where: } t = \tau \text{ at } X = X_0$$

Substituting t for τ in the re-written equation (5.1) and solving for X , noting that at this point X , A , Q , and I_0 are constants, produces:

$$X1 = (AI_0/Q) \sum G\Delta T \quad 5.5$$

$$\text{where: } Q = (\Delta T/\Delta t, \text{ cooling rate})$$

and $G\Delta T$ is summed from T to T_e , the equilibrium temperature.

Similarly, for the continuous nucleation transformation:

$$X2 = [(B^{1/2}/Q) \sum (IG)^{1/2} \Delta T]^2 \quad 5.6$$

where $(IG)^{1/2} \Delta T$ is summed from T to T_e . Then, if the two reactions are occurring simultaneously and impingement is

neglected, the total transformation is the sum of equations (5.5) and (5.6), or:

$$X_{\text{total}} = (AI_0/Q)\Sigma G\Delta T + [(B^{1/2}/Q)\Sigma (IG)^{1/2}\Delta T]^2$$

Then, corrected for total impingement:

$$X_{\text{total}} = 1 - \exp-(X_1 + X_2) \quad 5.7$$

Similarly, the individual transformations can be approximated by:

$$X_{1\text{ actual}} = [1 - \exp-(X_1)](1 - X_{2\text{ actual}}) \quad 5.8$$

$$X_{2\text{ actual}} = [1 - \exp-(X_2)](1 - X_{1\text{ actual}}) \quad 5.9$$

It is obvious that many assumptions have been made throughout the analysis for the sake of simplicity, and thus the limitations of the model are equally obvious. A more rigorous development of this model would require an examination of these assumptions and the appropriate modifications. The most significant of these assumptions was to start with an assumed transformation mechanism. For example, a possible modification would be to include a martensitic transformation and/or a massive transformation. Both have been observed in these types of alloys (109). The prior assumption of specific transformation mechanisms also dictated the forms of the isothermal equations used. These could be modified to reflect different geometries such as plate lengthening and widening or modified to include a capillarity effect.

Once the isothermal equations were chosen, a second major assumption was that of the functionality of the nucleation and growth rates, specifically that they were not functions of time (in the two main transformations). For example, a more accurate approximation of nucleation rate could probably be made by using an Avrami formulation with exhaustable nucleation sites (104-106).

An in-depth analysis of the model would require evaluation of these and other assumptions, and extensive comparison of predicted and experimental results. Such an evaluation also requires that the parameters in the equations be based, as much as possible, on measured values of the fundamental components of these parameters. This type of analysis is beyond the scope of this investigation. However, for the purpose of this investigation, the model can be used to explain the evolution of the observed microstructures in terms of system changes and their effects on the kinetics of the transformation.

5.1.4.5 Calibration to Ti-6Al-4V Results The constants and coefficients in the above equations represent combinations of physical quantities and empirically determined values, based on isothermal transformation kinetics. In the absence of these data, the model was calibrated based on the transformation temperatures and microstructures observed in

Ti-6Al-4V cooled at 10°C/s . This resulted in equations (5.7), (5.8), and (5.9), which describe the transformation behavior of a theoretical alpha-beta titanium alloy, "BKD-007". Equations (5.7-5.9) can be used to predict transformation kinetics and microstructures of this theoretical alloy at any particular cooling rate selected. Examples of these predictions are shown in Figures 5.21 and 5.22. Figure 5.21 is a plot of volume percent transformation versus temperature for the individual and overall transformations for BKD-007 cooled at 5°C/s . Figure 53 shows the corresponding transformation rates plotted versus temperature for the same cooling rate.

5.1.4.6 Effects of System Changes Two system variables which were investigated were cooling rate and alloy content. Their effects can be analyzed by examination of their the equations for nucleation and growth as well as the final transformation equation. To re-iterate, the final transformation equations are:

$$X1 = (A1_0/Q)\{G\Delta T \quad 5.5$$

$$X2 = [(B^{1/2}/Q)\{(IG)^{1/2}\Delta T\}^2 \quad 5.6$$

The basic equations for nucleation and growth are, respectively:

$$I = A\exp(-B/f(T)), \text{ where } f(T) = T(\Delta T)^{1/2}$$

$$G = C\Delta T\exp(-D/T) \text{ for the colony structure}$$

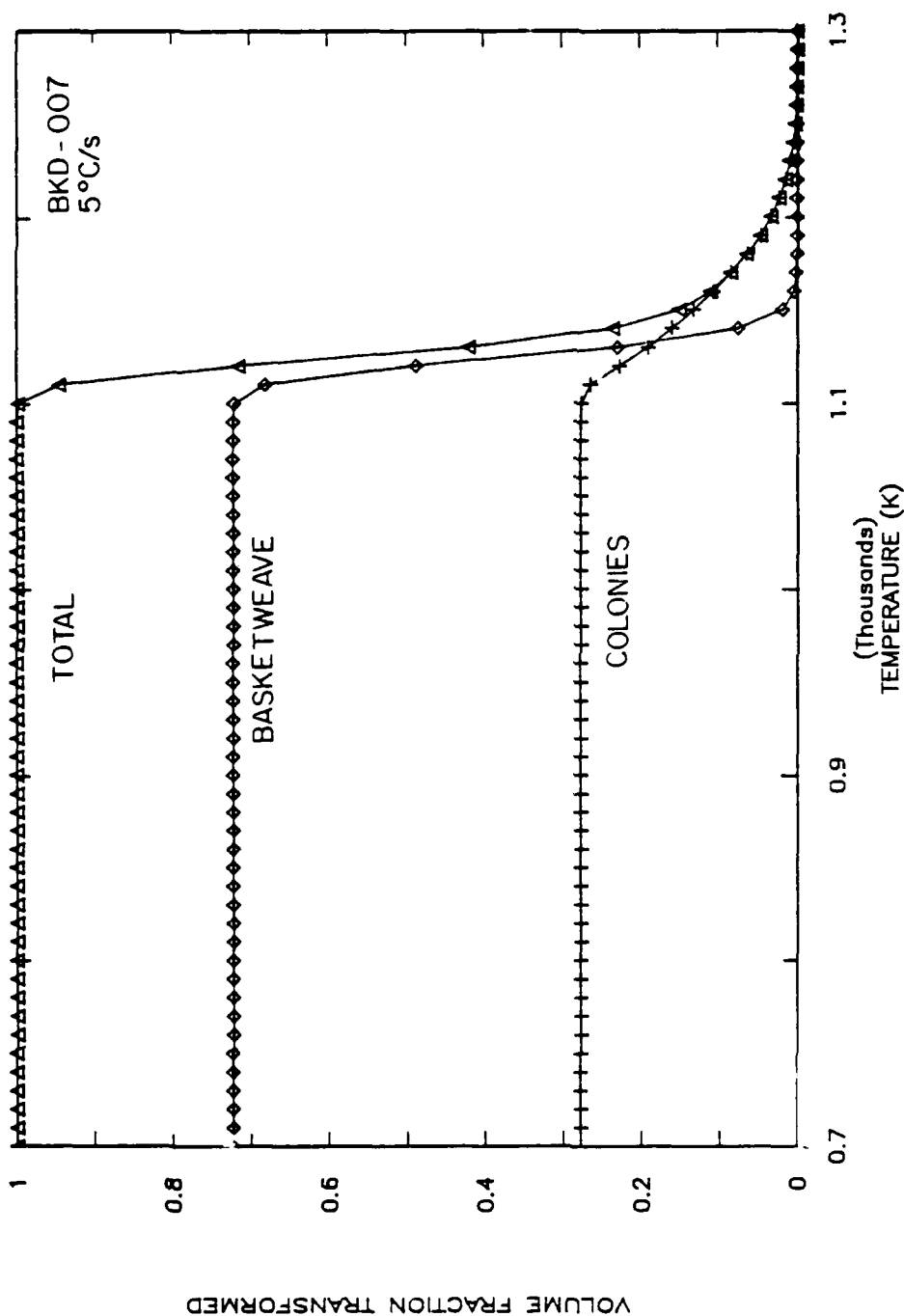


Figure 5.21 Predicted microstructure generation for model alloy BKD-007. Volume fraction of colony and basketweave microconstituents, and total volume fraction transformed, versus temperature.

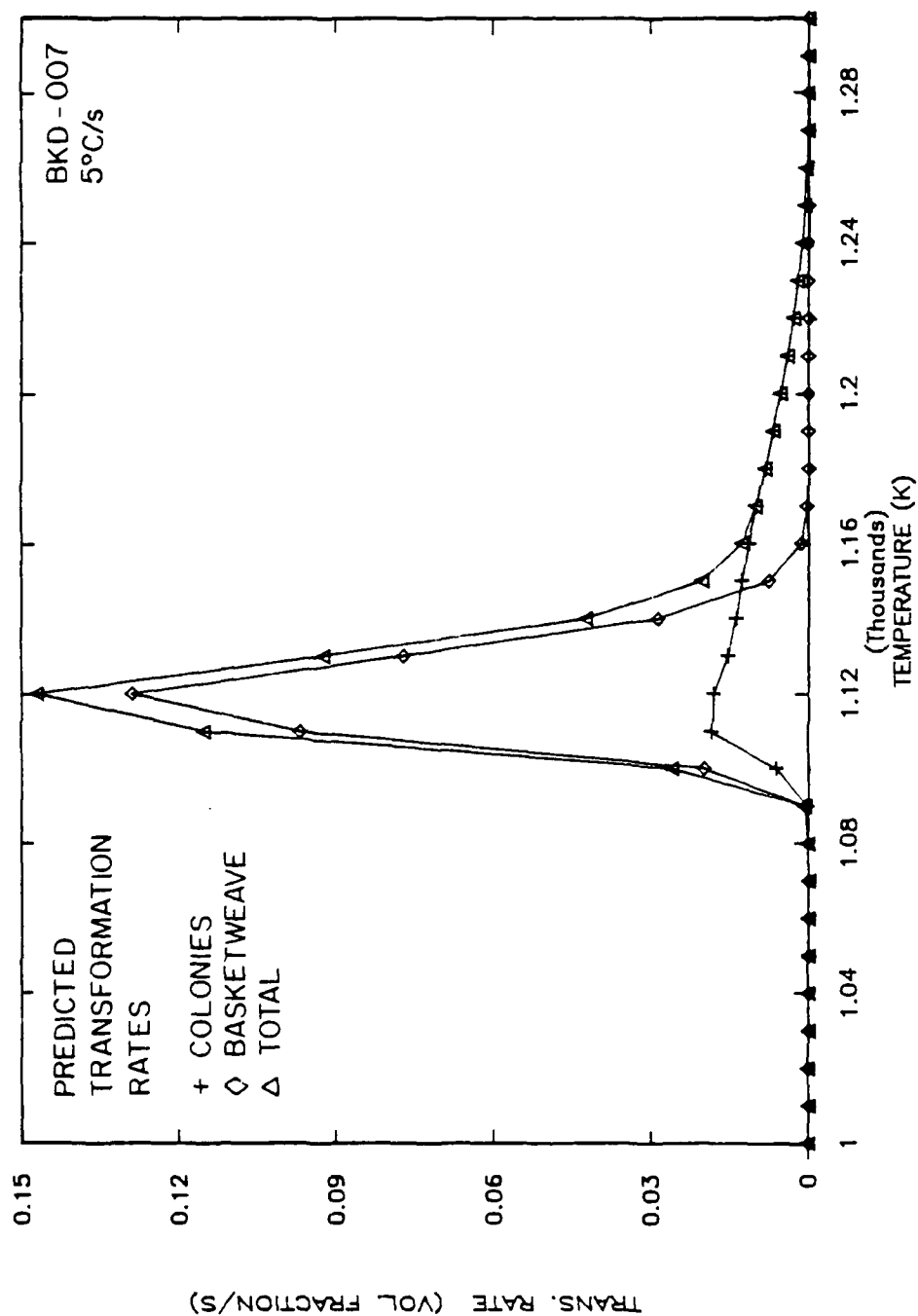


Figure 5.22 Predicted transformation rates for colony and basketweave microconstituents, and total transformation, model alloy BKD-007 cooled at 5°C/s.

$G = C\Delta T \exp(-D/T)t^{-1/2}$ for the grain boundary allotriomorph

Cooling rate appears both explicitly in the final transformation equations, and implicitly, in the form of undercooling, in the expressions for nucleation and growth. Conceptually, the major effect of an increase cooling rate is to cause the transformation to occur at higher undercooling and lower temperature. Because undercooling appears in an exponential in the nucleation expression, this is the dominant effect. This can be demonstrated by using the model to generate curves of X_1 and X_2 as functions of temperature for several cooling rates. An example was shown in Figure 5.21. When this data is analyzed, the volume percent of either microconstituent can be plotted as a function of cooling rate. This is done in Figure 5.23(b), a plot of volume percent basketweave structure versus cooling rate for theoretical alloy BKD-007 and cooling rates from 1°C/s to 100°C/s . For comparison purposes, the corresponding measured values for Ti-6Al-4V are superimposed on this figure and show a microstructural trend similar to that predicted by the model.

The data representing volume percent transformed as a function of temperature for several cooling rates can be combined with a criteria for measurable transformation start and finish points and used to generate a predicted CCT

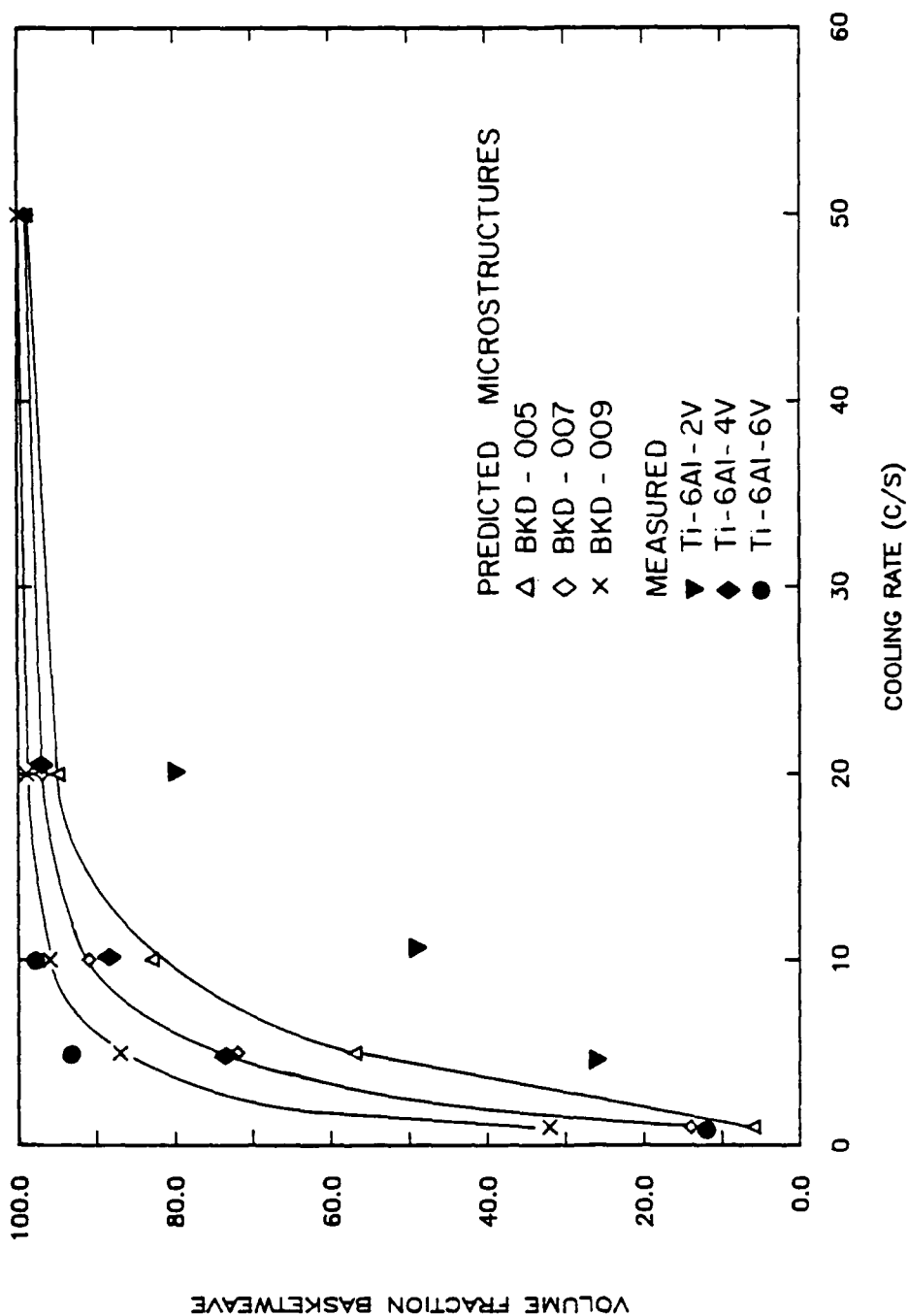


Figure 5.23 Predicted microstructures (volume percent basketweave microconstituent) in model alloys BKD-005, BKD-007, and BKD-009, for several cooling rates. Also shown is measured data for Ti-6Al-V ternary alloys.

diagram. This was done for the theoretical alloy BKD-007 using the arbitrary choices of 5 volume percent transformed as a start criteria and $\Delta X_T/\Delta T = 0.4$ as a finish criteria. The result is shown in Figure 5.24(b), a predicted CCT diagram for BKD-007 based on cooling from 1500°K (1227°C) and an equilibrium temperature of 1300°K (1027°C). Again, the corresponding measured data for Ti-6Al-4V are also shown. The Ti-6Al-4V was cooled from 1473°K (1200°C) and has an equilibrium temperature of 1266°K (993°C) (100).

Changes in beta stabilizer content are known to have two major effects. The first is to change the equilibrium transformation temperature. Examination of the psuedo binary diagram for the Ti-6Al-V system, Figure 5.15, shows that changing the alloy content by 2% will change the transformation temperature by approximately 30°C . An increase in T_e will raise the temperature at any level of undercooling, enhance diffusion, and thus favor growth over nucleation. This will decrease the amount of basketweave structure produced at any cooling rate.

The second major effect of changing the beta stabilizer content is to change the chemical potential gradient, the driving force for growth, which is contained in the " $C\Delta T$ " term in the growth equation. This driving force, in the absence of capillarity effects and assuming local

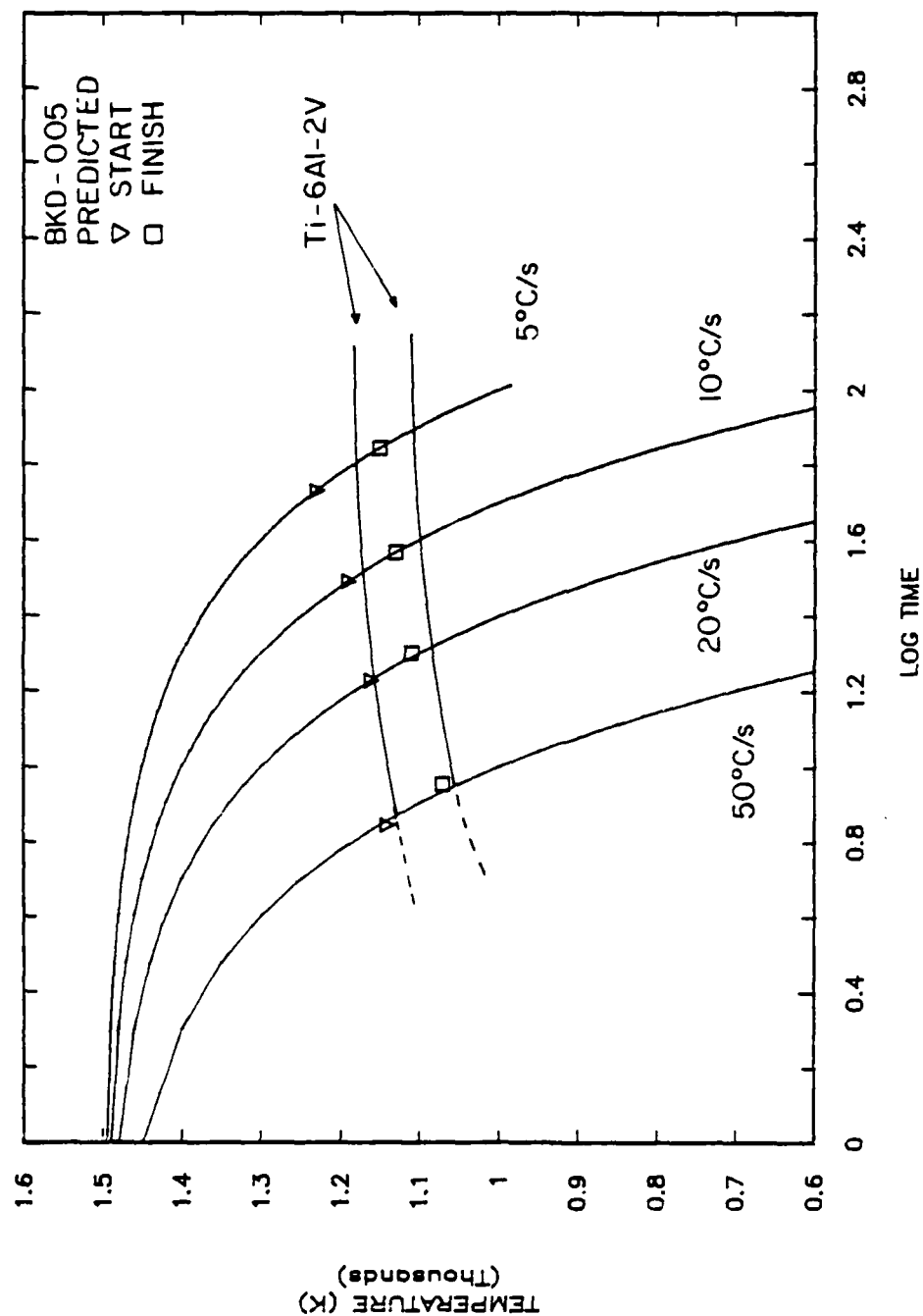


Figure 5.24(a) Predicted transformation temperatures for model alloy BKD-005 superimposed on the CCT diagram of Ti-6Al-2V.

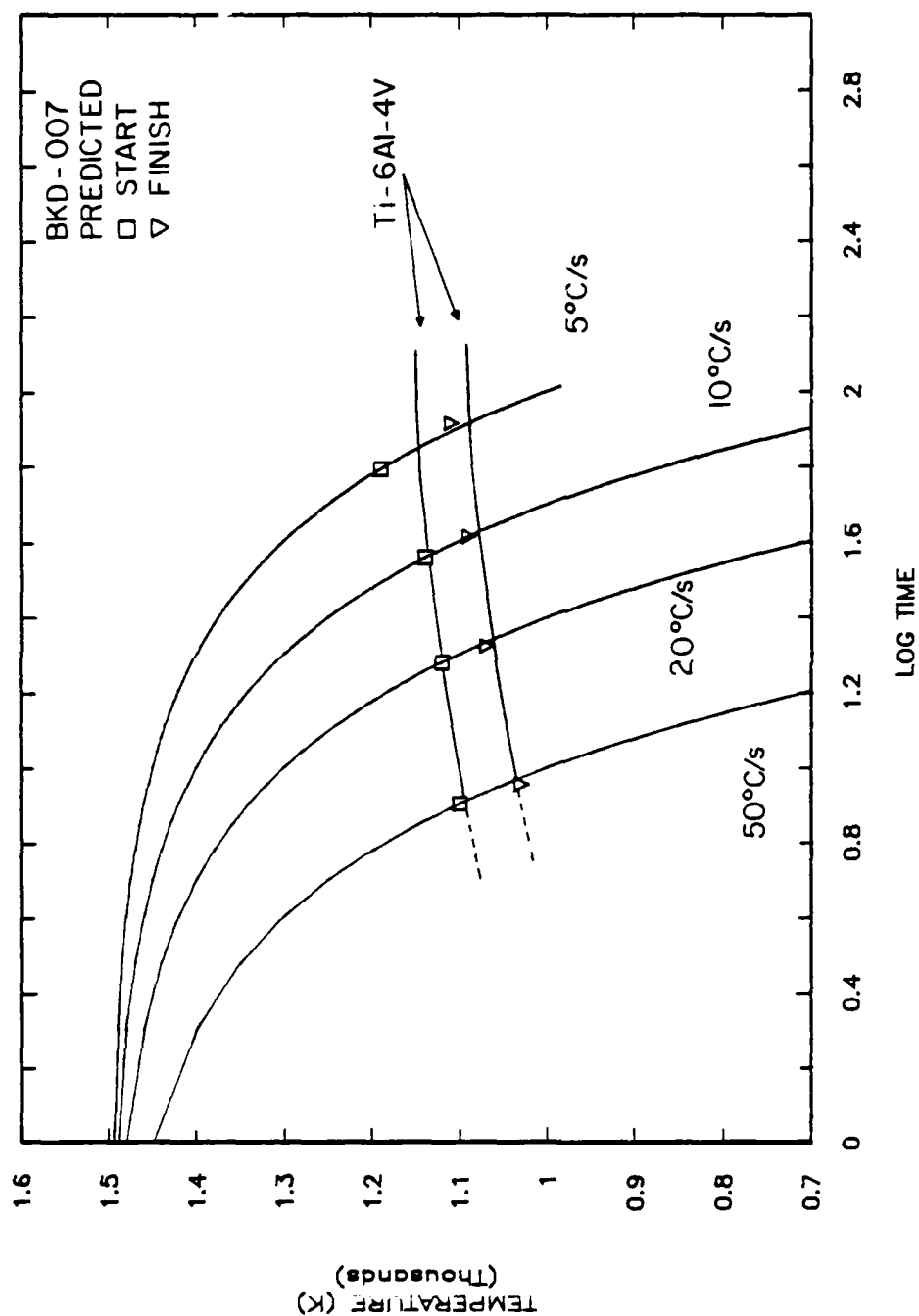


Figure 5.24(b) Predicted transformation temperatures for model alloy BKD-007 superimposed on the CCT diagram of Ti-6Al-4V.

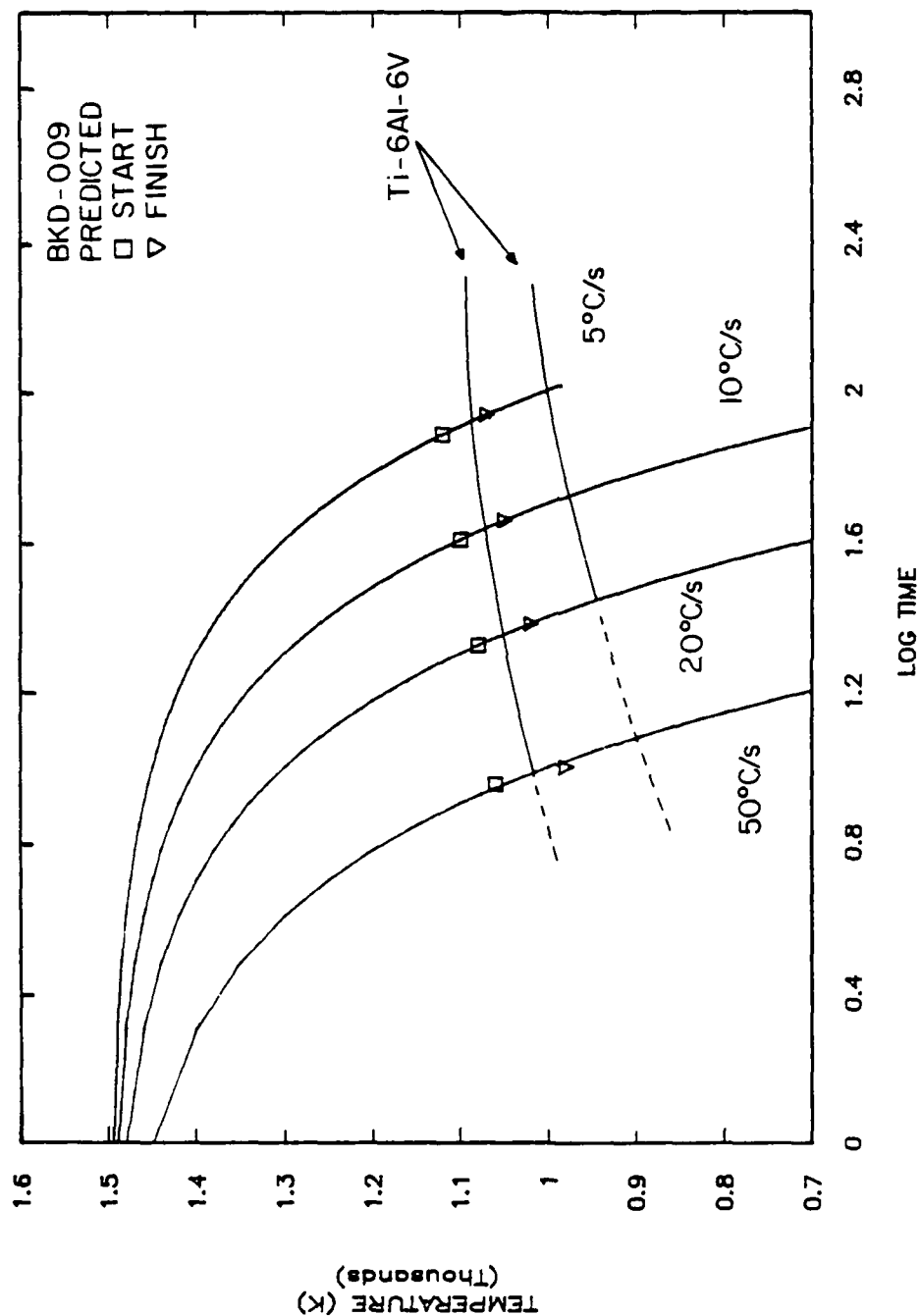


Figure 5.24(c) Predicted transformation temperatures for model alloy BKD-009 superimposed on the CCT diagram of Ti-6Al-6V.

equilibrium is proportional to:

$$(C_{\beta} - C_0) / (C_{\beta} - C_{\alpha})$$

where: C_{β} = beta stabilizer content of the beta phase

C_{α} = beta stabilizer content of the alpha phase

C_0 = the beta stabilizer content of the bulk alloy

Thus, an increase in C_0 will decrease the driving force and vice versa. In this analysis, the compositional driving force is described as a constant compositional term multiplied by undercooling. This functional form was chosen to approximate the affect of long range partitioning of the beta stabilizer element.

The magnitude of the equilibrium effect that compositional changes can have on this driving force term can be estimated by examination of the Ti-6Al-V psuedo binary diagram, Figure 5.15. At 900°C, the vanadium content of the beta phase is approximately 7.8 at% (8.5 wt%) and of the alpha, 1.4 at% (1.5 wt%). (These values will be used because they do not differ greatly from those reported by Farrar and Margolin (92), 8 wt% and 1 wt%.) Based on these values, the compositional factor in the growth expression for Ti-6Al-4V is $(7.8 - 3.7) / (7.8 - 1.4)$, or 0.64. Similar values for Ti-6Al-2V and Ti-6Al-6V are 0.94 and 0.37 respectively. The values for the molybdenum and niobium systems are listed in Table 5.2. In general, the model

Table 5.2

Compositional Driving Force, $(C_{\beta}-C_o)/(C_{\beta}-C_{\alpha})$, and Equilibrium Temperatures for Systems Ti-Al-V, Ti-Al-Mo, and Ti-Al-Nb

Alloy	C_o	C_{β}	C_{α}	$(C_{\beta}-C_o)/(C_{\beta}-C_{\alpha})$	$T_{eq}(^{\circ}\text{C})$
Ti-6Al-2V	1.8	7.8	1.4	0.938	1010
4V	3.7	7.8	1.4	0.641	980
6V	5.4	7.8	1.4	0.373	950
Ti-6Al-2Mo	1.0	8.1	0.3	0.915	1020
4Mo	2.0	8.1	0.3	0.788	1000
6Mo	3.0	8.1	0.3	0.660	980
Ti-6Al-2Nb	1.0	8.1	0.8	0.974	1020
4Nb	2.0	8.1	0.8	0.834	1000
6Nb	3.0	8.1	0.8	0.693	980

predicts less of an alloying effect for either of these alloy systems. The reduced beta transus slope causes both the compositional driving force and the temperature change with alloy content to be less severe.

Beginning with the model alloy BKD-007 at a beta stabilizer of 4% and having $T_e = 1300^\circ\text{K}$, the above changes were made and investigated. Alloys BKD-005 and BKD-009 were modelled as having beta stabilizer contents (C_β) and equilibrium temperatures of 2% and 1330°K , and 6% and 1270°K , respectively. The results of these changes are shown in Figure 5.23 and 5.24. Figure 5.23 predicts the microstructures generated in these alloys at several cooling rates compared with those of BKD-007. Figure 5.24 shows the predicted CCT curves for these alloys. Also shown in these figures are the corresponding measured data for Ti-6Al-2V, Ti-6Al-4V, and Ti-6Al-6V. It can be seen that the model correctly predicts the observed responses to alloy changes. However, the model predicts too large a cooling rate effect, and predicts transformation temperatures which are generally too high, Figure 5.23. As shown in Figure 5.24, the model predicts the effect of cooling rate on the transformed microstructures of Ti-6Al-4V and Ti-6Al-6V fairly well.

An important effect when changing from one beta stabilizer element to another is the change in the

diffusivity of the element (89, 90). A change in diffusivity will alter the activation energy terms "B" and "D" in the nucleation and growth expressions. The importance of this effect is made obvious by a comparison of the data in Table 5.2 and Figures 5.3-5.11. At the 2% level of beta stabilizer content, the model correctly predicts the relative positions of the CCT curves for the three alloys. The model also correctly predicts the relationship between the niobium and vanadium systems throughout the ranges of alloy content and cooling rate investigated. However, the model incorrectly predicts a small alloy effect within the molybdenum system and incorrectly predicts that the transformations in Ti-6Al-4Mo and Ti-6Al-6Mo would occur at higher temperatures than the corresponding vanadium alloys. As discussed earlier, the behavior of the molybdenum alloys is due to the unusually slow diffusion of molybdenum (89), and thus could be predicted by the model by incorporating changes in the activation energy terms "B" and "D".

Obviously, further development of the model is required, both to achieve better agreement with measured transformation temperatures, and also to more closely correspond with published physical data. However, at this point the model does serve to explain the formation of the observed microstructures and to make qualitative predictions

of trends in transformation kinetics and the microstructures created. The model can also be used to qualitatively describe the transformation rates involved in the production of a given transformed microstructure at specified conditions of temperature and cooling rate.

5.1.5 Rabbit Ears Martensite

One component of these microstructures which is somewhat anomalous and has been the subject of some discussion in the literature is the coarse lenticular component seen in Figure 5.17(b,c). This "rabbit ears" shaped constituent, which appears to have a distinct midrib and three habit planes approximately 120° apart, has been described as both nucleation and growth α and α' martensite (55, 109). These "rabbit ears" usually appear to be a far coarser version of the surrounding microstructure, also lenticular and also appearing to have three habit planes spaced 120° apart, Figure 5.25. The coarse "rabbit ears" are somewhat unique, appearing only in Ti-6211, and in Ti-6Al-4Nb and Ti-6Al-2Mo cooled at 50°C/s , Figures 5.17, 5.26, and 5.27, respectively. However, the acicular, triangular microstructures are essentially ubiquitous in this study.

Although the existence of an obvious crystallographic habit plane and midrib suggest that this microconstituent is



Figure 5.25 Optical micrograph of Ti-6211, cooled at 20°C/s, showing coarse, lenticular martensite.

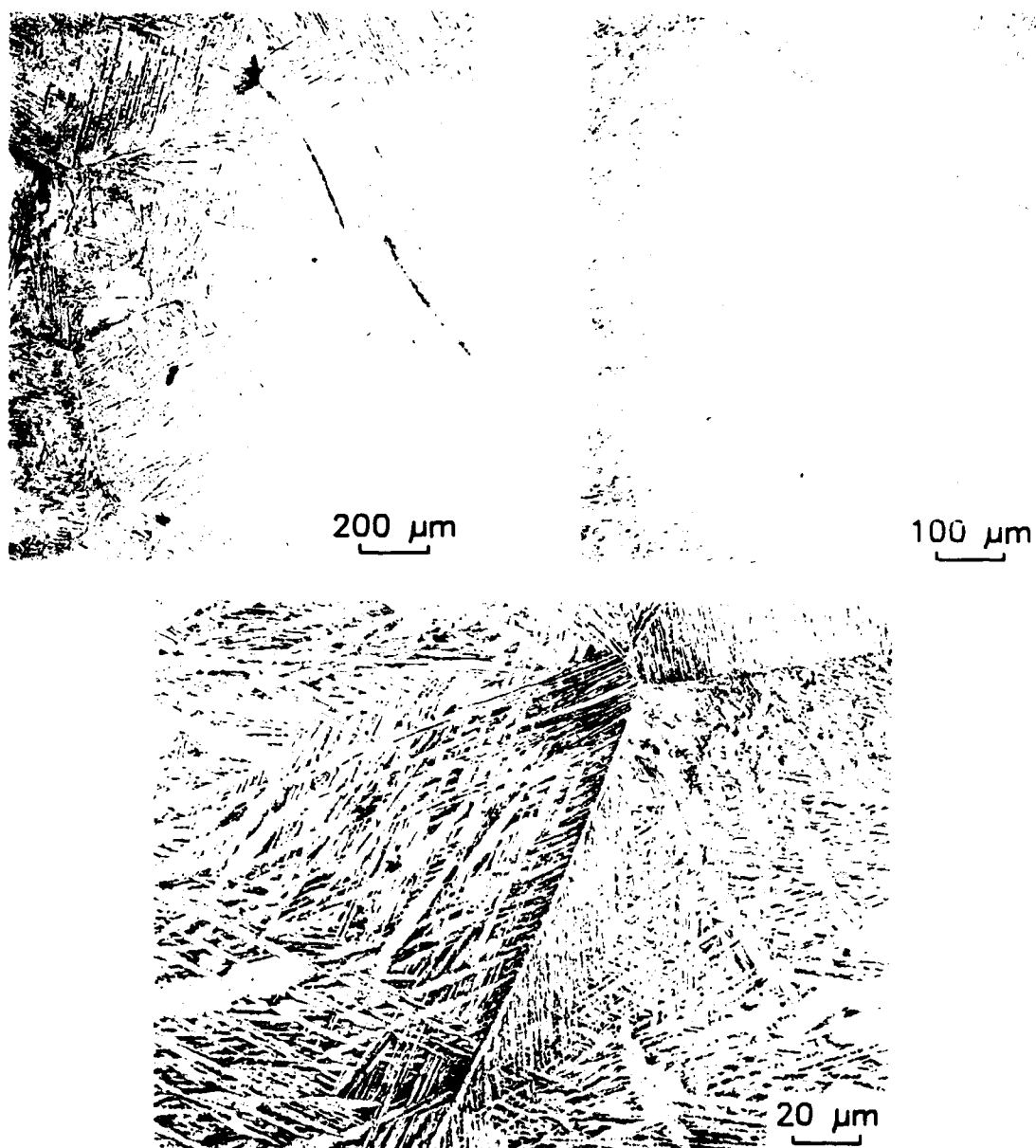


Figure 5.26 Optical micrographs of Ti-6Al-4Nb, cooled at 50°C/s, showing coarse, lenticular martensite.

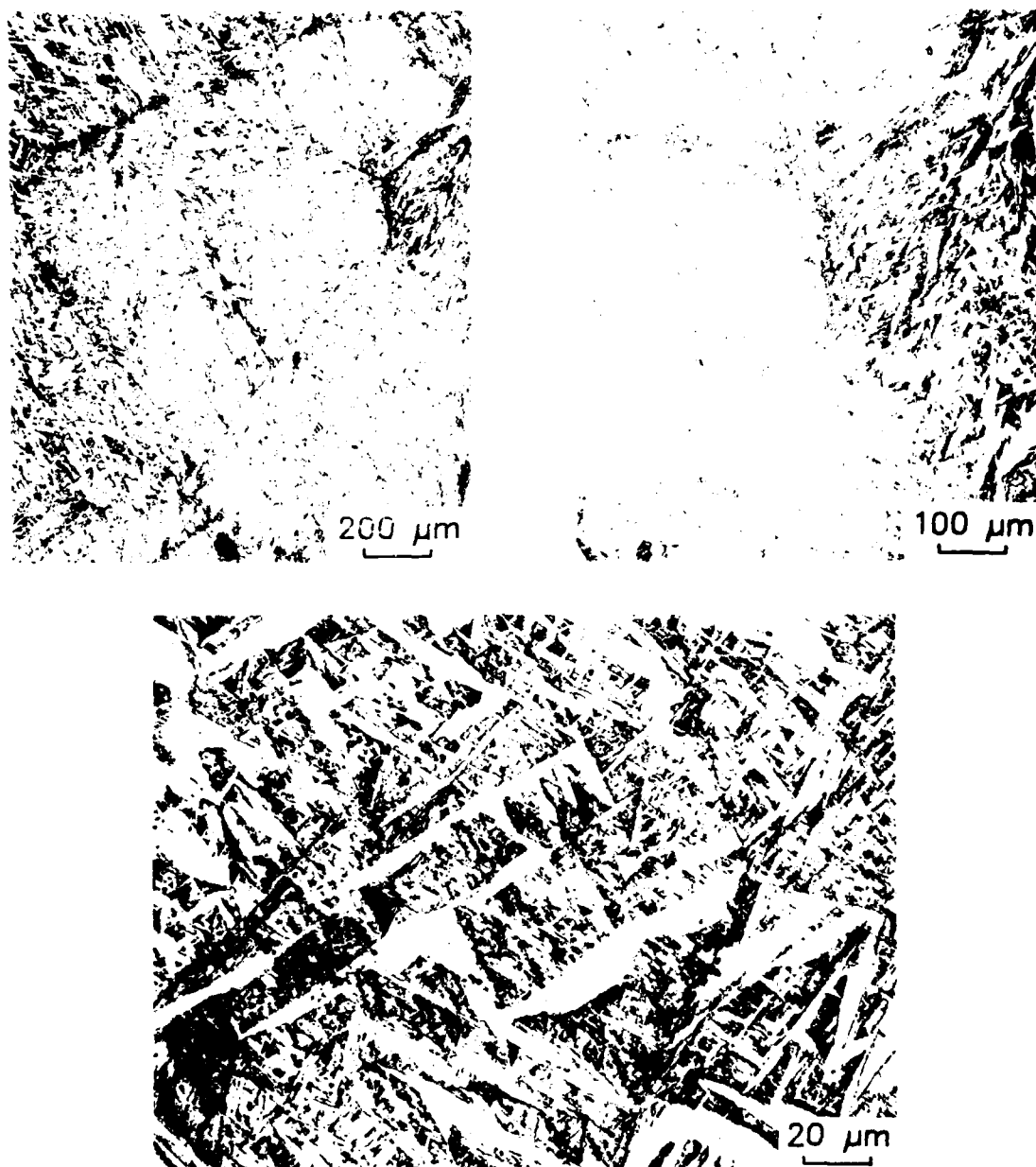


Figure 5.27 Optical micrographs of Ti-6Al-2Mo, cooled at 50°C/s , showing coarse, lenticular martensite.

alpha prime, the kinetics of its formation seem to be somewhat unusual. The CCT diagram for Ti-6211, Figure 4.5, shows a distinct nose which suggests that an equally distinct break exists between the martensitic transformation and the nucleation and growth transformations.

Microstructures produced by cooling rates rapid enough to avoid the nose of the curve, Figure 5.17(d), do not seem to contain the "rabbit ears" component. However, as the cooling rate in Ti-6211 is reduced below approximately 50°C/s , the size and extent of the "rabbit ears" are reduced and the midrib disappears. At a cooling rate of 4°C/s , the "rabbit ears" are eliminated and the microstructure contains Widmanstatten colonies at the prior beta grain boundaries and the fine, acicular, triangular microconstituent.

Lewis and Williams (109) examined the composition and dislocation substructure of this microconstituent in Ti-6211. They found that the composition of the "rabbit ears" was the same as the bulk alloy composition, indicative of either a massive or martensitic transformation. They also found a very high dislocation density and concluded that this microconstituent was martensite. If this conclusion is to be accepted, the identity of the finer lenticular microconstituent, traditionally referred to as "basketweave Widmanstatten alpha plus beta", then comes into question.

The basketweave structure appears with either three apparent habit planes, as previously shown, or with two. Both types are shown in Figure 5.28, a micrograph of Ti-6Al-2Mo cooled at 10°C/s. For the purpose of this study, the assumption will be made that the "rabbit ears", unique to Ti-6211 and rapidly-cooled Ti-6Al-4Nb and Ti-6Al-2Mo, are alpha prime martensite, and that the finer acicular microconstituent is basketweave Widmanstatten alpha plus beta, a nucleation and growth product.

5.2 Lattice Incompatibility

The lattice incompatibility model suggests that a direct relationship may be found between the high temperature ductility loss and the volumetric incompatibility during the beta to alpha transformation. To document this incompatibility, the relative sizes of the beta and alpha lattices which exist during the transformation must be known. This requires either the direct measurement of the lattices during the transformation or the calculation of these values from other data. Techniques exist which are theoretically capable of making direct lattice parameter measurements rapidly enough to document the instantaneous values existing at any point during the transformation. Three examples of such techniques are energy-dispersive diffraction using high-

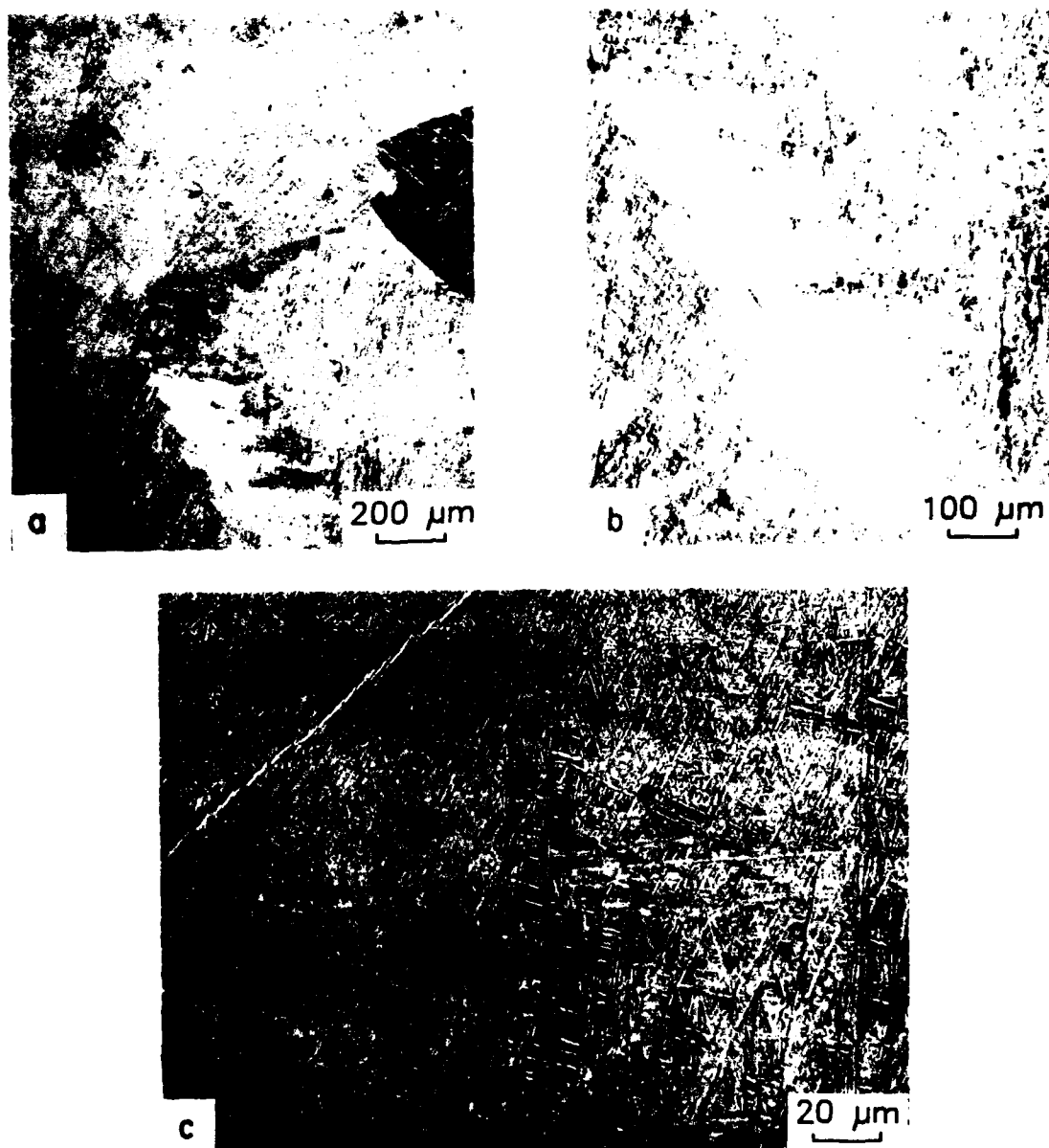


Figure 5.28 Optical micrographs of Ti-6Al-2Mo, cooled at 10°C/s , showing basketweave alpha plus beta structure with both two and three apparent habit planes (c).

energy synchrotron radiation (111) and either x-ray or neutron diffraction using a position-sensitive detector (112, 113). Unfortunately, the difficulties involved in adapting the available facilities for use with titanium at high temperatures prevented any of these techniques from being included in this investigation. However, measurements were made using neutron diffraction at the Danish National Laboratory at Risø. Although the existing experimental setup prevented instantaneous lattice parameter measurements from being made, the feasibility of using this system for such measurements was established. These measurements are discussed in Appendix A. Equilibrium lattice parameter measurements were made using both neutron diffraction and synchrotron radiation. The synchrotron radiation studies were performed by Dr. M.A. Imam of the Naval Research Laboratory (114). The results of the neutron diffraction and synchrotron radiation measurements are included in Appendix B.

Lattice incompatibility was determined using a combination of equilibrium lattice parameter values, measured by x-ray diffraction, and high-speed dilatometry. The results of both sets of tests will be discussed below, first individually, then as they were combined to measure lattice incompatibility.

5.2.1 Lattice Parameter Measurements

Lattice parameter data for binary alloys based on titanium have existed for some time (71, 76-78). A compilation of these data was made by Pearson (71) and the results are shown in Figure 3.15. However, very little data exists for ternary or more complex alloys. The most common way to predict the lattice constants of alloys is with the use of Vigard's scale law (115). Vigard's law predicts that the lattice spacing in a terminal solid solution can be estimated by adding the lattice spacings of the component elements, each weighted by their atomic percent in the alloy. For a binary alloy:

$$a_{\text{alloy}} = a_{\text{solvent}}(\text{at \% solvent}) + a_{\text{solute}}(\text{at \% solute})$$

Vigard's law was only proposed for and is mostly used for binary alloys, but perhaps be used on more complex alloys. A difficulty arises in the case of alpha titanium because the beta stabilizing elements usually have a crystal structure other than hcp. One possible solution would be to modify Vigard's law to use atomic diameters rather than lattice spacings. The problem with this approach is that Vigard's law only considers the sizes of the components. The difficulty is then the determination of a true atomic diameter for a given element - a value that remains constant from alloy to alloy and in various crystal structures. In a

review of previous work, Pearson (71) discussed the relative importance of the size factor compared to other effects, principally the valence effect. He found that the valence effect is often as large or larger than the size factor, particularly when the solvent and solute are in the same period.

In the absence of existing data or an accurate method of predicting lattice parameters, it was necessary to measure the lattice parameters of each of the alloys investigated. The room temperature lattice parameters for the alloys used in this investigation are listed in Table 5.3. Because of the shortage of existing data, it is impossible to directly compare most of these parameters to reported values. Examination of Figure 3.15 does show that the data in Table 5.3 is generally as expected based on the trends in the binary data.

Throughout this section, comparisons will be made between the data from this investigation and that generated in earlier studies. The bulk of the lattice parameter data for titanium alloys dates to the late 1950's and early 1960's. The data presented in Table 5.4 illustrates that the titanium lattice parameter measurements of the day were a bit crude. Table 5.4 compares the the reported lattice parameters for unalloyed titanium and Ti-5Al (53, 116-123).

Table 5.3

Room Temperature Lattice Parameters

Alloy	a (Å)	b (Å)	vol/cell (Å ³)
unalloyed titanium	2.9480	4.7010	35.381
Ti-6Al	2.9306	4.6805	34.813
Ti-6Al-2V	2.9261	4.6675	34.610
-4V	2.9269	4.6739	34.677
-6V	2.9214	4.6648	34.479
Ti-6Al-2Mo	2.9354	4.6720	34.864
-4Mo	2.9289	4.6725	34.714
-6Mo	2.9276	4.6700	34.663
Ti-6Al-2Nb	2.9381	4.6832	35.011
-4Nb	2.9331	4.6780	34.856
-6Nb	2.9249	4.6735	34.624
Ti-6211	2.9371	4.6804	34.978
Ti-6Al-2V-2Nb	2.9261	4.6690	34.620
Ti-6Al-2V-2Zr	2.9309	4.6779	34.801
-4Zr	2.9334	4.6832	34.899
-6Zr	2.9371	4.6879	35.022

Table 5.4

Measured Lattice Parameters for
Unalloyed Titanium and Ti-5Al

Source	a (Å)	c (Å)	vol/2-Atom cell (Å ³)
(unalloyed titanium)			
Haag (116)	2.953	4.729	35.713
J.D. Fast (117)	2.951	4.680	35.295
Gonser (118)	2.952	4.695	35.432
Greiner & Ellis (119)	2.951	4.694	35.401
Clark (53)	2.951	4.683	35.318
(53)	2.950	4.684	35.301
Szanto (120)	2.951	4.679	35.288
Bumps (121)	2.943	4.679	35.097
(Ti-5Al)			
Bumps (121)	2.929	4.667	34.674
Clark (53)	2.932	4.678	34.827
Ogden (123)	2.933	4.692	34.955

The data in this table shows that even the values for unalloyed titanium vary significantly from study to study. One possible explanation for the scatter in the data is that the material used contained varying degrees of contamination, particularly interstitial contamination. The effects on the lattice parameters of titanium caused by oxygen and nitrogen were investigated by Clark (53). He found that oxygen and nitrogen did not affect the "a" parameter of alpha titanium, but significantly changed the "c" parameter, increasing it approximately 0.0025Å, or 0.05%, for an addition of 0.1% nitrogen. A similar effect was found for oxygen additions. Worner (124), in an investigation of titanium-tin alloys, noted a significant effect on phase stability with relatively small additions of impurity elements. Several other early investigations also noted differences in lattice parameter values for titanium supplied by different sources and produced by different methods (116-123).

One reason that the effect of interstitial contamination is so large in titanium studies is because x-ray diffraction is a surface measurement. Titanium has a mass absorption coefficient for Cu K α radiation of 202.4 cm²/gm. This, combined with the density of titanium, 4.51 gm/cm³, gives a linear absorption coefficient of 912.8 cm⁻¹. Based on this,

90% of the incident radiation for a 2θ angle of 50° in a diffractometer is absorbed in the first 5μ of material, and 99% in the first 11μ (80). Because of this, the problem of interstitial contamination is particularly acute with powder specimens, commonly used in the early investigations.

The compositions of the alloys used in this investigation are listed in Table 4.2. When reported, the interstitial contents of the material are all low and of similar magnitudes. Comparisons of these levels with the results of Clark (53) suggest that the interstitial contaminants did not significantly affect the room temperature lattice parameters of these alloys. However, the bulk of the lattice parameter measurements made in this investigation were made at elevated temperatures, where the reactivity of titanium makes interstitial contamination a major concern. All measurements were made in high purity helium and the samples usually showed no evidence of interstitial contamination as evaluated by discoloration or hardness changes. Still, some increase in interstitial content was likely and probably contributed to the scatter in the data. Table 4.2 also shows that the level of major alloying element varied from one lot to the next for an individual alloy. When both materials were included, these differences probably contributed to the data scatter also.

A second source of error in lattice parameter calculation based on x-ray diffraction is the error in measurement of the peak positions themselves. As discussed in the Experimental Procedure section and in Appendix C, these errors were minimized by extrapolation of the calculated parameters against $\cos^2\theta/\sin\theta$ using Cohen's method (83) of least squares fitting.

Once the data was processed and lattice parameters were calculated, the volume of a two-atom cell was calculated for both the alpha and beta phases. These data were plotted for each alloy as cell volume versus temperature, Figures 5.29-5.41. These data will be discussed in the following two sub-sections. The first sub-section will discuss trends that can be seen in the data, regardless of alloy content. The second sub-section will discuss the differences between the data for the various alloys.

5.2.1.1 General Trends Several general trends can be noted when the data presented in Figures 5.29-5.41 are taken as a whole. The first is the general and expected increase in the alpha and beta lattice parameters with increasing temperature. The second observation that can be made is that over most of the temperature range studied, the equilibrium beta lattice is more dense than the equilibrium alpha lattice. This is significant because it is the

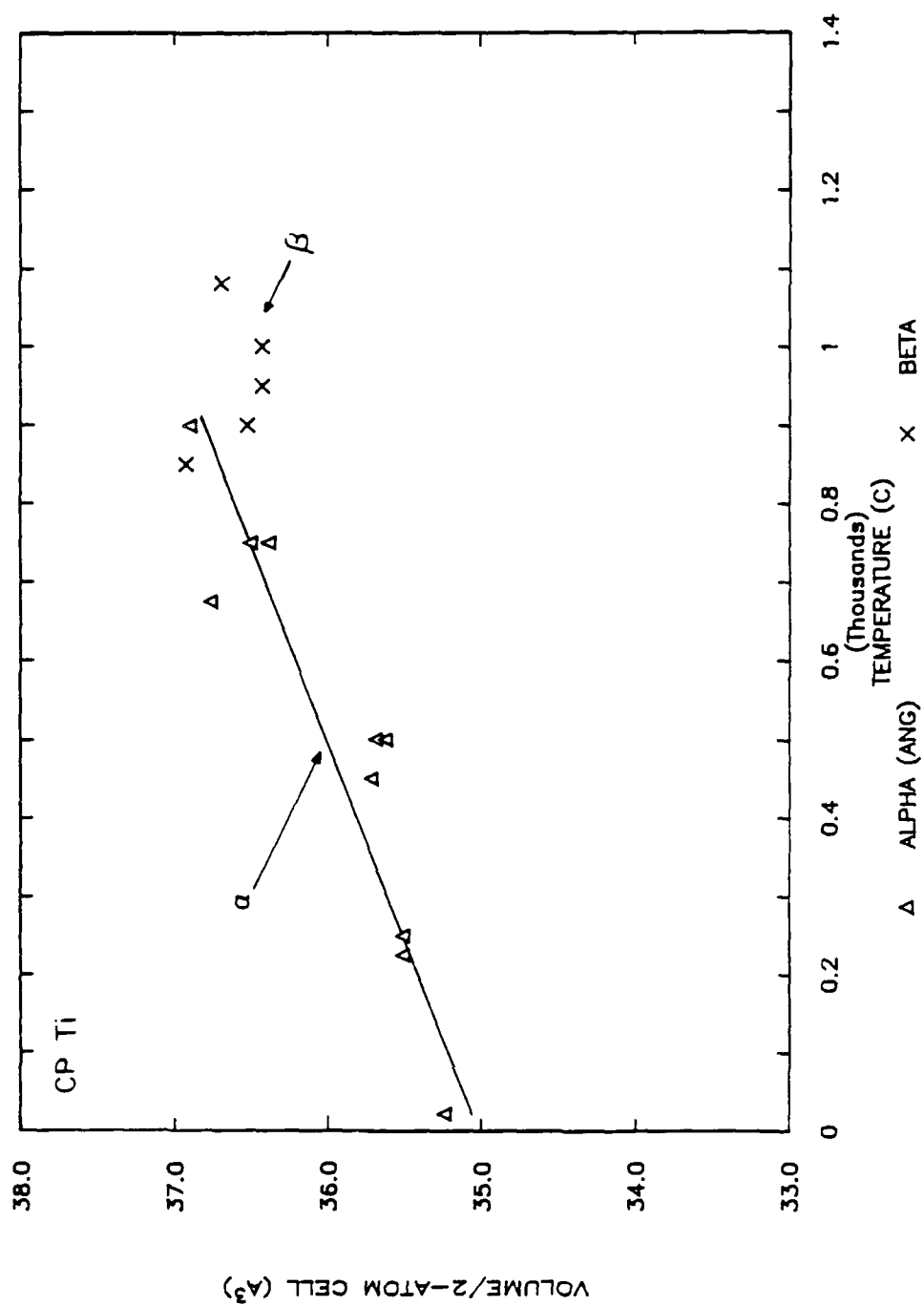


Figure 5.29 Lattice volume versus temperature for the alpha and beta phases of Grade 2 unalloyed titanium.

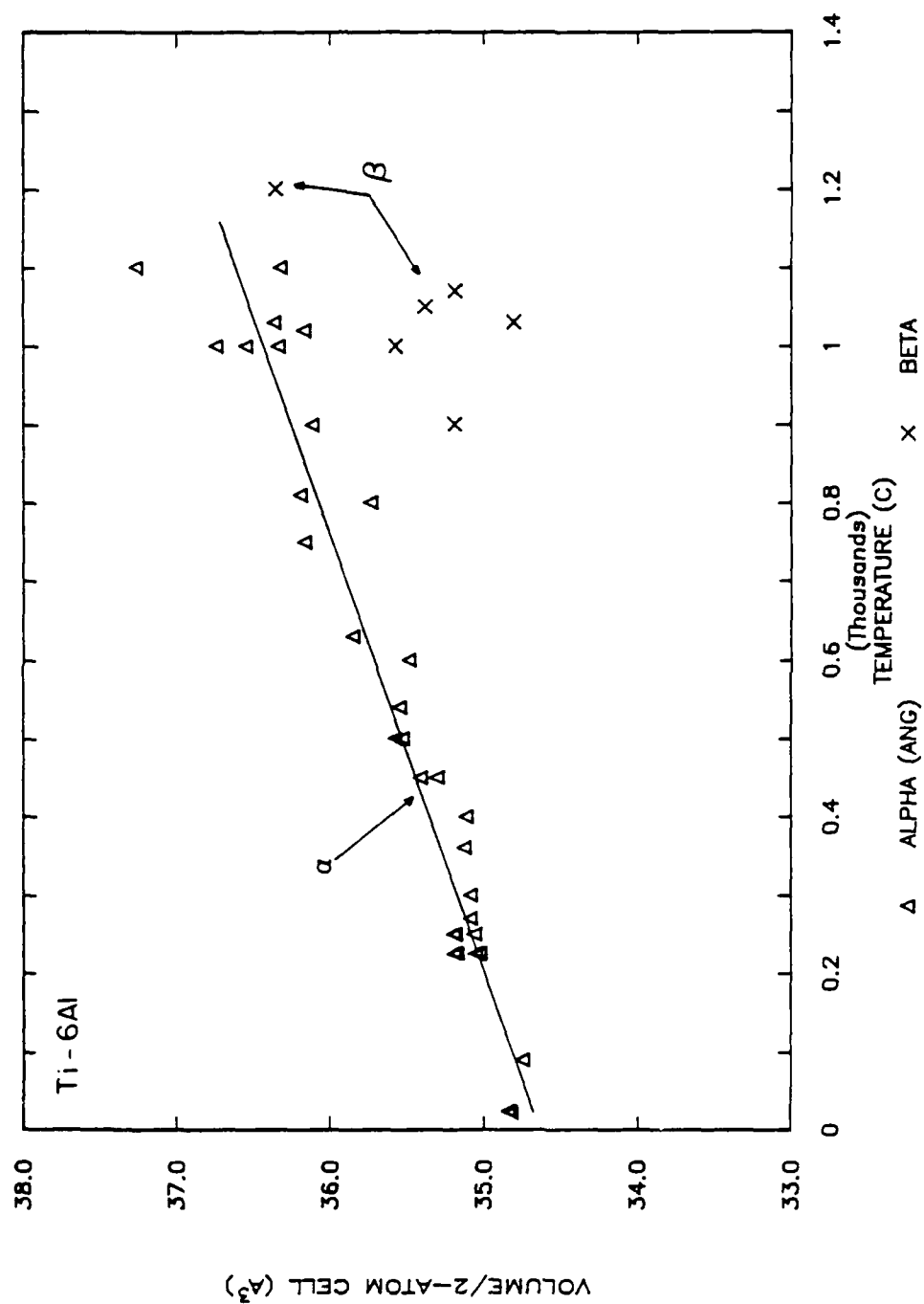


Figure 5.30 Lattice volume versus temperature for the alpha and beta phases of Ti-6Al.

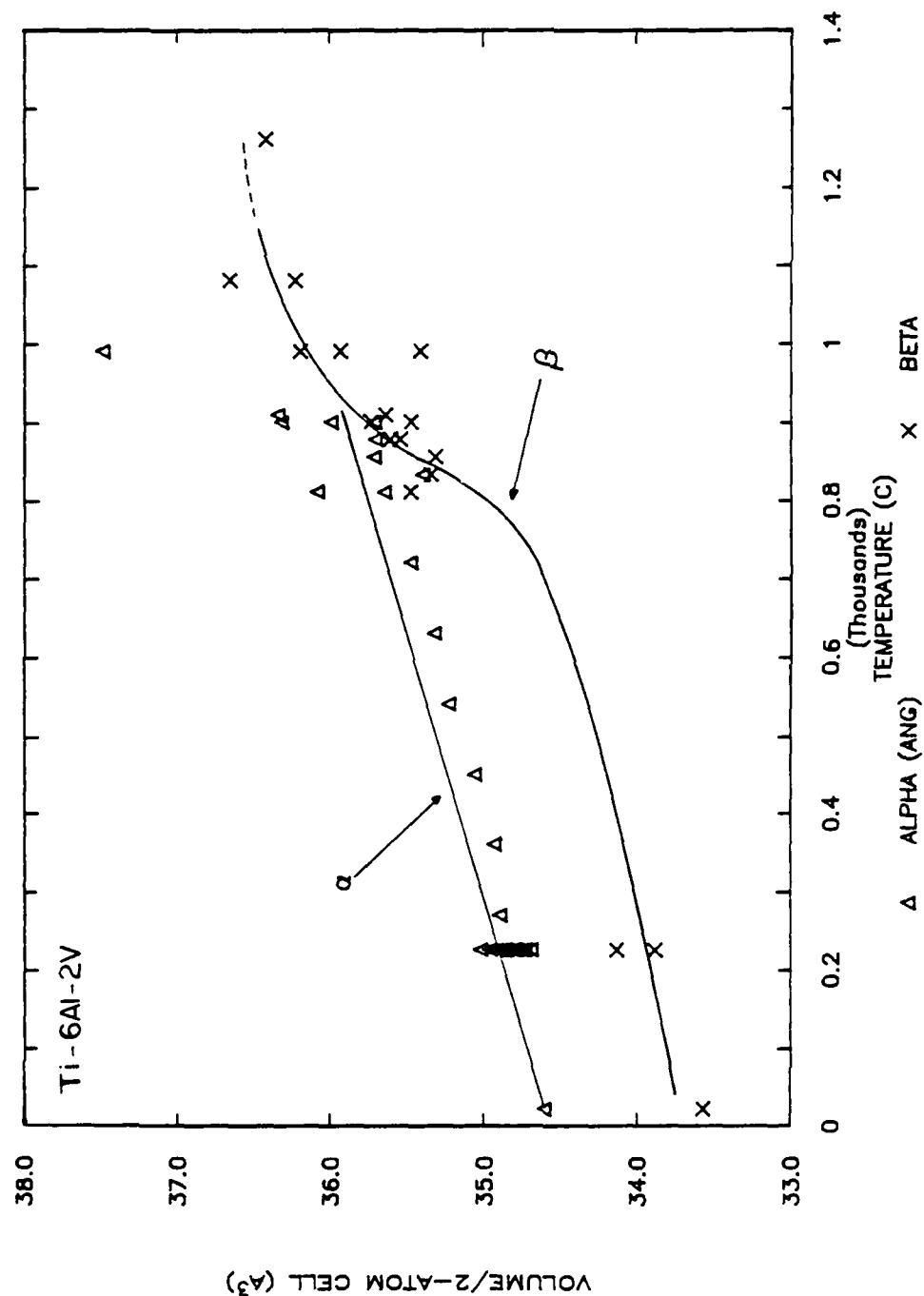


Figure 5.31 Lattice volume versus temperature for the alpha and beta phases of Ti-6Al-2V. Note that the volume of the beta lattice changes rapidly near the beta transus.

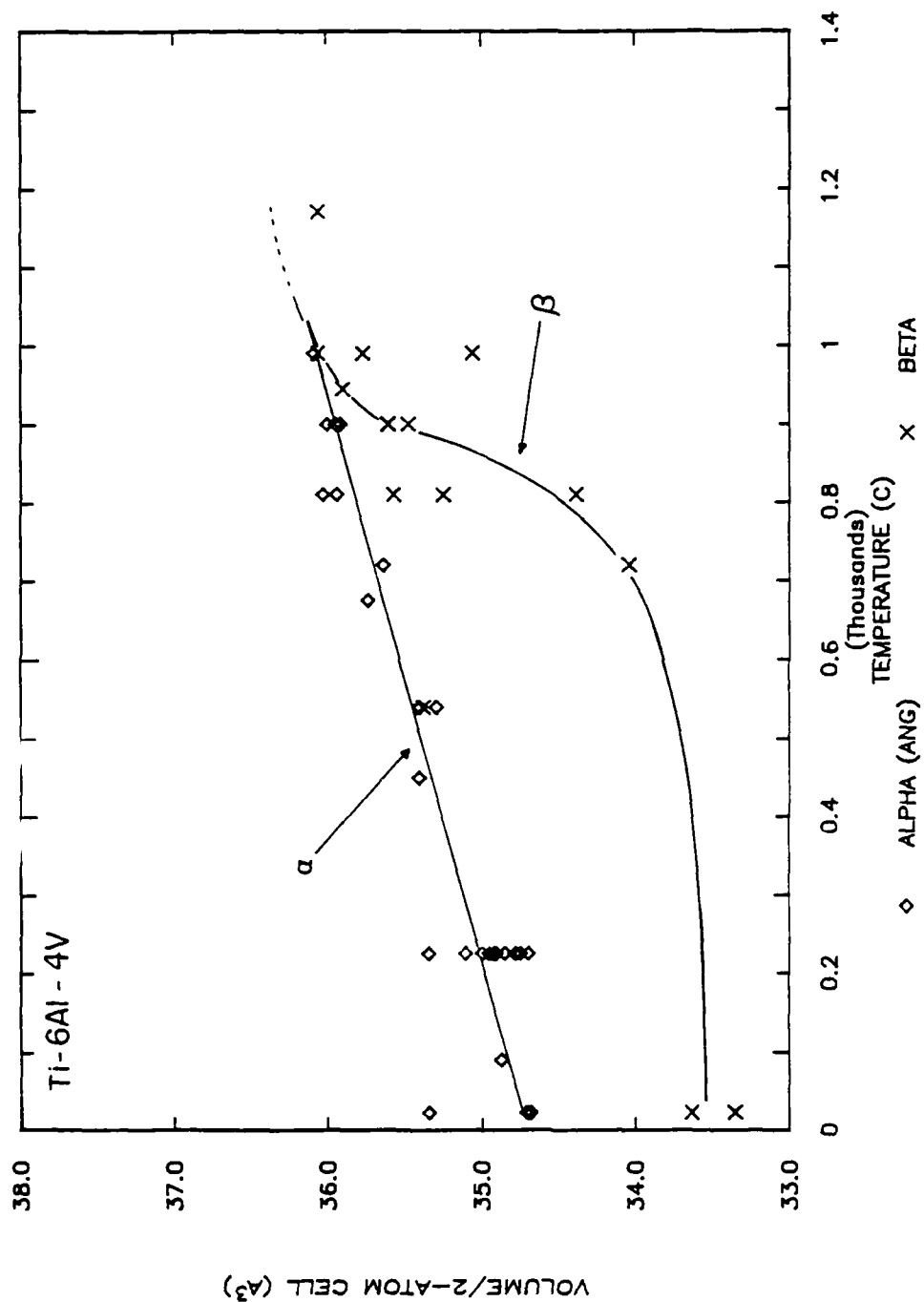


Figure 5.32 Lattice volume versus temperature for the alpha and beta phases of Ti-6Al-4V. Note that the volume of the beta lattice changes rapidly near the beta transus.

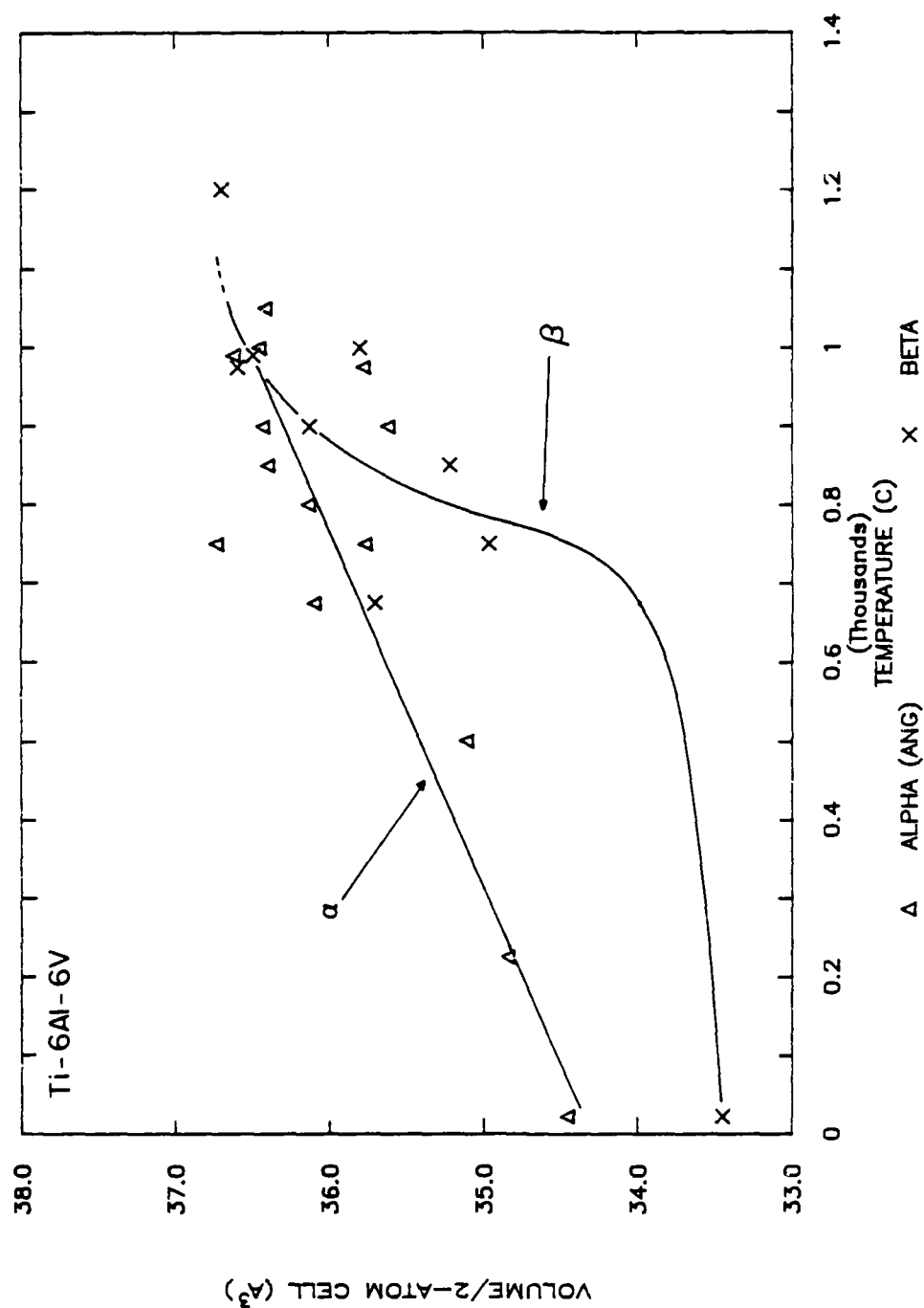


Figure 5.33 Lattice volume versus temperature for the alpha and beta phases of Ti-6Al-6V. Note that the volume of the beta lattice changes rapidly near the beta transus.

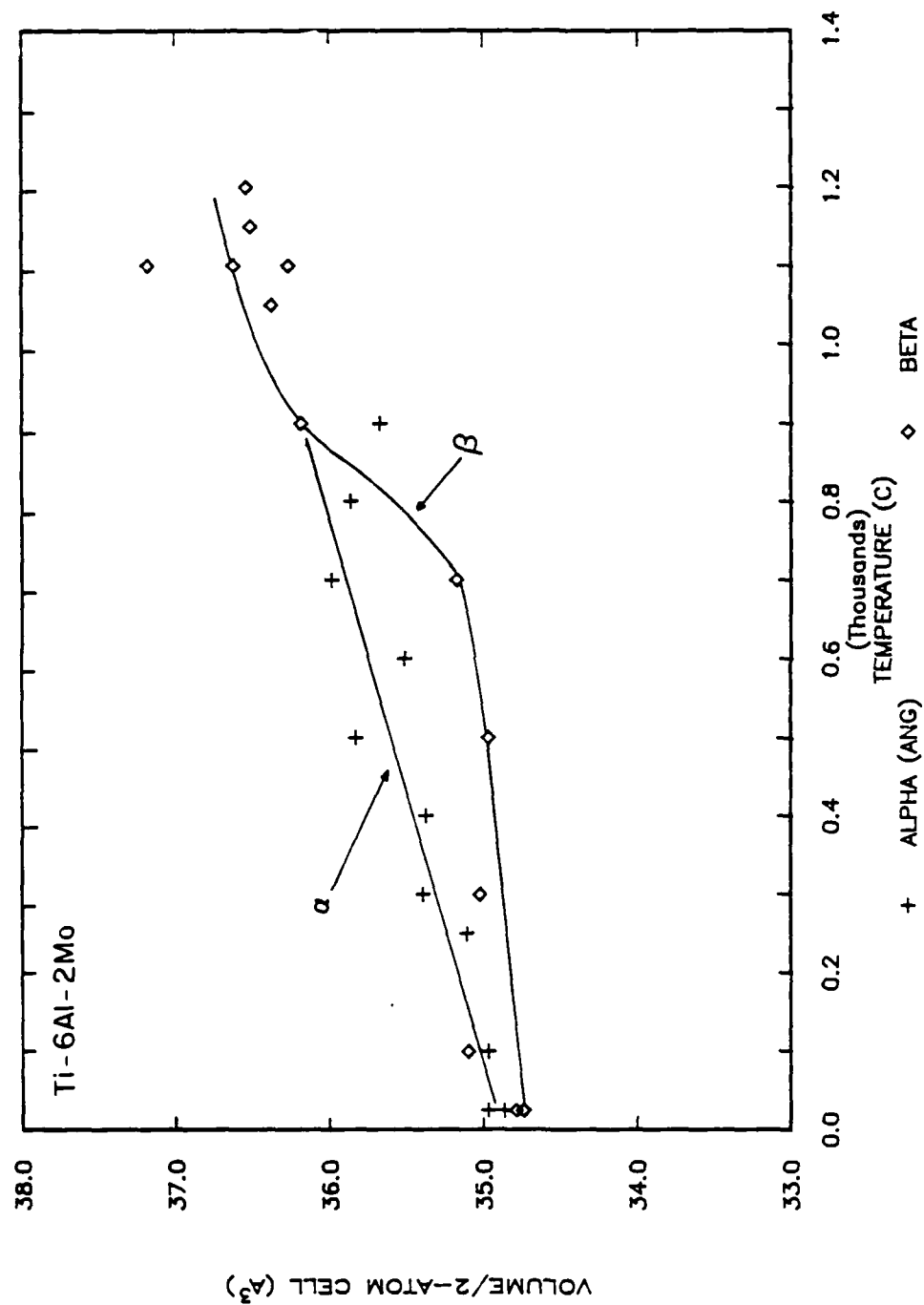


Figure 5.34 Lattice volume versus temperature for the alpha and beta phases of Ti-6Al-2Mo.

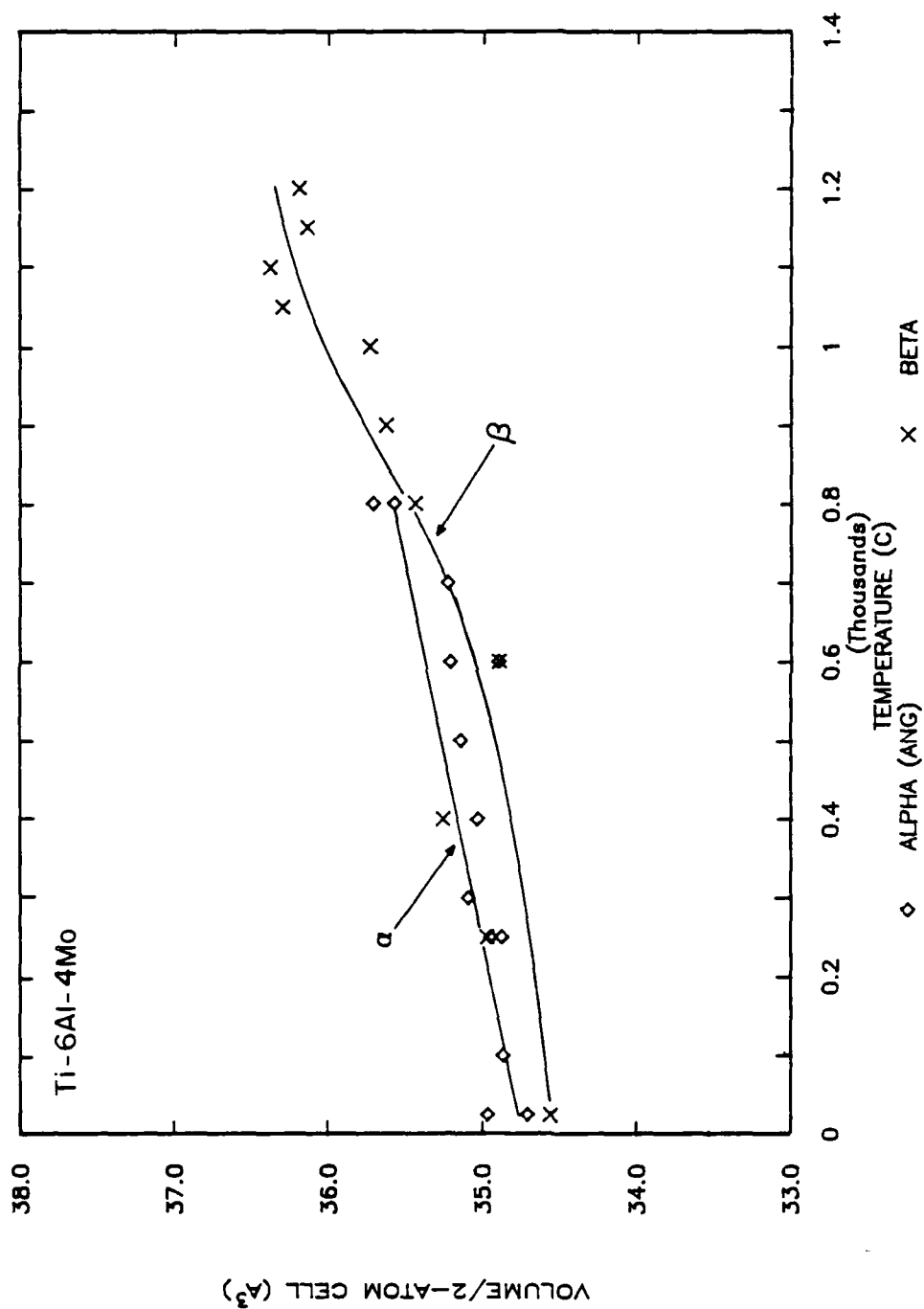


Figure 5.35 Lattice volume versus temperature for the alpha and beta phases of Ti-6Al-4Mo.

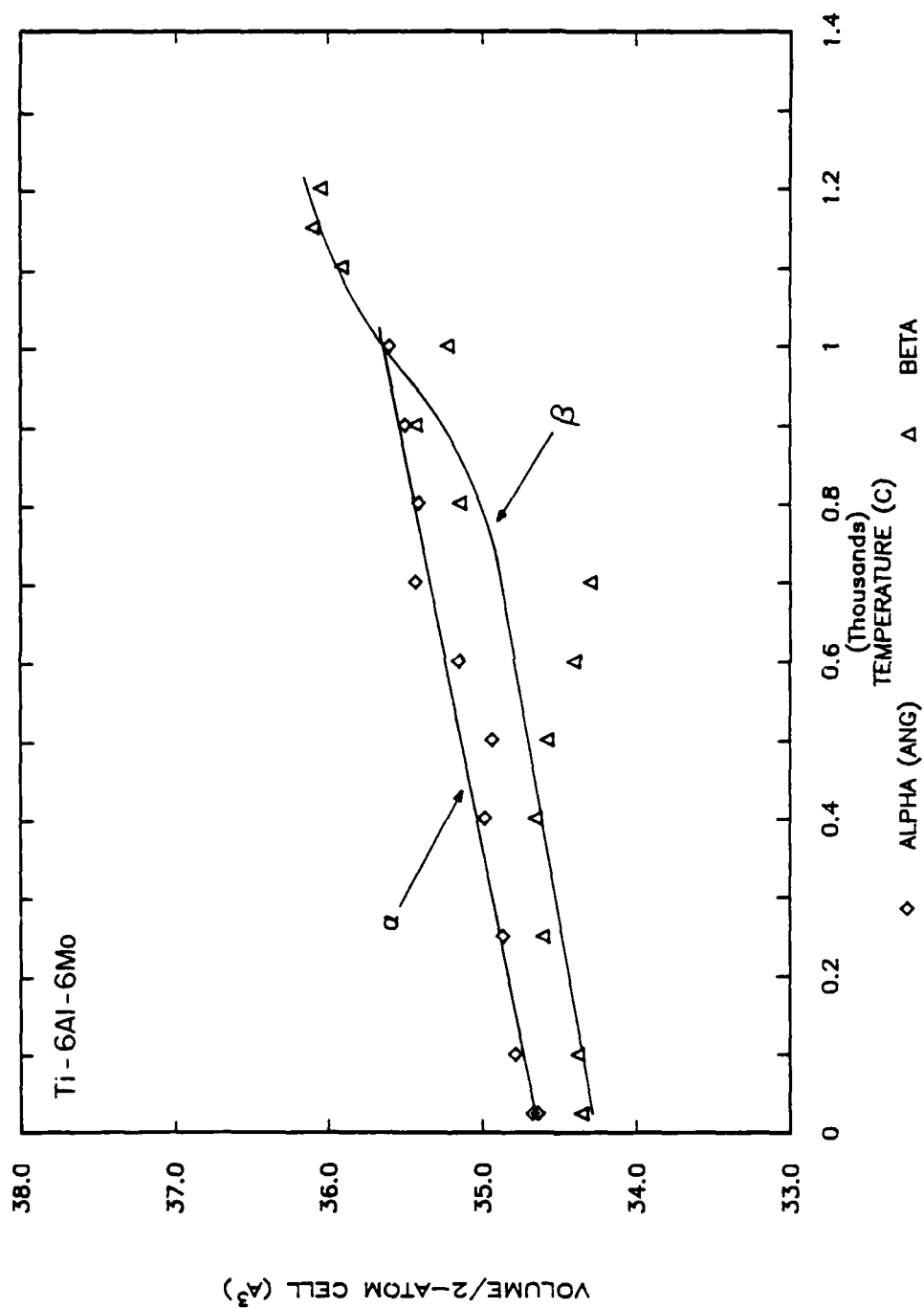


Figure 5.36 Lattice volume versus temperature for the alpha and beta phases of Ti-6Al-6Mo.

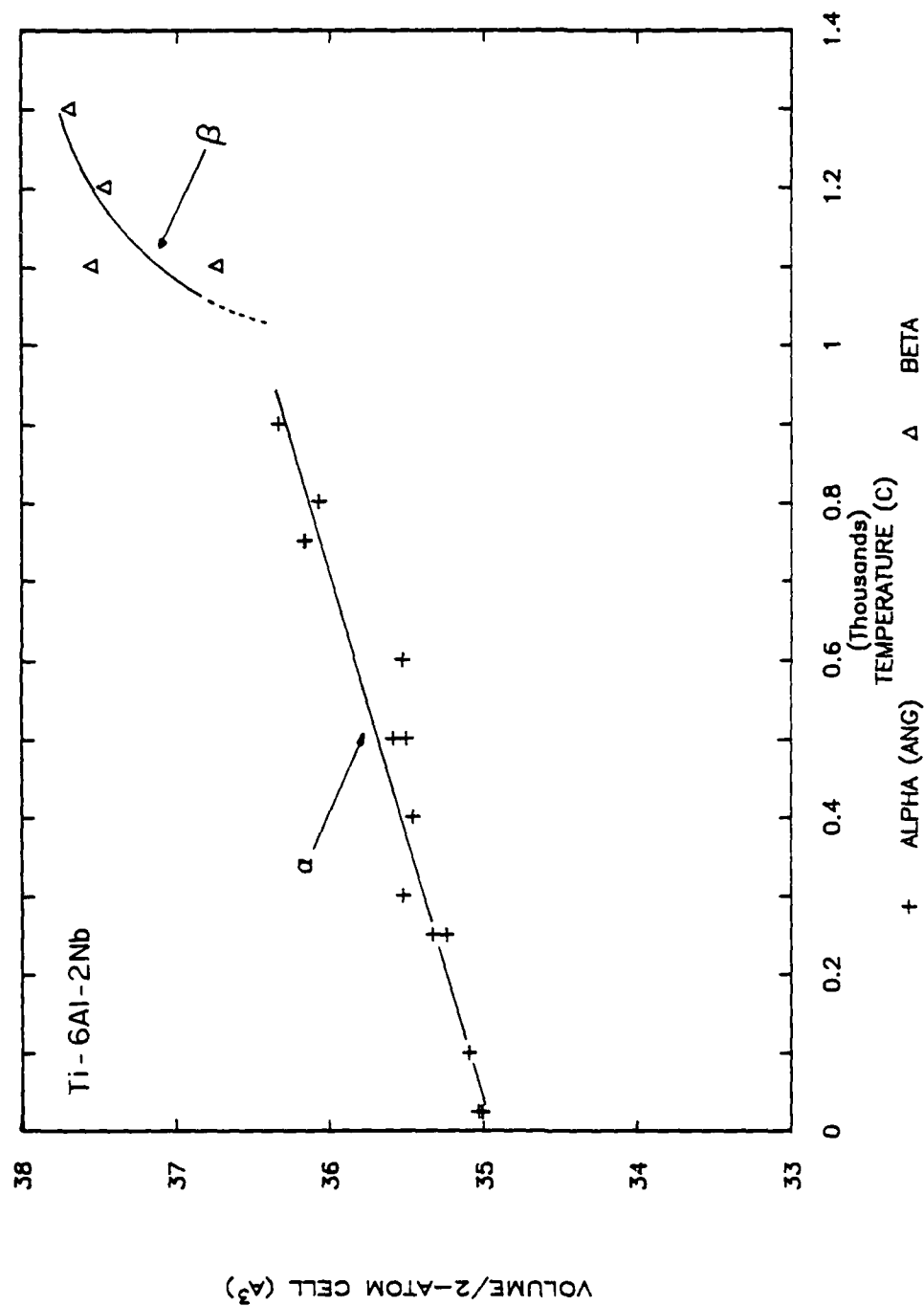


Figure 5.37 Lattice volume versus temperature for the alpha and beta phases of Ti-6Al-2Nb. Note that the beta lattice volume is large and cannot be measured below the beta transus.

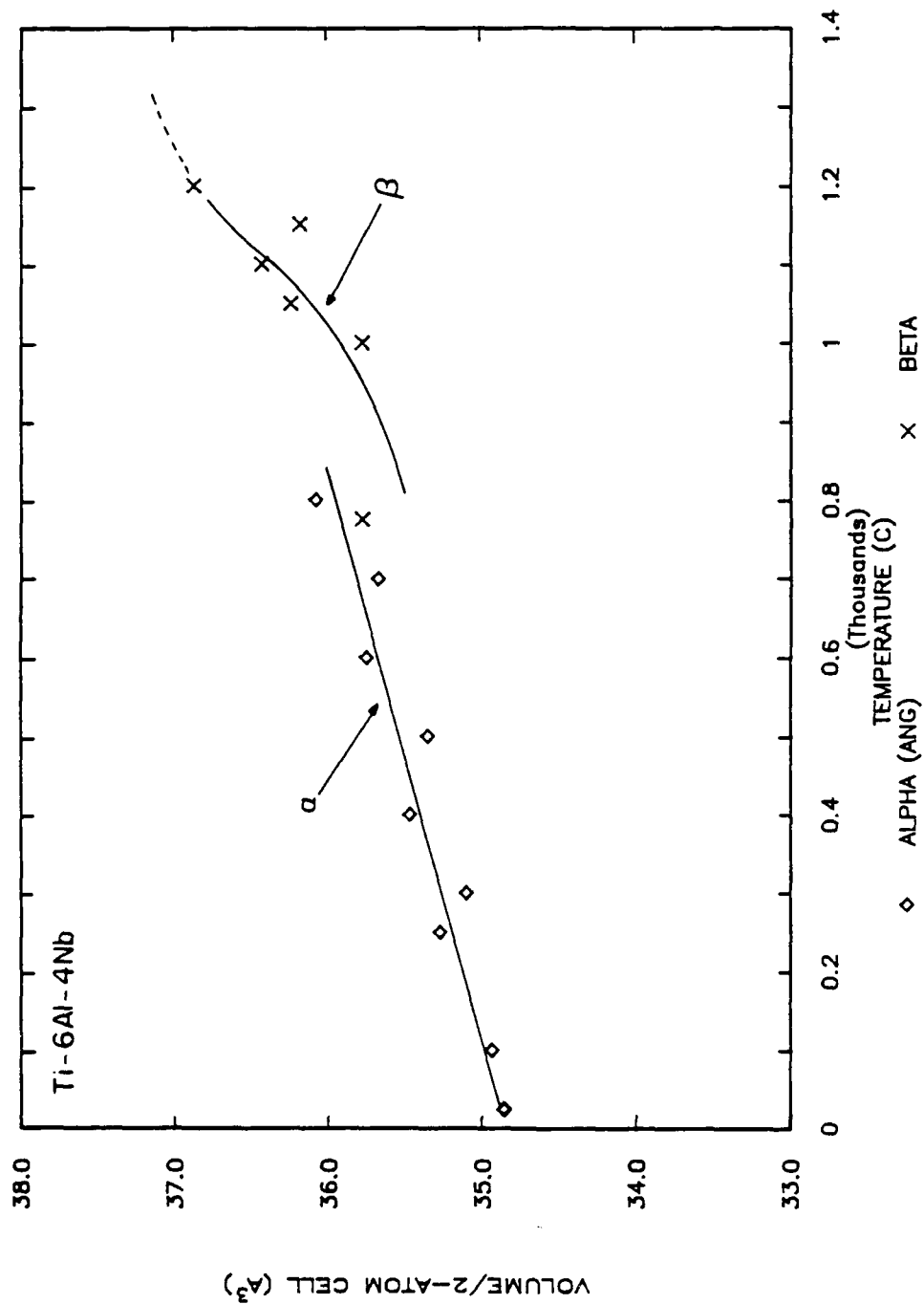


Figure 5.38 Lattice volume versus temperature for the alpha and beta phases of Ti-6Al-4Nb. Note that the beta lattice volume is large and cannot be measured below the beta transus.

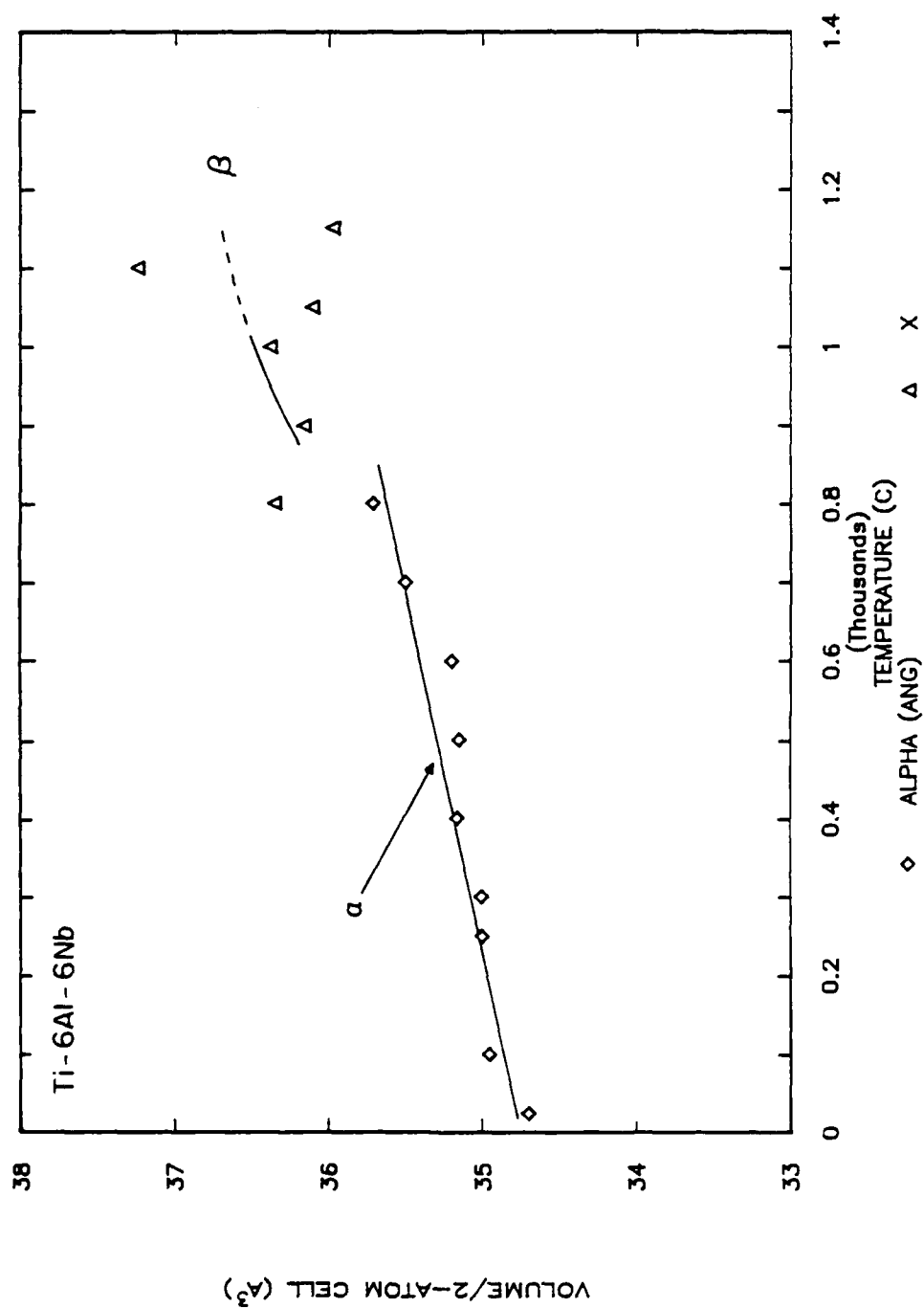


Figure 5.39 Lattice volume versus temperature for the alpha and beta phases of Ti-6Al-6Nb. Note that the beta lattice volume is large and cannot be measured below the beta transus.

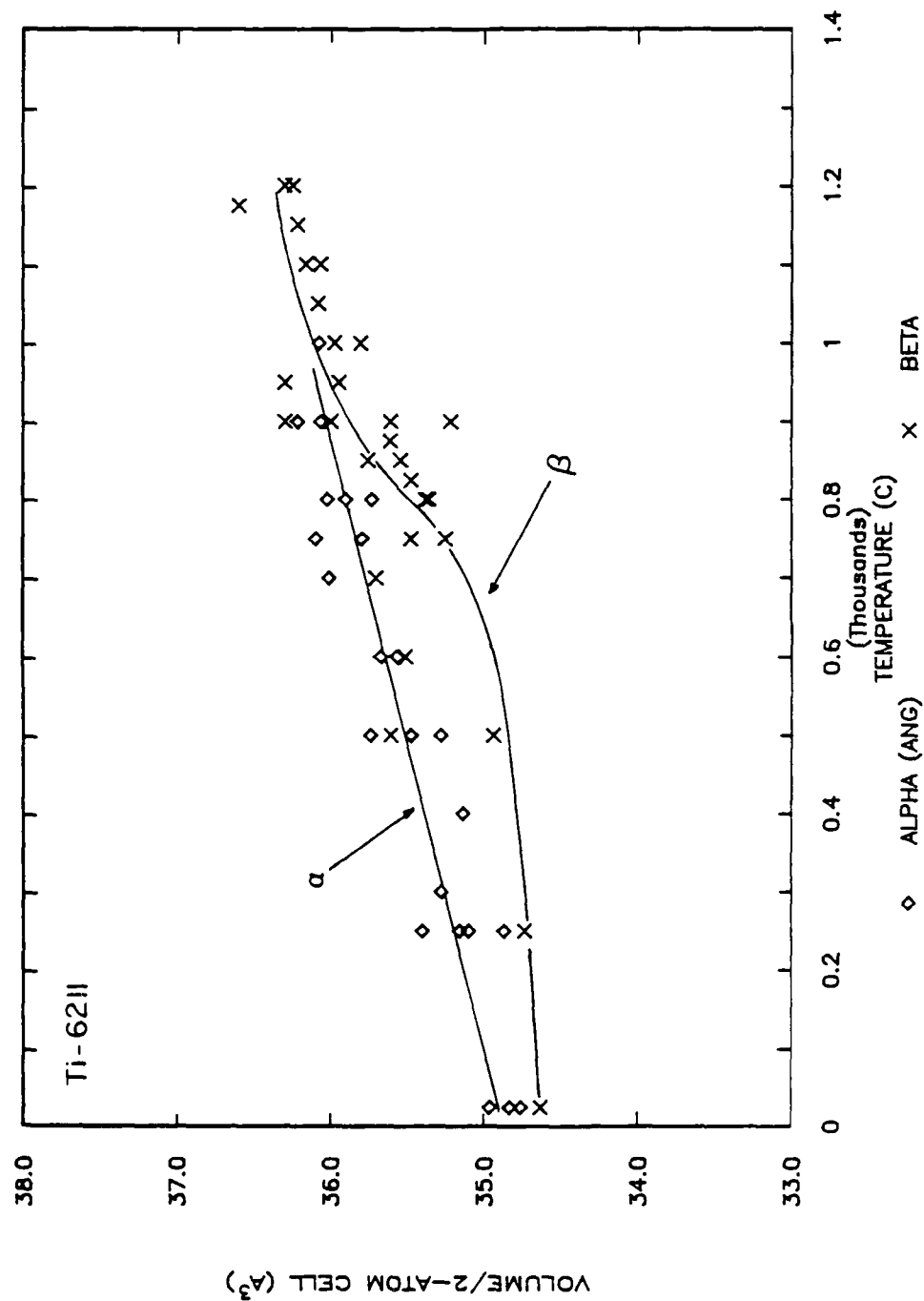


Figure 5.40 Lattice volume versus temperature for the alpha and beta phases of Ti-62II.

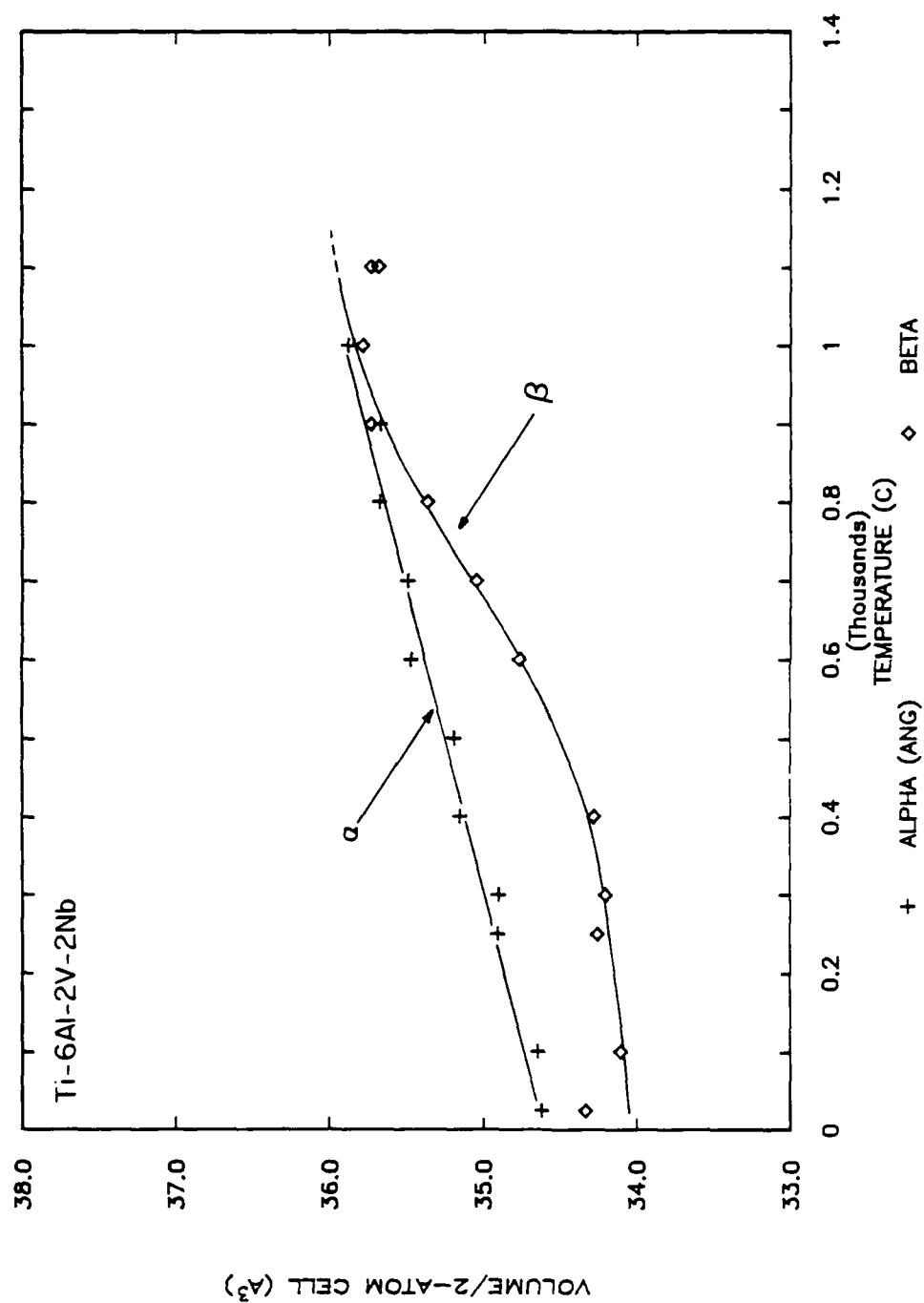


Figure 5.41 Lattice volume versus temperature for the alpha and beta phases of Ti-6Al-2V-2Nb.

opposite of what is expected. The alpha phase is hcp, hence close-packed, and the beta phase, which is bcc, is not. This observation also contradicts several dilatometric studies (13, 125) which show that there is a definite contraction associated with the formation of the alpha phase. This suggests that the dilatometric studies were conducted at conditions far enough removed from equilibrium to reverse the volume relationship.

A third trend that can be noticed in Figures 5.28-5.41 is that the beta lattice parameters increase much more significantly with temperature than do the alpha parameters. This is particularly true near the beta transus because of the rapidly changing composition of the beta phase. Vanadium and molybdenum significantly decrease the lattice parameter of beta titanium. Thus, as the temperature nears the beta transus on heating, and the beta becomes progressively leaner, its volume increases both because of thermal expansion and because of the compositional effect (126). The beta stabilizer content of the alpha phase, on the other hand, remains fairly constant (93) so no such accelerated expansion occurs. This "compositional step" in the beta lattice volume versus temperature curves can be seen to a varying degree in all of the alloys tested, Figures 5.19-5.41. This step is clearly shown in Figure

5.42. In this figure, the data for Ti-6Al-4V measured in this investigation are compared with a lattice volume versus temperature curve based on published data (92, 110). Figure 5.42 also serves to show the general agreement between published results and those obtained in this investigation.

5.2.1.2 Alloy Differences

Figures 5.29-5.41 also illustrate the relationship between the lattice parameters of the three alloy systems. These differences will be discussed first with respect to the alpha phase and then as they apply to the beta phase.

The alpha lattice size of several alloys are plotted against temperature in Figure 5.43. This figure shows that the most significant change in the alpha lattice is the 2.5%-3% contraction that results from the addition of 6% aluminum to titanium. The effects of the beta stabilizer elements caused further, but much smaller, changes in the alpha lattice. Ti-6Al-4Nb and Ti-6211 had an alpha phases which were slightly larger, approximately 0.5% and 0.2% respectively, than that of Ti-6Al. Compared to Ti-6Al, the alpha phases of Ti-6Al-4Mo and Ti-6Al-2V-2Nb were slightly smaller, 0.1% and 0.5%. The alpha lattice of Ti-64 was found to be approximately the same size as that of Ti-6Al. Because the errors in the measurement of cell volumes are on the order of 0.1% (Appendix D), this figure supports the

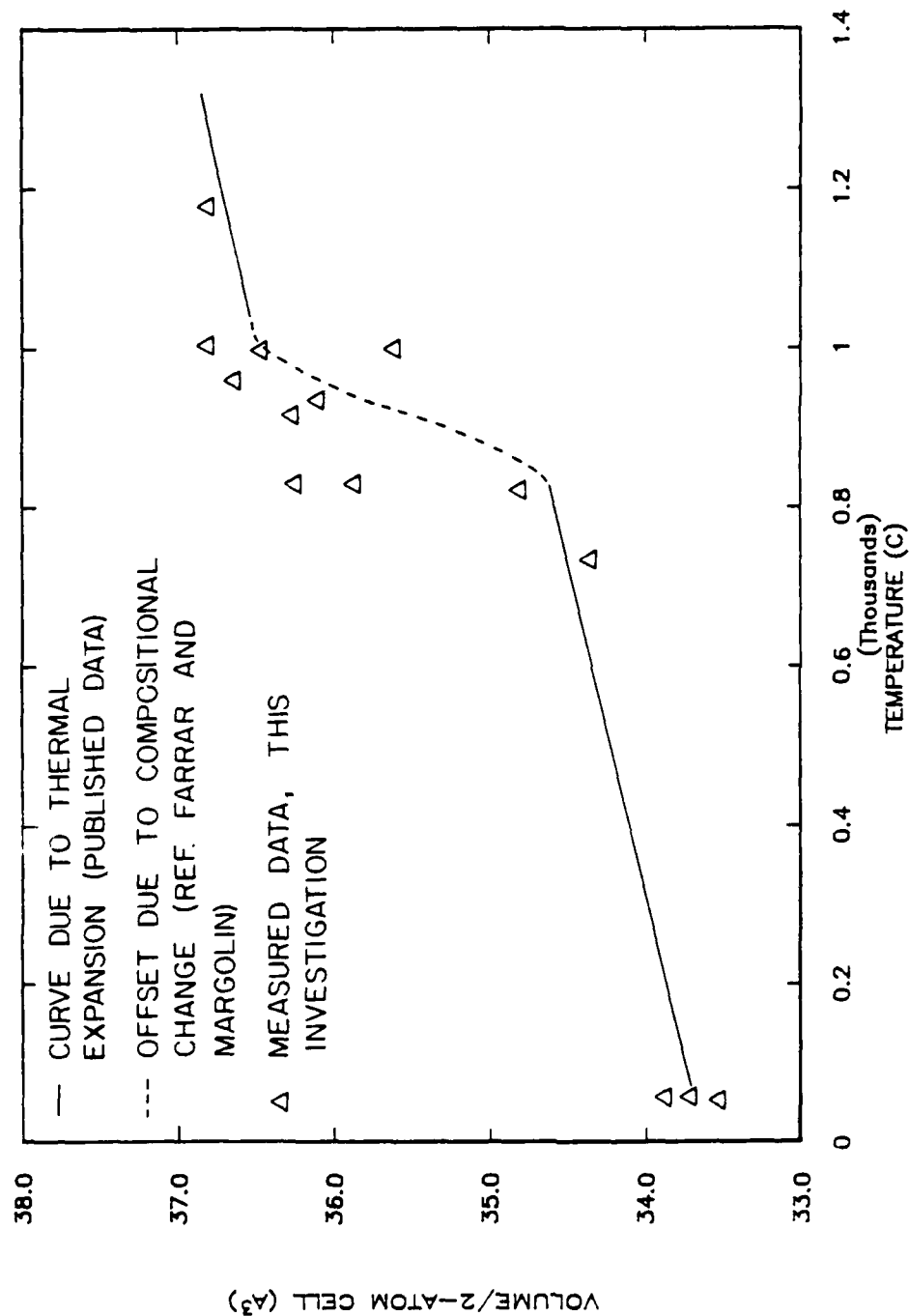


Figure 5.42 Lattice volume versus temperature for the beta phase of Ti-6Al-4V, illustrating the effect of composition on beta phase lattice volume.

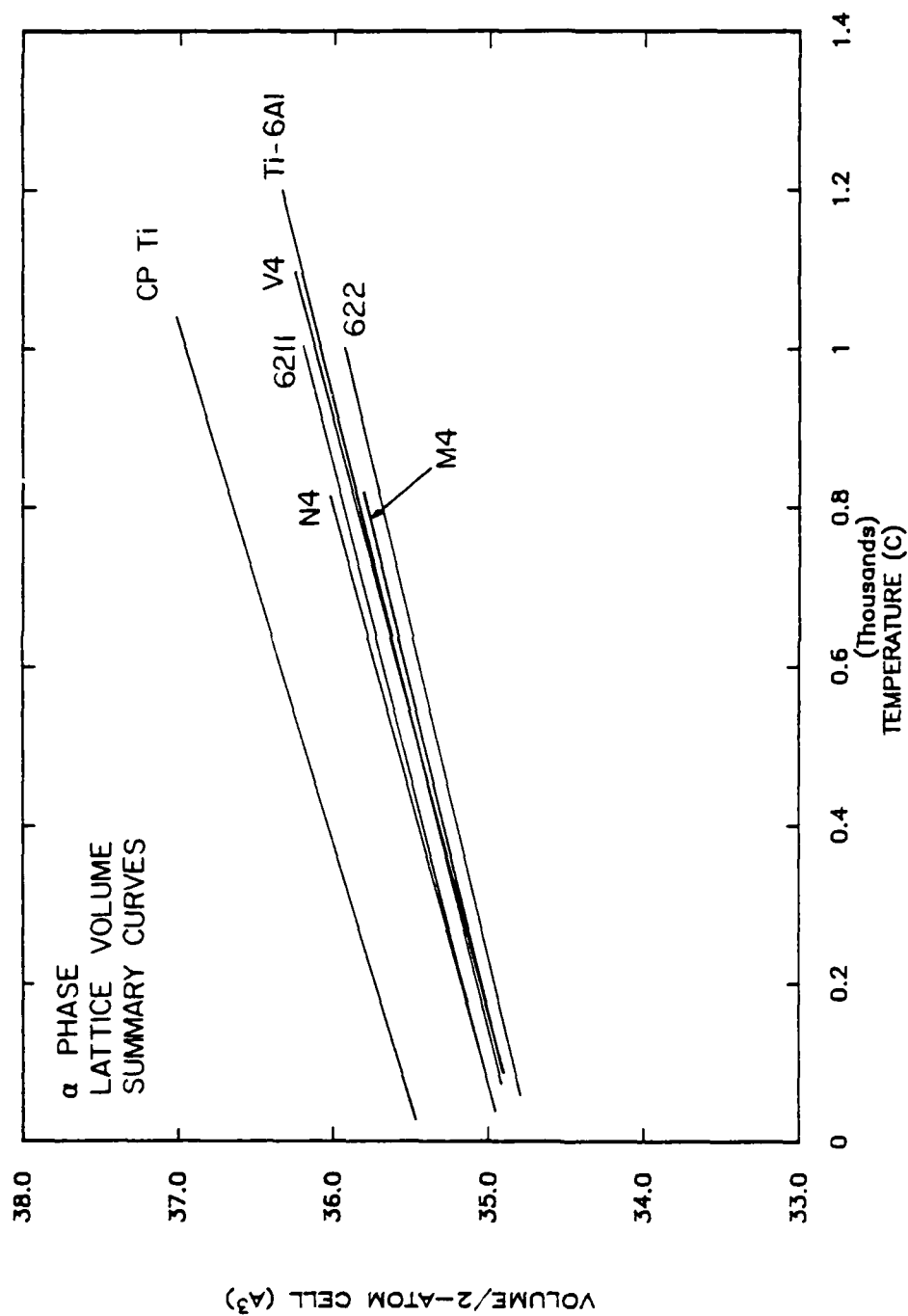


Figure 5.43 Lattice volume versus temperature summary curves for the alpha phase of several alloys. Note that the alpha phase lattice volume for all alloys is very similar to that of Ti-6Al.

assumption that the alpha phase in these alloys is essentially Ti-6Al.

Thermal expansion coefficients for the alpha phase of several alloys were calculated from the lattice parameter data. The coefficients for Ti-6211, Ti-6Al-4Nb, and Ti-6Al-4V were all very similar, approximately 1.3×10^{-5} °C/s. Ti-6Al-4Mo was found to have a lower coefficient, 1.0×10^{-5} °C/s. These values can be compared to values reported for bulk Ti-6Al-4V, which contains alpha and beta. The values for Ti-6Al-4V range from 0.95×10^{-5} °C/s to 1.12×10^{-5} °C/s (127-131). Although no similar data is available for Ti-Al-Mo or Ti-Al-Nb alloys, it is unlikely that the thermal expansion coefficients for these systems will differ appreciably from 1.0×10^{-5} °C/s. The thermal expansion coefficients published by TIMET (110) for the range of alloys they produce, including alpha, alpha-beta, and metastable beta alloys, are all between 0.95×10^{-5} °C/s and 1.0×10^{-5} °C/s. Although these data differs slightly from those of this investigation, it does support the observation that the thermal expansion coefficient for the alpha phase of titanium alloys does not vary significantly with composition.

Figures 5.29-5.41 also show the different characteristics of the beta phase of the different alloys.

These differences include relative stability of the beta phase, relative size of the beta phase, and the shape of the lattice volume versus temperature curve. In a qualitative sense, the x-ray measurements showed that molybdenum and vanadium both to stabilize the beta phase more than niobium. In Ti-6Al-4V and Ti-6Al-4Mo, relatively intense, distinct, beta diffraction peaks were seen throughout the temperature range investigated. These peaks were not observed in Ti-6Al-4Nb until temperatures very near or above the beta transus. This agrees with the results of Hansen, et. al. (132), as well as with predictions based on binary phase equilibria or electron/atom ratios (7).

The measured beta lattice volumes for all the alloys investigated are plotted against temperature in Figure 5.44, and for alloys with 4% beta stabilizer in Figure 5.45. As discussed earlier, no beta diffraction peaks could be detected at low temperatures for the niobium alloys. Among the other alloys, the vanadium alloys were the smallest at room temperature and the molybdenum alloys were the largest. The difference between the two sets was approximately 4%. Ti-6211 was approximately the same size, at room temperature, as the molybdenum alloys, and Ti-6Al-2V-2Nb was midway between the vanadium alloys and the molybdenum alloys. These relationships did not hold, however, at high

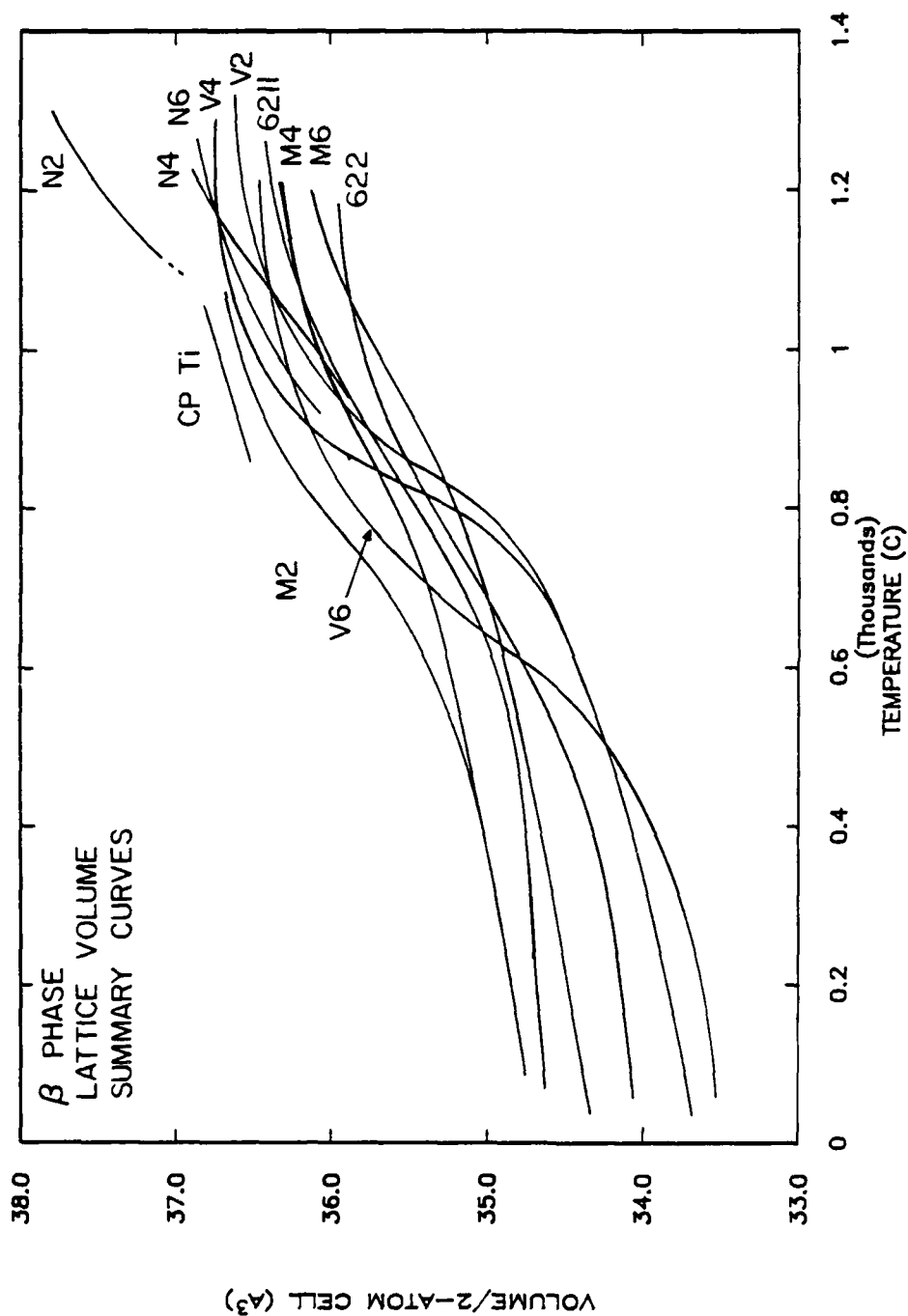


Figure 5.44 Lattice volume versus temperature summary curves for the beta phase of all alloys tested, showing that the niobium containing alloys have the largest beta lattice.

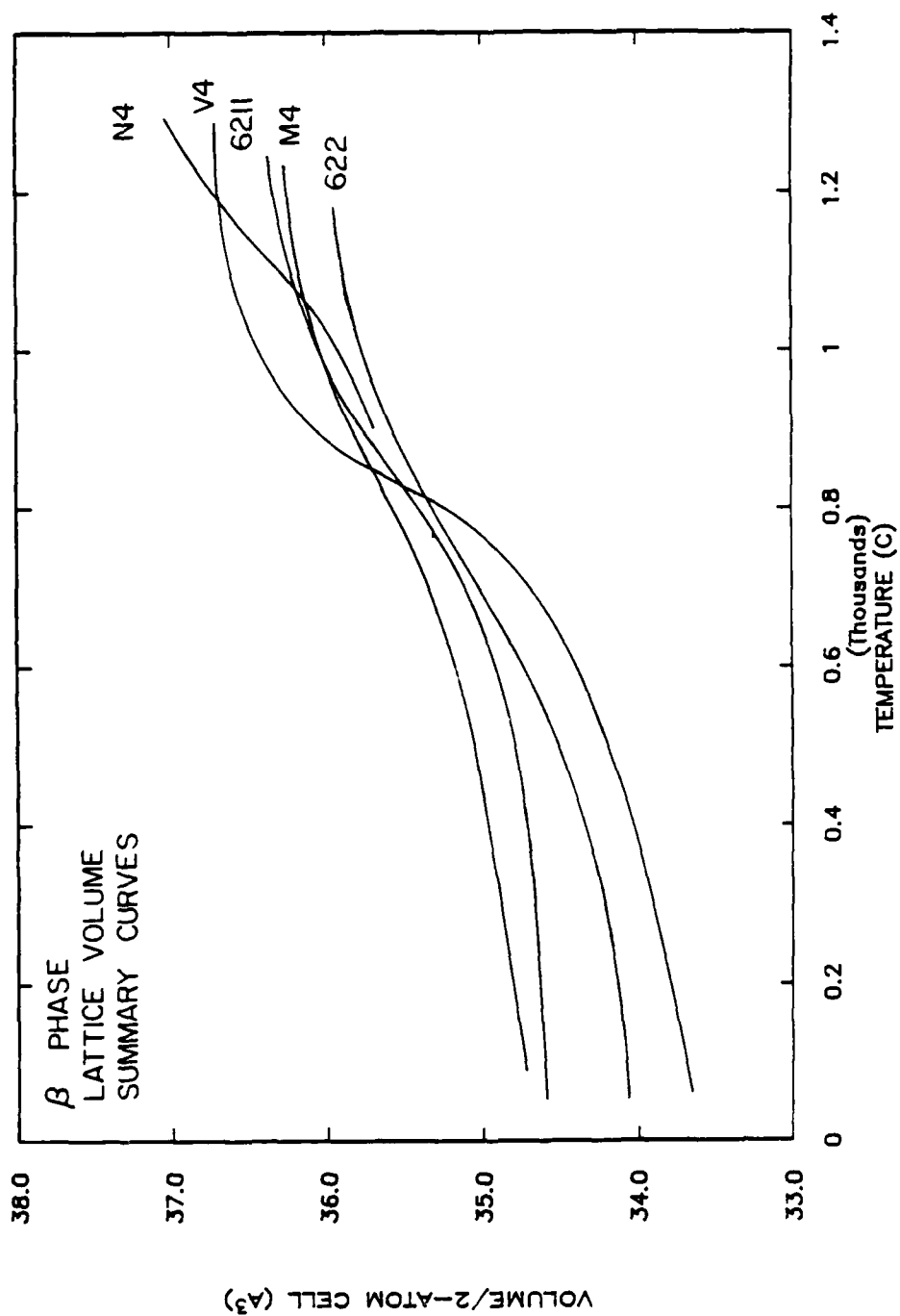


Figure 5.45 Lattice volume versus temperature summary curves for the β phase of alloys containing 4% beta stabilizer. Again note that the β phase lattice is largest for the niobium containing alloy.

temperatures. Above the beta transus, the vanadium alloys were all grouped fairly closely, the curves for Ti-6Al-2V and Ti-6Al-6V differing by approximately 0.4%. Ti-6Al-2Mo was at the upper end of this range, Ti-6Al-4Mo and Ti-6Al-2Nb slightly below the bottom end, and Ti-6Al-6Mo and Ti-6Al-2V-2Nb were smaller still, by approximately 1%. Figure 5.44 shows that all of these alloys had beta lattices which were smaller than that of unalloyed titanium. This is as predicted by the binary effects of these elements (71).

The titanium-aluminum-niobium alloys were significantly different from the other alloys, also as predicted by the binary relationships. The beta phase in Ti-6Al-6Nb was larger than in any of the the vanadium or molybdenum alloys, but still slightly smaller than that in unalloyed titanium. Ti-6Al-4Nb was slightly larger, approximately the same size as in unalloyed titanium, and Ti-6Al-2Nb 2% larger still.

Plots of beta lattice volume versus temperature are presented for the vanadium, niobium, and molybdenum systems as Figures 5.46, 5.47, and 5.48, respectively. In addition to the size comparisons discussed above, these figures show that the shapes of the curves differ as well. Figures 5.46-5.48 also illustrate that the shapes of these curves are dominated by the large change in the beta lattice size due to the change in composition near the beta transus. These

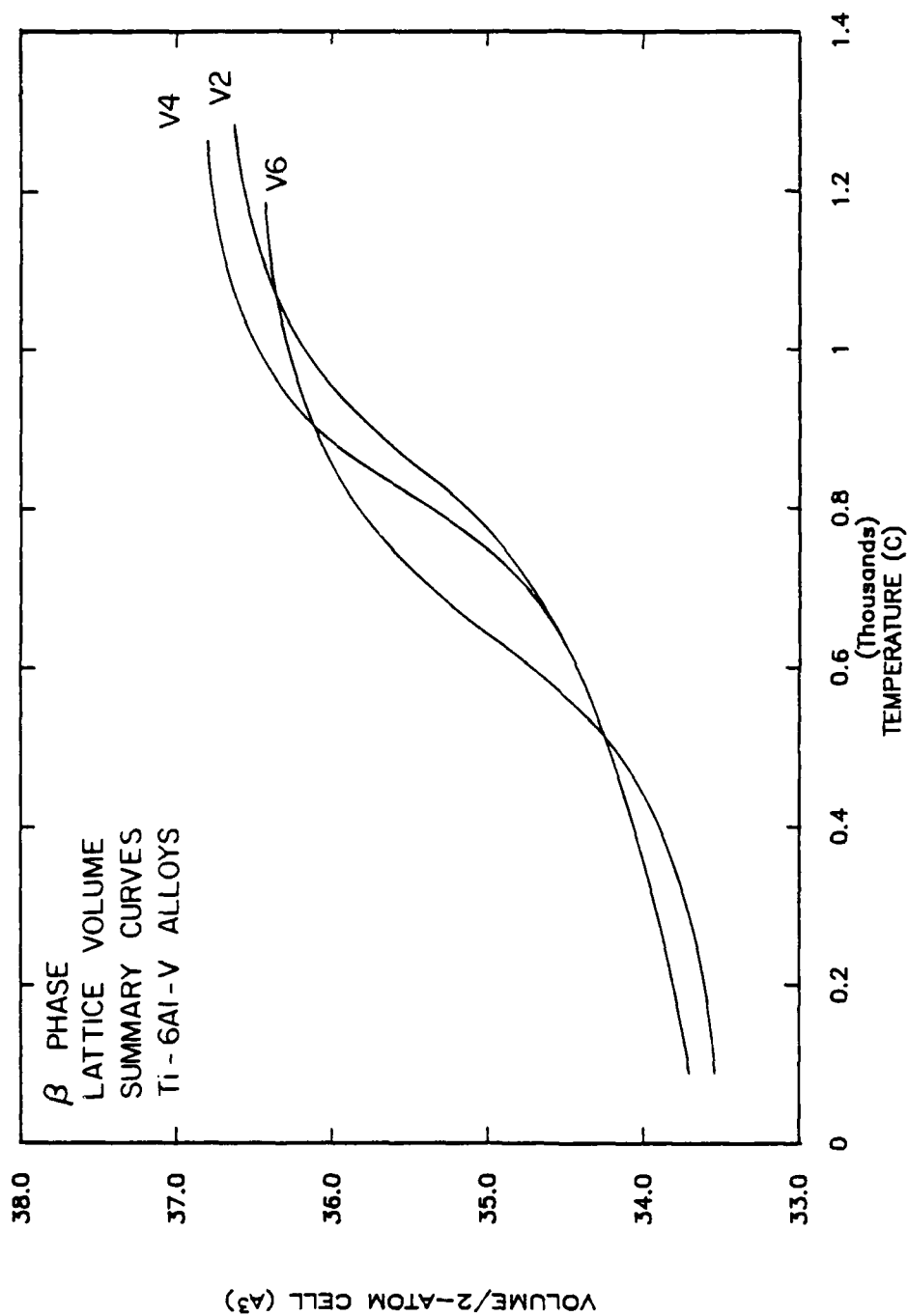


Figure 5.46 Lattice volume versus temperature summary curves for vanadium containing alloys, showing the large effect of changing composition near the beta transus.

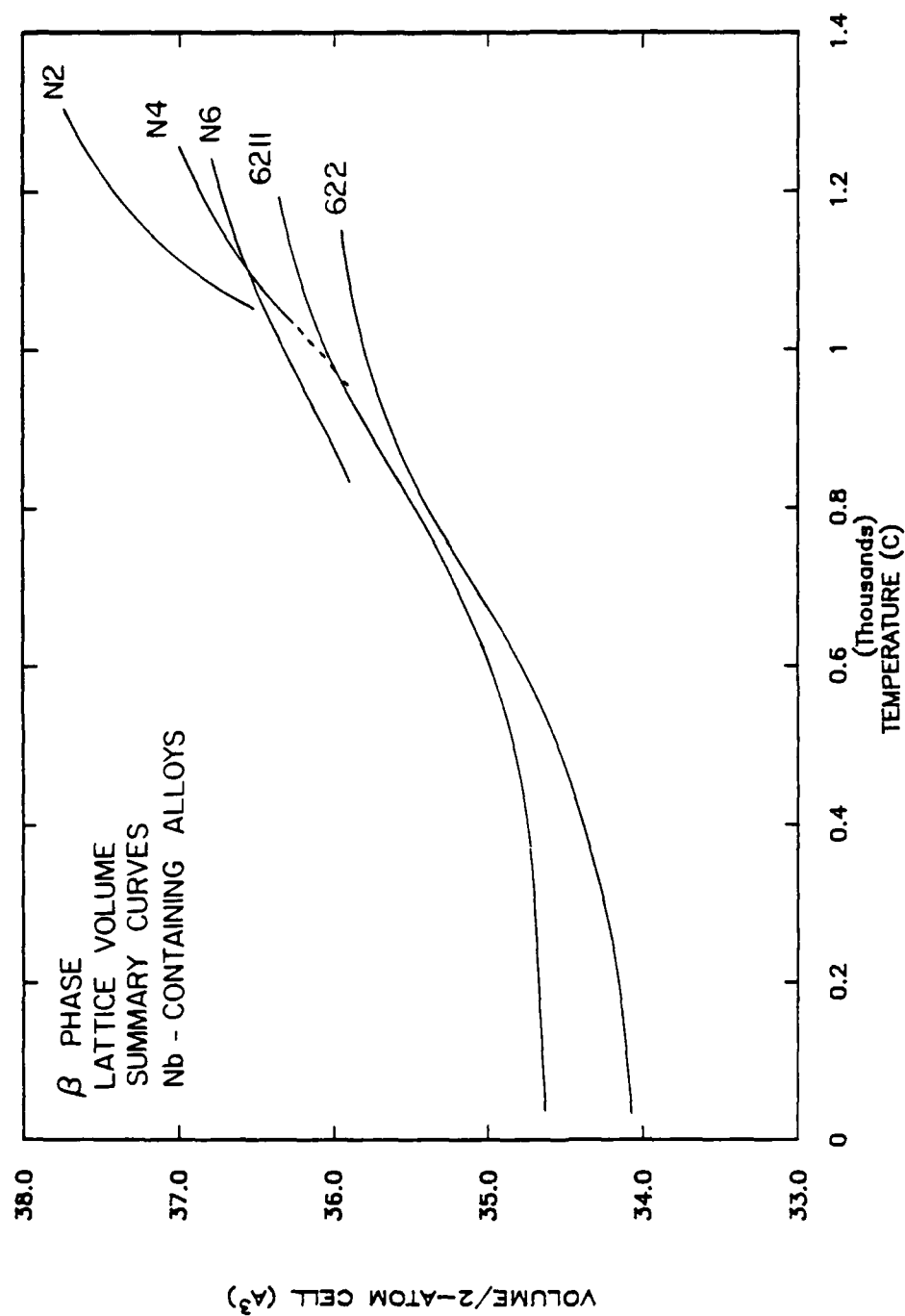


Figure 5.47 Lattice volume versus temperature summary curves for niobium containing alloys, showing that the beta lattice is larger for Ti-6Al-Nb ternary alloys than for more complex alloys.

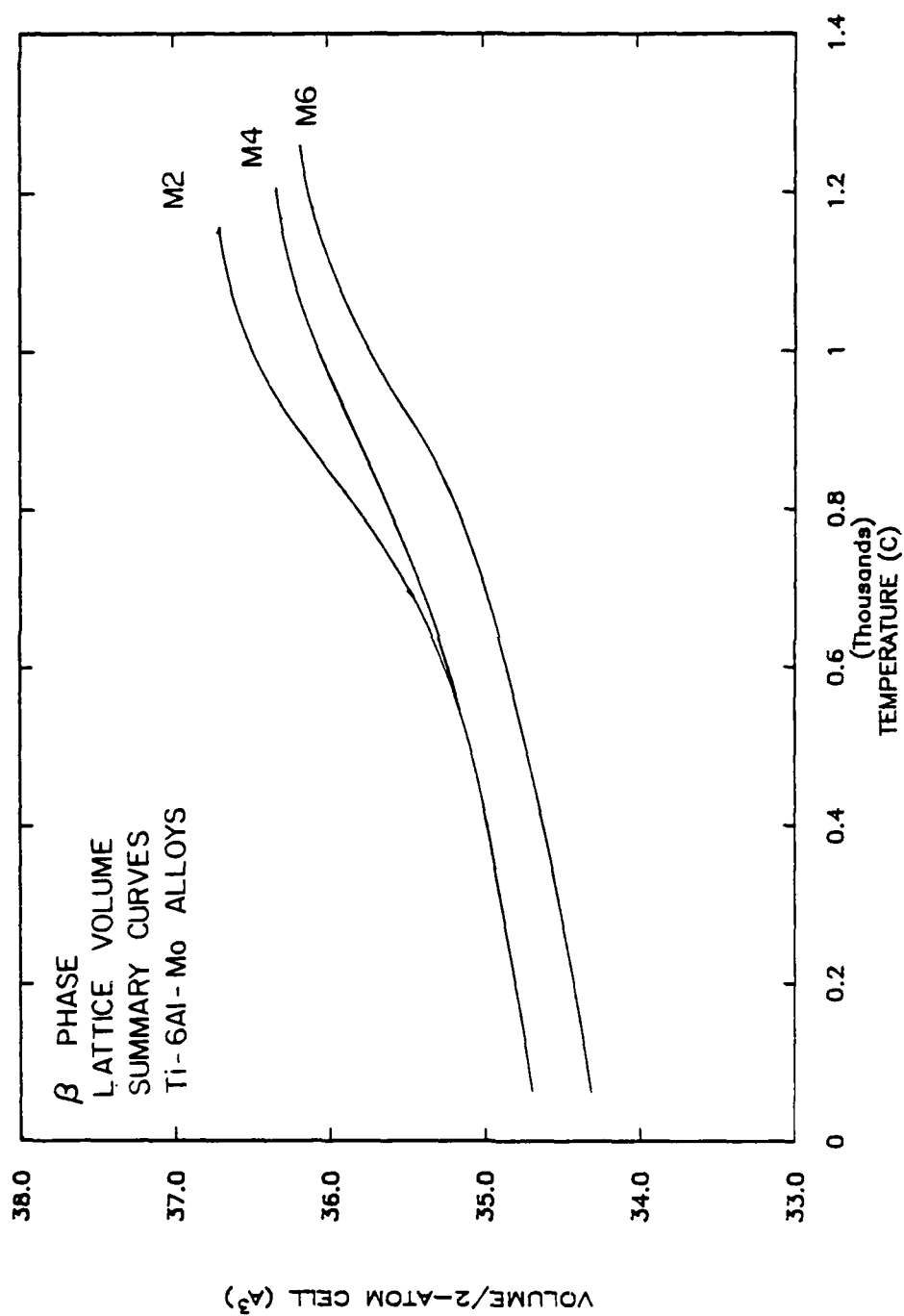


Figure 5.48 Lattice volume versus temperature summary curves for molybdenum containing alloys.

figures clearly show that this effect is large in all of the alloys, but largest for the vanadium alloys and smallest for the molybdenum alloys.

5.2.1.3 Conclusions Based on Lattice Parameters

Several conclusion may be drawn based on the data shown in in Figures 5.29-5.48. These figures show that, to a certain extent, the lattice parameters in ternary alpha-beta titanium alloys can be predicted by the binary effects of the alloy additions on titanium. However, predictions made for more complex alloys are less successful. Also, these results show that the elemental partitioning to the alpha and beta phases when both are present can not be predicted accurately and has a significant effect on the beta lattice parameters. The final conclusion that can be drawn regarding the lattice parameter measurements is that niobium contracts the beta lattice far less than either vanadium or molybdenum. The respective alpha phases of all of these alloys were very close in size. Therefore, niobium will increase the beta to alpha lattice incompatibility more than either vanadium or molybdenum, if the assumption can be made that some method based on equilibrium relationships will accurately predict the situation existing during rapid cooling.

5.2.2 High Speed Dilatometry

As discussed earlier, lattice incompatibility was calculated by combining the equilibrium lattice parameter measurements with radial dilatometry. The Gleeble 1500 thermal mechanical testing system was used for the dilatometry, allowing the size of the beta retained during rapid cooling to be measured. Tabulated values for sample size versus cooling rate and temperature for four example alloys are shown in Table 5.5. It was found that the shape of the dilatometry curve does not vary appreciably with either cooling rate or alloy content. Because of this consistency, an average curve was calculated to describe the behavior of all of the alloys in this investigation. This curve is also presented in Table 5.5 and labelled in the following figures as "AVE".

The slopes of the dilatometry curves were found to be approximately constant, decreasing only slightly near the beta transus. This permits the behavior of each alloy to be described reasonably well by a constant expansion coefficient. However, because these curves were produced under conditions where the specimen length was held fixed, Usually, the relationship between initial diameter d_0 and the diameter at some temperature T , d_T , is:

$$d_T = d_0(1 - \alpha T)$$

Table 5.5

Sample Diameter at Several Temperatures, Normalized
to Sample Diameter at 1200°C

Alloy	Temperature (°C/s)	D _T /D ₁₂₀₀ for Specified Cooling Rates			
		5 °C/S	10 °C/S	20 °C/S	50 °C/S
Ti-6Al -4Nb	1200	1	1	-	-
	1150	0.9992	0.9992	-	-
	1100	0.9981	0.9981	-	-
	1050	0.9969	0.9971	-	-
	1000	0.9959	0.9961	-	-
	950	0.9946	0.9941	-	-
	900	0.9935	0.9941	-	-
Ti-6Al	1200	1	-	1	1
	1150	0.9992	-	0.9992	0.9992
	1100	0.9983	-	0.9984	0.9984
	1050	0.9975	-	0.9977	0.9977
	1000	0.9966	-	0.9971	0.9970
	950	0.9956	-	0.9964	0.9964
Ti-6211	1100	1	1	1	1
	1050	0.9992	0.9993	0.9993	0.9993
	1000	0.9986	0.9987	0.9984	0.9979
	950	0.9979	0.9981	0.9976	0.9971
	900	0.9972	0.9974	0.9970	0.9965
	850	0.9970	0.9968	0.9950	0.9959
Ti-6Al -6V	1100	1	1	1	1
	1050	0.9993	0.9995	0.9993	0.9994
	1000	0.9987	0.9989	0.9986	0.9988
	950	0.9982	0.9982	0.9980	0.9981
	900	0.9987	0.9975	0.9973	0.9974
	850	0.9971	0.9969	0.9967	0.9968

However, because of the sample ends being held fixed, the relationship in this case is:

$$V_T = V_0(1-\alpha T)^2$$

or: $V_T = V_0(1-2\alpha T)$

Based on this calculation and the average dilatometry curve determined in this investigation, the thermal expansion coefficient for the beta phases of the alloys investigated was found to be $10 \times 10^{-6} \text{ }^\circ\text{C}^{-1}$. Other researchers have reported similar results. Adenstedt, et. al. (133) found that the thermal expansion coefficient for beta titanium was $9.41 \times 10^{-6} \text{ }^\circ\text{C}^{-1}$ between room temperature and 100°C , and increased only to $9.77 \times 10^{-6} \text{ }^\circ\text{C}^{-1}$ when the temperature range was increased to go from room temperature to 650°C . They also found that the thermal expansion coefficient did not vary significantly with the addition of vanadium. Expanding on this and other work, Levinger (134) reported thermal expansion coefficients for beta titanium of $11.1 \times 10^{-6} \text{ }^\circ\text{C}^{-1}$ and $10.1 \times 10^{-6} \text{ }^\circ\text{C}^{-1}$ between room temperature and 1000°C . These values were used to calculate volumetric dilatometry curves and are labelled as "PUB" in the following figures.

Figure 5.49 compares relative volume curves for several alloys cooled at 10°C/s with results predicted by both the average curve from this investigation and the published

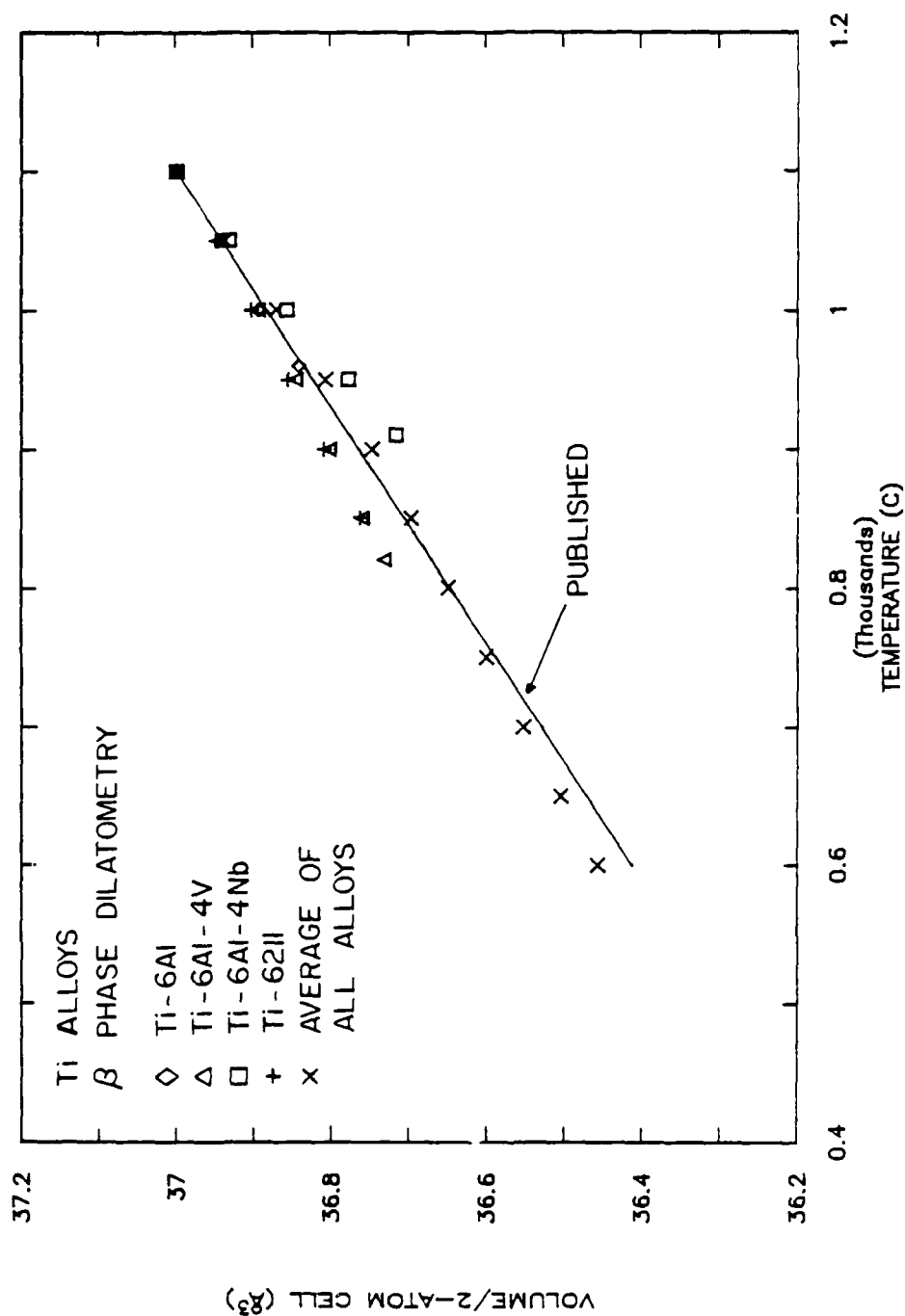


Figure 5.49 Beta phase dilatometry curves for several alloys cooled at 10°C/s. Data agrees closely with an average of all data and with a published thermal expansion curve (134).

thermal expansion coefficient. This figure shows the agreement between the predicted curves and the data for individual alloys. Figure 5.50 shows relative size curves for Ti-6Al and the vanadium alloys compared with the predicted curves. Good agreement is again seen. Figure 5.51 shows data for Ti-6Al-4V cooled at several cooling rates and compares this data with the average curve. Figure 5.51 figure shows the largest variation in the data and seems to indicate that the expansion coefficient is slightly greater when higher cooling rates are used. However, this trend was not observed in any of the other alloys and is not believed to be significant. In all cases, the data is within 0.2% of both the average curve and the curve predicted using the published linear expansion coefficients, and in most cases, within 0.1%.

Several sources of error exist in the dilatometry procedure. They are discussed briefly in Appendix D. Because of the errors inherent in the dilatometry procedure, it seems likely that the curve derived from the average of all of the data is an adequate representation of the sample size during cooling. This is supported by examination of the above figures and the data in Table 5.5, which show that the random errors between runs of one material at one cooling rate are on the same scale as errors between alloys

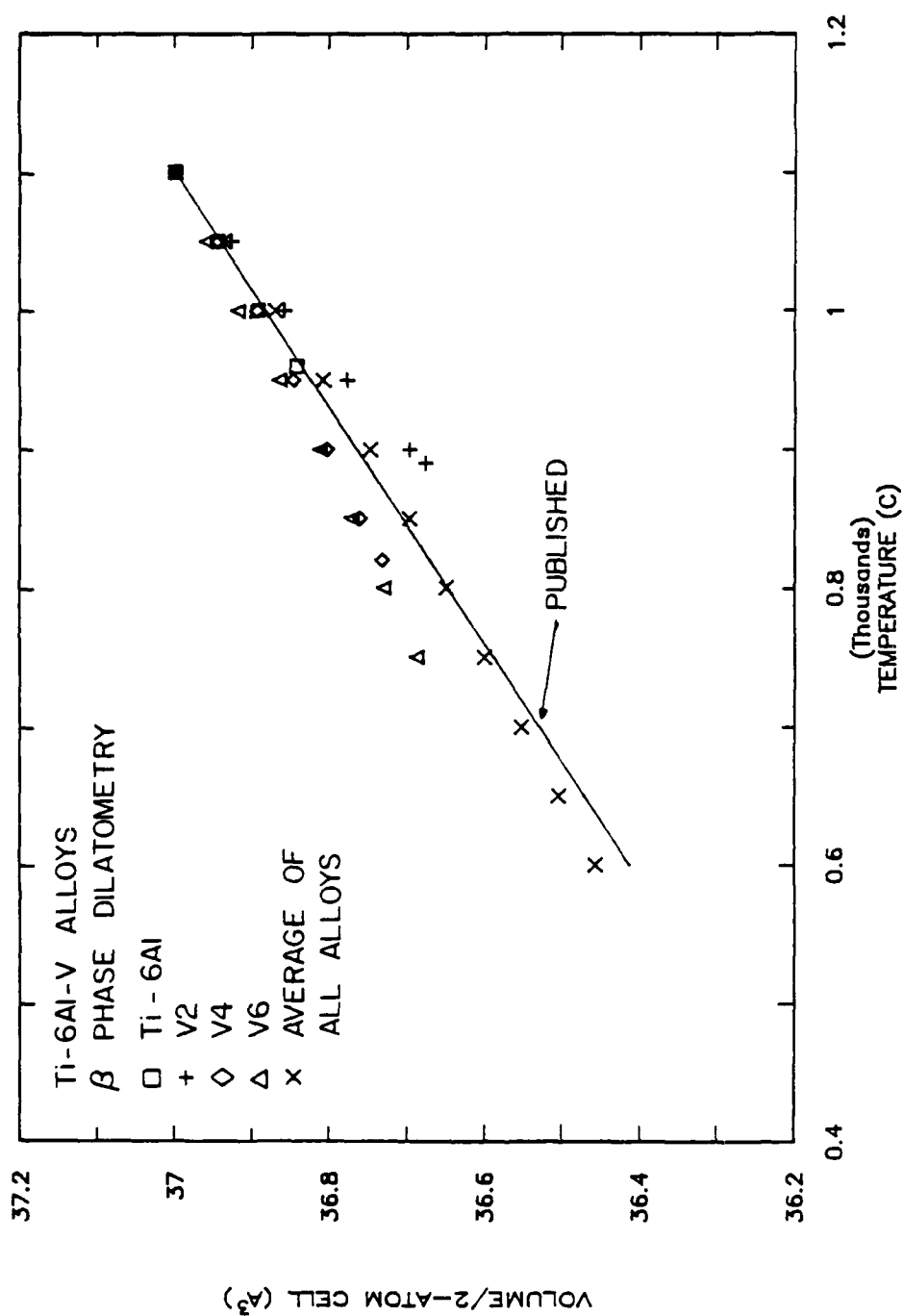


Figure 5.50 Beta phase dilatometry curves for vanadium containing alloys cooled at 10 C/s. Again, data compares well with an average of all data and published results (134).

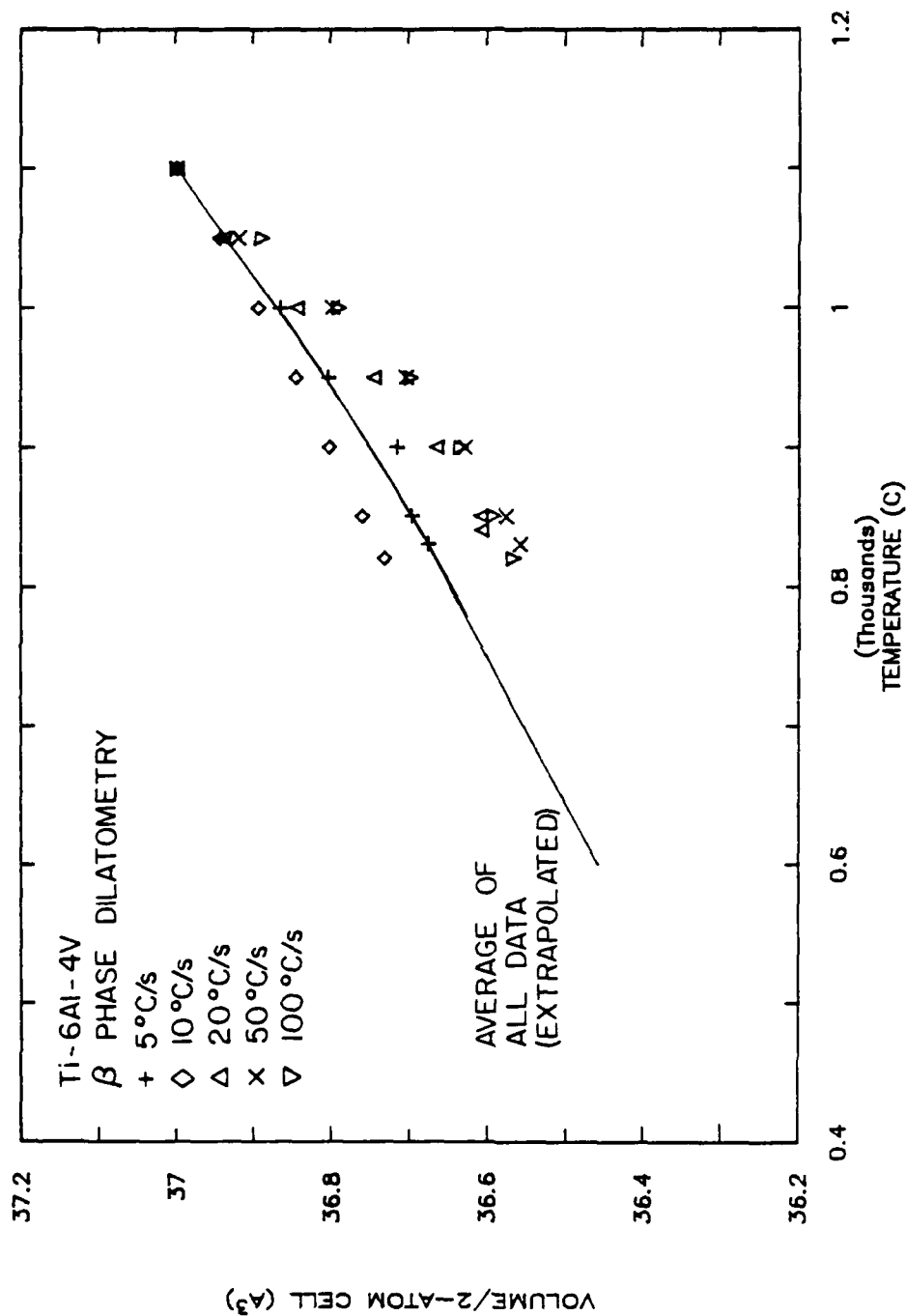


Figure 5.51 Beta phase dilatometry curves for Ti-6Al-4V cooled at several rates. Data is compared with an average of all data.

or between cooling rates.

5.2.3 Lattice Incompatibility Calculation

The average dilatometry curve and the equilibrium lattice parameters were combined to calculate lattice incompatibility in two ways. The first was based on the original Rath (4) model which assumes that the transformation stress is developed during the formation of the grain boundary alpha film. In this case, the transformation is from a supercooled beta phase to an equilibrium alpha phase. The second method is based on the assumption that the development of stress due to lattice incompatibility continues throughout the formation of the Widmanstatten colonies. Although this situation will exist only up to some maximum value of volume percent transformed, no attempt was made to find this upper limit. Each of these calculations will be discussed individually in following sub-sections.

5.2.3.1 Supercooled Beta to Equilibrium Alpha The amount of grain boundary alpha present did not vary significantly from alloy to alloy or with cooling rate. Therefore, the amount of grain boundary alpha was not taken into account in these calculations. Thus a single value for volumetric lattice incompatibility was calculated for each

alloy. This value is labelled as ΔV_α in Figure 5.52 and values for the lattice incompatibility of the model alloys are listed in Table 5.6. Because the temperature where the grain boundary alpha is forming is not known, lattice incompatibility is reported at both the transformation start and finish temperatures. This data shows that there are basically three groups of alloys, based on beta to alpha lattice incompatibility. The first group is the alloys which have little or no lattice incompatibility. These include CP Ti, Ti-6Al, Ti-6Al-4V, Ti-6Al-6V, Ti-6Al-2V-2Nb, and Ti-6211. The second group, alloys with moderate lattice incompatibility, approximately 0.4%, consists of the molybdenum alloys. The third group has the largest lattice incompatibility, approximately 1%-2%. This group includes Ti-6Al-2V and the niobium alloys. These results support the earlier conclusion that the addition of niobium has the greatest effect on lattice incompatibility in ternary alloys, but that this trend cannot be extended to more complex alloys because of the different partitioning of the alloying elements. Thus, superposition of binary lattice parameter effects, while a good indicator, does not accurately predict the lattice parameters or lattice incompatibility of alloys containing more than one beta stabilizer element.

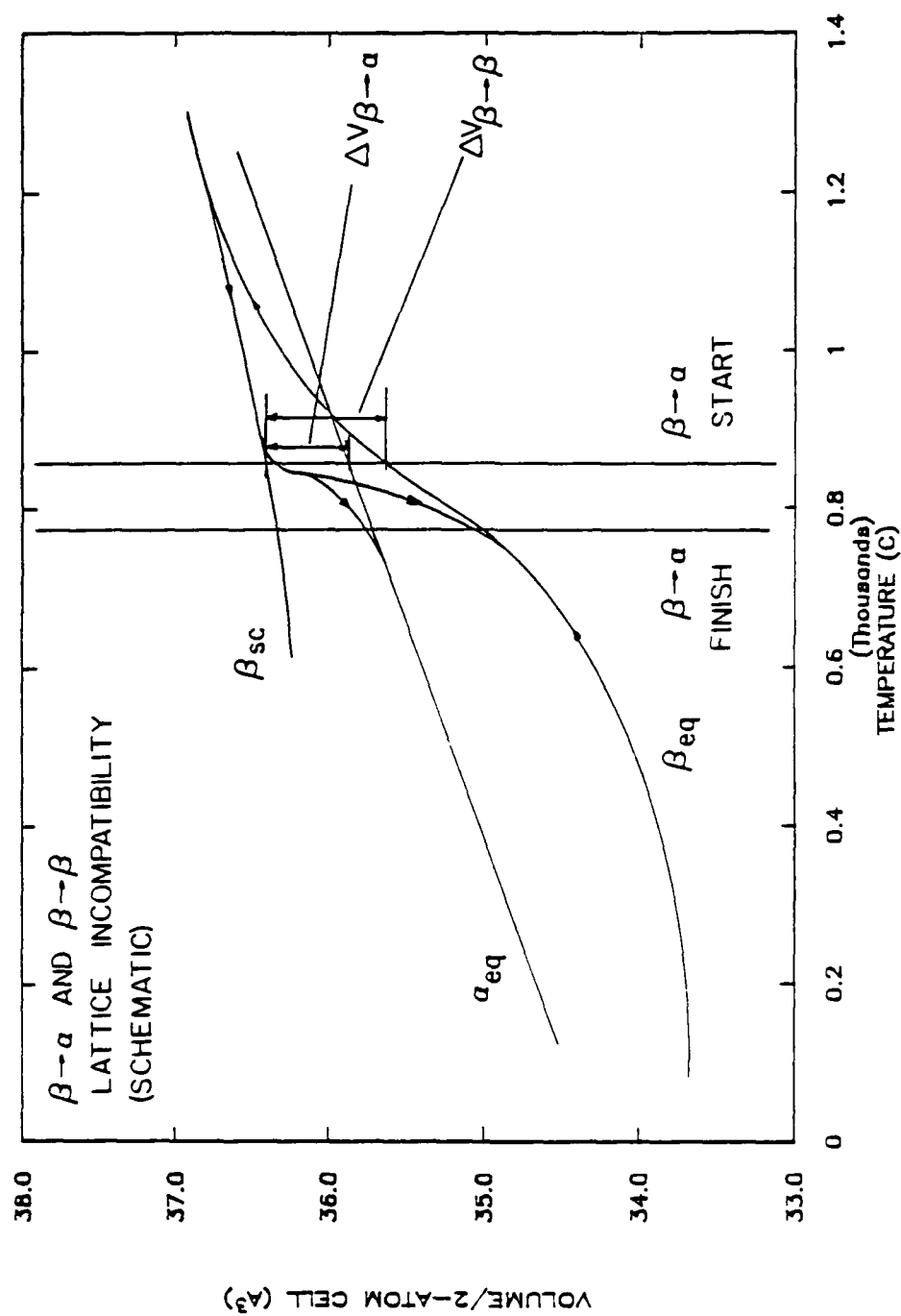


Figure 5.52 Schematic illustrating the measurement of beta to alpha and beta to beta lattice incompatibility.

Table 5.6

Lattice Incompatibility of Alloys Investigated,
Measured Between Supercooled Beta and Equilibrium Alpha

Alloy	Lattice Incompatibility (%) @ Temperatures		
	$\beta \rightarrow \alpha$ Start	$\beta \rightarrow \alpha$ Finish	$\beta \rightarrow \alpha$ Finish - 100°C
Cp Ti	0.0	0.0	0.0
Ti-6Al	0.0	0.0	0.0
Ti-6Al-2V	0.9	1.0	1.0
4V	0.0	0.0	0.0
6V	0.0	0.0	0.0
Ti-6Al-2Nb	2.2	2.3	2.4
4Nb	1.1	1.3	1.3
6Nb	1.7	1.6	1.6
Ti-6Al-2Mo	0.4	0.6	0.6
4Mo	0.4	0.5	0.6
6Mo	0.4	0.4	0.5
Ti-6211	0.2	0.3	0.4
Ti-6Al-2V -2Nb	0.0	0.0	0.0

5.2.3.2 Supercooled Beta to Widmanstatten Colonies

Although the colony structure is mostly alpha, it does contain some beta, Figures 5.18(a) and 5.19(a). In this case, the "alpha-beta" lattice incompatibility ($\Delta V_{\alpha\beta}$) is the sum of the two individual incompatibilities, supercooled beta to equilibrium alpha (ΔV_{α}) and supercooled beta to equilibrium beta (ΔV_{β}), each weighted by its respective volume percent:

$$\Delta V_{\alpha\beta} = X_{\alpha}(\Delta V_{\alpha}) + X_{\beta}(\Delta V_{\beta})$$

Because the amount of Widmanstatten colony structure present varies with alloy content and cooling rate, the actual lattice incompatibility is then calculated by multiplying the alpha-beta lattice incompatibility, $\Delta V_{\alpha\beta}$, by the volume fraction colony structure. The components and results of these calculations are presented in Table 5.7.

The data in Table 5.7 shows that the results of this lattice incompatibility calculation differ slightly from those obtained when only the grain boundary alpha film is considered. The alloys divide into groups roughly based on level of beta stabilization, with the leaner alloys having greater incompatibility. The largest values of lattice incompatibility are again found in Ti-6Al-4Nb and Ti-6Al-2V. Similarly, Ti-6Al-6V and Ti-6Al-2V-2Nb are again found to have small incompatibility values. Ti-6Al-4V and Ti-6211

Table 5.7

Lattice Incompatibility Calculated Between Supercooled Beta
and Equilibrium Widmanstätten Alpha-Beta
Cooling Rates ($^{\circ}\text{C/s}$) are Indicated

Alloy		β colony (vol %)	% colony (vol %)	Lattice Incompatibility (%)			total
				α	β	$\alpha+\beta$	
unalloyed							
titanium (10)	-		-	0	-	0	0
Ti-6Al (10)	-		-	0	-	0	0
Ti-6Al							
-2V (50)	5		20	0.9	2.0	0.96	0.19
(20)	5		40	0.9	2.0	0.96	0.38
(10)	5		53	0.9	1.6	0.93	0.49
(5)	5		74	0.9	1.1	0.91	0.67
-4V (20)	10		6	0	4.0	0.40	0.02
(10)	10		15	0	3.8	0.38	0.06
(5)	10		26	0	3.8	0.38	0.10
(1)	10		50	0	3.3	0.33	0.17
-6V (10)	15		1	0	4.7	0.71	0.01
(5)	15		4	0	4.3	0.65	0.03
(1)	15		12	0	4.0	0.60	0.07
Ti-6Al							
-2Mo (10)	8		-	0.4	1.4	0.5	-
-4Mo (10)	16		1	0.4	1.0	0.5	0.05
-6Mo (5)	24		-	0.4	0.4	0.4	-

Table 5.7 (cont.)

Alloy		β colony (vol %)	% colony (%)	Lattice Incompatibility (%)			total
				α	β	$\alpha+\beta$	
<hr/>							
Ti-6Al							
-2Nb	(10)	3	-	2.2	0	2.2	-
-4Nb	(50)	6	10	1.1	0	1.0	0.10
	(20)	6	47	1.1	0	1.0	0.49
	(10)	6	57	1.1	0	1.0	0.59
	(5)	6	62	1.0	0	0.9	0.59
-6Nb	(10)	9	-	1.7	1.2	1.7	-
Ti-6Al							
-2V-2Nb	(20)	16	26	0	0.4	0.06	0.02
	(10)	16	29	0	0.3	0.05	0.02
	(1)	16	60	0	0.2	0.03	0.02
Ti-6211							
	(50)	10	17	0.2	0.9	0.27	0.05
	(10)	10	39	0.2	0.6	0.24	0.09
	(5)	10	60	0.2	0.4	0.22	0.13

are now found to have moderate incompatibility values. The data in Table 5.7 for the three vanadium alloys also shows that the lattice incompatibility differences resulting from changes in alloy content within one alloy system are on the same scale as the differences caused by a change of alloy systems. The data in Table 5.7 also shows that this is also true for changes in cooling rate for an individual alloy.

The data in Table 5.7 can be better understood by examination of the three factors that contribute to the beta to colony lattice incompatibility. The first factor is the relative volumes of the individual transformation components. The beta to alpha incompatibility was determined as before and again found to be largest for the niobium alloys and Ti-6Al-2V. The beta to beta incompatibility is largely controlled by two things, the size of the step associated with the compositional effect (discussed earlier and shown in Figures 5.46-5.48), and the relative position of the transformation start temperature with respect to the step. When only this is considered, the effect of an increase in cooling rate is to lower the transformation start temperature and increase the beta to beta incompatibility. Table 5.7 shows that the beta to beta incompatibility is largest for the vanadium alloys and smallest for the niobium alloys, as would be expected based

on Figures 5.46-5.48.

The second factor which contributes to the beta to colony lattice incompatibility is the volume fraction of beta in the colony structure. Although this quantity is very difficult to measure, reasonable estimates can be made based on metallographic observations and an analysis of the applicable phase diagrams. The values used are given in Table 5.7. The extent to which actual lattice incompatibility is controlled by the relative amounts of alpha and beta within the colony structure depends on the magnitudes of the beta to alpha and beta to beta incompatibility values. For example, the niobium alloys have a large beta to alpha incompatibility and no beta to beta incompatibility. In these alloys, $\Delta V_{\alpha\beta}$ will be the highest for lean alloys. The opposite is true when Ti-6Al-4V and Ti-6Al-6V are compared.

The third factor that contributes to the beta to colony lattice incompatibility is the amount of the colony structure formed. This is controlled by the kinetics of the beta to alpha transformation which, in turn, are controlled by the alloy content and cooling rate. The amount of colony structure formed is greater for lower cooling rates, leaner alloys, and for niobium and vanadium containing alloys in general. All are conditions which are associated with a

beta to alpha transformation which occurs at high temperatures and under conditions approaching equilibrium.

All of the above factors combine to determine the beta to colony lattice incompatibility for each combination of alloy and cooling rate. In all cases, an increase in cooling rate reduces the total incompatibility because of the reduced amount of colony structure formed. Table 5.7 shows that this is the dominant effect when an individual alloy is cooled at different rates. When two different alloys are compared, the relative incompatibilities may be controlled by either the relative amounts of colony structure or the respective values of $\Delta_{\alpha\beta}$. As an example of the first situation, the data for Ti-6Al-4V and Ti-6Al-6V shows that $\Delta_{\alpha\beta}$ is larger for Ti-6Al-6V, but that this difference is more than offset by the greater amount of colony structure in Ti-6Al-4V. On the other hand, the comparison between a high incompatibility alloy like Ti-6Al-2V and a low or moderate incompatibility, Ti-6211 or Ti-6Al-2V-2Nb, shows that the alloys have similar amounts of colony structure but drastically different $\Delta_{\alpha\beta}$ values.

5.2.4 Summary of Lattice Incompatibility Testing

Lattice incompatibility has been calculated based on two different assumptions regarding the beta to alpha transformation. In the first case, the transformation is

assumed to occur between a supercooled beta phase and an equilibrium alpha phase, the grain boundary allotriomorph. The size of the allotriomorph was not a strong function of either alloy content or cooling rate, so the incompatibility was determined solely by the relative sizes of the beta and alpha. Looking at selected alloys, Ti-6Al-4Nb was found to have a large incompatibility, Ti-6Al-4Mo a moderate incompatibility, and Ti-6Al-4V, Ti-6211, and Ti-6Al-2V-2Nb, small incompatibilities. The highest and lowest values of incompatibility differed by a factor of approximately four.

The second method of calculating lattice incompatibility was based on an assumed transformation between a supercooled beta phase and an equilibrium alpha-beta mix, the Widmanstatten colony structure. In this case, alloy content and cooling rate combined to control several factors which determined the overall lattice incompatibility. Ti-6Al-4Nb again had the largest incompatibility, Ti-6Al-6V and Ti-6Al-2V-2Nb again the smallest, now with Ti-6211 and Ti-6Al-4V in between. The most significant difference between results obtained with the two methods resulted from the second method weighting the calculated "alpha-beta" incompatibility, $\Delta_{\alpha\beta}$, by the amount of colony structure formed. Because of this, lattice incompatibility as calculated by the second method was

significantly affected by changes in alloy content within each alloy system and by changes in cooling rate. These changes were as large as those between different alloy systems. The largest incompatibility values were obtained for lean alloys and low cooling rates.

Several aspects of lattice incompatibility have not been addressed by this investigation and bear mentioning. The first is the applicability of equilibrium parameters to dynamic conditions. The calculation method used was chosen as the best available way to estimate the dynamic lattice incompatibility of several alloys relative to one another, based on measurements that could be made. However, a comparison of the lattice parameter measurements and the results of dilatometric studies demonstrate the difference between equilibrium and dynamic cooling conditions. The most serious inadequacy of this approach is that it is unable to address the partitioning which can take place during a continuous cooling transformation. The compositions of both the alpha and beta phases vary with time, temperature, volume percent transformed, and position. It is quite possible that the critical lattice incompatibility exists under conditions which are too dynamic and/or too local to bear any resemblance to bulk equilibrium measurements.

A second and less severe criticism is that the measurements and calculations are too crude to accurately estimate the lattice incompatibility, but that the approach is valid. This must be considered because the calculations, particularly the second set, are based on several measurements, each subject to error. The most severe of these potential errors, in terms of the ratio of error size to significant measurable differences, is involved in the lattice parameter measurements. Significantly less severe errors, relative to the quantities being measured, include those in measurement of x-ray sample temperatures, determination of transformation start temperatures, and quantitative metallography. These errors are discussed in Appendix D. However, the ability of these calculations to discern between various levels of lattice incompatibility is supported by agreement with published results and the fact that a significant range of incompatibility was observed within the investigation.

5.3 High Temperature Ductility

The high temperature ductility of several alloys was investigated using the Gleeble 1500 thermal-mechanical testing system. The alloys investigated included Ti-6Al-2V, Ti-6Al-4V, Ti-6Al-6V, Ti-6Al-4Nb, Ti-6Al-2V-2Nb, and Ti-6Al-2Nb-1Ta-0.8Mo. Unalloyed titanium and Ti-6Al were also

investigated, but not as extensively as the other alloys. The hot ductility testing procedure consisted of tensile testing during linear cooling at several rates, following an anneal at 1200°C. The tensile tests were performed at temperatures above, within, and below the temperature range of the beta to alpha transformation. Load versus elongation curves were generated for most of these tests. These curves are compiled under separate cover (87). The purpose of this testing was to characterize the high temperature ductility loss with respect to alloy content and cooling rate. The behavior described as the "high temperature ductility loss" was discussed earlier, Figure 1.1, and is shown schematically in Figure 5.53.

The results of the hot ductility testing are presented in Figures 5.54-5.61. These figures are plots of reduction in area versus test temperature for several cooling rates and each of the alloys tested. For comparison, the beta to alpha transformation start and finish temperatures for a cooling rate of 10°C/s are indicated on these figures.

5.3.1 Alloy Effects

Several observations can be made when these data are viewed as a whole. Most significantly, the mechanical behavior of all of the alloys tested is fairly similar. With the exception of unalloyed titanium, all the alloys

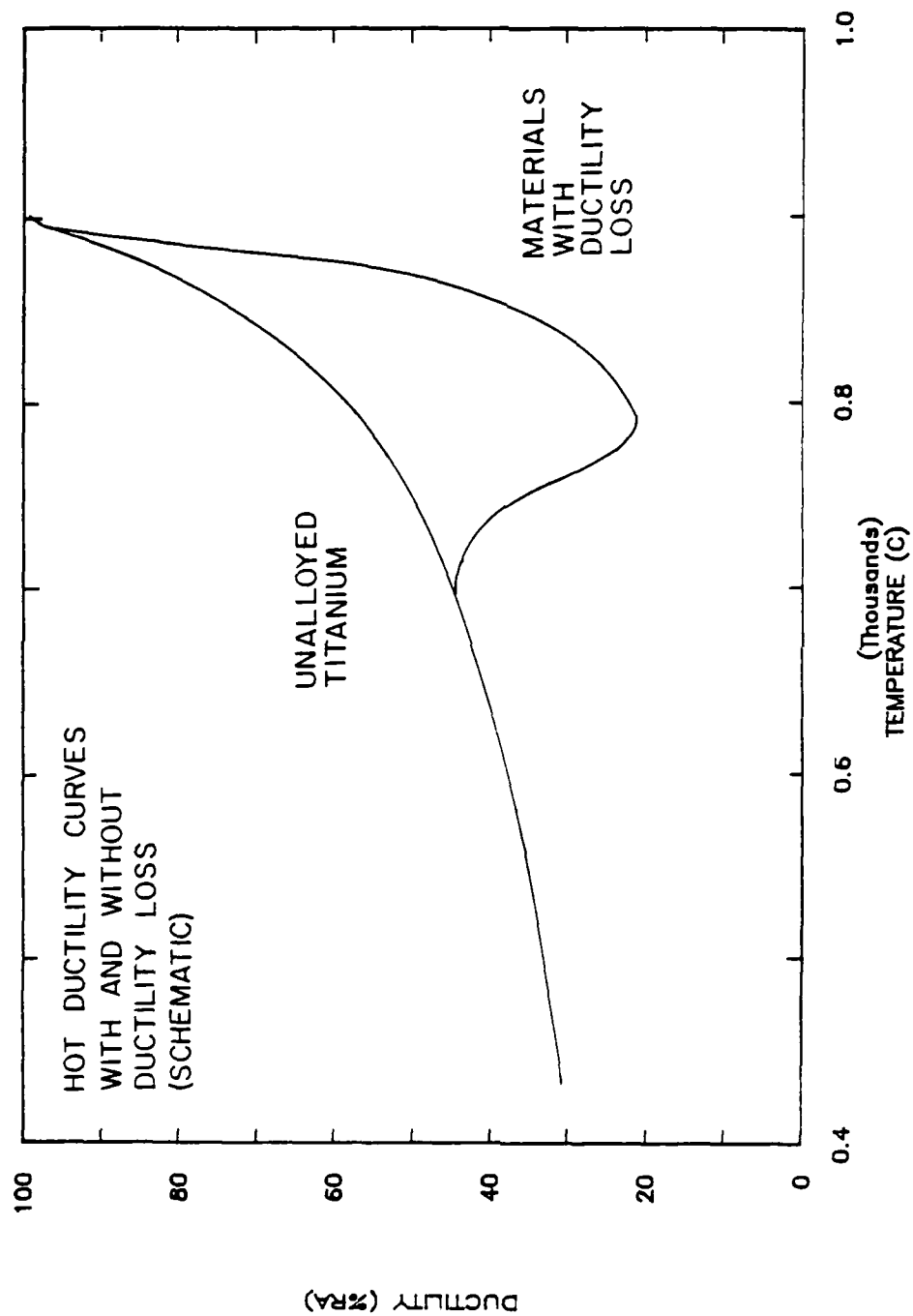


Figure 5.53 Schematic diagram of ductility versus temperature for two materials, illustrating the high-temperature ductility loss behavior.

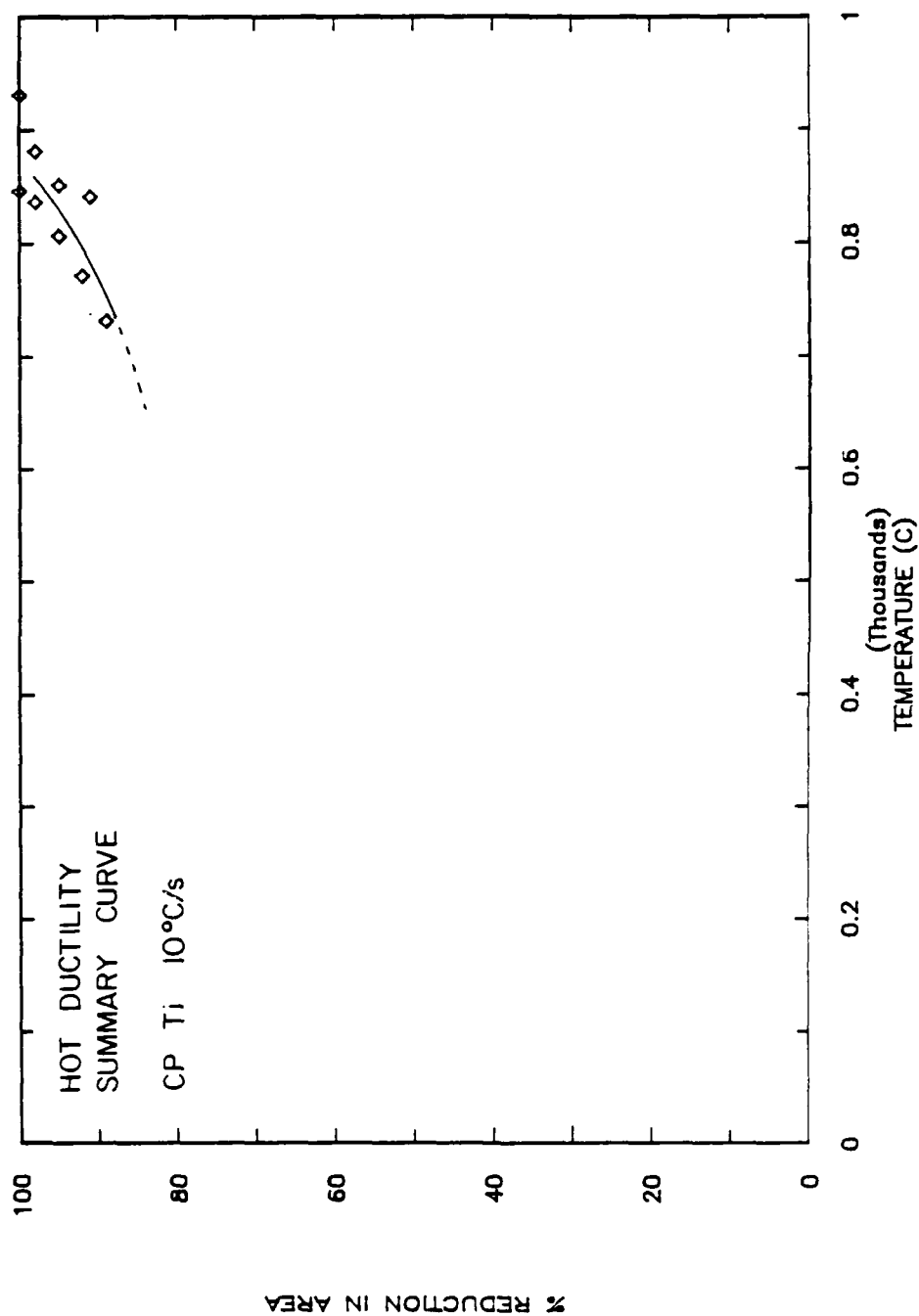


Figure 5.54 Ductility versus temperature for Grade 2 unalloyed titanium cooled at 10°C/s, showing essentially no ductility loss.

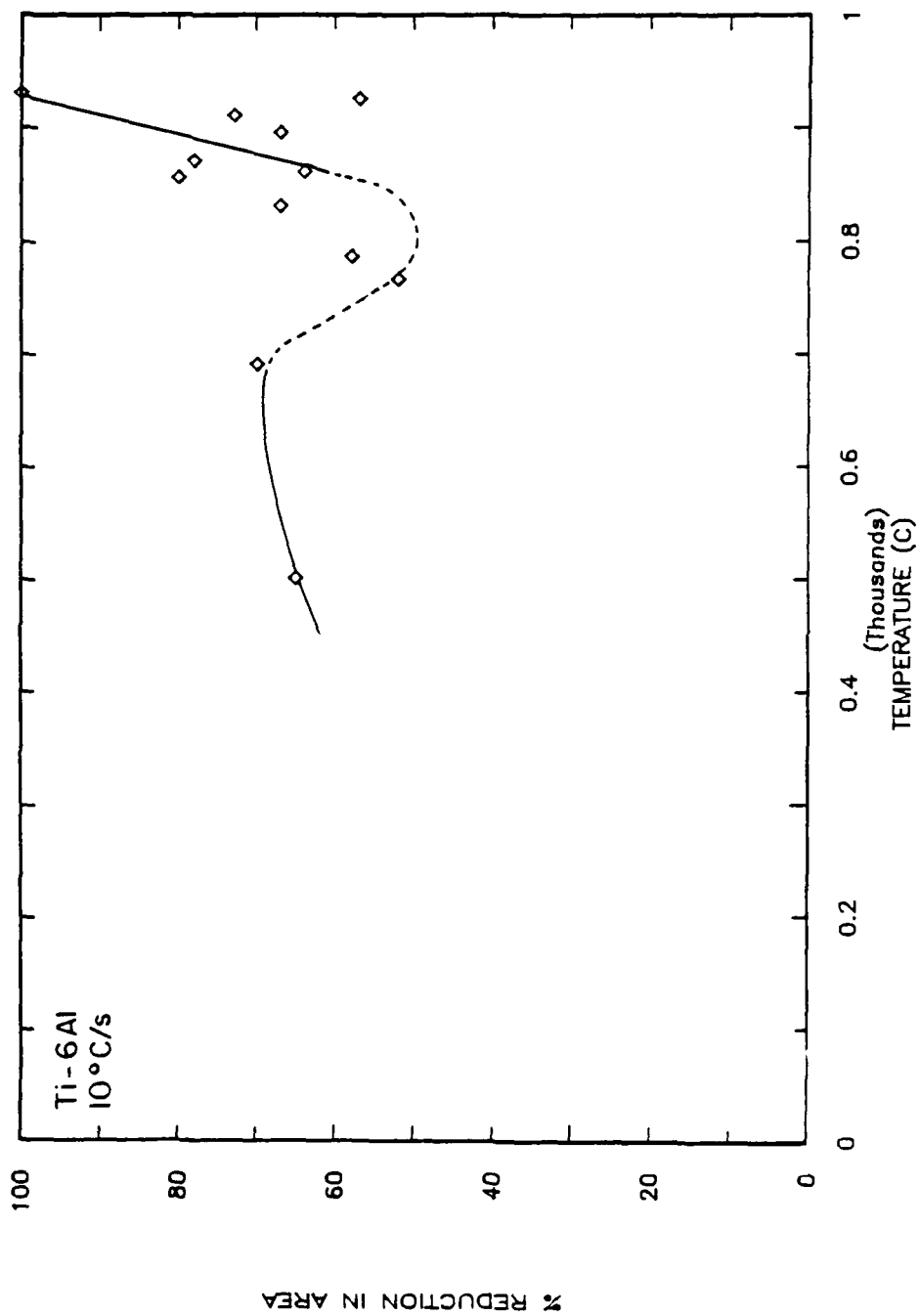


Figure 5.55 Ductility versus temperature for Ti-6Al cooled at 10°C/s, showing a moderate ductility loss.

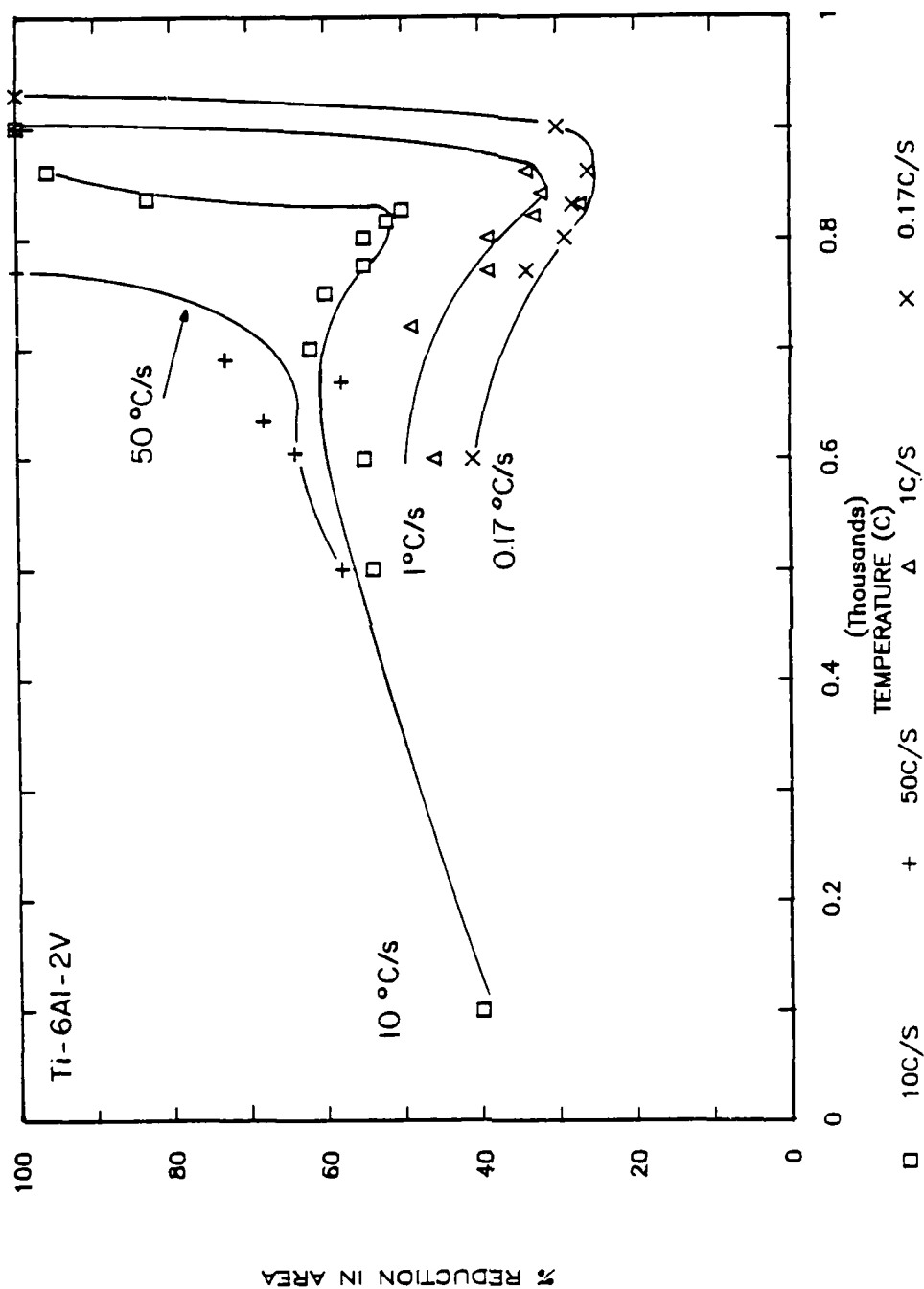


Figure 5.56 Ductility versus temperature curves for Ti-6Al-2V cooled at rates between 0.17°C/s and 50°C/s. Severity of the ductility loss decreases with increasing cooling rate.

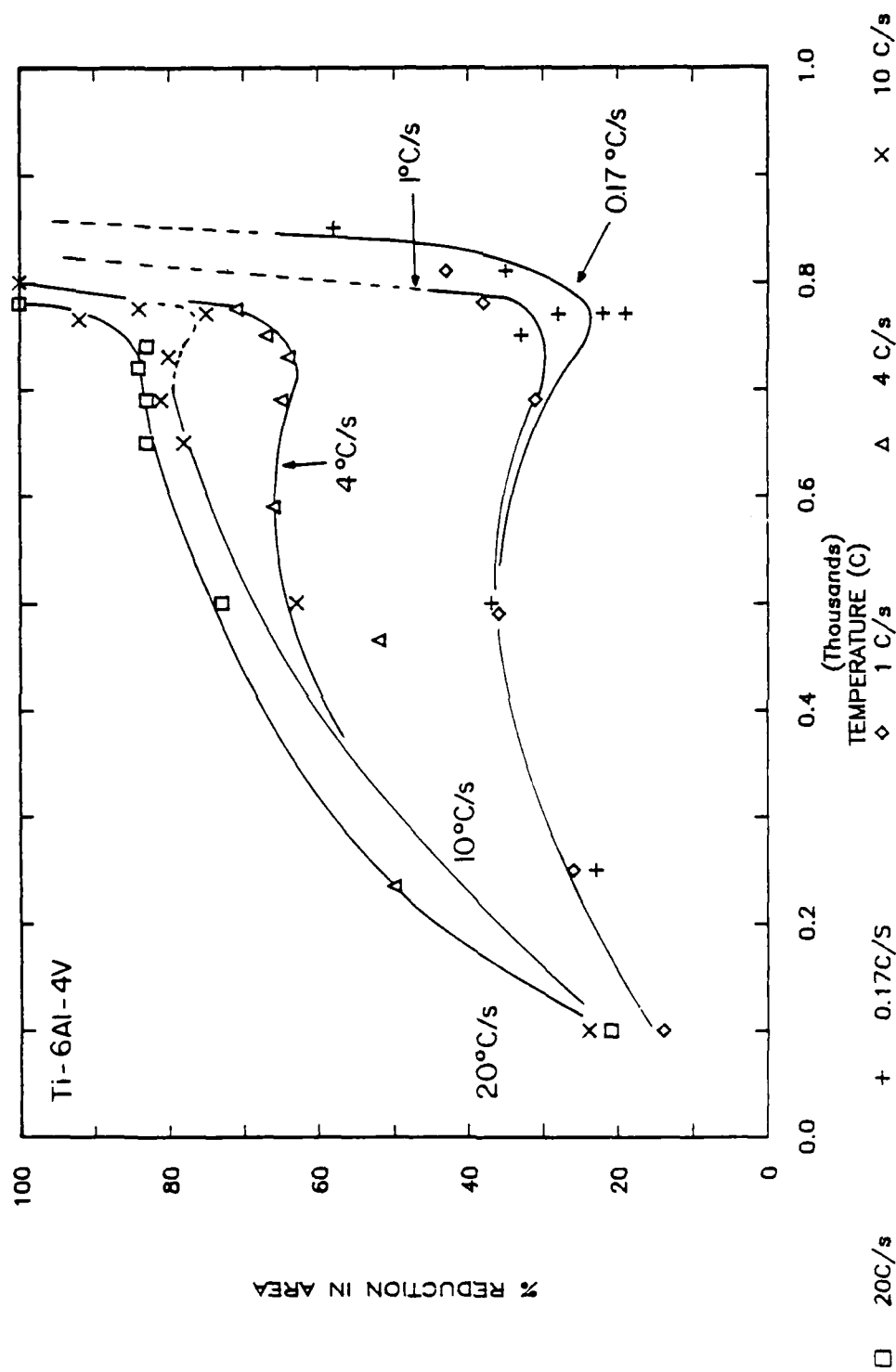


Figure 5.57 Ductility versus temperature curves for Ti-6Al-4V cooled at rates between 0.17°C/s and 20°C/s. Severity of the ductility loss decreases with increasing cooling rate.

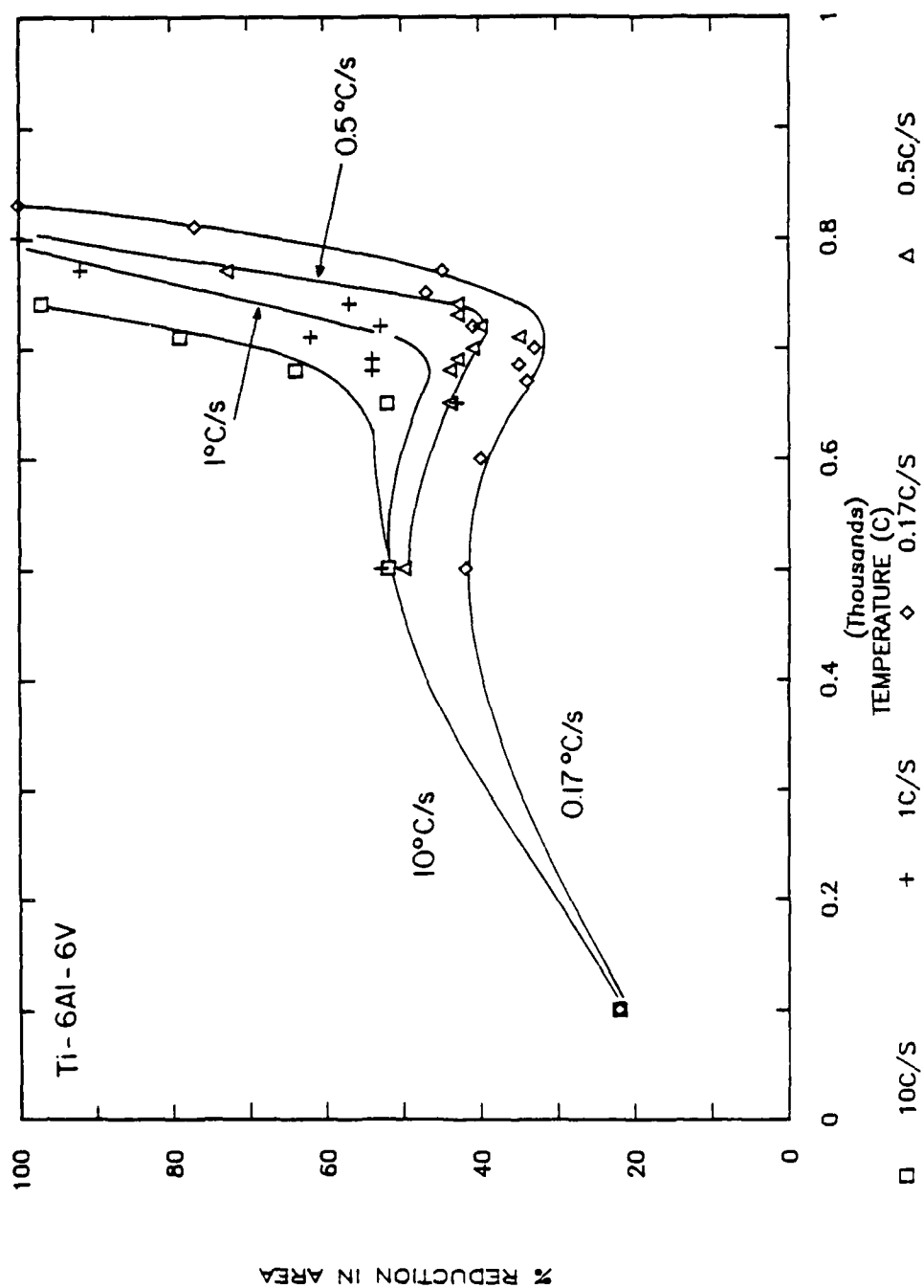


Figure 5.58 Ductility versus temperature curves for Ti-6Al-6V cooled at rates between 0.17°C/s and 10°C/s. Severity of the ductility loss decreases with increasing cooling rate.

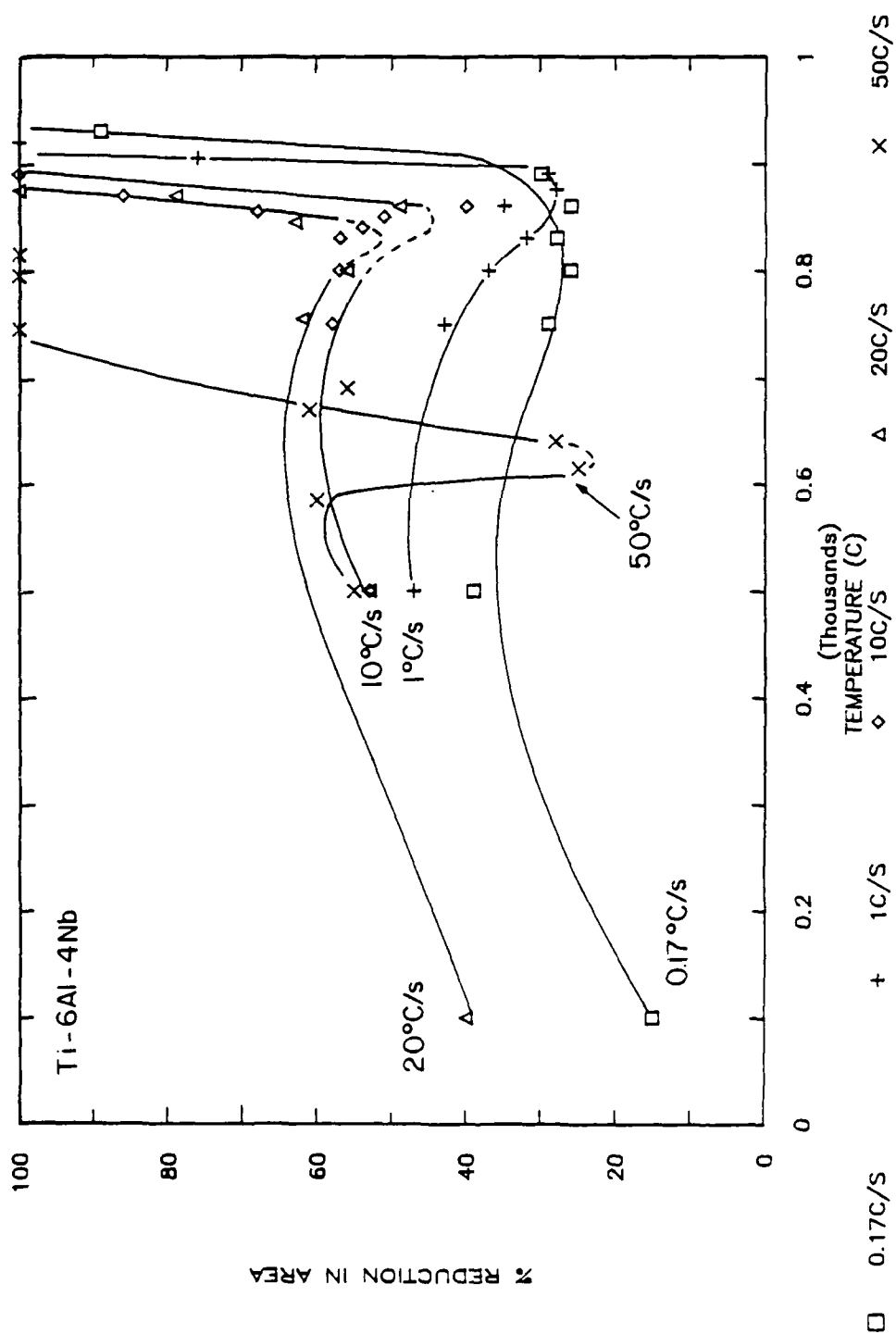


Figure 5.59 Ductility versus temperature curves for Ti-6Al-4Nb cooled at rates between 0.17°C/s and 50°C/s. Note severe loss of ductility in material cooled at 50°C/s.

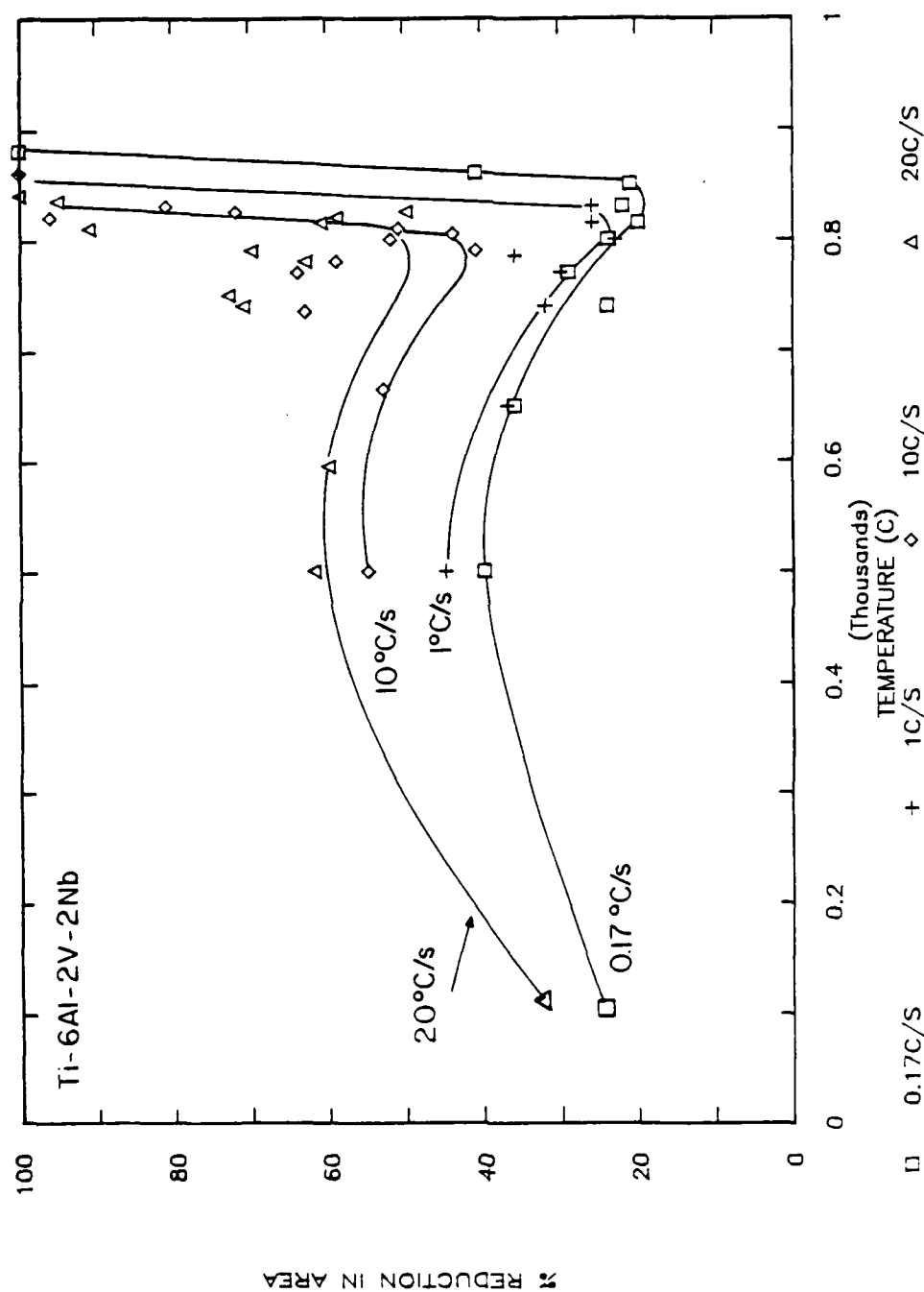


Figure 5.60 Ductility versus temperature curves for Ti-6Al-2V-2Nb cooled at rates between 0.17°C/s and 20°C/s. Ductility loss decreases with increasing cooling rate.

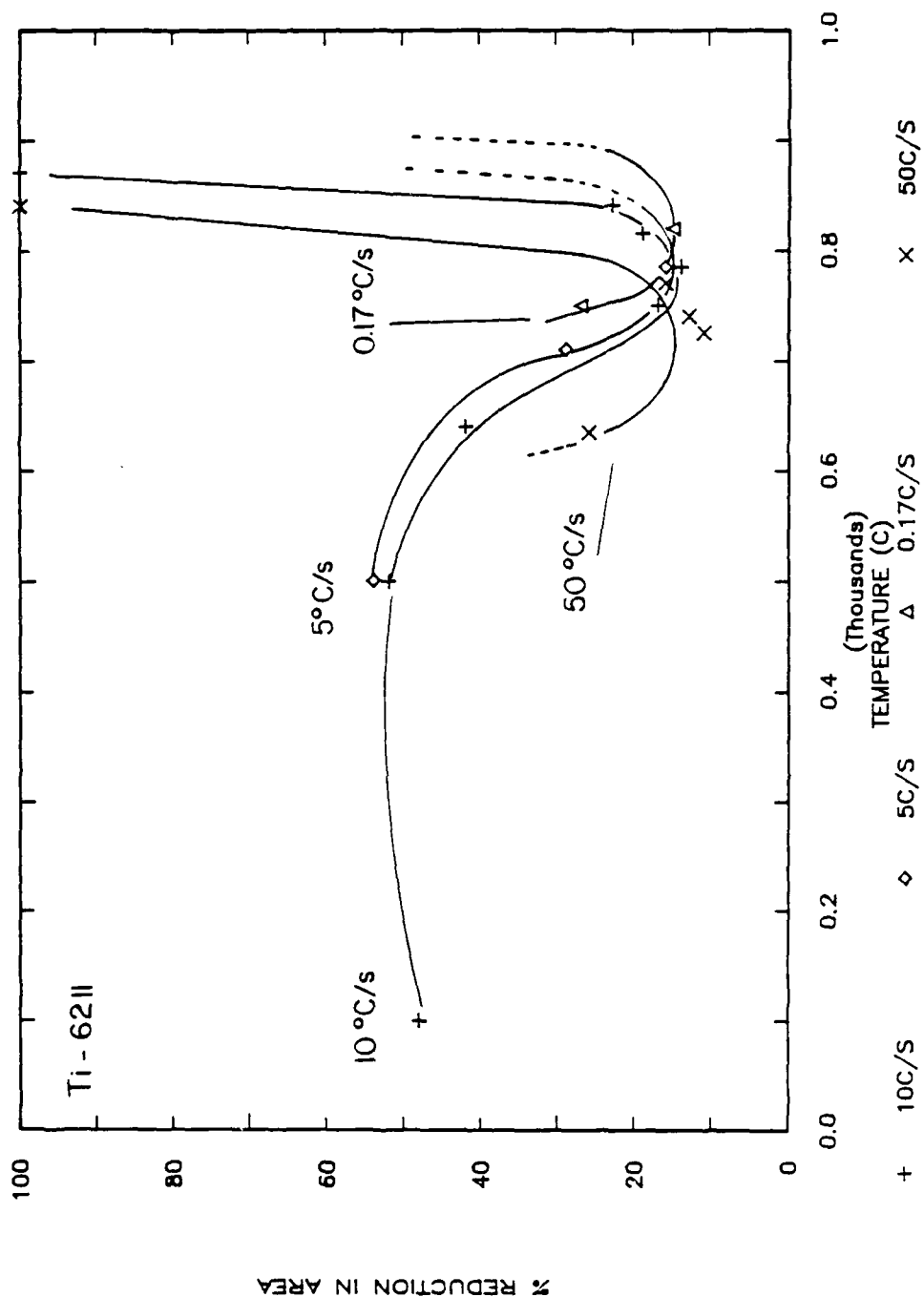


Figure 5.61 Ductility versus temperature curves for Ti-6211 cooled at rates between 0.17 °C/s and 50 °C/s. Note that the ductility loss is unaffected by changes in cooling rate.

tested show a definite loss of high temperature ductility at temperatures near the beta to alpha finish temperature. Superficially, this contradicts the results of earlier investigations (6, 59-66) which showed that the severity of the ductility loss varied significantly from alloy to alloy. The earlier investigations however, used either one thermal cycle or a group of thermal cycles which varied over a very narrow range. Figures 5.54-5.61 show that when the cooling rate is varied over a wide range, the behavior of all of the alloys tested is very similar. Thus, the high temperature ductility loss is a problem which may occur in any of these alloys when exposed to an appropriate thermal cycle.

A second aspect of the high temperature ductility loss is the irreversible nature of the loss. Earlier studies have demonstrated this behavior for Ti-6211 (6, 55). In this investigation, the irreversibility was found to occur to an equal extent in both Ti-6211 and Ti-6Al-4V. When the as-received Ti-6211 was tensile tested at 800°C on heating, it failed in a ductile manner with 75% reduction in area. When tested during a cool of 1°C/s following a 1200°C anneal, the failure was macroscopically brittle with only 31% reduction in area. In the case of Ti-6Al-4V, testing at 750°C during heating resulted in ductile failure with 78% reduction in area. However, testing during a cool of 1°C/s

again resulted in a macroscopically brittle failure with only 27% reduction in area. This is further evidence that the high temperature ductility loss occurs in all of these alloys.

A second result of the testing which is apparent upon examination of Figures 5.54-5.61 is that, with the exception of Ti-6211, the severity of the ductility loss for an individual alloy is a function of cooling rate. This further supports the conclusion that a major portion of the alloy dependence observed in earlier investigations was, in fact, the cooling rate dependence of the alloys tested. The cooling rate dependence is very similar for all of the alloys and the general trends can be easily seen in Figure 5.57, the plot of ductility versus temperature for Ti-6Al-4V. The severity of the ductility loss is greatest for the slowest cooling rate, in this case, 0.17°C/s . As the cooling rate is increased, the ductility loss is decreased, both in severity and in extent (in terms of temperature).

It must be noted that the relationship between ductility loss and cooling rate seen in Figure 5.57 is accentuated by a change in overall ductility with a change in cooling rate. This figure shows that, independent of the ductility loss, the overall ductility of the material is lowest at slow cooling rates and highest at high cooling

rates. This trend, which becomes apparent above 500°C, can also be seen in the corresponding figures for the other alloys. The severity of the ductility loss can be better illustrated when it is separated from the overall ductility effects. This was done by comparing the actual ductility versus temperature curve with a curve estimated to describe the behavior of the material in the absence of the ductility loss. The estimated curves were based on data from tests conducted during heating of the as-received material, normalized to the 500°C ductility measured on cooling, and published data where available (55, 59). This procedure, shown in Figure 5.62, results in the calculation of a quantity referred to as "net ductility loss". The actual minimum ductility value is referred to as "minimum hot ductility". Both quantities were calculated at the minimum ductility point of each ductility versus temperature curve, and both are expressed as percent reduction in area. These values, along with the corresponding reduction in area values, are listed in Table 5.8.

Figure 5.63 shows a plot of minimum hot ductility versus cooling rate for the alloys tested, and Figure 5.64 is the corresponding plot of net ductility loss versus temperature. First examining Figure 5.63, the trend of minimum hot ductility increasing with increasing cooling

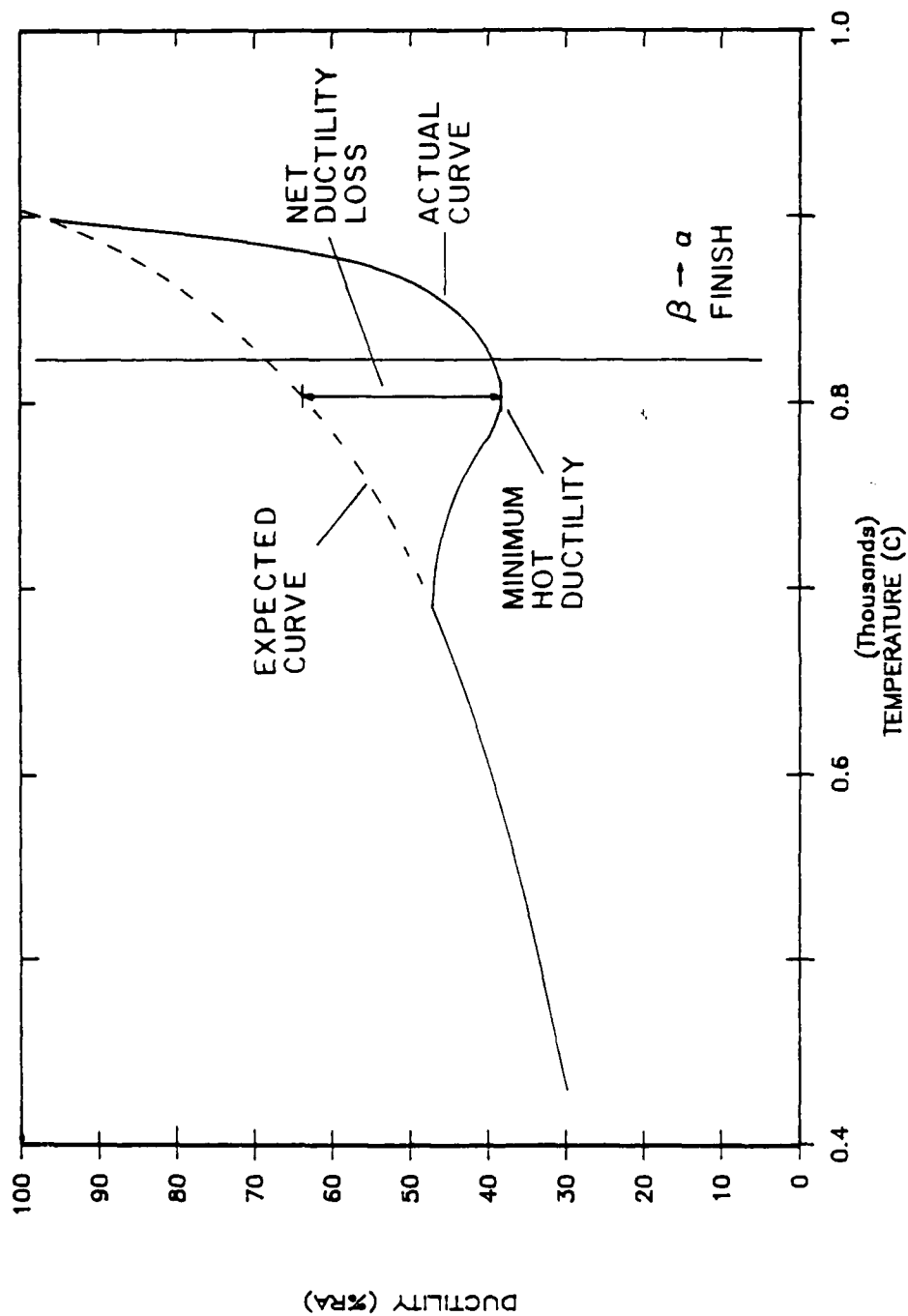


Figure 5.62 Schematic diagram of ductility versus temperature illustrating the quantities "minimum hot ductility" and "net ductility loss".

Table 5.8

Minimum High Temperature Ductility and Net Ductility Loss
for Alloys Tested at Several Cooling Rates

Alloy	Cooling Rate (°C/s)	Minimum Hot Ductility (%)	Net Ductility Loss (%)
Ti-6Al-2V	0.17	25	37
	5	40	32
	10	50	21
	(1)	49	-
	(2)	46	-
	(3)	49	-
	20	67	-
	50	75	8
Ti-6Al-4V	0.17	26	40
	1	35	29
	5	67	29
	10	82	12
	20	95	9
Ti-6Al-6V	0.17	33	27
	0.5	40	23
	1	47	18
	2	50	-
	5	50	-
	10	54	8
Ti-6Al-4Nb	0.17	26	48
	5	32	42
	10	45	39
	20	54	31
	50	26	34
Ti-6Al-2V-2Nb	0.1	19	45
	1	33	45
	10	49	32
	20	55	36

Table 5.8 (cont.)

Alloy	Cooling Rate (°C/S)	Minimum Hot Ductility (%)	Net Ductility Loss (%)
Ti-6211	0.17	16	65
	5	17	67
	10	16	60
	50	16	63
Ti-6211 (1)	0.17	24	60
	(1) 4	32	56
	(1) 10	24	60
	(1) 20	30	57

(1) beta anneal of 5 minutes/1100°C

(2) beta anneal of 5 minutes/1300°C

(3) beta anneal of 10 minutes/1300°C

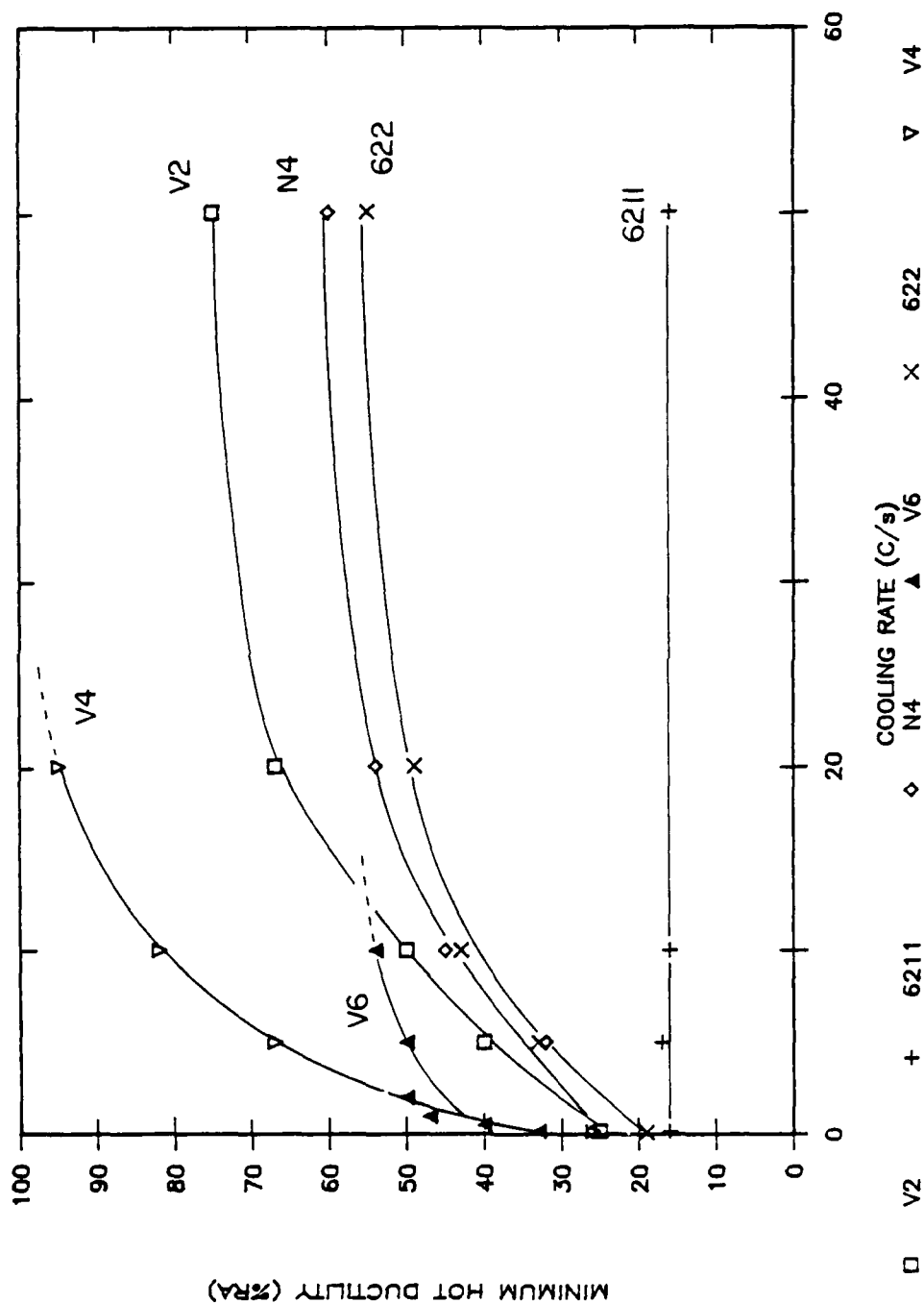


Figure 5.63 Minimum hot ductility versus cooling rate for all alloys tested, showing increasing ductility with increasing cooling rate.

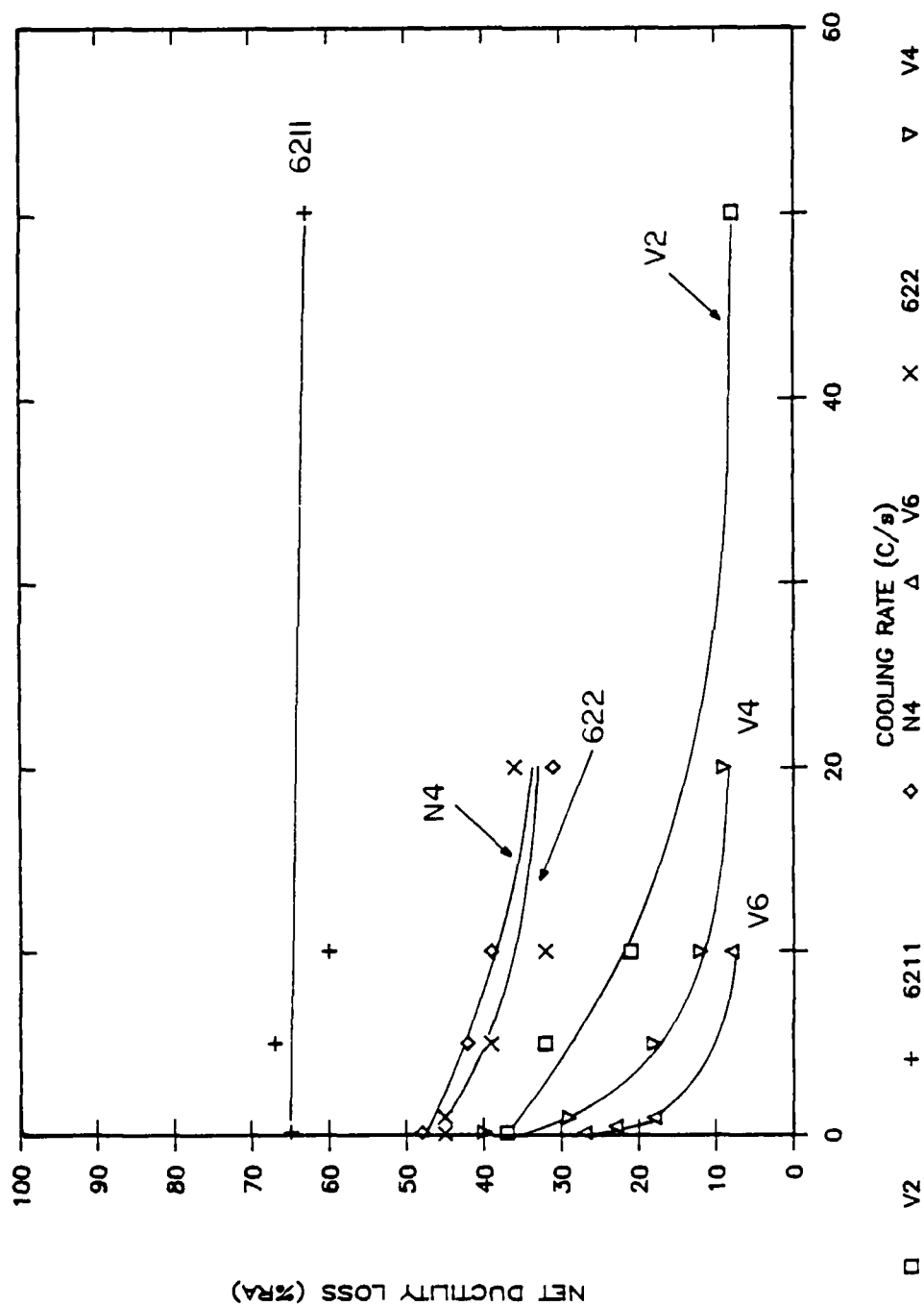


Figure 5.64 Net ductility loss versus cooling rate for all alloys tested, showing decreasing ductility loss with increasing cooling rate.

rate can be seen for all of the alloys except Ti-6211. This figure shows that the minimum hot ductility of Ti-6211 is uniformly less than that of the other alloys and not affected by cooling rate over the range tested. The minimum hot ductility values for the vanadium alloys, particularly Ti-6Al-4V, are the highest and most susceptible to cooling rate changes. The behavior of Ti-6Al-2V-2Nb and Ti-6Al-4Nb is between that of the vanadium alloys and Ti-6211.

The same behavior is seen in Figure 5.64, the plot of net ductility loss versus cooling for all of the alloys tested. The vanadium alloys have the least net ductility loss, Ti-6211 the greatest, and Ti-6Al-2V-2Nb and Ti-6Al-4Nb, intermediate values. Also, the net ductility loss is strongly affected by cooling rate in the vanadium alloys, affected moderately in Ti-6Al-2V-2Nb and Ti-6Al-4Nb, and essentially unaffected in Ti-6211. Additional observations can be made based on Figure 5.64. This figure suggests that, as the cooling rate is increased, net ductility loss of each alloy decreases to a minimum level which then remains constant as the cooling rate is further increased. For the vanadium alloys, this minimum level is 5-10%, and for Ti-6Al-2V-2Nb and Ti-6Al-4Nb, 30-40%. One possible interpretation of the data for Ti-6211 is that all of the testing was performed in the range where the net ductility

loss of Ti-6211 has already reached its minimum value. However, because the testing was carried out at cooling rates slow enough to approximate equilibrium conditions, this is unlikely. The possibility does exist, however, that the cooling rates used were not high enough to highlight any cooling rate dependence in Ti-6211.

The data shown in Figure 5.64, particularly that for the vanadium alloys, supports the idea that the high temperature ductility loss is connected with the beta to alpha transformation. The effects of vanadium additions on the kinetics of the transformation and the transformed microstructures have been discussed earlier. In general, the addition of vanadium will move the CCT curve for these alloys down in temperature and to the right, to longer times. Therefore, for the transformation to proceed in roughly equivalent fashion for alloys with 2, 4, and 6% vanadium, a slow cooling rate would be required for the 6V alloy, a moderate rate for the 4V alloy, and a high rate for the 2V alloy. The data in Figure 5.64 shows exactly this relationship. At a net ductility loss of approximately 20%, Ti-6Al-6V was cooled at 1°C/s , Ti-6Al-4V at 5°C/s , and Ti-6Al-2V at 10°C/s . The same relationship is shown at approximately 8% net ductility loss, where the cooling rates are 10°C/s , 20°C/s , and 50°C/s .

An additional observation that can be made on the basis of Figures 5.63 and 5.64 is that the hot ductility behavior of these alloys cannot be linked to level of beta stabilization. Among the heavily stabilized alloys, Ti-6Al-6V has a small ductility loss susceptibility and Ti-6Al-2V-2Nb a moderate susceptibility. Viewed as groups, the moderately stabilized alloys, Ti-6Al-4V and Ti-6211, and the lean alloys, Ti-6Al-2V, Ti-6Al-4Nb, both contain alloys which have widely varying hot ductility loss behavior as well.

The ultimate tensile strength of the material was also measured in each hot ductility test. Figures 5.65-5.72 are plots of ultimate tensile strength versus temperature for all of the alloys tested. Again, each figure contains data for several cooling rates, all tested at an effective strain rate of 1.5 s^{-1} . As was the case with the ductility measurements, the mechanical behavior of all of the alloys tested is fairly similar. The trends shown in all the alloys are well illustrated by the plot for Ti-6Al-2V-2Nb, Figure 5.71. As the test temperature is decreased through the beta to alpha transformation, the ultimate tensile strength of the material increases rapidly. The curve then goes through an inflection point at a temperature near the transformation finish and increases more slowly with

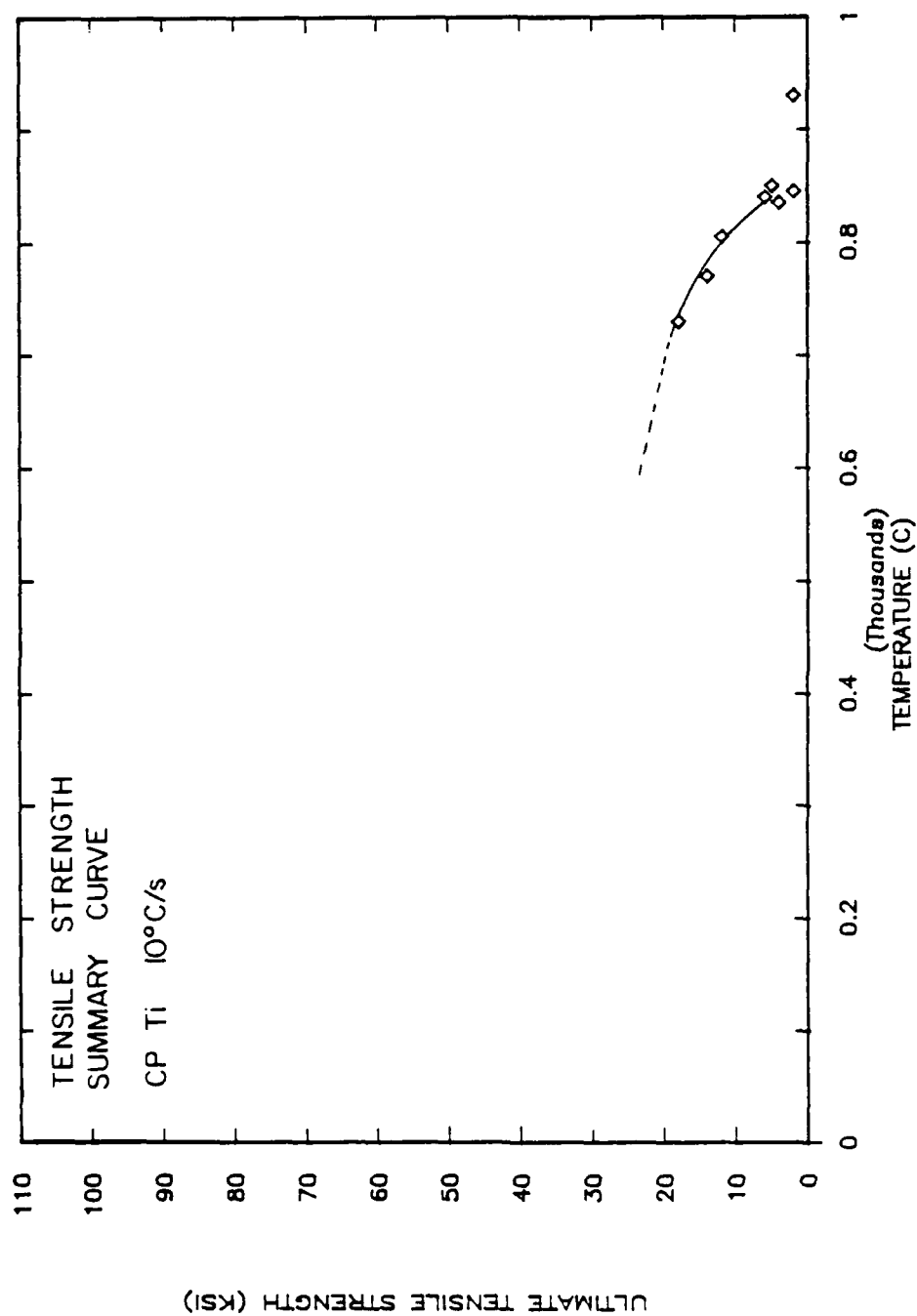


Figure 5.65 Ultimate tensile strength (UTS) versus temperature for Grade 2 unalloyed titanium cooled at 10°C/s.

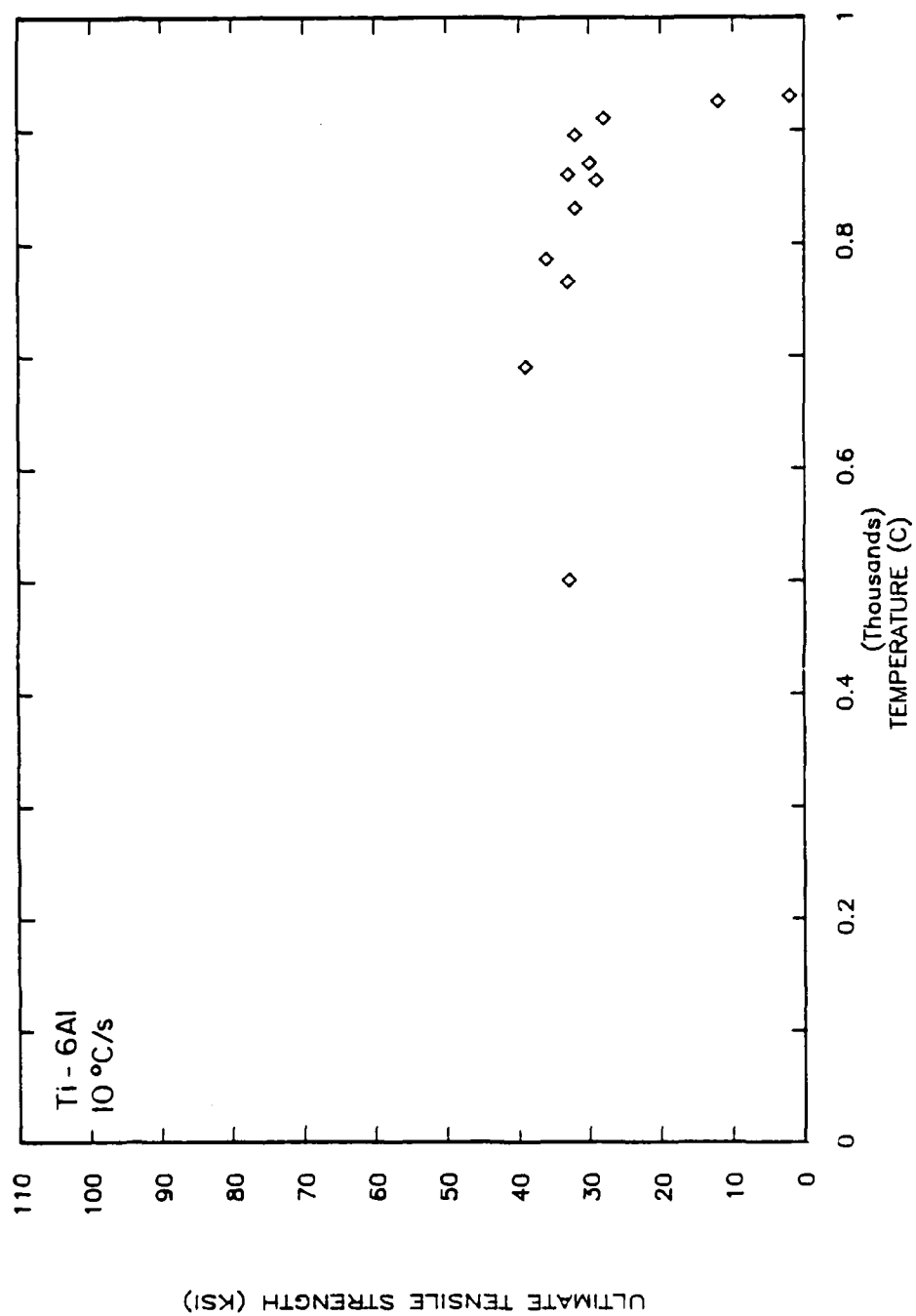


Figure 5.66 UTS versus temperature for Ti-6Al showing rapid increase in strength during the beta to alpha transformation and much slower increase below the transformation.

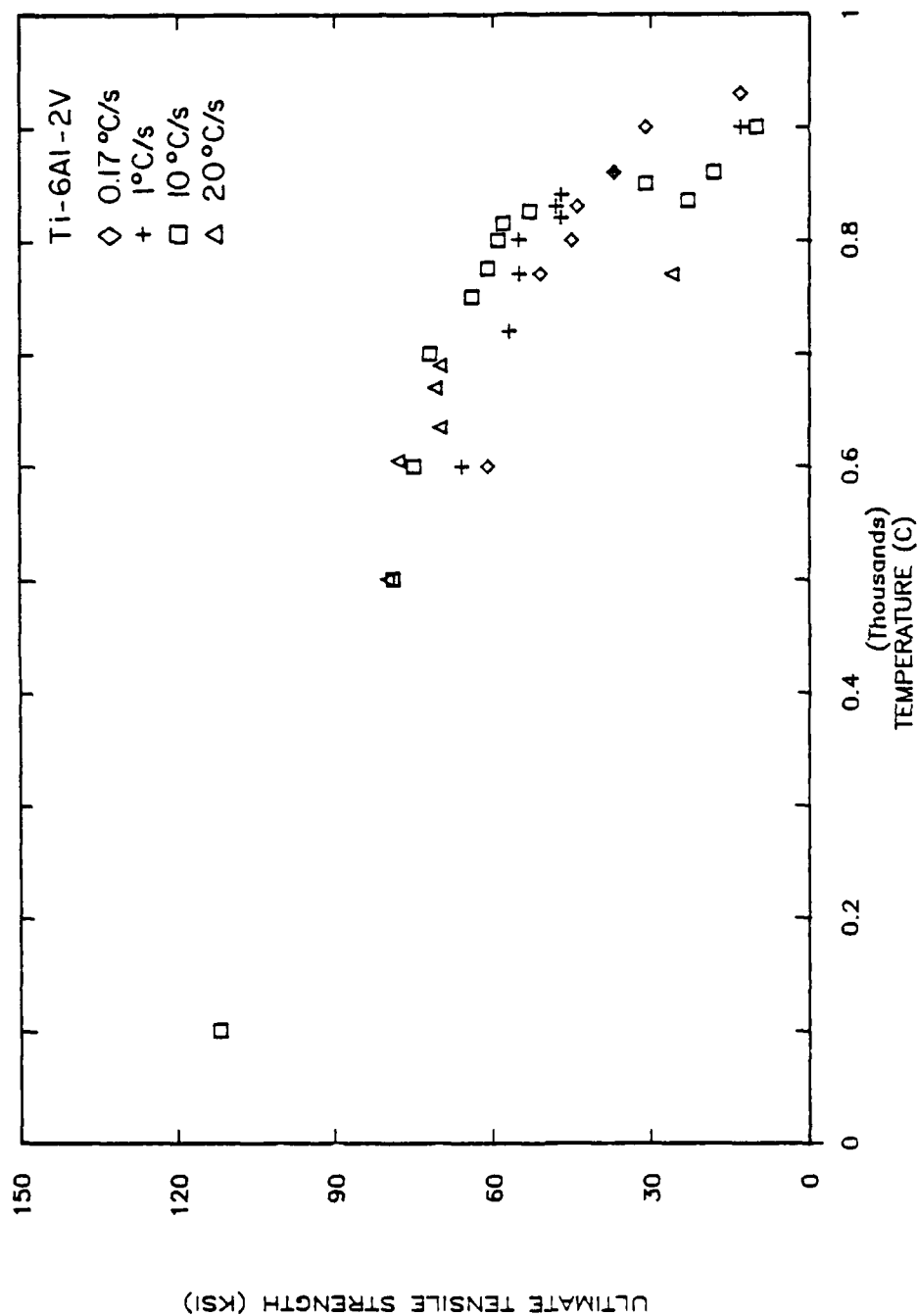


Figure 5.67 UTS versus temperature for Ti-6Al-2V, cooled at several different rates. Strength increases rapidly during the beta to alpha transformation.

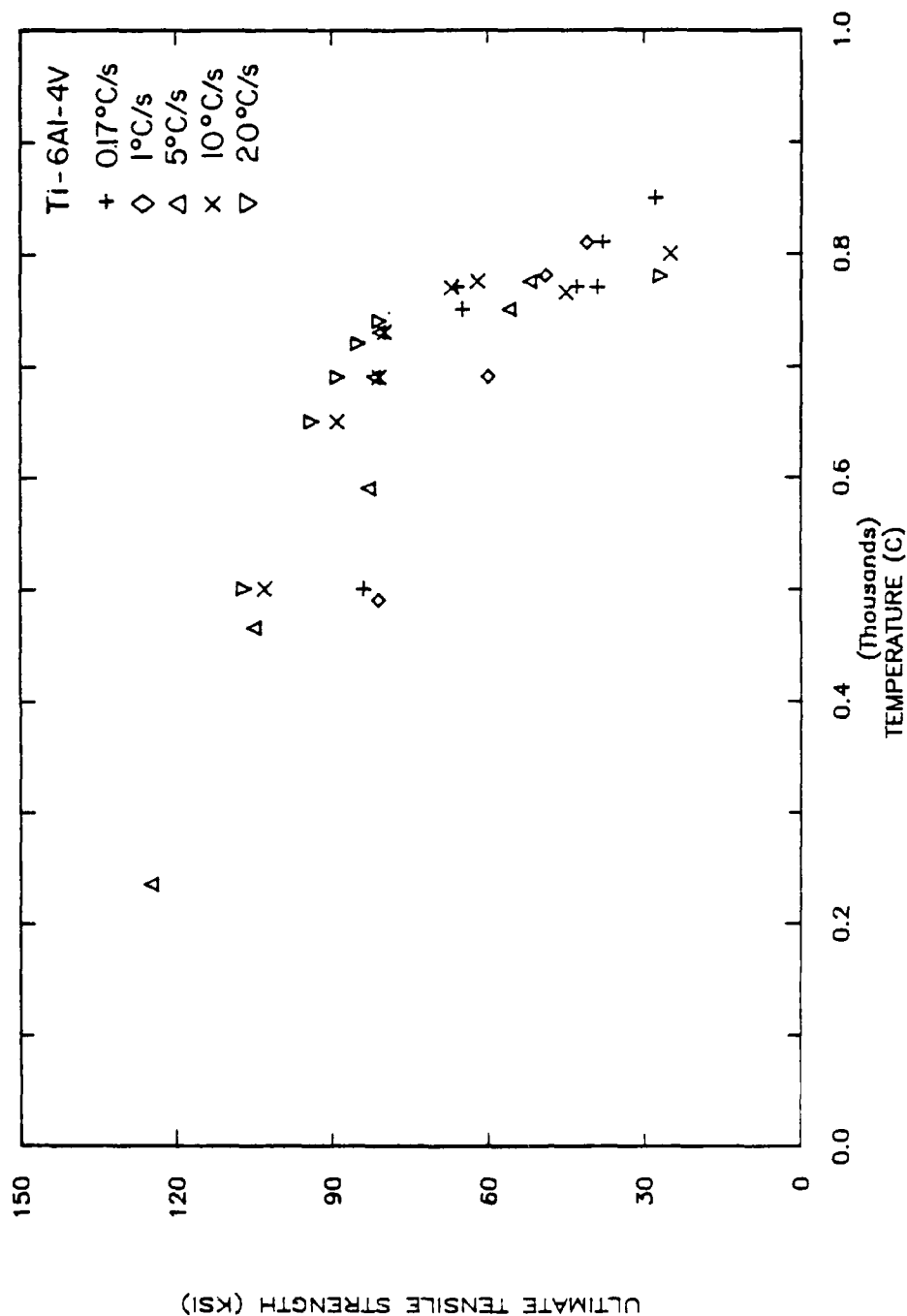


Figure 5.68 UTS versus temperature for Ti-6Al-4V, cooled at several different rates. Strength increases rapidly during the beta to alpha transformation.

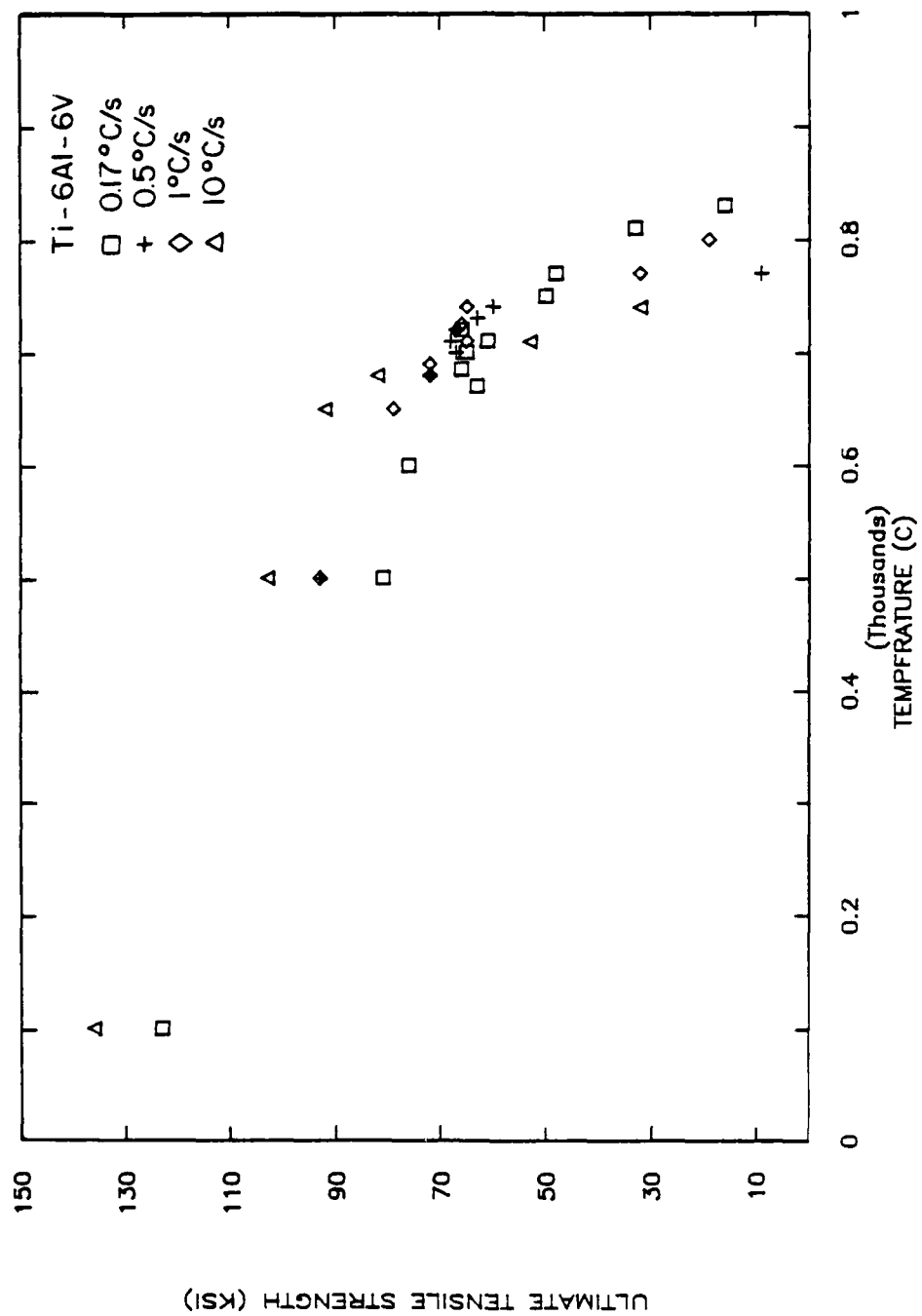


Figure 5.69 UTS versus temperature for Ti-6Al-6V, cooled at several different rates. Strength increases rapidly during the beta to alpha transformation.

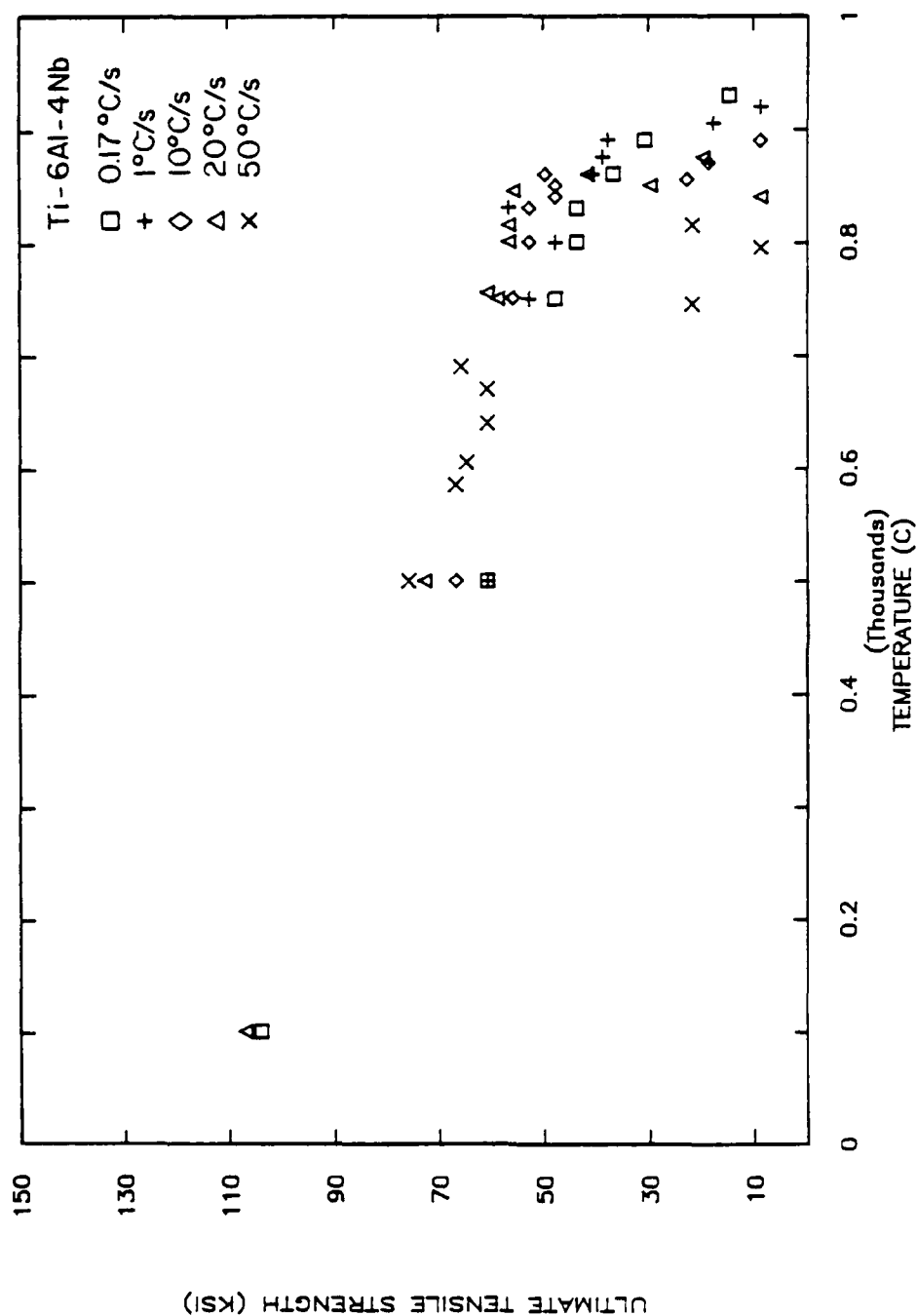


Figure 5.70 UTS versus temperature for Ti-6Al-4Nb, cooled at several different rates. Note relatively low overall strength and very rapid increase during the transformation.

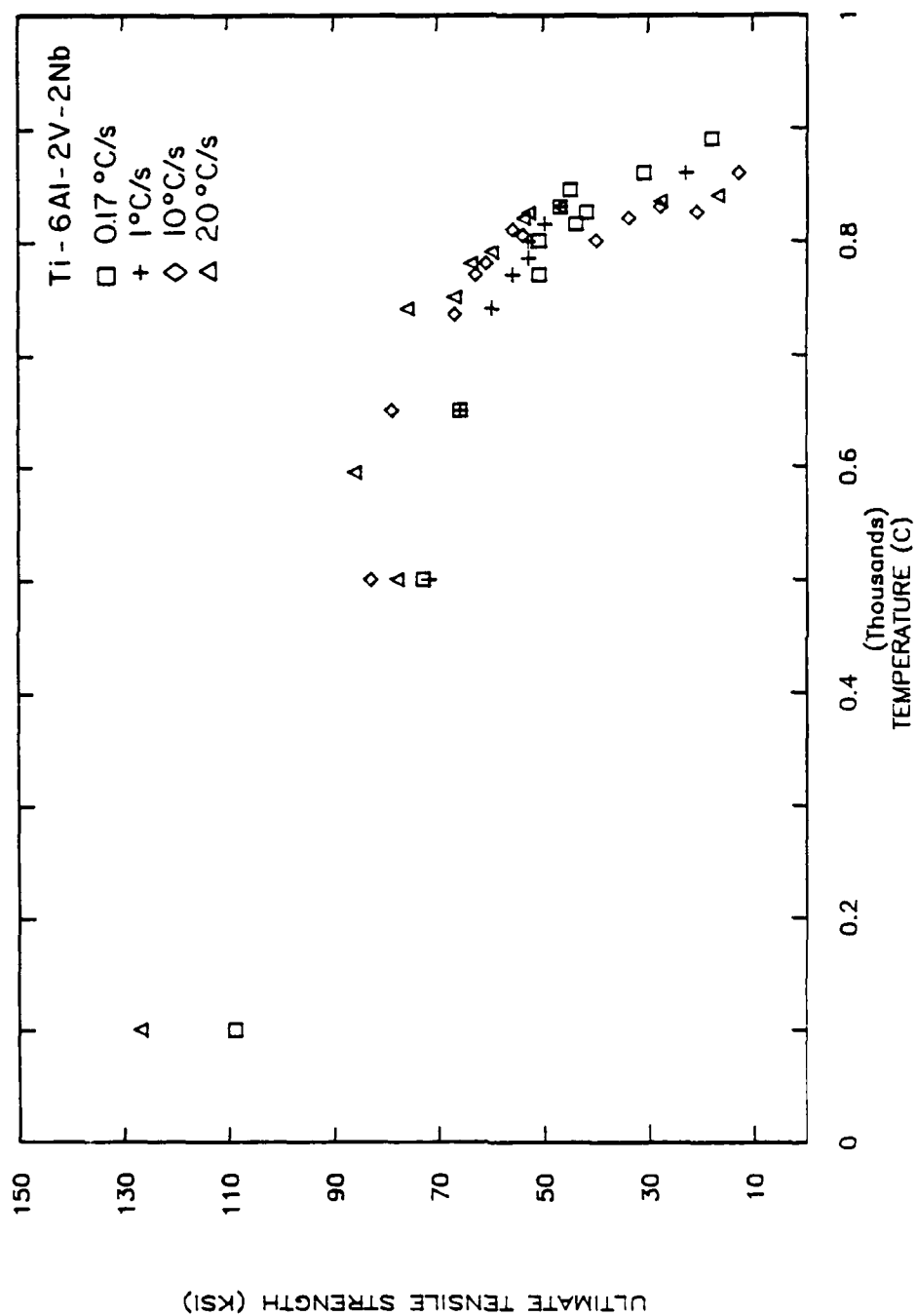


Figure 5.71 UTS versus temperature for Ti-6Al-2V-2Nb, cooled at several different rates. Strength increases rapidly during the beta to alpha transformation.

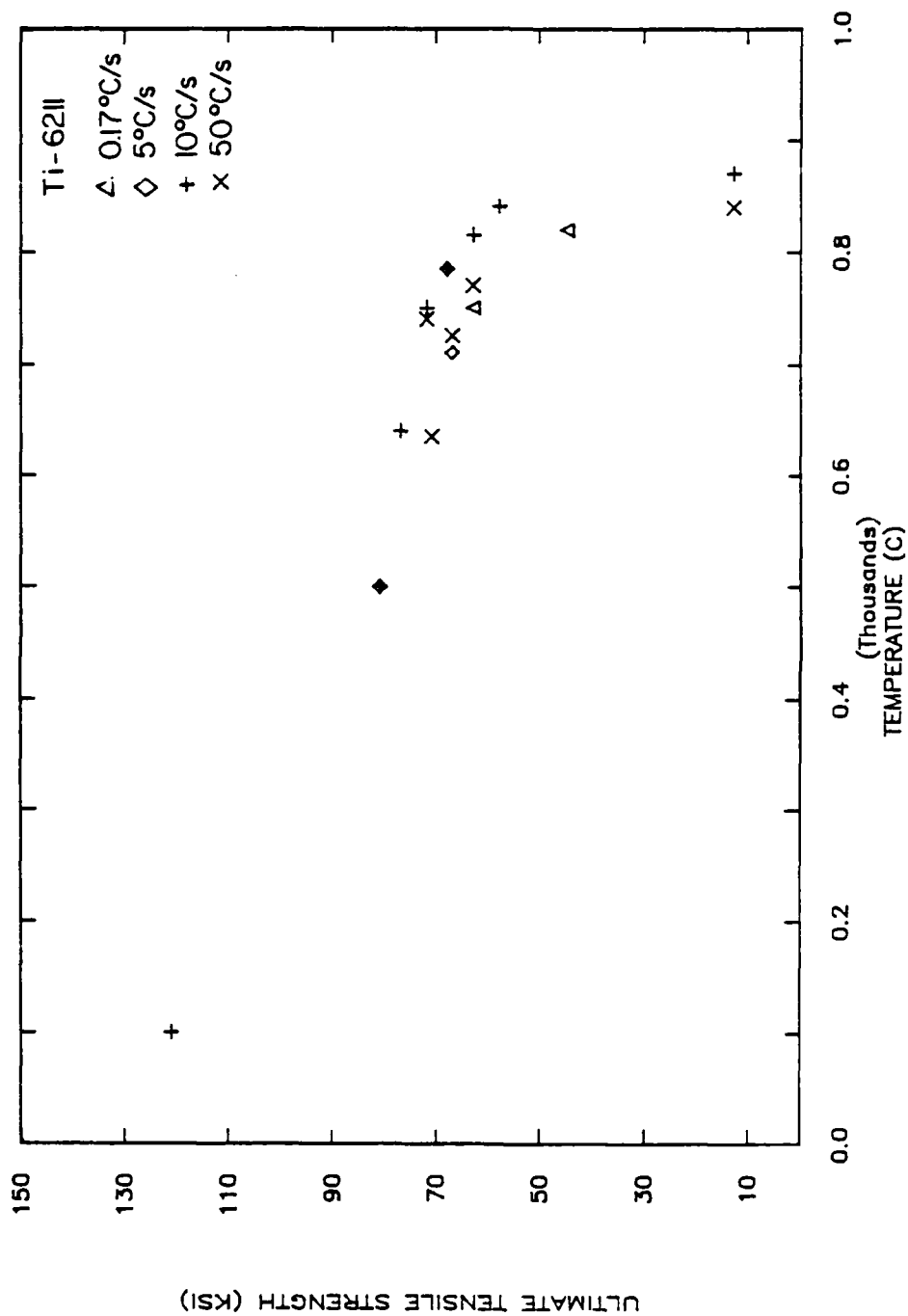


Figure 5.72 UTS versus temperature for Ti-62II, cooled at several different rates. Note very rapid strength increase during the transformation.

decreasing test temperature. This agrees with the results of others (6) which indicate that ultimate tensile strength is a strong function of the amounts of the phases being tested, but the strength of the stable two-phase transformed microstructure is not strongly temperature dependent.

Two other general observations can be made based on the data shown in Figure 5.65-5.72 and easily seen in Figure 5.71. The first observation is that the slope of the curve within the transformation, hence the strength of the transformed material, increases with increasing cooling rate. This is consistent with the previously discussed microstructural refinement associated with rapid cooling rates. The second observation is that below the transformation, the curves are roughly parallel. Thus, the ultimate tensile strength of the transformed material varies with cooling rate but the temperature dependence of the ultimate tensile strength does not. These observations are further illustrated by Figure 5.73, a plot of ultimate tensile strength versus temperature for all the alloys tested at 10°C/s . In all cases, the strength level at any temperature seems to be controlled by the strength level at the beta to alpha finish.

The curves for the three Ti-6Al-V ternary alloys show additional interesting trends. Figure 5.73 shows that in

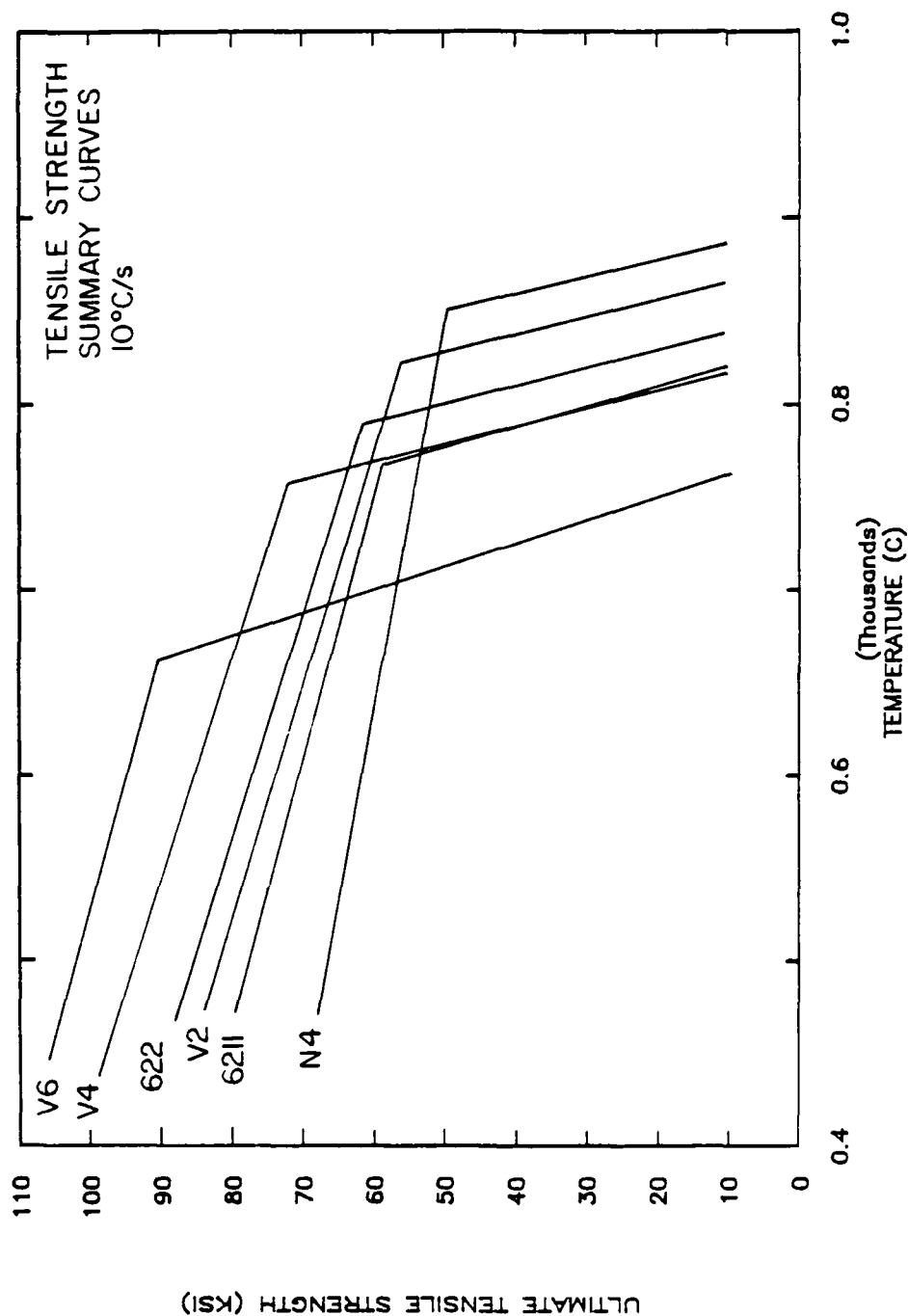


Figure 5.73 UTS versus temperature summary curves for all alloys tested, cooled at 10°C/s, showing relative strengths of the various alloys.

the case of these alloys, both portions of the curves are essentially parallel. The strength level is determined by the extent to which the portion of the curve within the transformation continues. This portion of the curve is far more extensive in the case of Ti-6Al-6V than Ti-6Al-4V or Ti-6Al-2V. This suggests that the transformation occurs over a larger temperature range for Ti-6Al-6V than for Ti-6Al-4V or Ti-6Al-2V, a result which contradicts the results of the dilatometry associated with the CCT diagram development. This is particularly interesting because one apparent shortcoming of the previously discussed transformation kinetics model was that it did predict a "spreading out" of the transformation with increasing beta stabilizer content.

An additional trend which can be observed in Figure 5.73 is that the strength of the alloys increases with increasing beta stabilization. This effect is somewhat isolated in Figure 5.74, a plot of strength versus temperature for Ti-6Al-2V, Ti-6Al-4V, and Ti-6Al-6V, cooled at 10°C/s , 5°C/s , and 1°C/s , respectively. These cooling rates were chosen to create transformed microstructures which were approximately equivalent in terms of refinement, differing only in level of beta stabilization. Comparison of the curves in Figure 5.74 with the corresponding curves

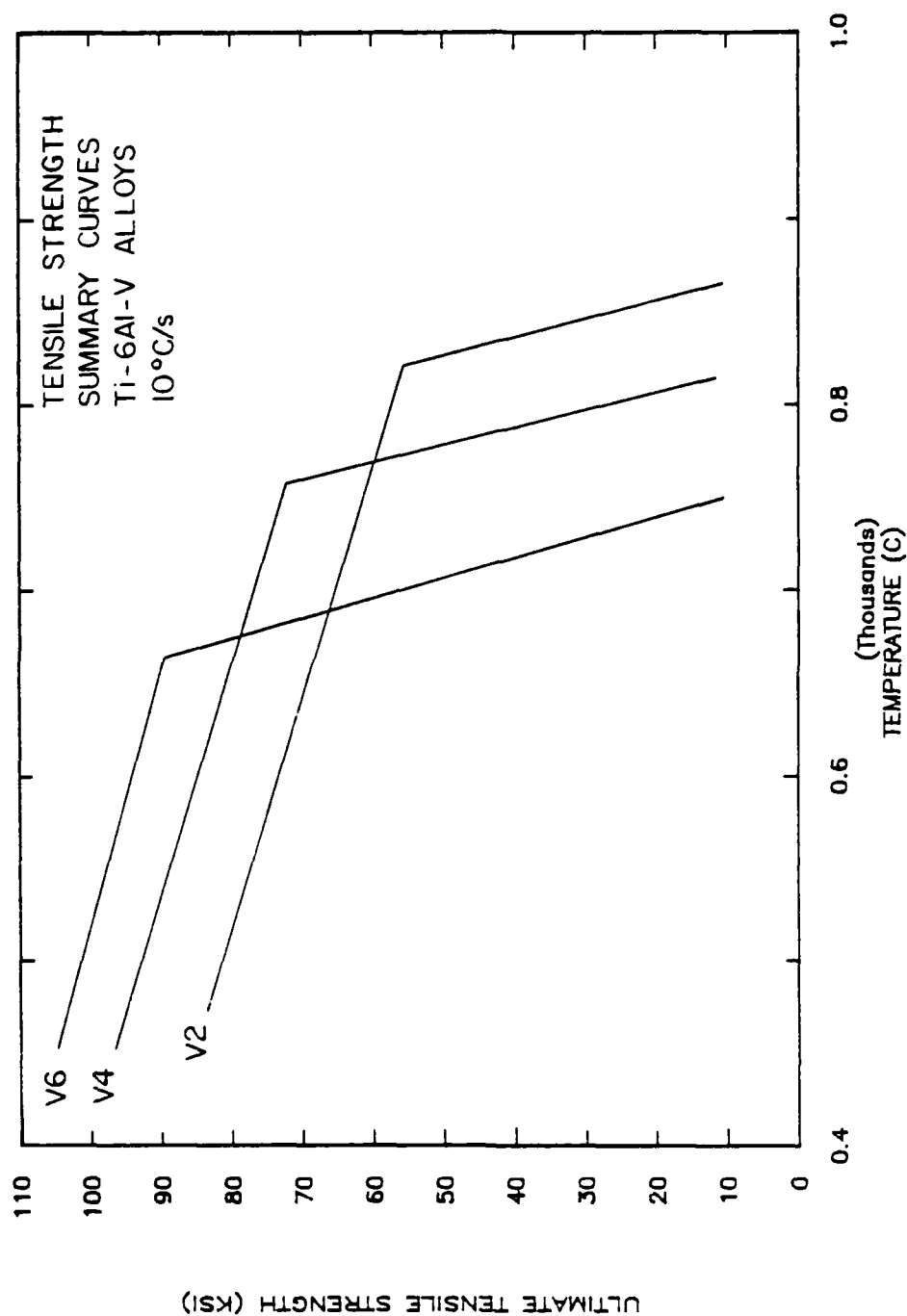


Figure 5.74 UTS versus temperature summary curves for vanadium containing alloys cooled at rates chosen to produce microstructural similarity. Strength differences are due to different levels of beta stabilization.

in Figure 5.73 (where a constant cooling rate of 10°C/s was used), shows that the two sets of curves differ only slightly in position. Thus, it is the level of beta stabilization that is dominating the relative positioning of the three curves for the vanadium alloys, not the effect of changes in transformed microstructure. This suggests that the strength of the alloys tested, Figure 5.73, is controlled primarily by their beta stabilization and only secondarily by their transformed microstructure.

It has been shown that all of the alloys tested in this study are susceptible to the ductility loss. This susceptibility varies with alloy content, but not to as great an extent as has been previously reported. A far greater effect was that of cooling rate, with ductility being the lowest and ductility loss the greatest when slow cooling rates are used. These results suggest that a significant portion of the reported differences between the behavior of different alloys is actually due to the cooling rate dependence of the individual alloys tested. However, overall ductility and the severity of the ductility loss does vary from alloy to alloy with the vanadium alloys being the least susceptible to the ductility loss and Ti-6211 being the most susceptible. In contrast to the ductility behavior, it was found that the ultimate tensile strength of

the alloys tested was controlled by level of beta stabilization and only secondarily by cooling rate.

5.3.2 Lattice Incompatibility

To test the validity of the lattice incompatibility model, the results of the hot ductility testing were compared with the results of the lattice incompatibility measurements and calculations. This comparison can be made by combining the results given in Tables 5.6, 5.7, and 5.8, with those shown in Figures 5.63 and 5.64. As was discussed earlier, lattice incompatibility was calculated in two ways. The first method of calculating lattice incompatibility was based on the assumption of transformation stress being developed only during formation of the grain boundary alpha film. These values are referred to as "beta to alpha lattice incompatibility" or " Δ_α " and are listed in Table 5.6. Based on this lattice incompatibility, it was found that the alloys tested could be ranked in order of decreasing lattice incompatibility as follows: Ti-6Al-4Nb, Ti-6Al-2V, Ti-6211, followed by Ti-6Al-2V-2Nb, Ti-6Al-6V and Ti-6Al-4V, all at zero incompatibility. In Figures 5.75 and 5.76, the lattice incompatibility of these alloys is plotted against minimum high temperature ductility and net ductility loss, respectively. These figures show that no correlation can be made between lattice incompatibility calculated in

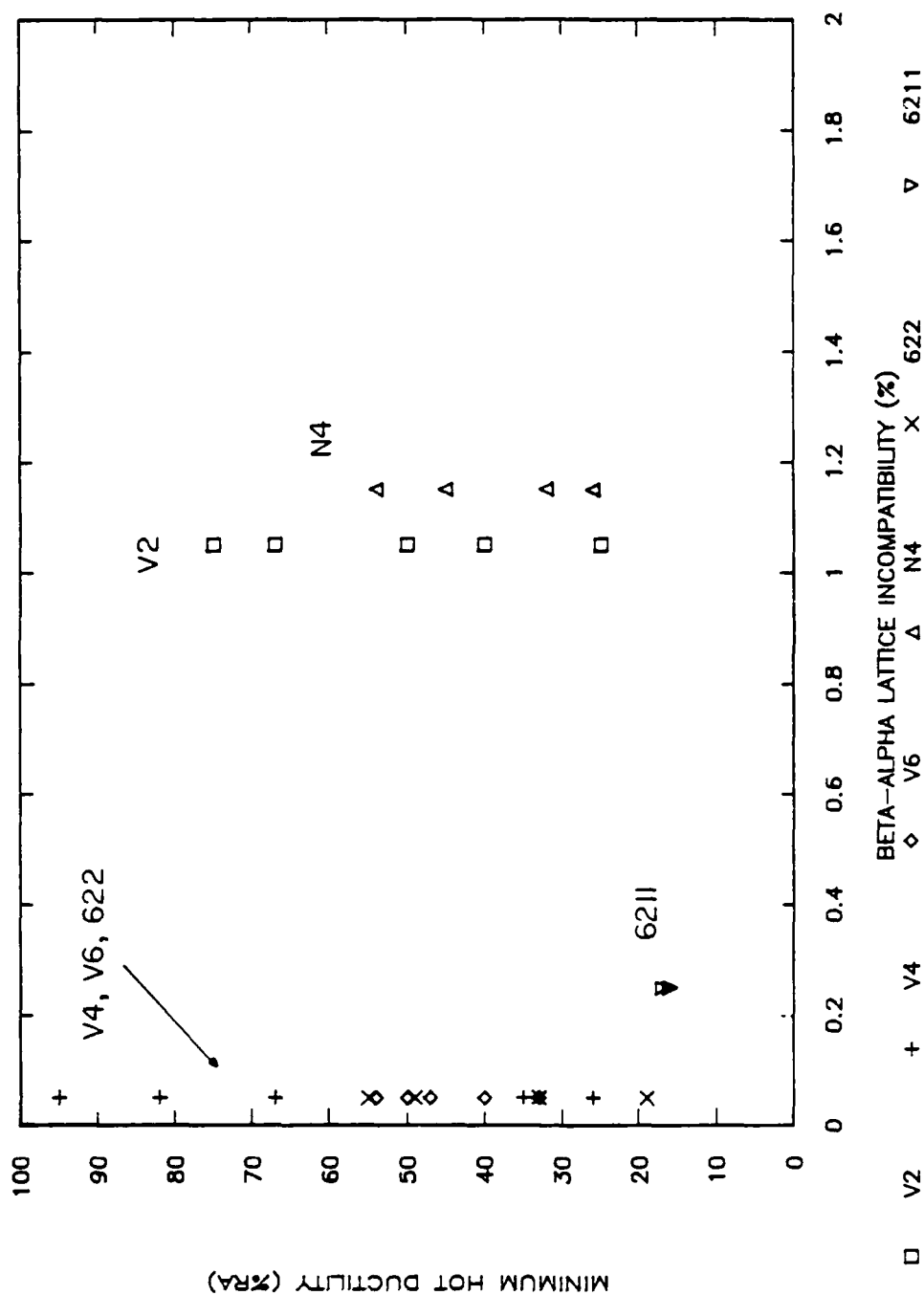


Figure 5.75 Minimum hot ductility versus beta to alpha lattice incompatibility for all alloys tested, showing lack of correlation, between the two parameters.

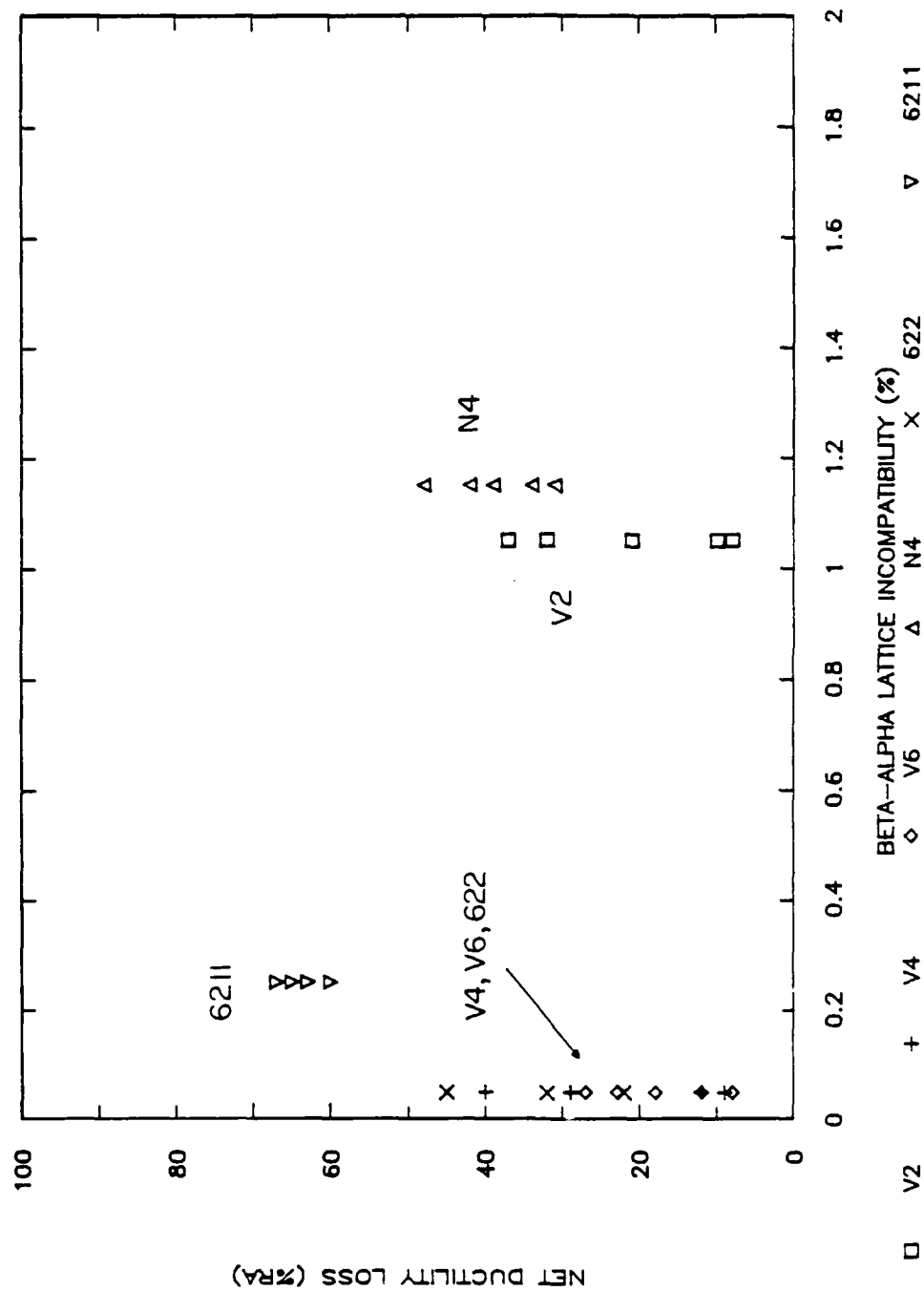


Figure 5.76 Net ductility loss versus beta to alpha lattice incompatibility for all alloys tested, showing lack of correlation between the two parameters.

this manner and either minimum hot ductility or net ductility loss.

The second method of calculating lattice incompatibility was based on the assumption that the development of the transformation stress continued throughout the formation of the Widmanstätten alpha-beta colonies. In this case, lattice incompatibility was measured between the supercooled beta and a mixture of the alpha and beta phases, " $\Delta_{\alpha\beta}$ ". This value was then weighted by the amount of the colony structure formed and the final result is referred to as "beta to colony lattice incompatibility". The results of this calculation are given in Table 5.7 and plotted against minimum hot ductility and net ductility loss in Figures 5.77 and 5.78, respectively. In contrast with the first method of lattice incompatibility calculation, it was now found that lattice incompatibility varied widely not only from alloy to alloy, but also within an alloy system and with cooling rate for an individual alloy. These results agree qualitatively with the hot ductility measurements.

Figures 5.77 and 5.78 show that the alloys split crudely into three groups, the ductility behavior of each described by a linear relationship with lattice incompatibility. Because the data do not all fall within

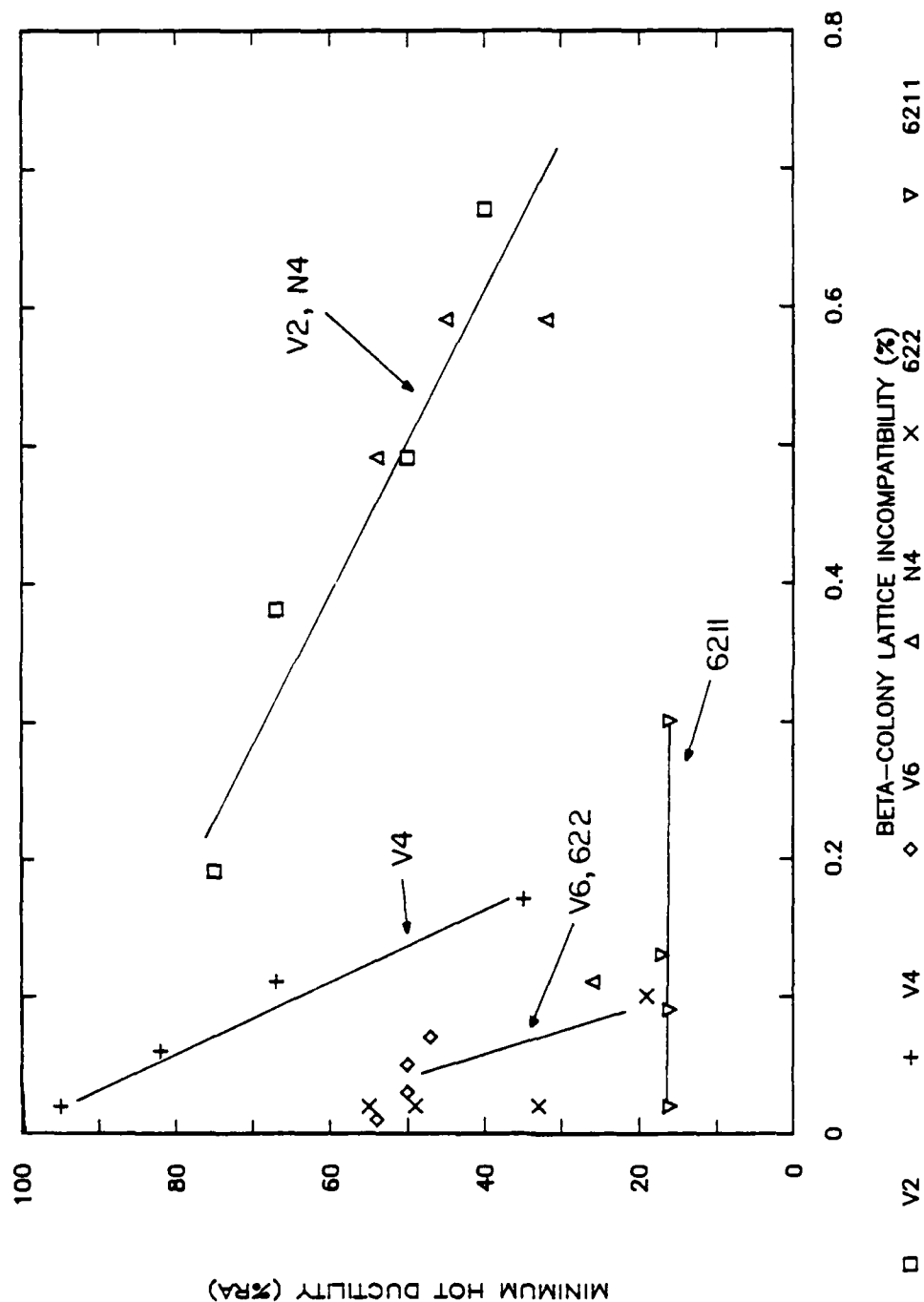


Figure 5.77 Minimum hot ductility versus beta to colony lattice incompatibility, showing lack of overall correlation but good individual correlations for each alloy.

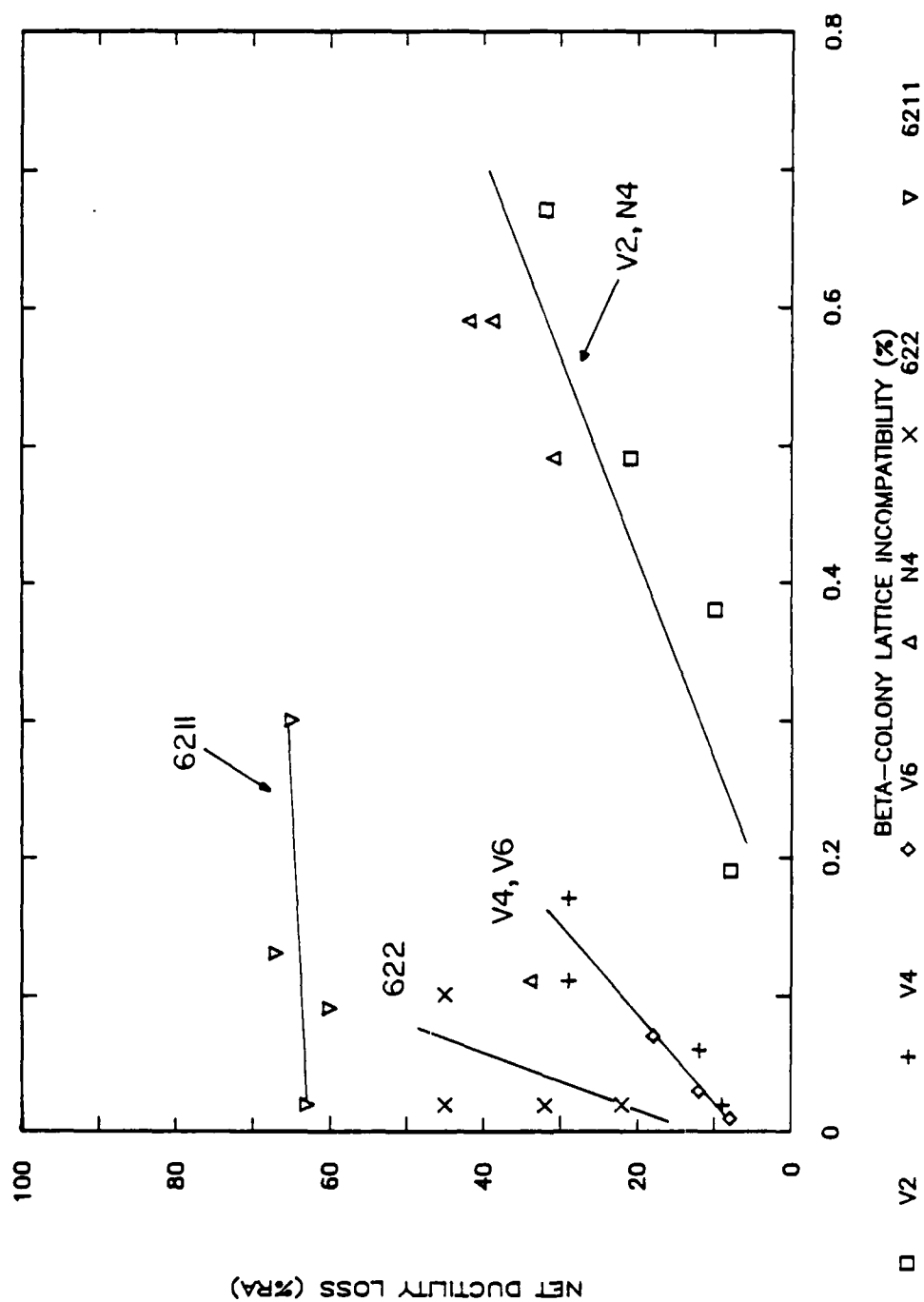


Figure 5.78 Net ductility loss versus beta to colony lattice incompatibility. Again, no unique correlation exists, but each alloy shows a reasonable trend.

the same group, these data show that the ductility behavior of these alloys cannot be uniquely described by lattice incompatibility, calculated in this fashion. However, the relationship between lattice incompatibility and ductility or ductility loss within each of the three groups suggests that perhaps a correlation does exist. When evaluating the data shown in Figures 5.77 and 5.78, it must be remembered that the beta to colony lattice incompatibility was shown to be dominated by the amount of Widmanstätten colony structure formed. Because of this, the question exists as to whether the apparent correlations are between ductility and lattice incompatibility or between ductility and Widmanstätten colony structure, independent of lattice incompatibility. This will be addressed in the following section, where possible correlations between ductility behavior and several microstructural variables are examined.

Several points must be made concerning the data in Figures 5.77 and 5.78. First, the case for the existence of a relationship between lattice incompatibility and ductility behavior would obviously be strengthened if more of the data shown in Figures 5.77 and 5.78 were included in one group. Second, the calculation of lattice incompatibility relies on several assumptions. While each individual assumption is reasonable, the result is calculated values which are

somewhat removed from the measurements they are based on. Third, the measurements themselves, lattice volume, beta phase dilatometry, and the measurement of transformation temperatures, are all subject to errors which have been discussed elsewhere. These points must be briefly examined to determine if the failure of the alloys to group together perhaps results from previous measurement errors or specific assumptions in the calculation procedure.

Figures 5.77 and 5.78 and Table 5.7 show that the lattice incompatibility of these alloys may be grouped based on their relative beta stabilization. This suggests that the calculation of lattice incompatibility may not have weighted the volumetric difference between the supercooled beta and the equilibrium beta, "beta to beta incompatibility", heavily enough. This is possible in the case of the vanadium ternary alloys, where the beta to beta incompatibility was large with respect to the beta to alpha incompatibility was very large. With these alloys, a heavier emphasis on the beta to beta incompatibility could make the behavior of Ti-6Al-4V and Ti-6Al-6V similar to that of Ti-6Al-2V. Such a change could possibly be justified if the amount of beta in the colony structure was found to be much greater than the values assumed in the incompatibility calculations. In the case of Ti-6Al-2V-2Nb however, the

incompatibility values are too small to make any change in weighting significant. Even with drastic changes in the weighting of the incompatibility values, the behavior of this alloy still differs greatly from that of the other alloys.

Another factor must be considered because of the apparent grouping of the alloys along the lines of beta stabilization. This is the relative strength of the colony structure in each alloy. If the assumption is made that the colony structure is loaded to the material yield strength in each case, the residual stress level would be much higher in a stronger alloy. Although the strength of these alloys was shown to generally increase with beta stabilization, Ti-6Al-2Nb-2V is again an exception. Figure 100 shows that at any temperature, the strength of Ti-6Al-2V-2Nb is lower than that of either Ti-6Al-4V or Ti-6Al-6V. The strength difference is magnified by the fact that the transformation temperature of Ti-6Al-2V-2Nb is much higher than that of the vanadium alloys. Thus, if the calculations were modified to include the strength of the material, the behavior of Ti-6Al-2V-2Nb would still differ significantly from that of the other alloys.

Using the described method of lattice incompatibility calculation, the difference between the three groups in

Figures 5.77 and 5.78 is caused, to a large degree, by differences in beta to alpha incompatibility. Although these values are subject to error, as discussed in Appendix D, the most accurate values of beta to alpha incompatibility include those for the alloys Ti-6Al-4Nb and Ti-6Al-2V-2Nb. The position of these two alloys at opposite ends of the lattice incompatibility spectrum shows that the differences shown in Figures 5.77 and 5.78 are real and cannot be attributed to errors in measurement of the beta to alpha incompatibility. Although measurement of the beta to beta incompatibility is far more prone to error than the measurement of the beta to alpha incompatibility, the relative small amount of beta present in the colony structure prevents this from being a major consideration.

5.3.3 Microstructural Analysis

As has been previously discussed, the susceptibility to the high temperature ductility loss exists in all of the alloys tested, with the exception of unalloyed titanium. The severity of the ductility loss varies from alloy to alloy, but also with cooling rate for each individual alloy. It has also been found that different alloys within one alloy system can be made to have similar hot ductility behavior by correctly choosing the cooling rate for each alloy. These results suggest that much of the variation in

behavior previously attributed to alloy differences is actually due to the cooling rate dependence of the individual alloys.

Viewed within the context of this investigation, changes in cooling rate will have two major effects on the alloys studied. One is to change the lattice incompatibility as calculated between supercooled beta and an equilibrium Widmanstätten colony structure. The second effect is to change the resulting transformed microstructure. Starke, et. al. (55) studied the high temperature deformation of Ti-6211 and found that only prior beta grain shape and grain boundary alpha affected ductility. Other factors which were investigated and found to have little or no effect included prior beta grain size, grain boundary alpha thickness, and the presence (or absence) of alpha' martensite. Lewis et. al. (133) reached similar conclusions. However, because the current investigation has demonstrated that Ti-6211 has the least cooling rate dependence of any of the alloys studied, these conclusions may not be universally applicable. A microstructural factor not studied by either Starke or Lewis is the possible effect of the existence and/or extent of the two morphologies of Widmanstätten structure, colony and basketweave. As shown earlier, the relative amounts of

these two microconstituents vary greatly with cooling rate and alloy content.

Studies made of alpha-beta titanium alloys at room temperature have demonstrated general, if not universal, trends between mechanical properties, deformation characteristics, and microstructures (25-48). Most often, it has been found that the tensile ductility of these alloys at room temperature is governed first by the extent of planarity of slip, and second, by the length of the active slip paths. These concepts were most clearly evaluated and demonstrated by Lutjering, et. al. (31). However, the ductility variation seen at room temperature and described by the modelling of Lutjering and others is very small compared to that observed at high temperatures (31, 54-66). Additionally, the fracture surfaces of the low ductility tensile failures more closely resembles those of creep failures than of room temperature tensile failures (55, 134). These observations suggest that the room temperature concepts are not generally applicable at high temperatures. Still, the high strain rates used in the current study make the room temperature ideas useful as a reference point for the evaluation of microstructure-mechanical property relationships.

5.3.3.1 Prior Beta Grain Size. In previous investigations (55, 133), no relationship has been found between prior beta grain size and high temperature ductility. To test this result, the effect of prior beta grain size was investigated for both Ti-6211 and Ti-6Al-2V. The results of these tests are shown in Figures 5.79 and 5.80. Figure 5.79 shows ductility versus temperature curves for Ti-6Al-2V cooled at 10°C/s following four different beta anneals. In this case, the curves are all essentially the same although the prior beta grain size ranged from 0.25mm to 1.0mm. Figure 5.80 shows a plot of net ductility loss versus cooling rate for two sets of Ti-6211 data, one annealed at 1100°C and the other at 1200°C . Again, the results of the two sets of tests are very similar.

These results verify that prior beta grain size is not related to the high temperature ductility of these two specific alloys, Ti-6211 and Ti-6Al-2V. It has been shown that these two alloys rest at opposite ends of the spectrum in terms of the cooling rate, hence microstructural, effect on ductility. Thus, it is reasonable to conclude that the ductility of all of the alloys tested is equally immune to the effect of prior beta grain size. The conclusion that may then be reached is that if the concepts of planarity of slip and slip path length, applicable at room temperature,

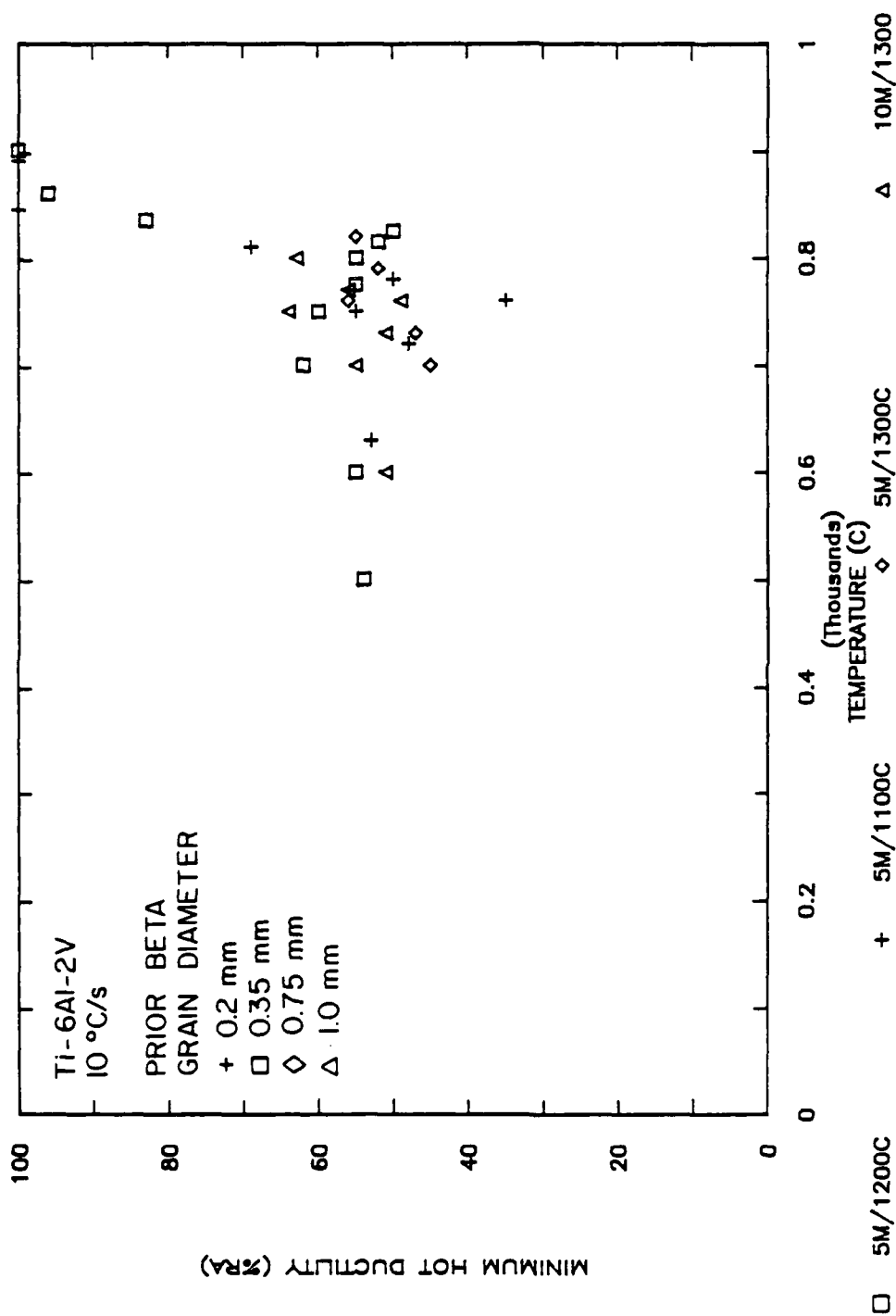


Figure 5.79 Ductility versus temperature for Ti-6Al-2V samples with different prior beta grain sizes, showing that ductility is unaffected by prior beta grain size.

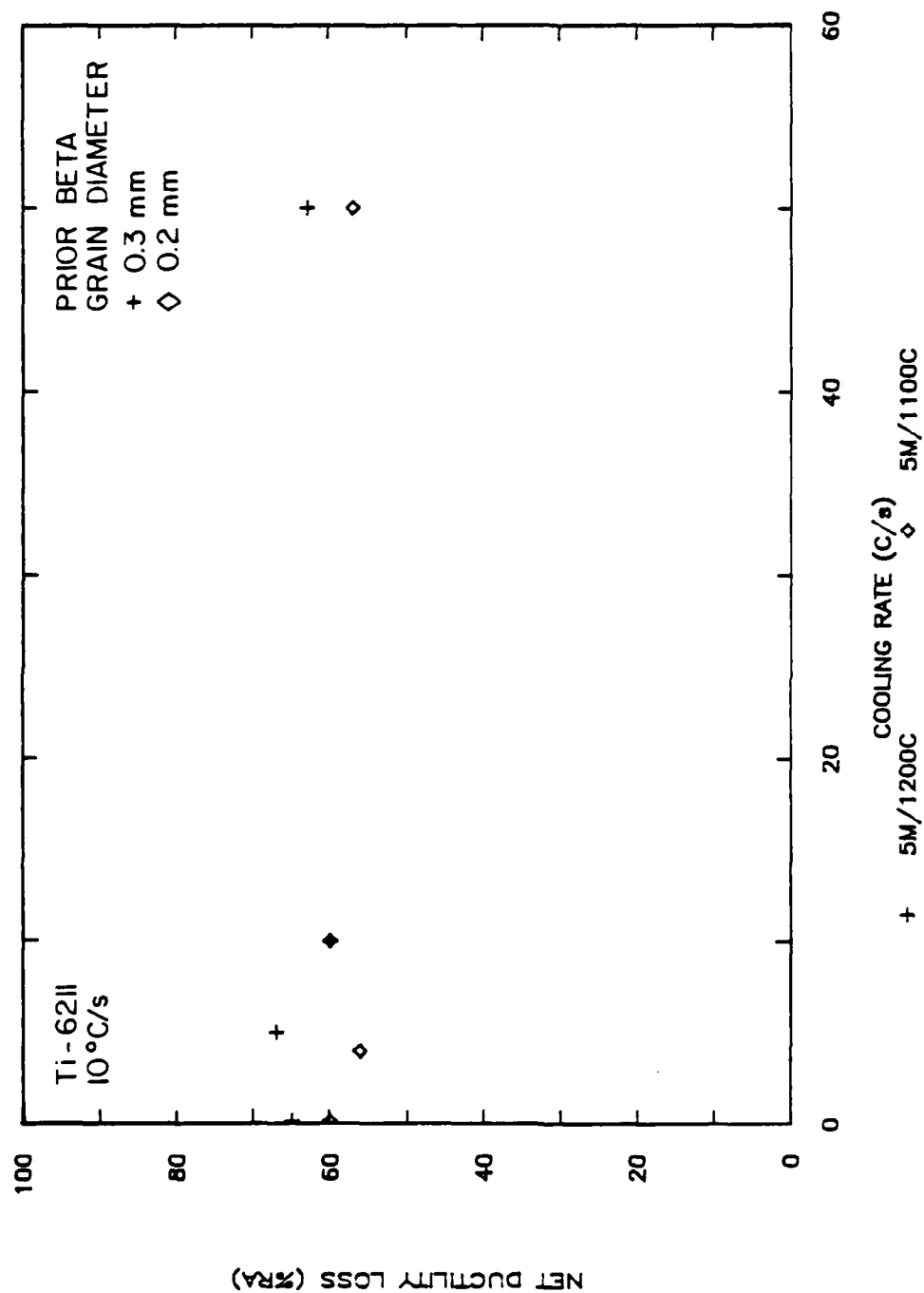


Figure 5.80 Net ductility loss for Ti-6211 samples with different prior beta grain sizes, showing that ductility loss is unaffected by prior beta grain size.

are governing the high temperature ductility of these alloys, the slip path length is independent of the prior beta grain size.

5.3.3.2 Grain Boundary Alpha Thickness. Earlier studies have shown that when the low ductility failures occur, the mechanism of failure is microvoid nucleation and coalescence (25-48). These processes have been observed to occur almost exclusively at the interface between a grain boundary alpha film and the matrix. The only exceptions which have been reported are occasional void nucleation at alpha'-matrix interfaces and at the interface between large alpha platelets and the matrix (43-48). In proposing his "differential strength" model, Starke (55) suggested that the low ductility failures were due to dislocation pile ups associated with concentrated slip within the grain boundary alpha layer. However, attempts (55, 133) to relate grain boundary alpha thickness with high temperature ductility in Ti-6211 have failed to show a clear correlation. Qualitatively, similar results have been obtained in this investigation. The amount and thickness of the grain boundary alpha film was not found to vary significantly throughout the range of alloys and cooling rates studied. The only exceptions to this were rapidly-cooled Ti-6Al-6V and Ti-6Al-4V, which had noticeably less grain boundary

alpha than the other alloys. These results lead to the conclusion that deformation of the grain boundary alpha film is not the mechanism controlling the high temperature ductility of these alloys.

It must be pointed out however, that the amount of grain boundary alpha film present in a given microstructure is very difficult to accurately determine. One way to estimate the amount of grain boundary alpha present is to develop a relationship describing the relative amounts of Widmanstatten colony structure and grain boundary alpha. As was discussed earlier, the colonies grow as the result of the breakdown of the allotriomorph interface. Thus, their presence at a prior beta grain boundary will generally be associated with an allotriomorph, even if the allotriomorph cannot be metallographically detected. It is true that a grain boundary alpha film can exist without an associated Widmanstatten colony. It is also true that colonies can be associated with nuclei other than grain boundary alpha. Finally, any relationship describing the relative amounts of grain boundary alpha and colony structure would only be expected to hold at low volume percents, where a change in amount of colony structure is associated with further saturation of the prior beta grain boundaries. In spite of these limitations, the amount of colony structure should

provide a rough idea about the relative amounts of grain boundary alpha in different microstructures. Table 5.9 lists the volume percent and width of the Widmanstatten colonies in all the microstructures studied. Table 5.9 shows that for small amounts of Widmanstatten colony structure, the colony width is approximately 0.001 in., or 0.025 mm. Based on this and spherical prior beta grains with a diameter of 0.3 mm, the prior beta grain boundaries will be saturated at approximately 15% colony structure. Table 5.9 shows that using 15% colony structure as an arbitrary cutoff point for grain boundary saturation, the only microstructures which would be expected to have unsaturated boundaries are Ti-6Al-4V cooled at 20°C/s, Ti-6Al-6V at 1, 2, 5, and 10°C/s, and Ti-6Al-4Nb and Ti-6Al-2V-2Nb at 50°C/s. In general, this is in agreement with the metallographic observations. In any case, the ductility of these alloy-cooling rate combinations is not markedly different from that expected based on the test matrix as a whole, Figures 5.63 and 5.64.

5.3.3.3 Widmanstatten Colony Structure Previous investigations have focussed on the grain boundary alpha film as the microconstituent associated with the low ductility failures (55, 133). However, no correlation has been demonstrated between the grain boundary alpha film, the

Table 5.9

Widmanstatten Colony Size and Volume Percent Widmanstatten
in Alloys Tested at Several Cooling Rates

Alloy	Cooling Rate (°C/s)	Volume Percent Colony (%)	Colony Size (in. $\times 10^{-3}$)
Ti-6Al-2V	0.17	100	17
	5	74	9
	10	53	5
	20	40	1
Ti-6Al-4V	0.17	100	10
	4	26	3
	10	15	2
	20	6	1
Ti-6Al-6V	0.17	100	12
	0.5	25	3
	1	12	2
	2	5	1
	5	4	1
	10	1	1
Ti-6Al-4Nb	0.17	100	15
	5	62	12
	10	57	9
	20	47	4
	50	10	2
Ti-6Al -2V-2Nb	0.1	100	14
	5	40	3
	10	29	4
	20	26	2
	50	11	2

Table 5.9 (cont.)

Alloy	Cooling Rate (°C/s)	Volume Percent Colony (%)	Colony Size (in. $\times 10^{-3}$)
Ti-6211	0.17	100	4
	5	57	3
	10	39	2
	50	17	1
Ti-6211 (1)	0.17	100	10
	4	57	4
	10	39	3
	20	26	1

(1) beta anneal of 5 minutes/1100°C

amount and size of which varies little with alloy content and cooling rate, and hot ductility, which varies widely. As has been discussed, the grain boundary alpha film is usually associated with a Widmanstatten colony structure, shown in Figures 44-46. Unlike the grain boundary alpha film, the amount and size of the Widmanstatten colonies vary significantly with both alloy content and cooling rate. This is shown in Figures 5.81 and 5.82, and in Table 5.9.

It is well established that when the colony microstructure is strained at room temperature, the retained beta between the alpha laths does not block the passage of dislocations. Once nucleated, slip traverses the entire colony. This behavior has been observed at high temperatures as well. Figure 5.83 contains micrographs taken of a longitudinal section of a Ti-6211 Gleeble specimen which was tested under conditions producing low ductility failure. In this micrograph, microvoids which have nucleated away from the fracture surface appear to be associated with localized planar slip across an entire Widmanstatten colony. The transmission microscopy of Starke, et. al. (55) shows similar results, intense localized slip occurring across a grain boundary alpha film and Widmanstatten colony. These results suggest that the critical microconstituent, in terms of high temperature

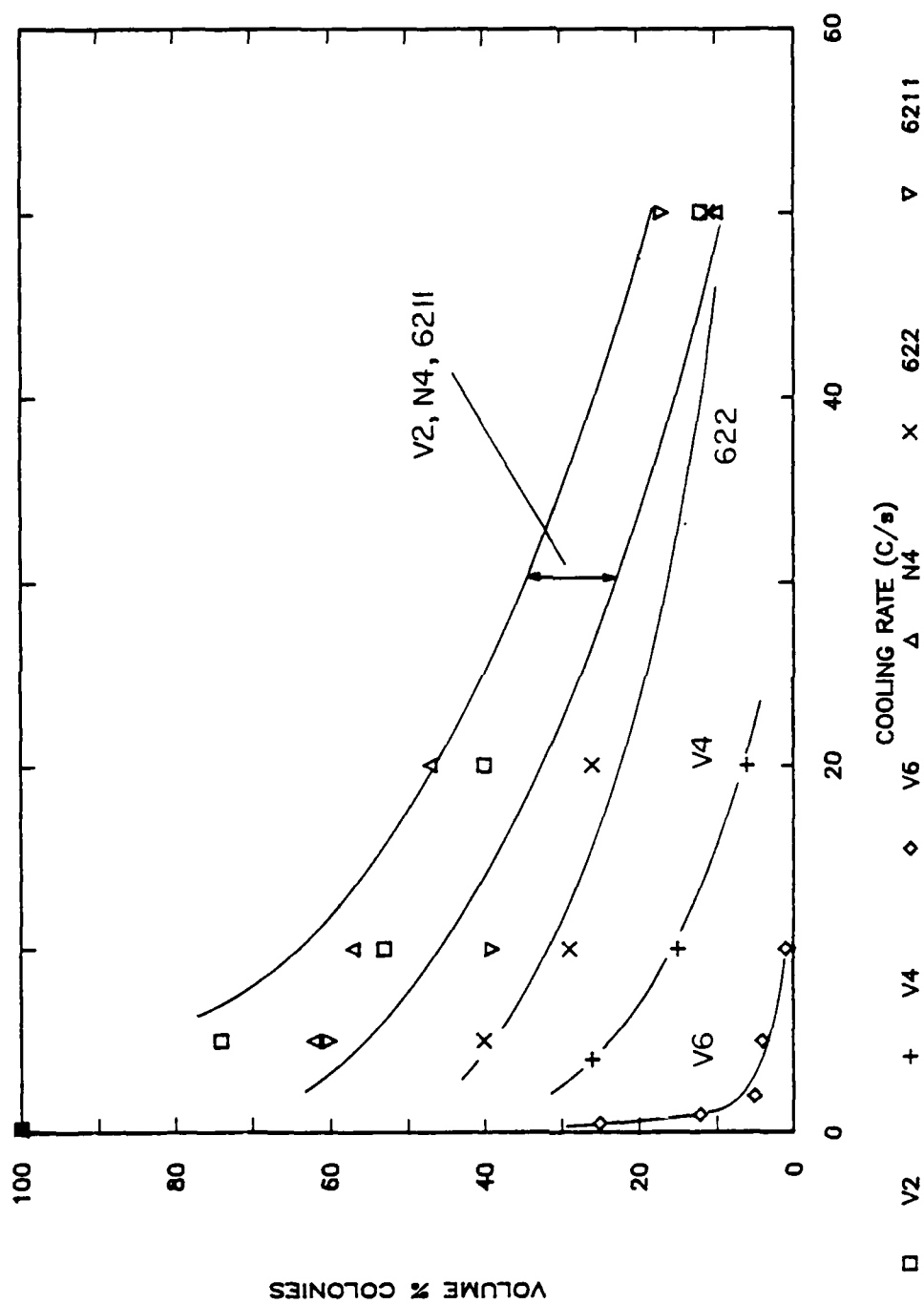


Figure 5.81 Volume percent Widmanstatten colony structure versus cooling rate for all alloys tested. Amount of colony structure increases with decreasing cooling rate.

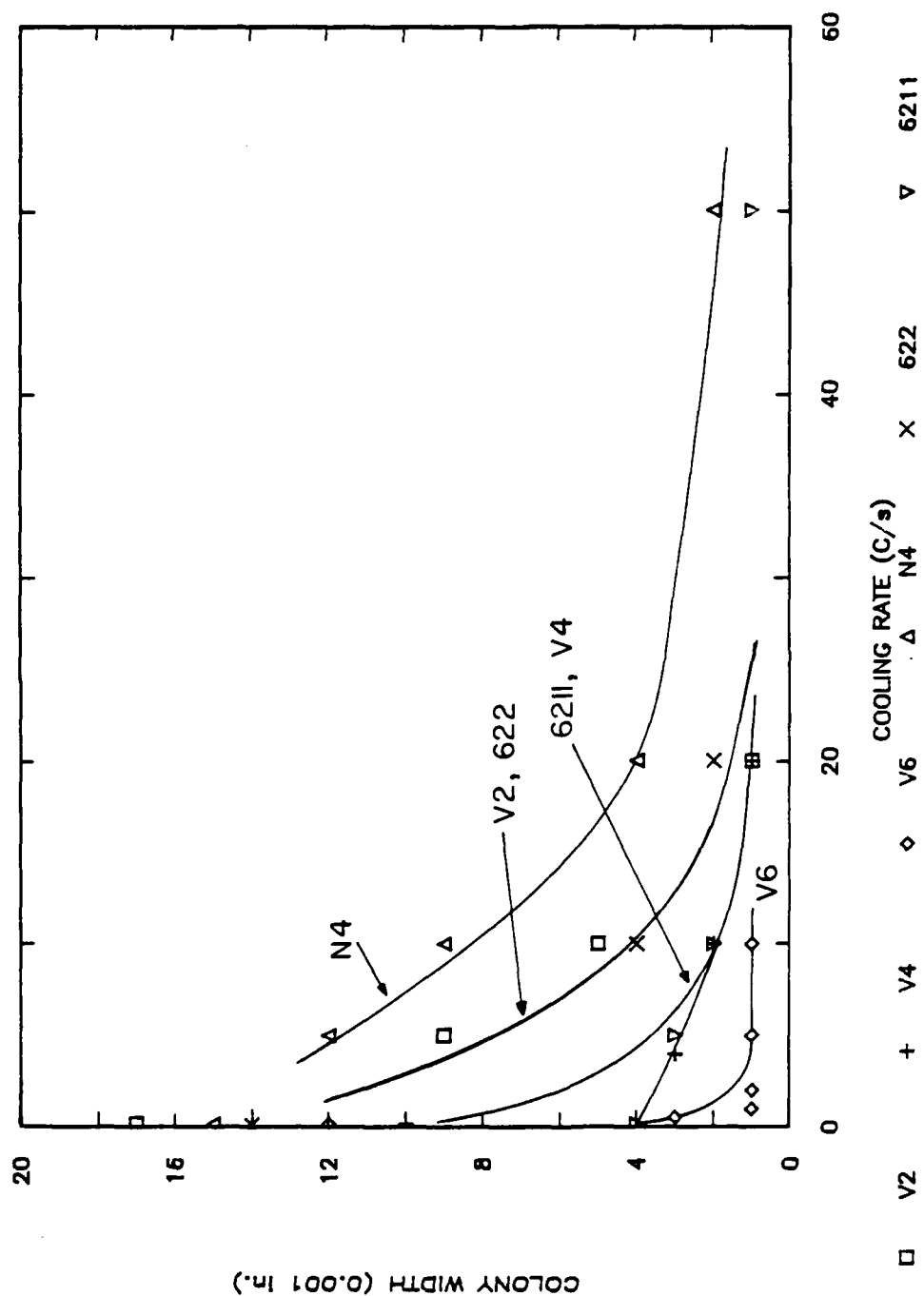


Figure 5.82 Widmanstätten colony width versus cooling rate for all alloys tested, showing increase in colony width with decreasing cooling rate.



Figure 5.83 Optical micrographs of a failed Ti-6211 gleeble specimen, (10°C/s , 760°C) sectioned longitudinally, showing local deformation of Widmanstätten colonies near microvoids.

ductility, is the Widmanstatten colony structure rather than the grain boundary alpha film.

To test for a possible correlation between the Widmanstatten colony structure and the high temperature ductility of these alloys, the minimum hot ductility and net ductility loss were plotted against the volume percent of colony structure, Figures 5.84 and 5.85, respectively. In both figures, a general correlation can be seen. Figure 5.84 shows that the various alloys all have different levels of minimum hot ductility. However, the minimum hot ductility of each alloy decreases with increasing amount of the colony structure in a fairly linear manner, and the slope of the lines are all fairly similar. Figure 5.84 suggests two things. The first is that there is in fact a relationship between the Widmanstatten colony structure and the ductility of these alloys. The second is that although each alloy has a different intrinsic ductility level, the effect of the amount of colony structure is approximately the same for all the alloys studied. An obvious exception to this is the behavior of Ti-6211 which will be discussed separately in a later section.

In Figure 5.85, net ductility loss is plotted against volume percent of the colony structure. This figure shows that when the different intrinsic ductilities of the alloys

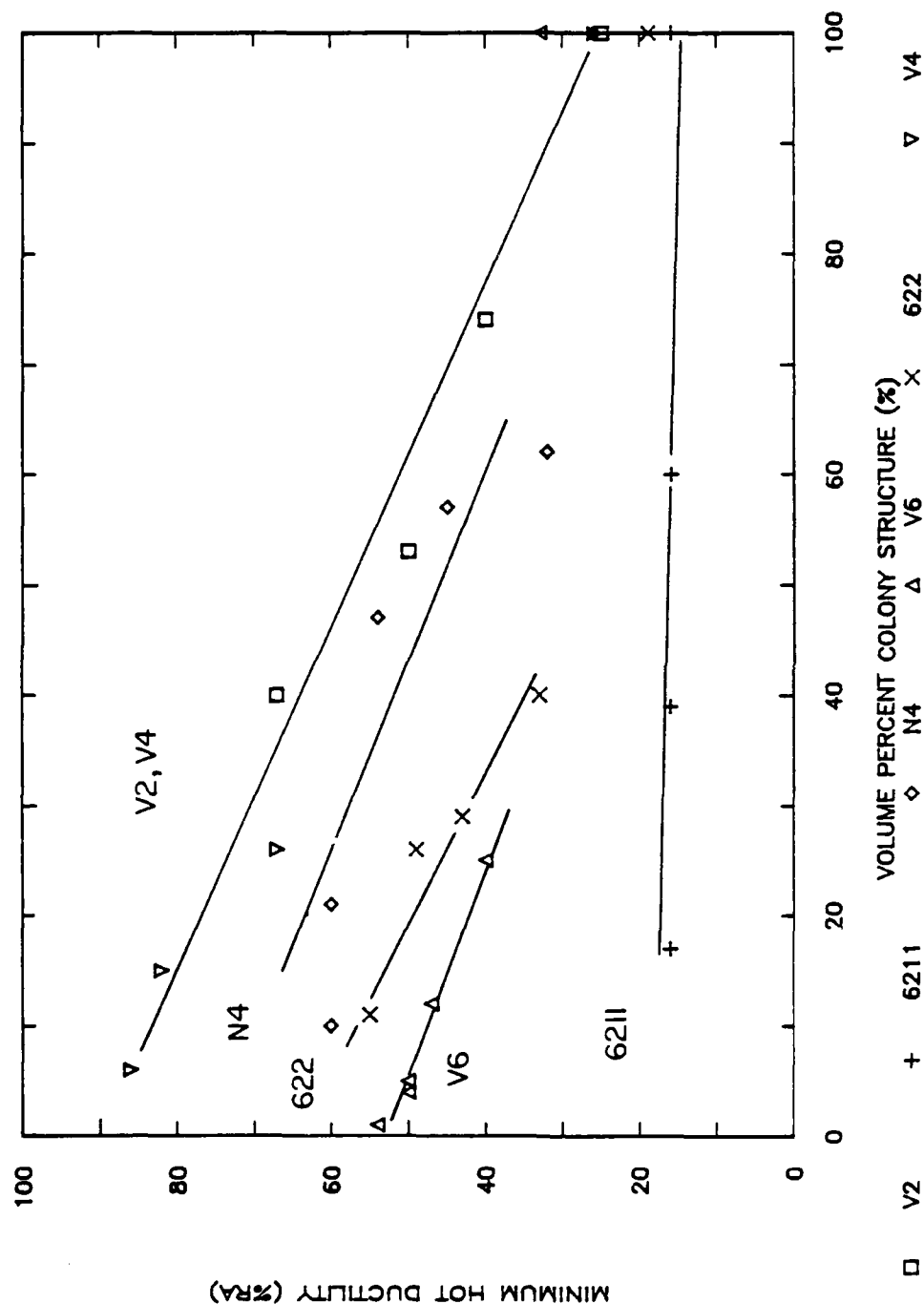


Figure 5.84 Minimum hot ductility versus volume percent Widmanstatten colony structure. Ductility of all alloys increases at a similar rate with decreasing amount of colony structure.

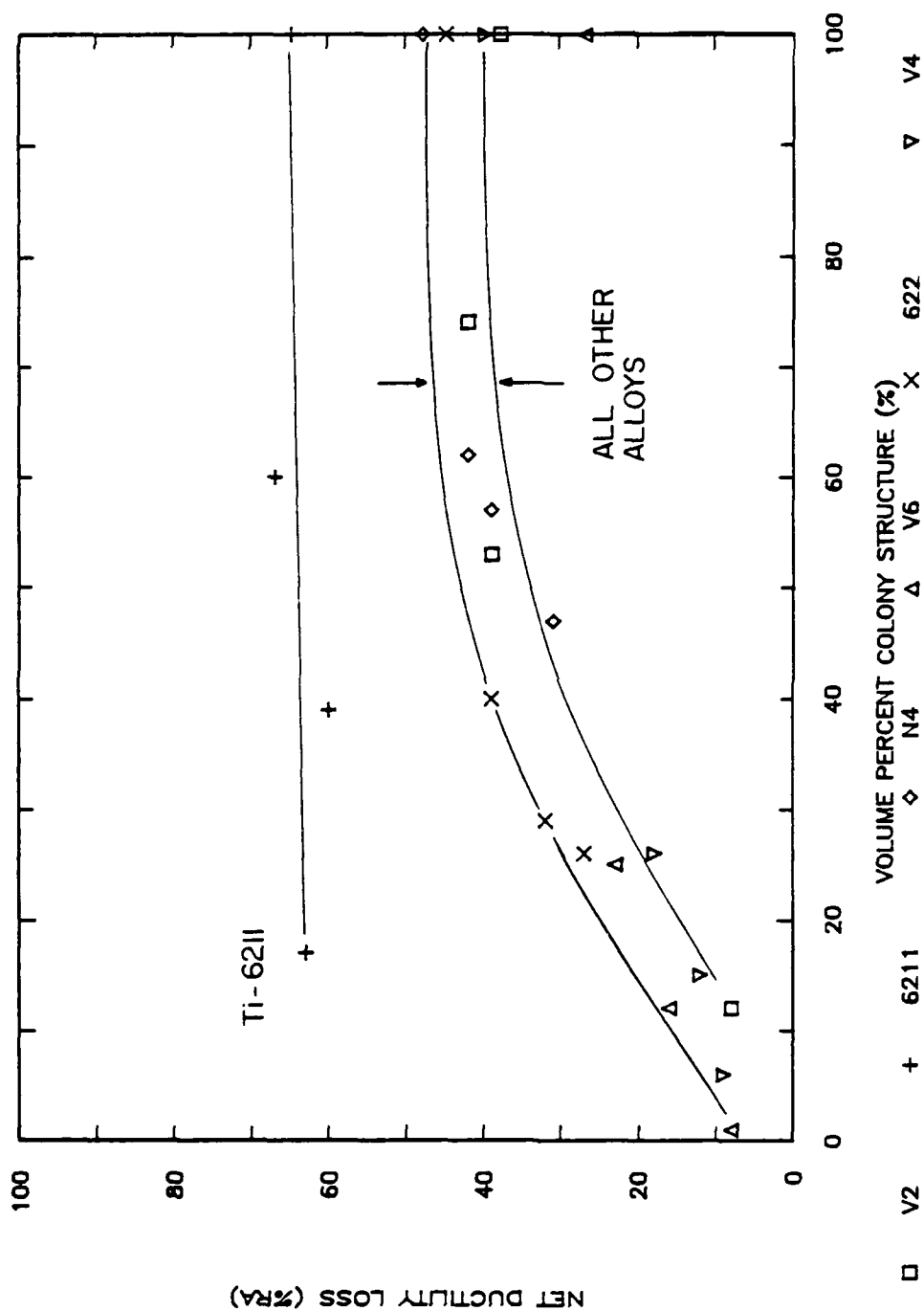


Figure 5.85 Net ductility loss versus volume percent Widmanstatten colony structure. Net ductility loss increases with increasing amount of colony structure and the behavior of all alloys is similar.

are eliminated, the correlation between ductility loss and the amount of Widmanstatten colony structure is very obvious. The data for all of the alloys falls within a narrow band. At low volume percents of the colony structure, the net ductility loss increases monotonically with volume percent colony structure. However, there is little additional increase in net ductility loss beyond approximately 50% colony structure. This suggests two possibilities. The first is that the system becomes somehow saturated at higher volume percents of the colony structure. The most obvious type of saturation is that of the prior beta grain boundaries. This is particularly appealing because the fracture surfaces of the low ductility failures are frequently intergranular with respect to the prior beta grain boundaries. As discussed earlier, the prior beta grain boundaries are saturated at far lower levels of volume percent colony structure than 50%. However, these calculations were based on a uniform colony width. The growth of the colonies is probably not uniform throughout the microstructures. Therefore, it is quite possible that the boundaries do not become saturated until the average colony width is much thicker and the volume percent colony structure much higher than the 15% calculated. Without a detailed microstructural investigation, which is beyond the

scope of this investigation, the question of prior beta grain boundary saturation must be left open.

The second possible explanation for the behavior shown in Figure 5.85 is that net ductility loss is actually related to the width of the colony structure, itself related to volume percent in roughly the manner shown in Figure 5.85. In a general sense, a consideration of colony width predicts the trend shown in Figure 5.85 because:

$$d \propto V^{1/3}$$

where: d = colony width

V = colony volume

Previous studies support, either directly or indirectly, the correlation between colony width and ductility in the presence of low ductility failures. In a detailed study of Ti-Al alloys which deformed by intense planar slip, Lutjering (31) showed that low ductility failures could be associated with a critical local stress at the head of a dislocation pile up. He also showed that the local shear stress could be described by the applied stress and the slip path length via a Hall-Petch relationship.

A Hall-Petch relationship is typically described by:

$$\tau_{\text{local}} = \tau_{\text{applied}} A D^{-1/2}$$

where: τ_{local} = local shear stress

τ_{applied} = applied shear stress

A = experimentally derived constant

D = slip path length

Lutjering (31) found that the critical local shear stress to cause low ductility failures was independent of all factors other than alloy content. Thus, this critical stress could be reached by any combination of applied stress and local stress concentration. If the assumption is made that the stress-strain relationship for a material can be described by the expression:

$$\sigma = K \epsilon^n$$

the criteria described by Lutjering can be grossly simplified and in the absence of particle strengthening, written as:

$$\epsilon_f = B(D^{-1/2})^{1/n}$$

where: ϵ_f = true failure strain

D = slip path length

n = exponent in stress-strain relationship

A = a constant which depends on material,
orientation, and dislocation type

If uniform deformation to failure was a reasonable assumption, constancy of volume could be used to convert true fracture strain to reduction in area. The criteria of Lutjering (31) could then be written as:

$$-\ln(1-\%RA/100) = A(D^{-1/2})^{1/n}$$

Unfortunately, virtually any measureable level of reduction in area is associated with some necking. Because of this, the reduction in area values obtained in this investigation cannot be used to calculate true fracture strain. However, this does show that if the slip path length in the Widmanstatten colonies is the critical microstructural parameter, this length should be related to some measure of fracture strain via a Hall-Petch expression.

In Figures 5.86 and 5.87, minimum hot ductility and net ductility loss are plotted against $D^{-1/2}$, where D is the Widmanstatten colony width. Obviously, these ductility measurements are only relative measures of true failure strain (and "loss" of failure strain). Still Figures 5.86 and 5.87 show that there is a definite correlation between hot ductility and Widmanstatten colony width. As was the case with Figures 5.84 and 5.85, the correlation is most obvious when the intrinsic ductilities of the materials are eliminated, Figure 5.86. Thus, although true failure strain cannot be calculated, the results shown in Figures 5.86 and

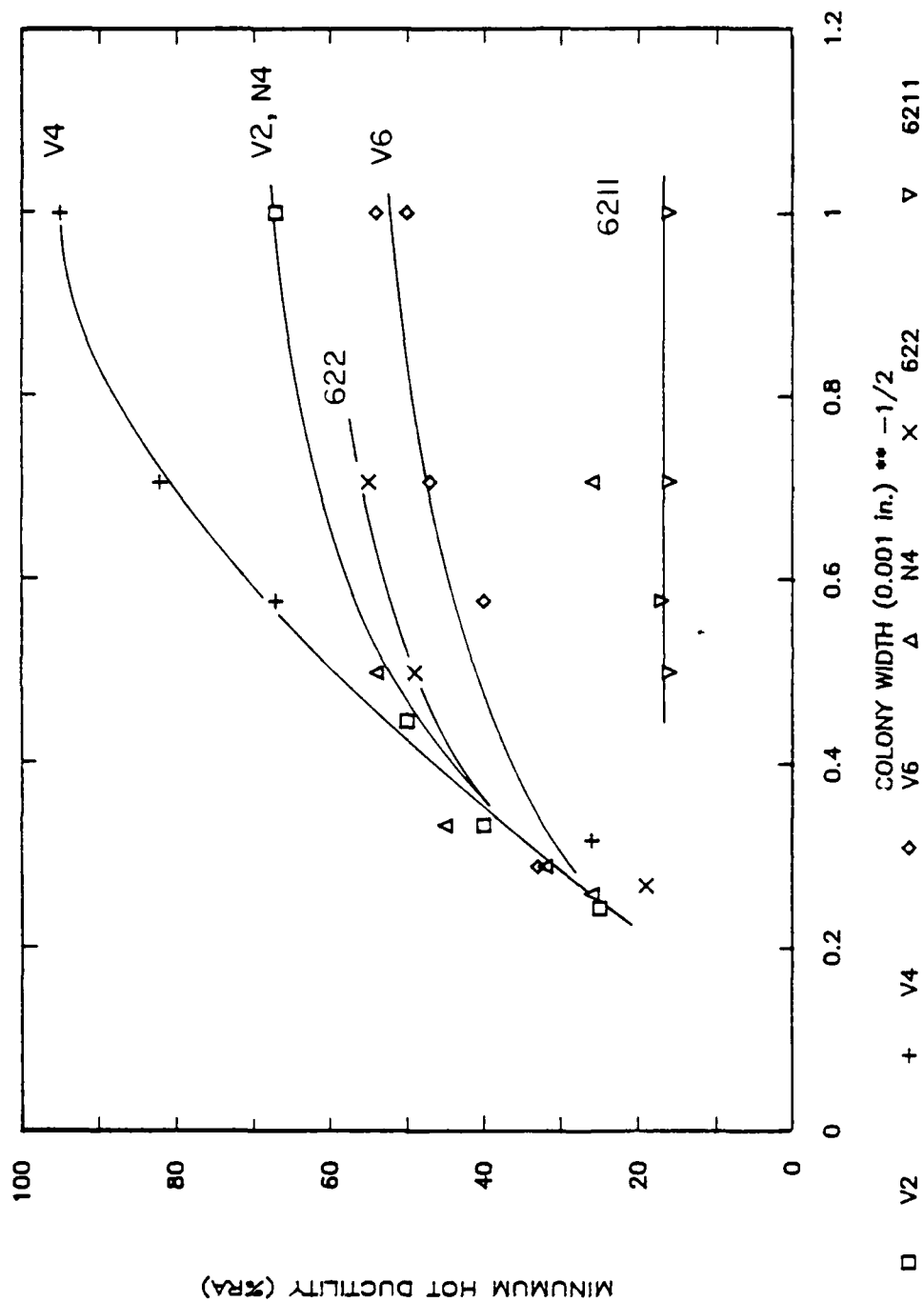


Figure 5.86 Hall-Petch plot of minimum hot ductility versus Widmanstätten colony width. Ductility increases with $d^{-1/2}$ at a similar rate for all alloys.

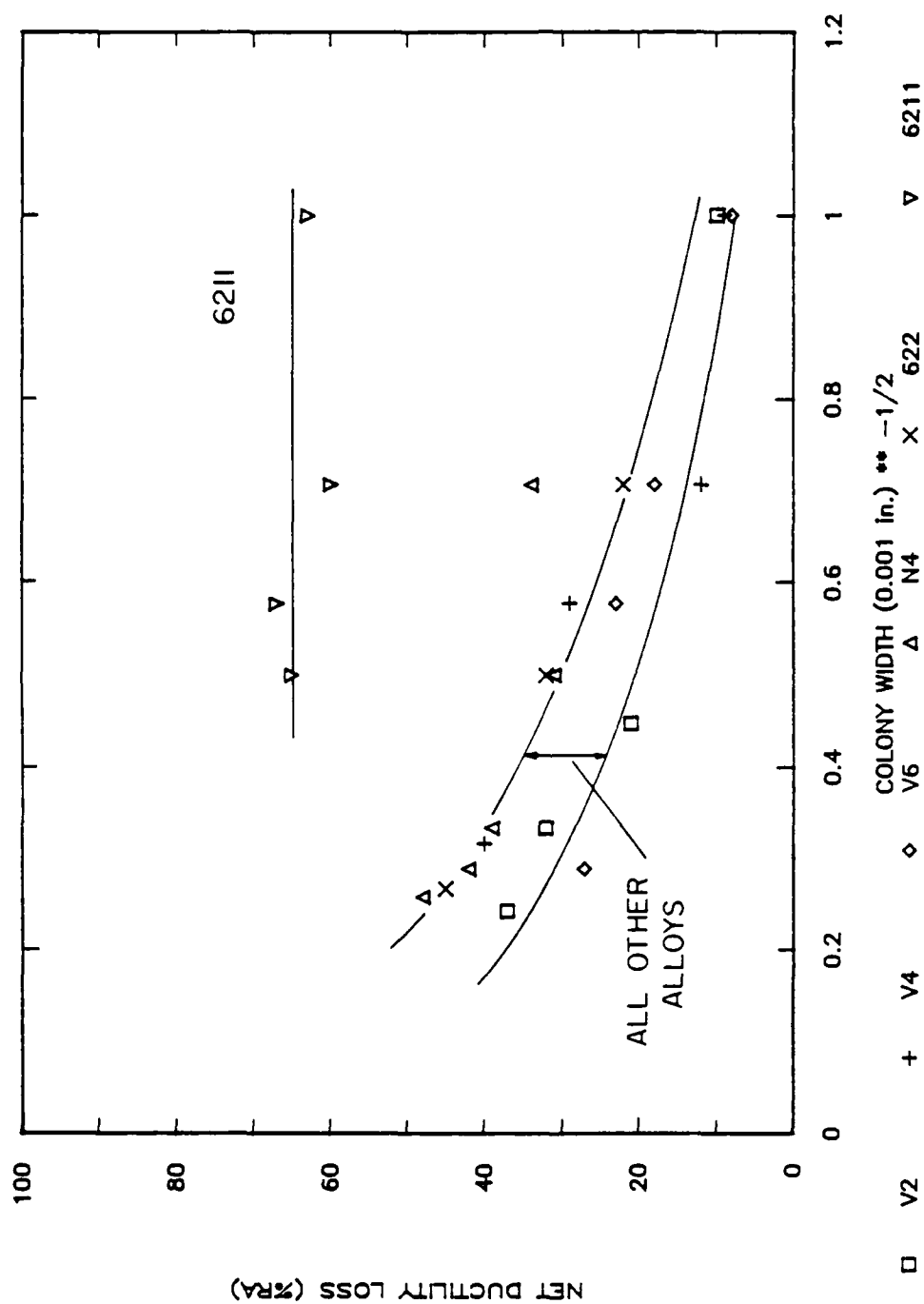


Figure 5.87 Hall-Petch plot of net ductility loss versus Widmanstätten colony width. Ductility loss decreases with increases in $d^{-1/2}$ and the behavior of all alloys is similar.

5.87 support the conclusion that the Widmanstatten colony structure is the critical microconstituent. Additionally, these results suggest that the functional form seen in Figure 5.85 exists because the critical parameter is colony width.

An additional and significant characteristic of the relationship between the Widmanstatten colony structure and the ductility behavior of these alloys is that it only applies within the hot ductility dip region. This study has shown the relationship between colony parameters and ductility within the ductility region. However, no such correlation can be made at low temperatures. When tests were performed at low temperature, the ductility was found to be essentially the same in samples with widely varying microstructures. The contrast between widely variable high temperature ductility and essentially constant low temperature ductility is clearly shown in Figures 5.57, 5.58, and 5.60, the ductility versus temperature curves for Ti-6Al-4V, Ti-6Al-6V, and Ti-6Al-2V-2Nb, respectively. These results agree with those previously reported (55).

The stress-strain curves shown in Figures 5.88 and 5.89 further support the observation that the relationship between the colony structure and mechanical behavior only applies at high temperatures. Figure 5.88 shows true

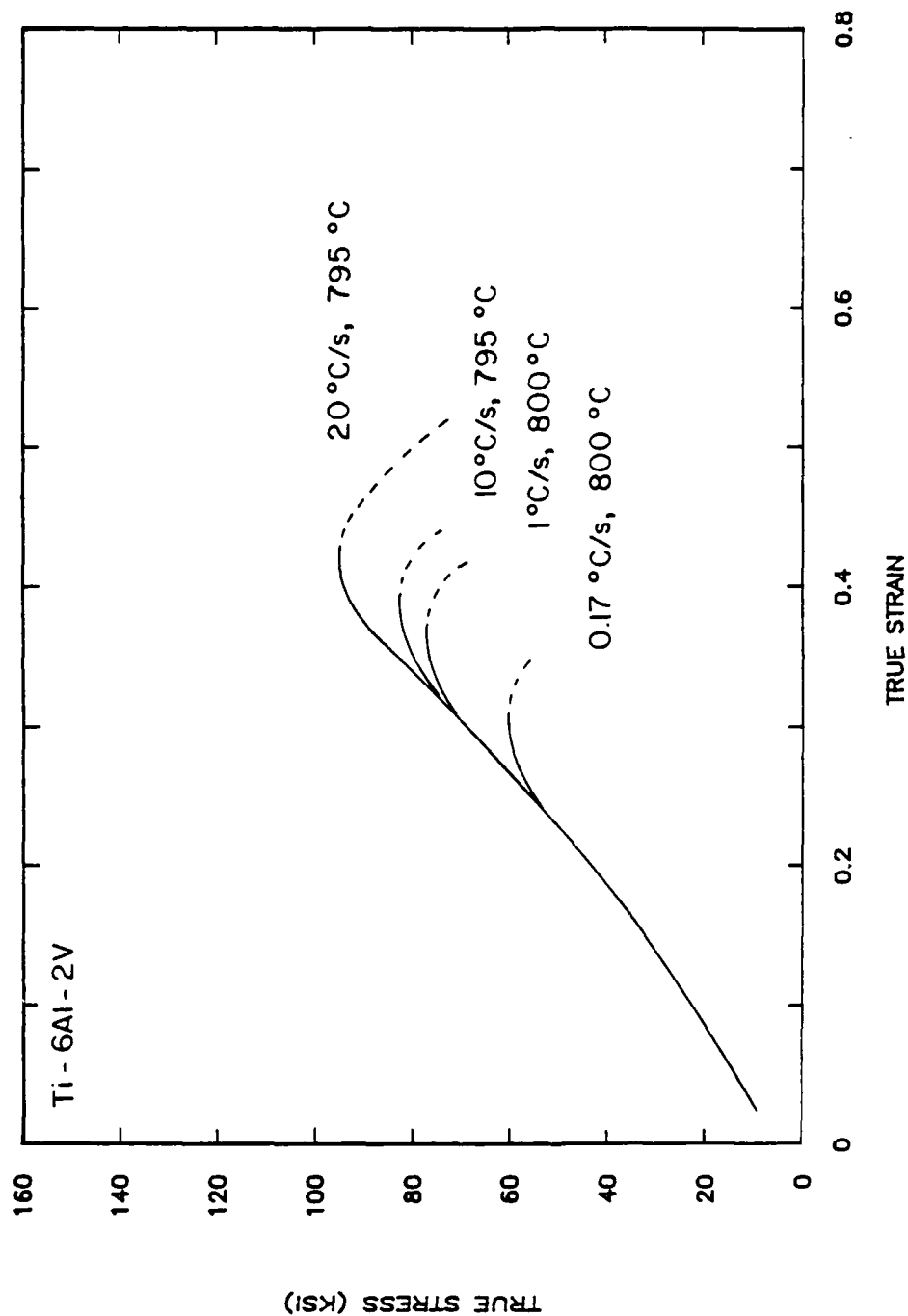


Figure 5.88 True stress-true strain curves for Ti-6Al-2V tested at 800 °C showing that strength and ductility increase with decreasing amount of Widmanstatten colony structure.

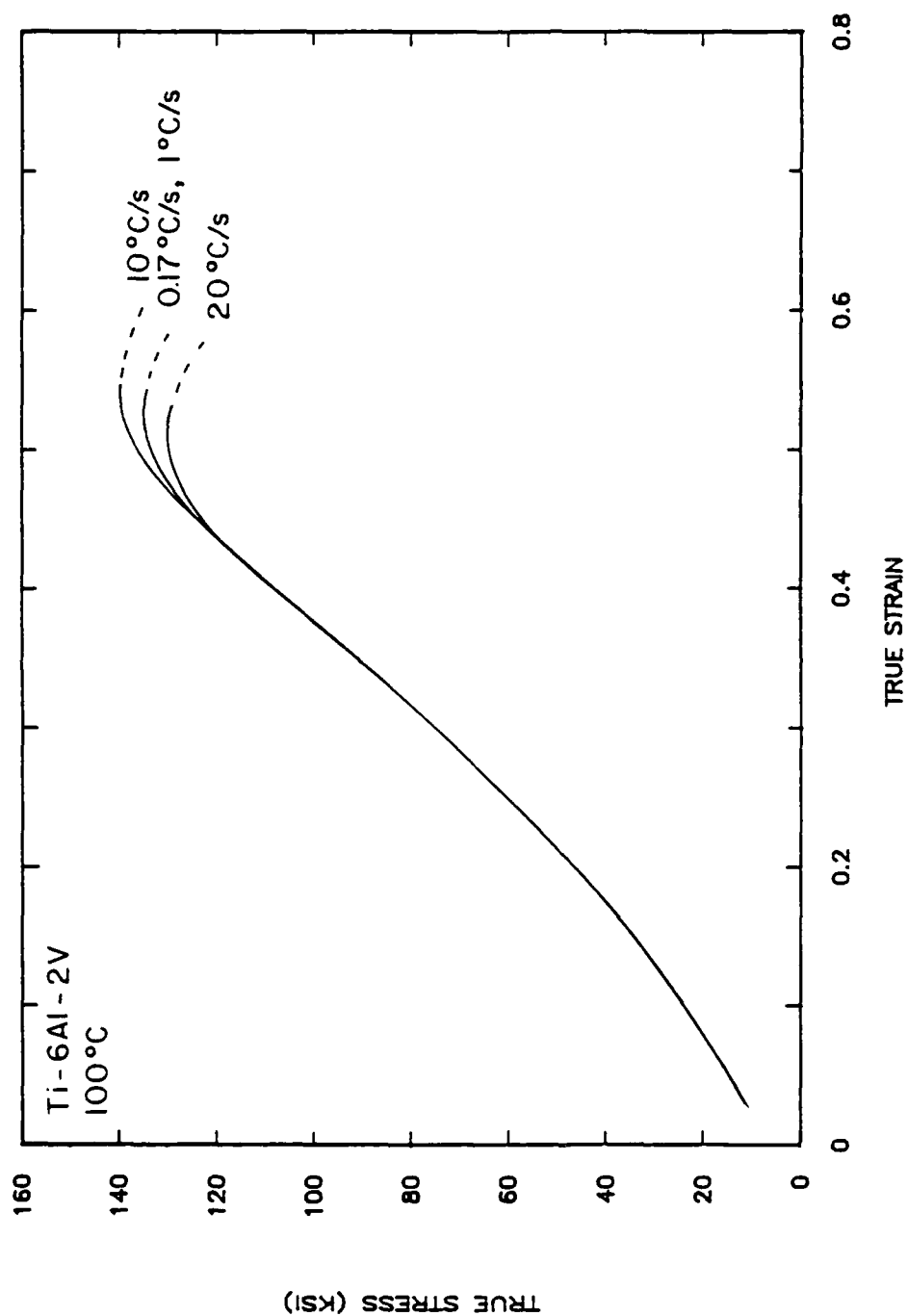


Figure 5.89 True stress-true strain for Ti-6Al-2V tested at 100°C. Note that at low temperature, strength and ductility are unaffected by microstructural changes.

stress-true strain curves for Ti-6Al-2V samples, cooled at various cooling rates to produce different microstructures, and each tested within the ductility loss region. This figure shows that the strength of the material increases with cooling rate, hence with decreasing colony width. Figure 5.89 is a similar figure, but in this case, the tests were performed at 100°C. In this figure, no clear correlation can be established between mechanical behavior and cooling rate, hence transformed microstructure.

The preceding discussion has led to two conclusions. The first is that the ductility behavior of the alloys studied is directly related to the amount and size of the Widmanstatten colony structure. This is in contrast with the conclusions drawn by previous investigators (55, 133), who associated the ductility loss with the grain boundary alpha film. The second conclusion is that the colony structure dominates the mechanical behavior of these alloys only at high temperatures. This suggests that the strain characteristics of the microstructures studied change with temperature.

An additional conclusion can be drawn when the results of the lattice incompatibility testing are now considered. Figures 5.77 and 5.78 plotted ductility and ductility loss versus beta to colony lattice incompatibility. In these

figures, the data was split into three groups, but each seemed to be described by a correlation between a hot ductility measure and lattice incompatibility. It was pointed out that the change in lattice incompatibility within each of the three groups was, for the most part, a change in amount of the colony structure. This section has shown that a correlation exists between amount of colony structure and the ductility parameters, regardless of lattice incompatibility. Thus, it is now apparent that the correlations shown in Figures 5.77 and 5.78 are actually between the hot ductility parameters and the Widmanstatten colony structure. In fact, the consideration of lattice incompatibility has the effect of obscuring the fairly universal correlation between the colony structure and hot ductility. Based on this, the conclusion must be drawn that no correlation exists between hot ductility and lattice incompatibility, as measured in this investigation.

5.3.3.4 Alpha' Martensite In all of the preceding figures, the data for Ti-6211 is obviously different from that of the other alloys. In particular, the ductility behavior of Ti-6211 is universally poor and seems to be immune to microstructural variables. This has also been reported in other investigations (55, 6). Examination of Table 5.9 shows that the data for Ti-6Al-4Nb cooled at

50°C/s also differs from the surrounding data, the ductility being much lower and the ductility loss much greater than expected.

In the CCT diagram section, it was shown that the transformed microstructures in Ti-6211 were slightly different from those of the other alloys. In particular, Ti-6211 had a transformed microstructure which contained grain boundary alpha and Widmanstatten alpha-beta colonies, but had alpha' martensite in the center of the prior beta grain, rather than basketweave alpha-beta. This was also shown to be true for Ti-6Al-4Nb cooled at 50°C/s. As was discussed, this microstructural interpretation is subject to some question. However, in the case of Ti-6211 and Ti-6Al-4V, for example, a similar classification has been made by others (109). These results suggest that the occurrence of extremely low ductility and an unusually severe ductility loss is associated with the presence of alpha' martensite. This observation is supported by studies where rare-earth additions made to Ti-6211 were found to eliminate the alpha' martensite (65). The rare-earth additions were also found to increase the high temperature ductility and lessen the severity of the ductility loss of Ti-6211 to levels similar to those of the other alloys in this study.

Another characteristic of the martensitic samples is that the fracture of these samples appears to be far more intergranular than is the case for the other samples. This is shown in Figures 5.90 and 5.91 which contain fractographs and longitudinal metallographic sections of martensitic and basketweave samples, respectively. Figure 5.90 shows that the fracture surface of the martensitic sample appears to be very faceted, with the facets corresponding to the prior beta grain boundaries. In Figure 5.91, the fracture surface appears to be a mix of intergranular and transgranular fracture. The longitudinal section of Figure 5.91 shows that the mixed fracture mode corresponds with failure along Widmanstatten colony boundaries as well as prior beta grain boundaries.

One possible explanation for this behavior is that in the martensitic samples, microvoid nucleation occurs preferentially at the prior beta grain boundaries, rather than at the colony boundaries. This agrees with the results of Lewis (133), who associated microvoid nucleation within the grain boundary alpha film with the presence of small pools of beta retained along the surface where the plane front interface broke down and the Widmanstatten side plates began to form. Such a regular array of retained beta would not be expected at a colony/alpha' interface. Another

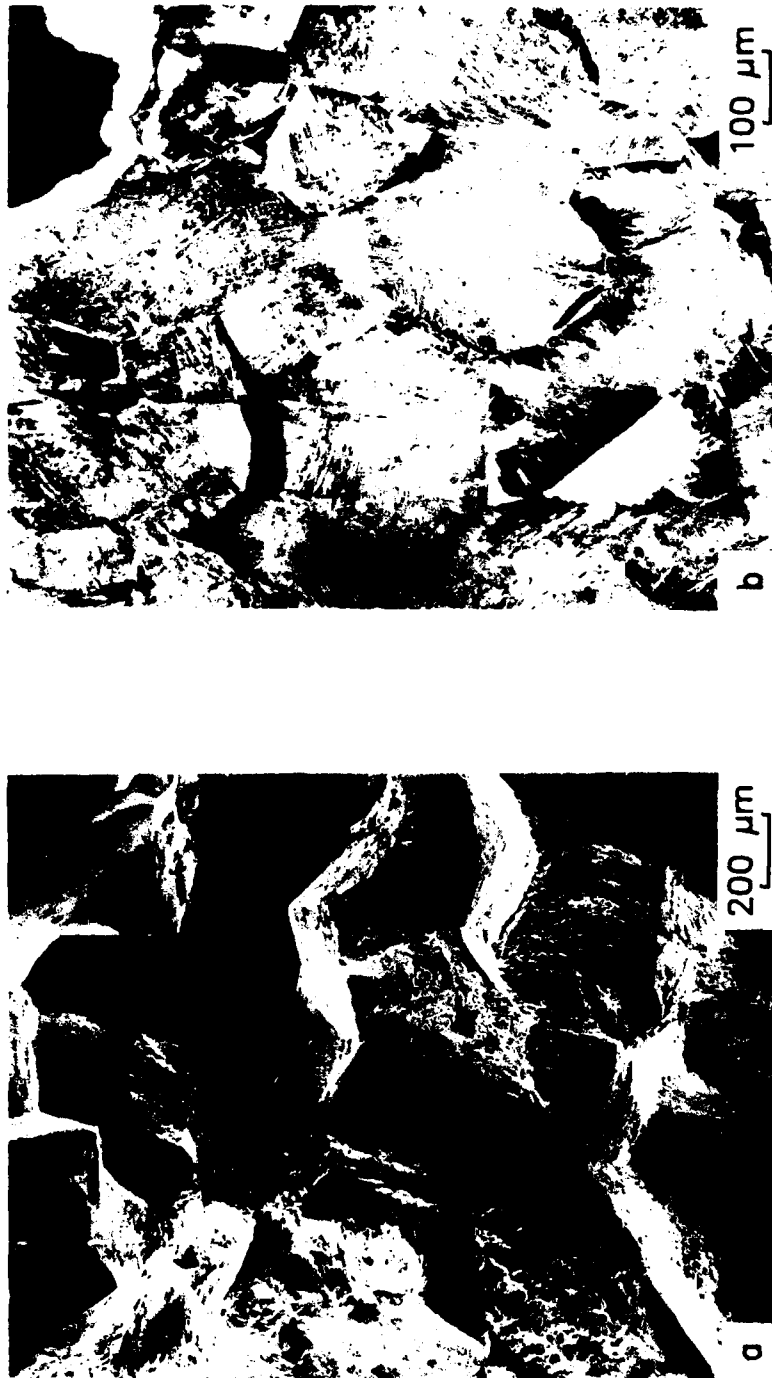


Figure 5.90 Fractograph (a) and optical micrograph (b) of Ti-6211 gleeble sample. Intergranular fracture is associated with failure along prior beta grain boundaries.

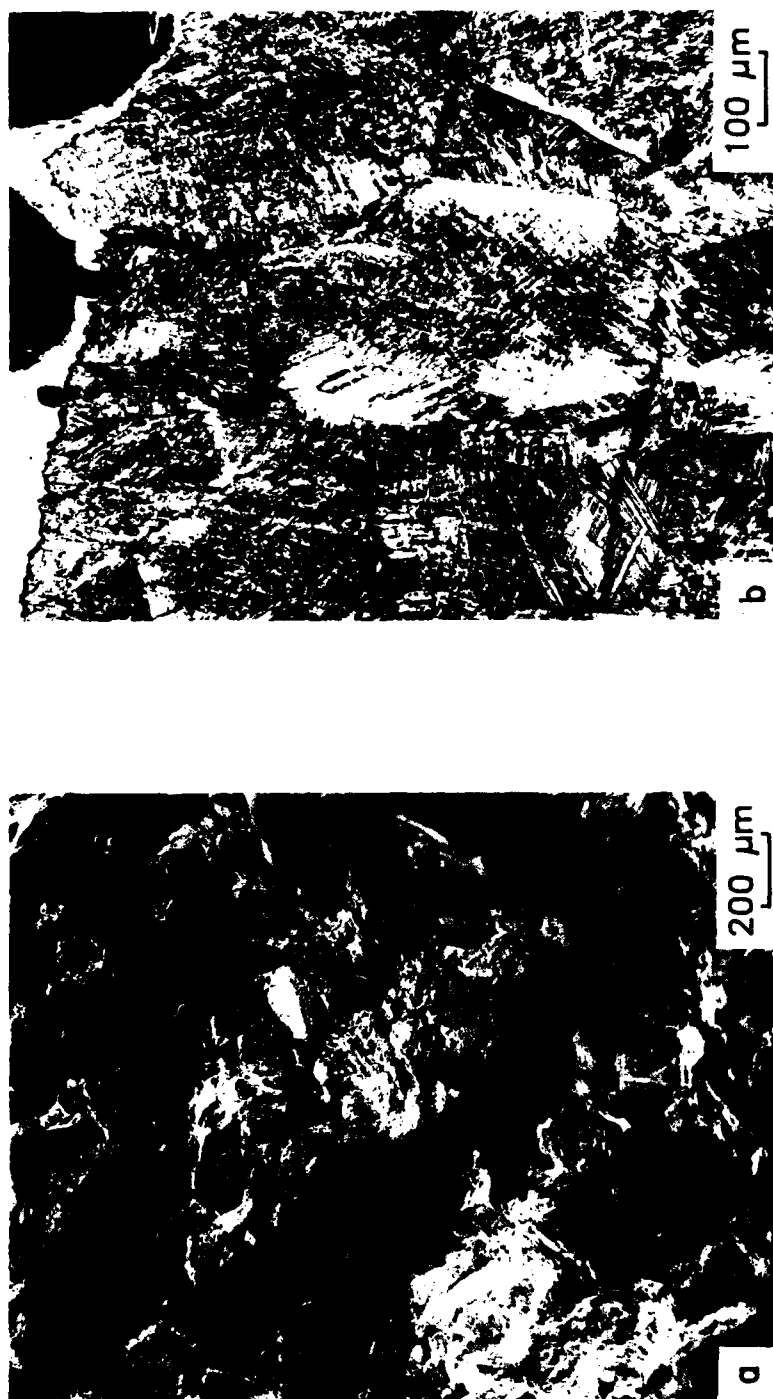


Figure 5.91 Fractograph (a) and optical micrograph (b) of Ti-6Al-2V tested at 800°C. Transgranular failure is associated with failure along Widmanstätten colony boundaries.

possibility, which will be discussed in a later section, is that the extent of strain localization within the colony structure is much greater in the case of the martensitic structures than in the basketweave structures.

5.4 Deformation of the Colony Structure

The implication of colony deformation by localized planar slip is consistent with previous work (135) describing the deformation of materials with lamellar microstructures. However, the characteristics of the high temperature ductility loss require that any proposed deformation mechanism be either activated or enhanced by an increase in temperature. One possible explanation is that an interaction stress of the type proposed by Margolin (136) contributes significantly to localized planar slip. In a study of alpha-beta brass bicrystals, Margolin calculated that the passage of slip from one phase to the other was further aided by the elastic stress field set up at the alpha-beta interface. He proposed that the alternating stress field set up in a lamellar structure would greatly enhance the passage of dislocations in a particular crystallographic direction, creating an effect similar to that of localized softening due to particle shearing. The interaction stress would have the requisite temperature dependence, having the greatest effect at temperatures

immediately below the beta to alpha transformation, where the bulk material strength was the lowest.

Chan, et. al, (135) studied the deformation of Ti-Al-Mn Widmanstatten colonies and got somewhat different results. They found that the extent of strain localization in a lamellar microstructure could not be associated with any particular orientation of alpha, beta, and stress axis, either crystallographic or microstructural. Because of this, they concluded that the stress field postulated by Margolin (136) was not a significant factor. Chan et. al. did allow however, that the magnitude and effect of any stress fields was a complex function of temperature and the properties of the two phases, and that generalizations should not be made.

More significantly, Chan, et. al. (135) found that two distinct classes of behavior existed in describing the deformation of Widmanstatten colonies. The first type of behavior was characterized by uniform deformation of the colony by slip contained within the alpha lamellae. In this case, deformation occurred in the alpha phase but the dislocations were not able to shear the beta phase. This happened when slip in the alpha occurred either on a single favorably-oriented slip system which was unable to shear the beta or simultaneously on several slip systems. In these

samples, there little or no evidence was found of gross, localized slip.

The second class of behavior identified by Chan, et. al. (135) was colony deformation by gross planar slip. In this case, the first alpha system on which slip occurred was able to shear the beta phase. Slip then continued on this system and led to very localized deformation. Chan et. al. observed macroscopic slip on all basal, prismatic, and pyramidal slip systems, but in all cases of gross localized deformation, slip within the alpha phase occurred on a basal system. This suggests that gross localized deformation of Widmanstatten colonies may be associated with the occurrence of primarily basal slip.

The slip character of alpha titanium is a sensitive function of composition and temperature. In an ideal hcp lattice, the c/a ratio is approximately 1.63 and slip occurs primarily on basal systems. However, alpha titanium has a c/a ratio of approximately 1.585 and slip occurs primarily on prismatic systems. In this study, it was found that the alpha phase of all the alloys was essentially Ti-6Al. In all cases, the room temperature c/a ratio was approximately 1.595. Because the alloys in this study very similar to those of Chan, et. al., it can be concluded that the addition of basal and pyramidal slip that they observed

results from the increase in c/a ratio. It was also found in this study that the c/a ratio of all of the alloys increased with temperature, from 5.595 at room temperature to approximately 1.610 at 900°C. Combined with the results of Chan, this suggests that an increased tendency toward localized deformation of the Widmanstatten colonies at high temperatures may be associated with a change in slip character of the alpha phase.

5.5 Overall Deformation Behavior

Based on the above observations, the conclusion can be made that within the temperature region associated with low ductility, the behavior of these materials is controlled by the deformation of the Widmanstatten colonies. Within this temperature range, the failures occur because of localized slip within the colonies, leading to microvoid nucleation and coalescence at the colony boundaries. The strength and ductility of the alloys tested can be directly related to the properties of the colony structure.

Outside the temperature range associated with the ductility loss, the mechanical properties of the material cannot be directly related to the characteristics of the colony structure. Two possible explanations exist for this behavior. The first is simply that the strength levels of the colony and basketweave microstructures are roughly the

same at room temperature, but vary enough at high temperature to concentrate slip within the colonies. This is the "differential strength" model proposed by Starke, et. al. (55) applied to the basketweave and colony microstructures, rather than to the grain boundary alpha film and grain matrix. The differential strength model, applied to the Widmanstatten colonies, is consistent with the behavior of the martensitic samples as well. In the case of Ti-6211, the majority of the samples have a microstructure consisting of Widmanstatten colonies and alpha' martensite. In these structures, the slip paths in the colony structure are short, but the strength differential is great enough to localize slip within the colonies. This leads to localized slip and microvoid nucleation, but on a much finer scale than is the case in the basketweave samples.

As the cooling rate is lowered, eventually a point is reached where the transformation structure of Ti-6211 is mostly Widmanstatten colonies. The material still has low ductility, but now the fracture surface appears to be a mixture of intergranular and transgranular failure. This mixed appearance corresponds to failure at both the prior beta grain boundaries and colony boundaries. In this case, the strength differential is not as great but the slip paths

in the colony structure are much longer. The result is that the slip band spacing and microvoid distribution are much coarser than in the martensitic samples. Figure 5.92 contains fractographs of both martensitic and non-martensitic Ti-6211 samples. A comparison of the relative size of the dimples in the two fractographs confirms that microvoid nucleation occurs on a much finer scale in the case of the martensitic sample.

This interpretation is further supported by the true stress-true strain curves for Ti-6211 shown in Figure 5.93. The curves in Figure 5.93 are for samples which have been cooled at different rates and tested within the temperature range of low ductility. The curves for cooling rates other than 0.17°C/s are all very similar. The microstructures associated with these cooling rates are martensitic. The curve for the sample cooled at 0.17°C/s differs markedly the others, this sample having far lower strength. This is consistent with the observation that the sample cooled at 0.17°C/s has a microstructure consisting of all Widmanstätten colonies.

An interesting observation that can be made in the case of the martensitic samples is that the fracture surfaces closely resemble those associated with creep failures, both in titanium and other alloy systems (55, 134). This

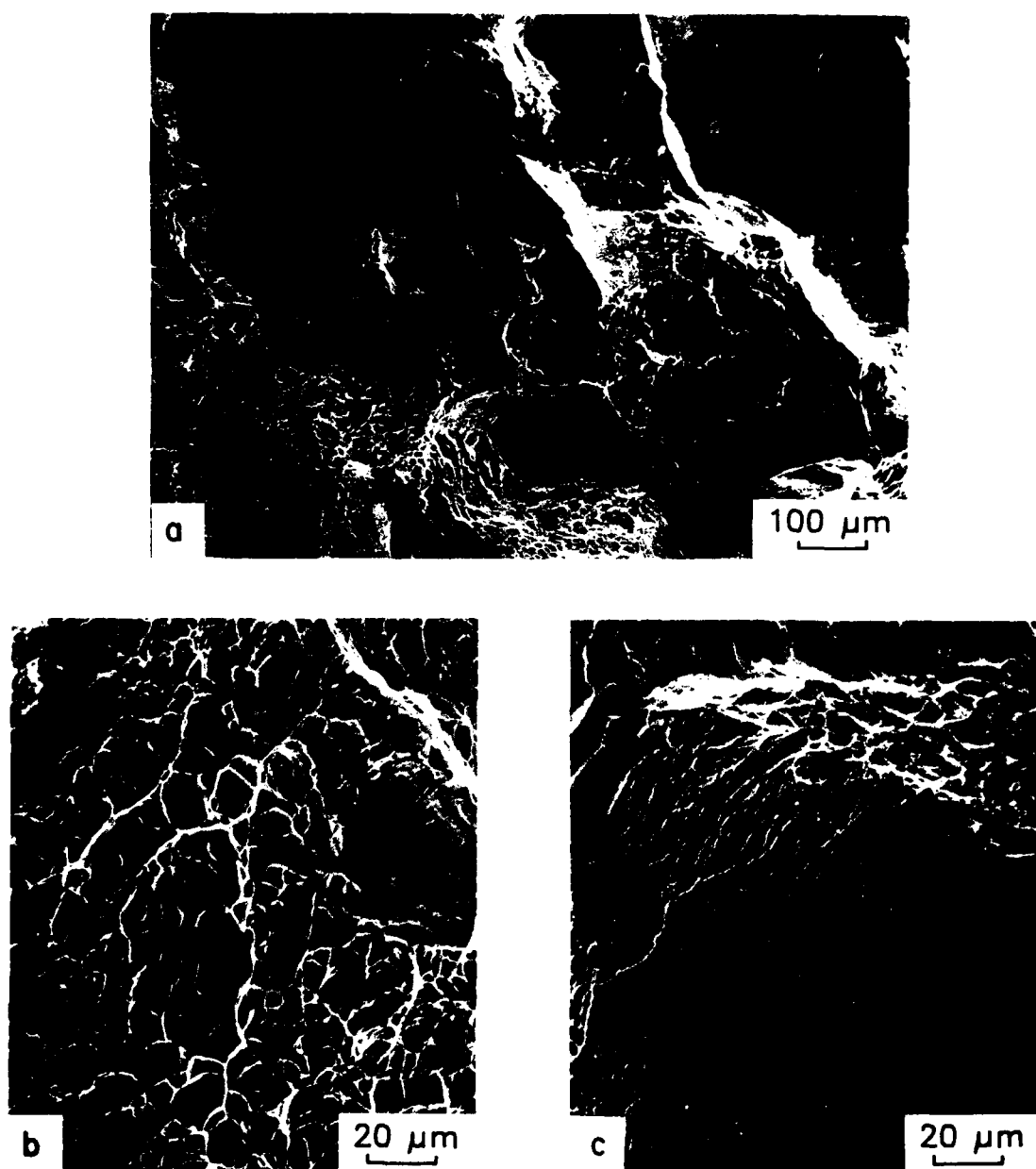


Figure 5.92 Fractographs of Ti-6211, tested at 770°C during a cool of 10°C/s . Fracture surface shows evidence of both transgranular (b) and intergranular (c) failure.

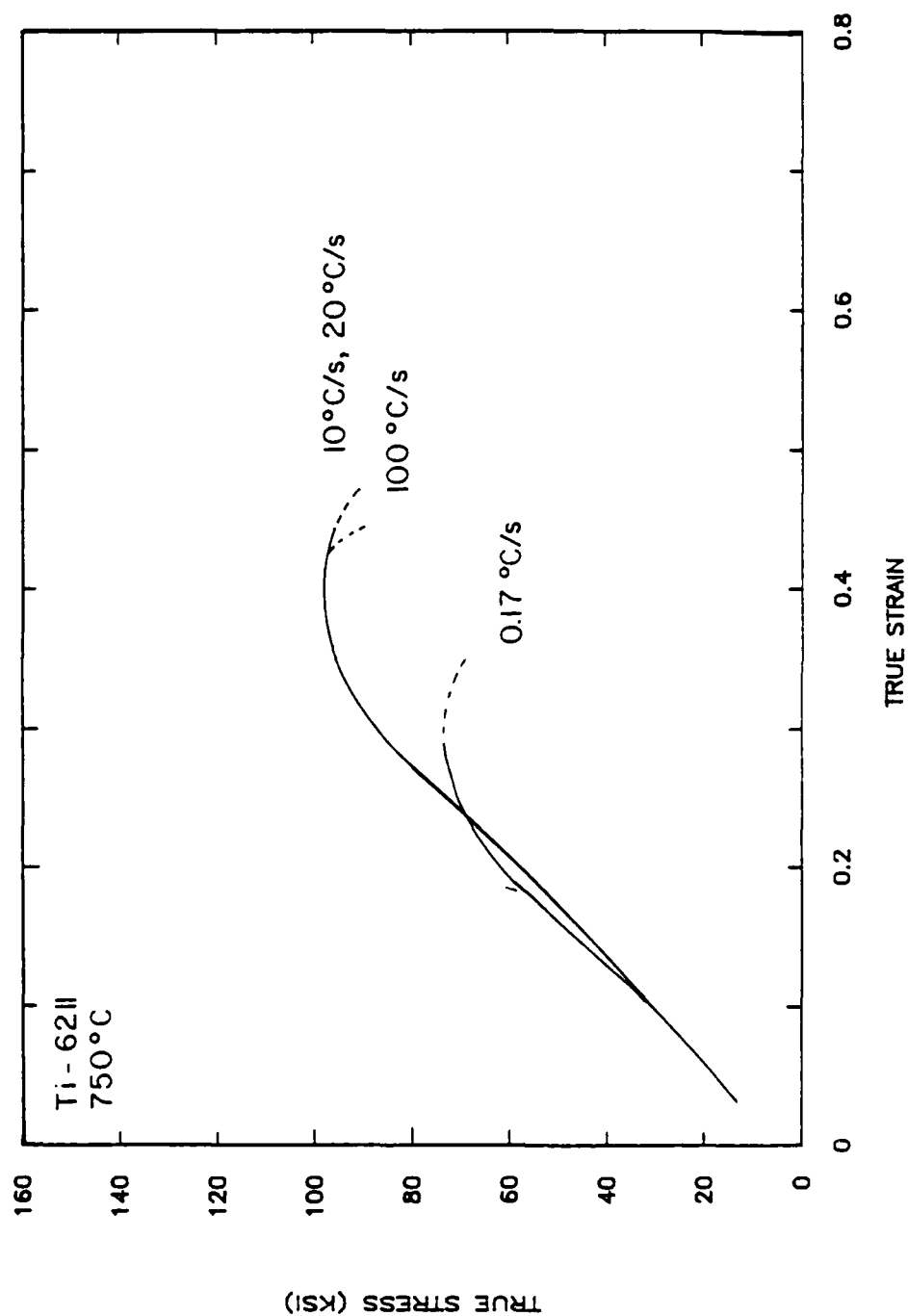


Figure 5.93 True stress-true strain curves for Ti-6211 tested at 750°C, showing different behavior of samples cooled at 0.17 °C/s to produce a Widmanstätten colony structure.

suggests that although the low ductility failures are associated with a stress and strain rate regime far removed from creep testing, there may be common elements in the failure mechanisms. In the case of the martensitic samples, the extremely low ductility appears to be related to a very fine distribution and high density of microvoids on the prior beta grain boundaries. Matlock (134) found that the ductility of Nickel, measured as creep strain to failure, behaved in a similar manner. He found that the creep strain to failure was significantly lowered by the introduction of pre-existing microvoids. He also observed a change in fracture surface appearance similar to that shown in Figure 5.89.

A second possible explanation for the temperature dependence of the strain localization within the colony structure is a change in the slip character of the alpha phase. At low temperatures, the c/a ratio of the alpha phase of the alloys studied is approximately 1.595. Slip in the alpha phase occurs on several systems, leading to fairly uniform deformation. The long slip paths of the colony structure have little effect on the overall slip character of the material. At temperatures within the ductility dip region however, the c/a ratio is approximately 1.61, much nearer the ideal hcp c/a ratio of 1.63. At these

temperatures, slip within the alpha phase occurs primarily on a single system. Because of the long slip paths in the colony structure, the tendency toward single slip makes this structure enough weaker than the grain matrix to localize slip in the colonies. This mechanism is supported by the transmission microscopy of Starke (55) and Lewis (133), both of whom show localized slip in Widmanstätten colonies tested at high temperature. Other investigators have shown localized slip in Widmanstätten colonies at low temperatures, but Chan et. al. (135) showed that while several slip systems are active at room temperature, gross localized slip could be achieved only by proper orientation of the basal slip system. This model could be tested fairly easily by an investigation of the slip character of the colony and basketweave structures at temperatures both within and outside of the hot ductility dip region. Unfortunately, such an investigation is beyond the scope of this study and will be left to a future investigation.

SUMMARY AND CONCLUSIONS

The phase stability, transformation kinetics, lattice incompatibility, and high temperature ductility of several model alloys have been studied. A particular mechanism has been proposed for the beta to alpha transformation of these alloys and has been found to be consistent with the metallographic observations. This mechanism has been modelled based on isothermal kinetic equations and the additivity principle. Although very rudimentary, this model has been shown to qualitatively predict the observed changes in microstructures and transformation kinetics caused by changes in system variables.

The lattice incompatibility of these alloys was calculated, based on a system of measurements and two specific assumptions regarding the development of a transformation-induced stress. In both cases, it was found that the lattice incompatibility varied with alloy content, being highest for Ti-Al-Nb ternary alloys and lowest for the commercial alloys Ti-6211 and Ti-6Al-4V.

The hot ductility testing of these alloys showed that the high temperature ductility loss previously reported in specific alloys occurred in all the alloys tested. The extent and severity of the ductility loss were found to be

strong functions of cooling rate. This suggests that the previously reported differences between various alloys are at least partially due to the cooling rate dependence of the individual alloys. It was found that the high temperature ductility of these alloys could not be related to lattice incompatibility, disproving the lattice incompatibility model originally proposed by Rath (4).

The ductility behavior of these alloys was found to correlate with their transformed microstructures. In particular, it was shown that within the hot ductility dip region, the ductility of these alloys is controlled by the deformation of the Widmanstätten colonies. Within this region, good correlation was found between the characteristics of the colony structure and the ductility loss. At temperatures outside of the hot ductility dip region, the ductility of these alloys could not be related to the colony structure. This shows that the strain characteristics of the microstructure change with temperature. At low temperatures, the strain is uniformly distributed. However, within the hot ductility dip region, strain is localized in the colony structure.

Two reasons for this temperature dependence have been proposed. The first is the "differential strength" model proposed by Ståke (55), now applied to the colony and

basketweave microstructures, rather than to the grain boundary alpha film and grain matrix. The second proposed explanation is that the slip character of the alpha phase changes in such a way that within the hot ductility dip region, the long slip paths in the colony structure become the dominant factor.

Based on the observations made in this study, the following conclusions can be drawn.

- 1) The high temperature ductility loss is universal in alpha-beta titanium alloys.
- 2) The extent and severity of the high temperature ductility loss vary with changes in alloy content, but vary more with changes in cooling rate for an individual alloy.
- 3) The extent and severity of the high temperature ductility loss cannot be related to gross volumetric lattice incompatibility, as was originally proposed by Rath (4).
- 4) The cooling rate dependence of the high temperature ductility loss is related to changes in transformed microstructure, rather than to the dynamic conditions of rapid cooling.
- 5) The microconstituent associated with the high temperature ductility loss is the Widmanstätten

colony structure rather than the grain boundary alpha film as has been previously reported.

- 6) Within the temperature range associated with the ductility loss, strain is concentrated in the colony structure, and the characteristics of this structure control the ductility of the material. Outside of this temperature range, the strain localization either does not occur or occurs to a far lesser degree.
- 7) The high temperature behavior of Ti-6211 is much worse than any of the other alloys tested, with the exception of Ti-6Al-4Nb cooled at 50°C/s. This is due to the presence of alpha' martensite in these samples. Alpha' localizes strain in the colony structure more effectively than the basketweave alpha-beta structure which exists in the other alloys.

FUTURE WORK

This study was designed to evaluate the validity of the lattice incompatibility model proposed by Rath (4). It was found that the gross volumetric lattice incompatibility could not be related to high temperature ductility. However, this conclusion was based on a specific interpretation of lattice incompatibility as well as a particular set of measurements and calculations. Both the concept of gross volumetric lattice incompatibility and the measurements used would benefit from further evaluation and development. Most significantly, it is quite possible that the concept and experimental techniques used do not accurately characterize the conditions that exist during the transformation. A particular concern is the possibility of dynamic and local partitioning during the transformation. The local partitioning could be studied by mapping the compositional profiles near the prior beta grain boundaries in quenched samples. A study of the dynamic aspect of the transformations would require further development of a facility capable of making lattice parameter measurements under dynamic condition. An example of such a facility is the neutron diffraction laboratory at Risø.

A second aspect of this investigation which would

benefit greatly from further work is the transformation kinetics modelling. In addition to further development in a general sense, this model should be supported by comparison of the experimentally derived constants with similar values based on isothermal studies. Reported values of physical quantities, diffusivity for example, could also be compared to those used in the model. A second source of verification for this model would be to compare its predictions with in-situ measurements of transformation kinetics. This experimental capability could also be developed using the neutron diffraction facility at Risø.

This investigation has shown that within the hot ductility dip region, the ductility is controlled by deformation of the Widmanstätten colony structure. However, strain localization in the colony structure does not occur at lower temperatures. One of the proposed explanations for this temperature dependence is based on the assumption of changing slip character of the alpha phase. This assumption, as well as characterization of the slip character of the various microconstituents, should be studied by transmission microscopy of samples containing a wide range of microstructures and tested at temperatures within and outside of the hot ductility dip region.

LIST OF REFERENCES

1. Smith, W. 1981. Structure and Properties of Engineering Alloys. New York: McGraw-Hill.
2. Jaffee, R. 1980. "An Overview of Titanium Development and Application". In Titanium '80, H. Kimura and O. Izumi, eds., 53-74. TMS-AIME, Warrendale, Pa.
3. Williams, J. 1980. "Marine Applications of Titanium". In The Science, Technology, and Application of Titanium. Pergamon, New York.
4. Rath, B. B., and Judy, R. 1982. Naval Research Laboratory, Washington, D.C. Private communication with D. Olson, Colorado School of Mines, 1982.
5. Lukins, W. 1982. David W. Taylor Naval Ship Research and Development Center, Annapolis, Md. Research in Progress.
6. Lewis, R., and Caplan, I. 1982. "Hot Ductility Behavior of Ti-6211". In Conference Proceedings, Ti-6211 Basic Research Program, B. B. Rath, B. A. MacDonald, and O. Arora, eds., 331-344. ONR, Arlington, Va.
7. Collings, E. W. 1984. The Physical Metallurgy of Titanium Alloys. ASM, Metals Park, Ohio.
8. Eylon, D., ed. 1981. Titanium for Energy and Industrial Applications. TMS-AIME, Warrendale, Pa.
9. Borradaile, J. and Jeal, R. 1980. "Critical Review: Mechanical Properties of Titanium Alloys". In Titanium '80, H. Kimura and O. Izumi, eds., 143-152. TMS-AIME, Warrendale, Pa.
10. Kusamichi, H., et. al. 1985. "Critical Review: Industrial Application". In Titanium Science and Technology, v. 4, G. Lutjering, U. Zwicker, and W. Bunk, eds., 1605-1612. Deutsche Gesellschaft für Metallkunde, e. V., Oberursel, FRG.

11. Duerig, T. W., and Williams, J. C. 1984. "Overview: Microstructures and Properties of Beta Titanium Alloys". In Beta Titanium In The 1980's, R. R. Boyer and H. W. Rosenberg, eds., 19-68. TMS-AIME, Warrendale, Pa.
12. Bowden, D. M., et. al. 1984. "Investigation of the Effect of Microstructure on the Deformation Modes and Mechanical Properties of Ti-6Al-2Nb-1Ta-0.8Mo". In Conference Proceedings, Ti-6211 Basic Research Program, v. 3, B. B. Rath, B. A. MacDonald, and O. Arora, eds., 55-118. ONR, Arlington, Va.
13. Edwards, G. R., Olson, D. L. and Matlock, D. K. "Titanium Welding Metallurgy: Cracking Susceptibility". In Conference Proceedings, Ti-6211 Basic Research Program, v. 3, eds. B. B. Rath, B. A. MacDonald, and O. Arora, 217-242, ONR, Arlington, Va.
14. Ingelbrecht, C. D. 1985. "The Effect of Ageing (sic) on Ti-8Al-1Mo-1V Alloy". In Titanium Science and Technology, v. 4, G. Lutjering, U. Zwicker, and W. Bunk, eds., 2541-2548. Deutsche Gesellschaft fur Metallkunde, e. V., Oberursel, FRG.
15. Rhodes, C., and Patton, N. 1979. "Formation Characteristics of the Alpha/Beta Interface Phase in Ti-6Al-4V". Met. Trans. 10A: 209-216.
16. Rhodes, C., and Williams, J. 1975. "Observations of an Interface Phase in the Alpha/Beta Boundaries in Titanium Alloys". Met. Trans. 6A: 1670-1671.
17. Margolin, H., et. al. 1977. "The Interface Phase in Alpha-Beta Titanium Alloys". Met. Trans. 8A: 373-377.
18. Rhodes, C., and Williams, J. 1975. "The Precipitation of Alpha-Phase in Metastable Beta-Phase Ti Alloys". Met. Trans. 6A: 2103-2114.
19. Baselack, W., and Mahajan, Y. 1979. "Intergranular Fracture of Heat Treated Weldments in a High-Strength Alpha-Beta Titanium Alloy". Scripta Met. 13: 959-964.

20. Lin, F., et. al. 1982. "Investigation of the Effect of Microstructures on the Deformation Modes and Mechanical Properties of Ti-6Al-2Nb-1Ta-0.8Mo". In Conference Proceedings, Ti-6211 Basic Research Program, B. B. Rath, B. A. MacDonald, and O. Arora, eds., 47-128. ONR, Arlington, Va.
21. Rhodes, C., and Patton, N. 1979. "The Influence of Alpha/Beta Interface Phase on Tensile Properties of Ti-6Al-4V". Met. Trans. 10A: 1753-1758.
22. Rhodes, C. 1980. "Influence of Alpha/Beta Interface on Fracture Toughness and Fatigue Crack Growth Rate in Ti-6Al-4V". In Titanium '80, H. Kimura and O. Izumi, eds., 1691-1700. TMS-AIME, Warrendale, Pa.
23. Isaac, G. H., and Hammond, C. 1985. "The Formation of Type 2 α Phase in Ti-3Al-8V-6Cr-4Zr-4Mo". In Titanium Science and Technology, v. 4, G. Lutjering, U. Zwicker, and W. Bunk, eds., 1605-1612. Deutsche Gesellschaft fur Metallkunde, e. V., Oberursel, FRG.
24. Banerjee, D., Rhodes, C. G., and Williams, J. C. 1985. "On the Nature of α/β Interfaces in Titanium Alloys". In Titanium Science and Technology, v. 4, G. Lutjering, U. Zwicker, and W. Bunk, eds., 1597-1604. Deutsche Gesellschaft fur Metallkunde, e. V., Oberursel, FRG.
25. Greenfield, M., et. al. 1980. "The Effect of Microstructure on the Control of Mechanical Properties in Alpha-Beta Titanium Alloys". In Titanium '80, H. Kimura and O. Izumi, eds., 1731-1741. TMS-AIME, Warrendale, Pa.
26. Margolin, H., and Stanescu, M. S. 1975. "Polycrystalline Strengthening". Acta Met. 23: 1411-1418.
27. Mahajan, Y., and Baeslack, W. 1979. "Intergranular Fracture of Heat-Treated Weldments in a High-Strength Titanium Alloy". Scripta Met. 13: 1125-1129.
28. Greenfield, M., and Margolin, H. 1972. "The Mechanism of Void Formation, Void Growth, and Tensile Fracture in an Alloy Consisting of Two Ductile Phases". Met. Trans. 3A: 2649-2659.

29. Greenfield, M., and Margolin, H. 1971. "The Interrelationship of Fracture Toughness and Microstructure in a Ti-5.25Al-5.5V-0.9Fe-0.5Cu Alloy". Met. Trans. 2A: 841-847.
30. Gerberich, W. 1967. "Some Observations on Crack Extension in Two Phase Materials". Trans. AIME. 239: p. 753.
31. Terlinde, G., and Lutjering, G. 1982. "Influence of Grain Size and Age-Hardening on Dislocation Pile-Ups and Tensile Fracture for a Ti-Al Alloy". Met. Trans. 13A: p. 1283-1292.
32. Margolin, H., and Mahajan, Y. 1978. "Void Formation, Void Growth, and Tensile Fracture in Ti-6Al-4V". Met. Trans. 9A: 781-791.
33. Baeslack, W., and Mahajan, Y. 1980. "Observation of Alpha-Beta Interface Sliding in a Titanium Alloy Weld Metal". Met. Trans. 9A: 1234-1238.
34. Mahajan, Y., and Margolin, H. 1978. "Surface Cracking in Alpha-Beta Titanium Alloys Under Unidirectional Loading". Met. Trans. 9A: 427-431.
35. Li, J. 1963. "Petch Relation and Grain Boundary Sources". Trans. AIME. 227: 239-247.
36. Zuhan, L., et. al. 1980. "The Initiation and Propagation of Shear Band and Crack During Torsional Deformation of Ti-7Al-4Mo". In Titanium '80, H. Kimura and O. Izumi, eds., 1757-1774. TMS-AIME, Warrendale, Pa.
37. Welsch, G., et. al. 1977. "Deformation Characteristics of Age Hardened Ti-6Al-4V". Met. Trans. 8A: 169-177.
38. Shull, R. D., et. al. 1984. "Phase Stability in the Ti-Al-Mo-Cb-Ta System". In Conference Proceedings, Ti-6211 Basic Research Program, v. 3, B. B. Rath, B. A. MacDonald, and O. Arora, eds., 1-32, ONR, Arlington, Va.
39. Blackburn, M. J., and Williams, J. C. 1969. "Strength, Deformation Modes and Fracture in Titanium-Aluminum Alloys". Trans. ASM. 62: 398-409.

40. Evans, K. R. 1969. "The Embrittlement and Fracture of Ti-8 pct Al Alloys". Trans. TMS-AIME. 245: 1297-1303.
41. Gysler, A., Lutjering, G., and Gerold, V. 1974. "Deformation Behavior of Age-Hardened Ti-Mo Alloys". Acta Met. 22: 901-909.
42. Cottrell, A. 1958. "Theory of Brittle Fracture in Steel and Similar Metals". Trans. AIME. 212: 192-200.
43. Margolin, H., et. al. 1980. "A Review of the Fracture and Fatigue Behavior of Ti Alloys". In Titanium '80, H. Kimura and O. Izumi, eds., 169-216. TMS-AIME, Warrendale, Pa.
44. Lin, F. S., et. al. 1984. "The Effect of Microstructure on the Deformation Modes and Mechanical Properties of Ti-6Al-2Nb-1Ta-0.8Mo: Part 1. Widmanstatten Structures". Met. Trans. 15A: 1229-1246.
45. Margolin, H. and Rozenberg, L. 1981. "Void Nucleation, Void Growth and Tensile Fracture in As-Quenched and Aged Ti-6Al-4V". In Titanium '80, H. Kimura and O. Izumi, eds., 1637-1643. TMS-AIME, Warrendale, Pa.
46. Baselack, W. A., and Becker, D. W. 1979. "Fusion Zone Fracture Behavior of Weldments in Alpha-Beta Titanium Alloys". Met. Trans. 10A: 1803-1806.
47. Chestnutt, J. C., Rhodes, C. G., and Williams, J. C. 1976. "Relationship Between Mechanical Properties, Microstructure, and Fracture Topography in $\alpha + \beta$ Titanium Alloys". In ASTM STP 600, 99-138. ASTM.
48. Ball, M. J. 1977. "Factors Affecting the Ductility and Microstructure of Ti-6Al-6V-2Sn Titanium Alloy Weldments". In The Science, Technology, and Application of Titanium, 573-584. Pergamon, New York.
49. Lewis, R. E. 1982. "Metallurgical Investigation of Fracture in the Ti-6211 Alloy". In Conference Proceedings, Ti-6211 Basic Research Program, B. B. Rath, B. A. MacDonald, and O. Arora, eds., 297-330. ONR, Arlington, Va.

50. Gordine, J. 1974. "Weld Heat-Affected Zones in Titanium-6Al-2Cb-1Ta-1Mo". Welding Journal 53: 117s-124s.
51. Inouye, H., and David, S. 1984. "Solidification Behavior and Microstructural Analysis of Titanium Alloy Welds". In Conference Proceedings, Ti-6211 Basic Research Program, v. 2, B. B. Rath, B. A. MacDonald, and O. Arora, eds., 229-244. ONR, Arlington, Va.
52. Lewis, R. E. Lockheed Missiles and Space Co., Palo Alto, California. Private communication, 1984.
53. Clark, H. T. 1949. "The Lattice Parameters of High Purity Alpha Titanium; and the Effects of Oxygen and Nitrogen on Them". Met. Trans. 185: 588-589.
54. Lin, F. S., Starke, E. A., and Gysler, A. 1984. "The Effect of Microstructure on the Deformation Modes and Mechanical Properties of Ti-6Al-2Nb-1Ta-0.8Mo: Part II. Equiaxed Structures". Met. Trans. 15A: 1873-1881.
55. Bowden, D. M., and Starke, E. A. 1984. "The Effect of Microstructure on the Hot Ductility of Ti-6Al-2Nb-1Ta-0.8Mo". Met. Trans. 15A: 1687-1698.
56. Miller, W. H., Chen, R. T., and Starke, E. A. 1987. "Microstructure, Creep, and Tensile Deformation in Ti-6Al-2Nb-1Ta-0.8Mo". Met. Trans. 18A: 1451-1468.
57. Inouye, H., and David, S. 1984. "Segregation and Influence of Boron on the Impact Toughness of Ti-6 Pct Al-2 Pct Nb-1 Pct Ta-0.8 Pct Mo Welds and Castings". Met. Trans. 15A: 1505-1506.
58. David, S. Oak Ridge National Laboratory, Oak Ridge, Tn. Private communication with D. Olson, Colorado School of Mines, 1984.
59. Ushkov, S. S. 1980. "Intergranular Fracture of Titanium Alpha-Alloys at Temperatures Above $0.5T_m$ ". In The Science, Technology, and Application of Titanium, 705-713. Pergamon, New York.

60. Rao, Y. K., et. al. 1980. "Fracture Mechanism Map for Alloy Ti-6Al-4V". In Titanium '80, H. Kimura and O. Izumi, eds., 1701-1707. TMS-AIME, Warrendale, Pa.
61. Krishnamohanrao, Y., et. al. 1986. "Fracture Mechanism Maps for Titanium and its Alloys". Acta Met. 34: 1783-1806.
62. Edwards, G. R., Olson, D. L., and Matlock, D. K. 1982. "Welding Metallurgy: Cracking Susceptibility". In Conference Proceedings, Ti-6211 Basic Research Program, B. B. Rath, B. A. MacDonald, and O. Arora, eds., 345-362. ONR, Arlington, Va.
63. Hayduk, D., et. al. 1986. "Cracking Susceptibility of Ti-6Al-2Nb-1Ta-0.8Mo as Determined by the Varestraint Test". Welding Journal 65: 251s-260s.
64. Hayduk, D. 1983. "The Cracking Susceptibility of Ti-6Al-2Nb-1Ta-0.8Mo as Determined by the Varestraint Test". Master's thesis, Colorado School of Mines, Golden, Colorado.
65. Nordin, M. C. 1984. "The Effect of Yttrium Additions on Grain Refinement and Cracking Susceptibility of Ti-6Al-2Nb-1Ta-0.8Mo Weld Metal". Master's thesis, Colorado School of Mines, Golden, Colorado.
66. Hayduk, D., et. al. 1984. "Titanium Welding Metallurgy". In Conference Proceedings, Ti-6211 Basic Research Program, v. 2, B. B. Rath, B. A. MacDonald, and O. Arora, eds., 167-203 ONR, Arlington, Va.
67. Lewis, R. E. Lockheed Missles and Space Co., Palo Alto, California. Private communication, 1984.
68. Berger, L. W., Williams, D. N., and Jaffee, R. I. 1957. "The Effect of Sulfur on the Properties of Titanium and Titanium Alloys". Trans. ASM. 49: 300-311.
69. Starke, E. A. University of Virginia, Richmond, Va. Private communication, 1984.

70. Judy, R. W., and Rath, B. B. 1983. "Role of Transformation Microstructure on High Temperature Deformation of Ti-Alloys". ONR Proposal No. 63-003-83-84, Submitted by the Naval Research Laboratory, Washington, D.C.
71. Pearson, W. B. 1965. Handbook of Lattice Spacings and Structures of Metals Alloys, v. 4. 872-878. Pergamon, New York.
72. Saito, S., Shimura, M., and Tanaka, E. 1980. "Fracture Behavior of Ti-6Al-4V Alloy Subjected to Hydrostatic Tension". In Titanium '80, H. Kimura and O. Izumi, eds., 1686-1690. TMS-AIME, Warrendale, Pa.
73. Price, C. and Hirth, J. 1972. "A Mechanism for the Generation of Screw Dislocations from Grain-Boundary Ledges". Matl. Sci. Engr. 9: 15-18.
74. Hull, D. and Rimmer, D. E. 1959. "The Growth of Grain-boundary Voids Under Stress". Phil. Mag. 4: 673-687.
75. Gleeble 1500 Product Information. 1985 Duffers Scientific Inc., Troy, New York.
76. Adenstedt, H. K., Pequignot, J. R., and Raymer, J. M. 1952. "The Titanium-Vanadium System". Trans. ASM 44: 990-1003.
77. Duwez, P. 1951. "Effect of Cooling Rate on the Alpha-Beta Transformation in Titanium and Titanium-Molybdenum Alloys". Trans. AIME, J. Metals 191: 765-771.
78. Hansen, M., et. al. 1951. "Systems Titanium-Molybdenum and Titanium-Columbium". Trans. AIME, J. Metals 191: 881-888.
79. Barrett, J. C. and Lane, I. R. 1954. "Effect of Atmospheric Contaminants on Arc Welds in Titanium". Welding Journal 33: 121s-128s.
80. Cullity, B. D. 1978. Elements of X-Ray Diffraction. 2nd ed. Reading, Massachusetts: Addison-Wesley.

81. Baun, W. L. 1961. "Design and Applications of a Variable-Temperature Diffractometer Specimen Mount". Technical Report, Wright Air Development Division, Dayton, Ohio.
82. Barrett, C. and Massalski, T. B. 1980. Structure of Metals. 3rd ed. Pergamon, New York.
83. Cohen, M. U. 1935. "Precision Lattice Constants from X-Ray Powder Photographs". Rev. Sci. Instrum. 6: 68-74.
84. Nelson, J. B. and Riley, D. P. 1945. "An Experimental Investigation of Extrapolation Methods in the Derivation of Accurate Unit-Cell Dimensions of Crystals". Proc. Phys. Soc. London 57: 160-177.
85. Vold, C. Naval Research Laboratory, Washington, D.C. Private communication, 1984.
86. Huppi, G. S., Damkroger, B. K., and Dallam, C. B. 1985. "Weldments". In Metallography and Microstructures, Metals Handbook. 9th ed. 9: 577-586.
87. Damkroger, B. K. and Edwards, G. R. 1987. Unpublished research.
88. Margolin, H. 1983. "Titanium-Aluminum Phase Diagram". In Atlas of Microstructures and Phase Diagrams, Metals Handbook. 8th ed. 8: 564.
89. Gibbs, G. B., Graham, D., and Tomlin, D. H. 1963. "Diffusion in Titanium and Titanium-Niobium Alloys". Phil. Mag. 8: 1269-1282.
90. Murdock, J. F., Lurdy, T. S., and Stansbury, E. E. 1964. "Diffusivities in the Body-Centered-Cubic Phase of Titanium". Acta Met. 12: 1033-1043.
91. Murakami, Y. 1980. "Critical Review: Phase Transformation and Heat Treatment". In Titanium '80, H. Kimura and O. Izumi, eds., 153-167. TMS-AIME, Warrendale, Pa.
92. Farrar, P. A. and Margolin, H. 1961. "The Titanium Rich Region of the Titanium-Aluminum-Vanadium System". Trans. AIME. 221: 1214-1221.

93. Mahajan, Y., Nadiv, S., and Fujishiro, S. 1982. "Interface Phase in Ti-6242 Alloy". Scripta Met. 16: 375-379.
94. Rath, B. B. 1982. "The Overall Kinetics of Isothermal Transformations". In Solid+Solid Phase Transformations, H. I. Aaronson, D. E. Laughlin, R. F. Sekerka, and C. M. Wayman, eds., 1097-1103. TMS-AIME, Warrendale, Pa.
95. Avrami, M. 1940. "Kinetics of Phase Change. II Transformation-Time Relations for Random Distribution of Nuclei". J. Chem. Phys. 8: 212-224.
96. Cahn, J. W. 1956. "Transformation Kinetics During Continuous Cooling". Acta Met. 4: 572-575.
97. Kuban, M. B., et. al. 1986. "An Assessment of the Additivity Principle in Predicting Continuous Cooling Austenite-to-Pearlite Transformation Kinetics Using Isothermal Transformation Data". Met. Trans. 17A: 1493-1503.
98. Pumphrey, W. I. and Jones, F. W. 1948. "Inter-Relation of Hardenability and Isothermal Transformation Data". J. Iron and Steel Inst. 159: 137-144.
99. Hawbolt, E. B., Chau, B., and Brimacombe, J. K. 1983. "Kinetics of Austenite-Pearlite Transformation in Eutectoid Carbon Steel". Met. Trans. 14A: 1803-1815.
100. Hawbolt, E. B., Chau, B., and Brimacombe, J. K. 1985. "Kinetics of Austenite-Pearlite Transformation in a 1025 Carbon Steel". Met. Trans. 16A: 565-578.
101. Umemoto, M., Horiuchi, K., and Tamura, I. 1982. "Transformation Kinetics of Bainite during Isothermal Holding and Continuous Cooling". Trans. ISIJ. 22: 854-861.

102. Umemoto, M., Komatsubara, N., and Tamura, I. 1982. "The Equivalent Cooling Curve --- A New Method to Describe Continuous Cooling Transformation Kinetics on TTT Diagrams". In Solid+Solid Phase Transformations, H. I. Aaronson, D. E. Laughlin, R. F. Sekerka, and C. M. Wayman, eds., 1111-1115. TMS-AIME, Warrendale, Pa.
103. Cahn, J. W. 1956. "The Kinetics of Grain Boundary Nucleated Reactions". Acta Met. 4: 449-459.
104. Manning, G. K. and Lorig, C. H. 1946. "The Relationship between Transformation at Constant Temperature and Transformation during Cooling". Trans. AIME. 167: 442-453.
105. Avrami, M. 1939. "Kinetics of Phase Change. I General Theory". J. Chem. Phys. 7: 1103-1112.
106. Avrami, M. 1941. "Granulation, Phase Change, and Microstructure Kinetics of Phase Change. III". J. Chem. Phys. 9: 177-184.
107. Johnson, W. A. and Mehl, R. J. 1939. "Reaction Kinetics in Processes of Nucleation and Growth". Trans. AIME 135: 416-459.
108. Scheil, E. 1935. Archiv. fur Eisenhuttenwesen 12: 565-567. See Hawbolt 1983 (99).
109. Lewis, R. E., et. al. 1982. "Continuous Cooling Transformations in Ti-6Al-2Nb-1Ta-0.8Mo". In Solid+Solid Phase Transformations, H. I. Aaronson, D. E. Laughlin, R.F. Sekerka, and C.M. Wayman, eds., 1499-1503. TMS-AIME, Warrendale, Pa.
110. Rosenberg, H. W. 1978. Properties and Processing of Ti-6Al-4V. TIMET, Pittsburg.
111. Skelton, E. 1984. "Rapid High-Pressure Structural Information from Energy Dispersive Analyses of Diffracted Synchrotron Radiation". Advances in Earth and Planetary Sciences 12: 403-420.
112. Ruud, C. O. 1979. "X-Ray Measurements Using a Position-Sensitive Detector". J. Metals 31 (6): 10-15.

113. Damkroger, B. K., Juul Jensen, D., and Edwards, G. R. 1987. "In-Situ Measurement of Phase Transformation Kinetics using Neutron Diffraction". Scripta Met. In press.
114. Imam, M. A. Naval Research Laboratory, Washington, D.C. Private communication, 1984.
115. Vegard, L. 1921. Z. Phys 5: 17-26. See Pearson 1965 (71) 1-5.
116. Haag, G. 1931. Ztsch. f. Phys. Chem. 11: 133. See Clark 1949 (53).
117. Fast, J. D. 1939. Rec. Trav. Chim. 58: 972-983. See Clark 1949 (53).
118. Gonser, B. W. 1949. Met. Prog. 55: 346. See Clark 1949 (53).
119. Greiner, E. S. and Ellis, W. C. 1949. Trans. AIME, Met. Tech. 180: 657. See Clark 1949 (53).
120. Szanto, I. 1955. Acta Tech. Sci. Hung. 13: 363. See Pearson 1965 (71).
121. Bumps, E. S., Kessler, H. D., and Hansen, M. 1952. "Titanium-Aluminum System". Trans. AIME, J. Metals 194: 609-614.
122. Crossley, F. A. 1966. "Titanium-Rich End of the Titanium-Aluminum Equilibrium Diagram". Trans. TMS-AIME 236: 1174-1185.
123. Ogden, H. R., et. al. 1951. "Constitution of Titanium-Aluminum Alloys". Trans. AIME, J. Metals 191: 1150-1155.
124. Worner, H. W. 1952-53. "The Structure of Titanium-Tin Alloys in the Range 0-25 at.% Tin". J. Inst. Met. 81: 521-528.
125. Wu, K. C. 1968. "Continuous-Cooling Transformation Diagrams of Ti-8Al-1Mo-1V". Reprinted from Transactions Quarterly 61 (3).

126. Isaac, G. H., and Hammond, C. 1985. "The Formation of Type 2 α Phase in Ti-3Al-8V-6Cr-4Zr-4Mo. In Titanium Science and Technology, v. 4, G. Lutjering, U. Zwicker, and W. Bunk, eds., 1605-1612. Deutsche Gesellschaft fur Metallkunde, e. V., Oberursel, FRG.
127. Titanium Metallurgical Laboratory 1958. Compilation of Available Information on Ti-6Al-4V Alloy. TML Memo 148. See Rosenberg 1978 (110).
128. North American 1957. Product information. See Rosenberg 1978 (110).
129. Rem-Cru Titanium Inc. 1956. REM-CRU C-120AV, Ti-6Al-4V. Data sheet. See Rosenberg 1978 (110).
130. Hatch, A. J. and Parris, W. M. 1957. Alloy Evaluation Program Summary for 1956. TIMET, Pittsburg. See Rosenberg 1978 (110).
131. Lockheed Georgia Co. 1962. "Determination of Design Data for Heat Treated Alloy Sheet". In Tables of Data Collected, Air Force Contract AF 33(616)-6346. See Rosenberg 1978 (110).
132. Levinger, B. W. 1953. "Lattice Parameter of Beta Titanium at Room Temperature". Trans. AIME, J. Metals 198: 195-196.
133. Lewis, R. E. 1987. Metallurgical Investigation of Hot Ductility Loss in Ti-6211. Final Technical Report for ONR Contract N00014-79-C-0449, LMSC Report LMSC-F108004.
134. Matlock, D. K. Colorado School of Mines, Golden, Colorado. Private communication.
135. Chan, K. S., Wojcik, C.C., and Koss, D.A. 1981. "Deformation of an Alloy with a Lamellar Microstructure: Experimental Behavior of Individual Widmanstatten Colonies of an α - β Titanium Alloy". Met. Trans. 12A: 1899-1907.
136. Margolin, H. 1984. "Investigation of the Deformation of an α - β Brass Bicrystal" Met. Trans. 15A: 103-117.

APPENDIX A

IN-SITU MEASUREMENT OF PHASE TRANSFORMATION
KINETICS USING NEUTRON DIFFRACTION

(Paper Submitted for Publication in Scripta Metallurgica)

IN-SITU MEASUREMENT OF PHASE TRANSFORMATION KINETICS USING NEUTRON DIFFRACTION

B.K. Damkroger, D. Juul Jensen*, and G.R. Edwards

Center for Welding Research, Colorado School of Mines
Golden, Colorado

*Department of Metallurgy, Risø National Laboratory
Roskilde, Denmark

INTRODUCTION

Mathematical models describing the kinetics of isothermal transformation kinetics were originally derived by Johnson and Mehl, and Avrami. (1-4) Over the years these equations have been studied and modified but still form the basis for a description of isothermal phase transformation kinetics. (5,6,7) For practical purposes however, a prediction of transformation behavior under continuous cooling conditons is desired. Several attempts to model transformation kinetics for continuous cooling have been made. (8-11) Usually, the approach taken has been to treat continuous cooling as a series of discrete isothermal steps. Each step is then an increment of transformation, to be added to the other increments. (8,9,11) In most cases, the attempts at theoretical models have been hampered by a relative lack of experimental verification.

EXPERIMENTAL TECHNIQUES

Most studies of transformation kinetics involve "after the fact" metallographic analysis or x-ray diffractometry of several samples, each partially transformed and quenched. For each sample, the amount transformed is related to the elapsed time, allowing volume fraction transformed to be plotted as a function of time. This type of experiment can yield information regarding the kinetics of nucleation and growth as well as of the overall transformation. (7,12) However, direct in-situ measurement of transformation kinetics offers many advantages, most notably speed and flexibility.

Of the standard methods used to determine volume fraction of phases present, diffraction offers the greatest potential for performing in-situ transformation kinetics measurements by mapping the integrated intensity of diffraction as a function of time. This requires that systems be developed to continuously monitor a range of 2θ , the Bragg diffraction angle. Multi-detector x-ray diffraction systems capable of this have been used with some success in texture studies. (13) Recently, systems incorporating fiber optics have been developed to produce a position-sensitive x-ray detector system. (14) However, because x-ray diffraction is essentially a surface phenomenon the requirements exist for very stringent specimen handling procedures and atmosphere control. This is particularly true at the elevated temperatures usually associated with allotropic phase transformations.

Neutron diffraction, by being a bulk rather than a surface measurement, eliminates many of the experimental difficulties associated with x-ray diffraction while functioning in much the same way. A range of 2θ is selected in which diffraction peaks from both phases of interest appear. The continuous monitoring of this 2θ range provides direct measurement of volume fraction transformed as a function of time. Ideally, this technique also permits measurement of the lattice parameters of both phases during a transformation.

In-situ measurement of transformation kinetics using any type of diffraction has inherent limitations. Most significantly, in polycrystalline materials, integrated intensity cannot simply be taken to be equivalent to volume fraction. The use of diffraction for measurement of volume fraction of phases present requires a thorough knowledge of the diffraction characteristics of the material being studied. Factors which affect the integrated intensity of specific samples must also be considered, for example, grain size and texture.

EXPERIMENTAL SETUP

Recent advances in the neutron diffraction facility at the Danish National Laboratory at Risø have demonstrated the feasibility of using this system to make in-situ transformation kinetics measurements. This system has been used for in-situ measurement of recrystallization kinetics. (15,16) The basic unit for the transformation kinetics

measurements is the multipurpose spectrometer TAS3, at the Risø [23] reactor. This unit is a standard triple axis spectrometer modified by the addition of a linear position-sensitive detector and an Euler goniometer. A given wavelength is selected by a crystal monochromator. The position-sensitive detector is placed horizontally to cover a 2θ range of approximately 60° . The detector is a ^3He detector operated in the proportional regime. It is 0.5 m long, 2.4×10^{-2} m diameter stainless steel tube with a 3×10^{-4} m quartz wire coated with colloidal graphite as the resistant anode (350 ohm/m). The position resolution of the detector system is about 0.5 cm (full-width half-maximum), and counting rates up to approximately 20,000 counts/s can be handled without appreciable dead time (for higher counting rates, dead time corrections are handled by a multi-channel analyzer system). For the initial investigation, the detector output recorded in the MCA was summed to give 300 "reduced channels" representing equivalent segments along the detector. The spectrometer and processing of the detector output are controlled by a PDP-11/23 computer. This system is shown in Figure A1.

The sample, a 15mm tall, 10mm diameter cylinder, is mounted in the Euler goniometer, where it can be rotated about three axes under computer control. The specimen is heated by radiation from a graphite element and its temperature is monitored by a fine wire thermocouple, either type K or type S. The thermocouple signal is fed through a 0°C reference junction and to the feedback loop of the furnace and output to a strip chart recorder. The specimen and furnace assembly were contained in a vacuum maintained at approximately 1×10^{-6} torr.

PRELIMINARY INVESTIGATION/DEMONSTRATION OF TECHNIQUE

A preliminary investigation has been performed to demonstrate the feasibility of using neutron diffraction to make in-situ measurements of transformation kinetics. Two ternary titanium-aluminum-vanadium alloys, Ti-6Al-2V and Ti-6Al-6V were selected for this investigation. On cooling, these alloys transform from bcc beta to hcp alpha. Under equilibrium isothermal conditions, or at moderate continuous cooling rates, this transformation proceeds by nucleation and growth. The kinetics of this transformation, particularly the growth of the alpha phase, are believed to be controlled by the diffusion of vanadium, which also acts to stabilize the beta phase. Hence for a given cooling rate, the transformation of Ti-6Al-2V would be expected to

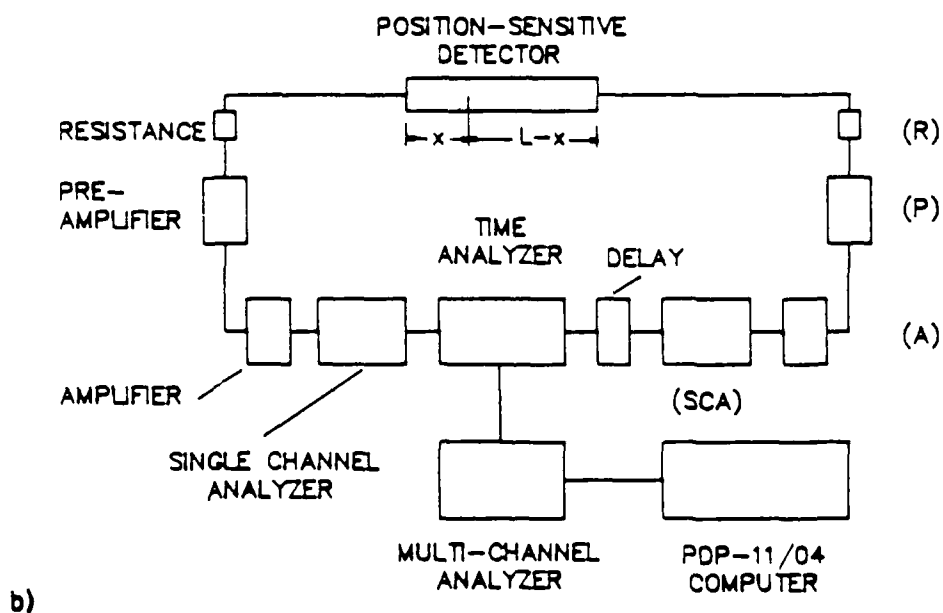
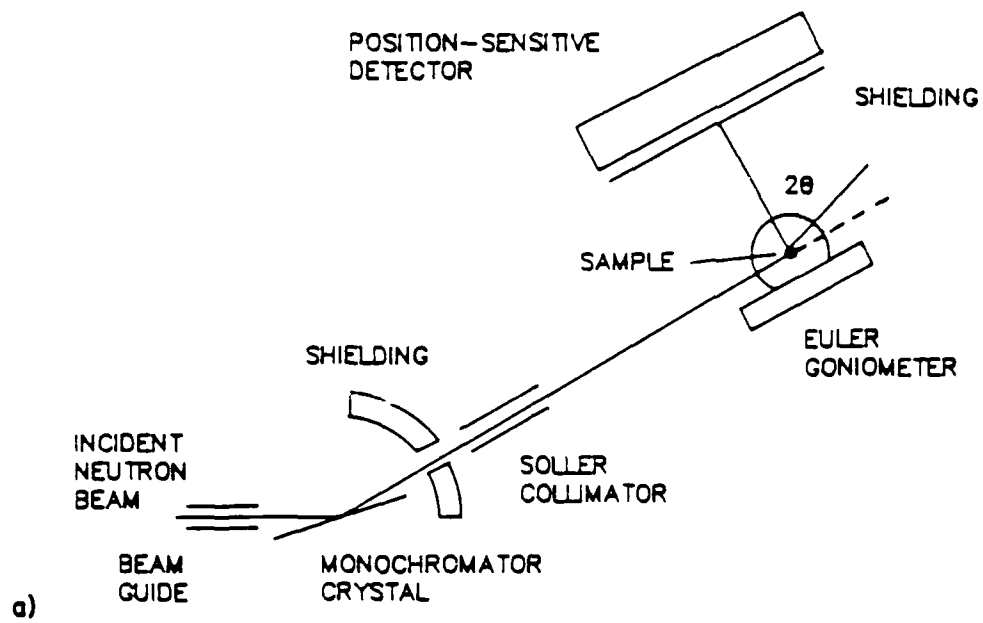


Figure A1. Experimental apparatus. Horizontal section of spectrometer layout (a) and block diagram of the electronic circuit for the position-sensitive detector (b).

be much more rapid than that of Ti-6Al-6V, to occur at a higher temperature, and to produce a microstructure which reflects a higher ratio of growth to nucleation. Dilatometric and metallographic studies support these assumptions. (17) For a cooling rate of 10°C/s , the beta to alpha transformation start temperatures are 865°C and 735°C for the 2V and 6V alloys, respectively. Similarly, the micrographs of Figure A2 show that the 2V alloy has a greater extent of grain boundary transformation product and a generally coarser microstructure, reflecting its higher growth/nucleation ratio.

Using neutron diffraction, the transformation kinetics of these alloys were studied under continuous cooling conditions. The cooling rate used was 15°C/s , taken as the average of the cooling rates immediately before and after the transformation. Prior to cooling, the samples were equilibrated in the beta region for times sufficient to produce a beta grain size of approximately 2mm. This large grain size was chosen so that a single grain would remain stable and that the diffracted intensity would be sufficiently large to permit the shortest counting times possible with the current data acquisition system. Similarly, a 2θ range of approximately 4° and a spatial resolution of approximately 0.2° 2θ were selected to permit the fastest possible sampling.

RESULTS

The results of these preliminary tests are shown in Figures A3, A4 and A5. Figure A3 shows a series of beta phase diffraction peaks for Ti-6Al-6V. As can be seen, the integrated intensity of these peaks remains constant prior to the transformation, decreases during the transformation, and then remains constant once the transformation has been completed. Figure A4 shows the integrated peak intensity versus time curves for Ti-6Al-2V and Ti-6Al-6V, and Figure A5 shows integrated intensity plotted versus temperature for these alloys. The dilatometric transformation start and finish points for equivalent cooling rates are superimposed on Figure A5, and show the agreement between the dilatometric and diffraction techniques. Similarly, Figure A4 verifies the assumption that the transformation of the 2V alloy occurs more rapidly than that of the 6V. Because of the preliminary nature of this investigation, no attempt was made to model the kinetics of these transformations. However, these data show the feasibility of using neutron diffraction to measure transformation kinetics.

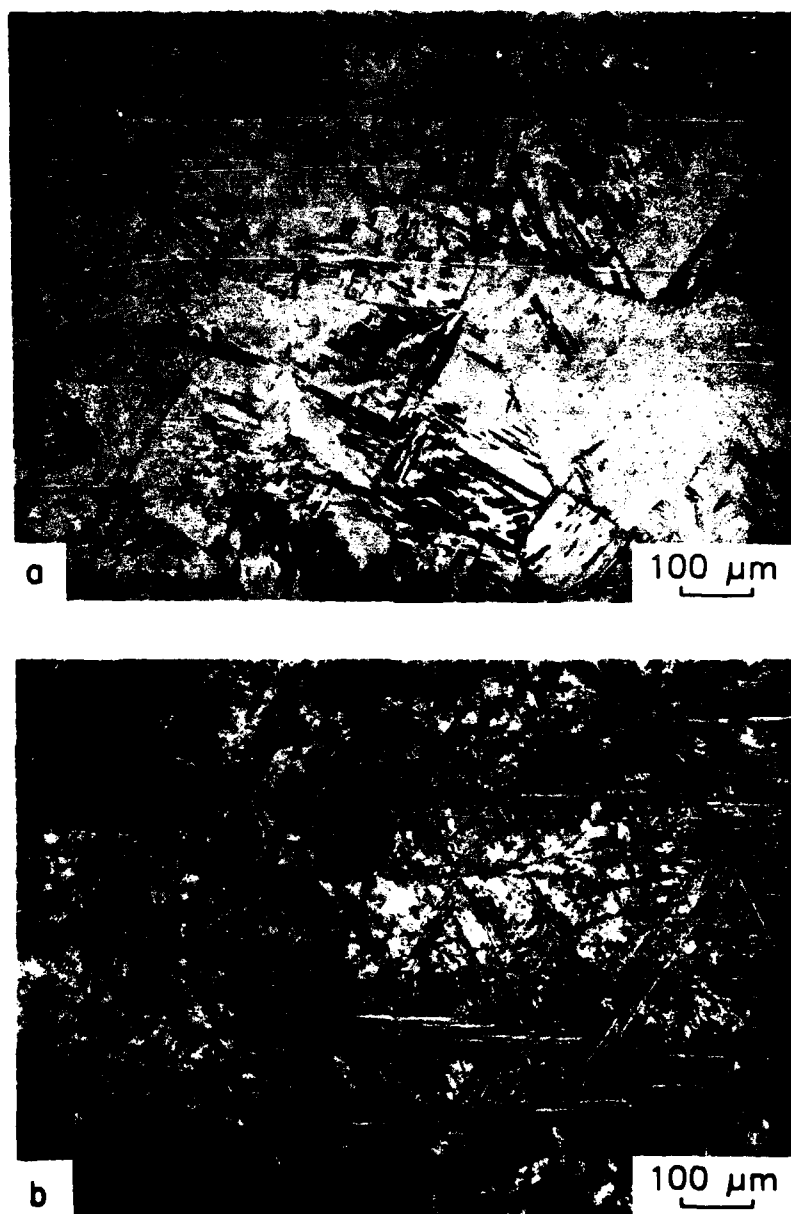


Figure A2. Photomicrographs of Ti-6Al-2V (a) and Ti-6Al-6V (b) cooled at 10°C/s. Note finer structure of Ti-6Al-2V reflecting relatively higher nucleation/growth.

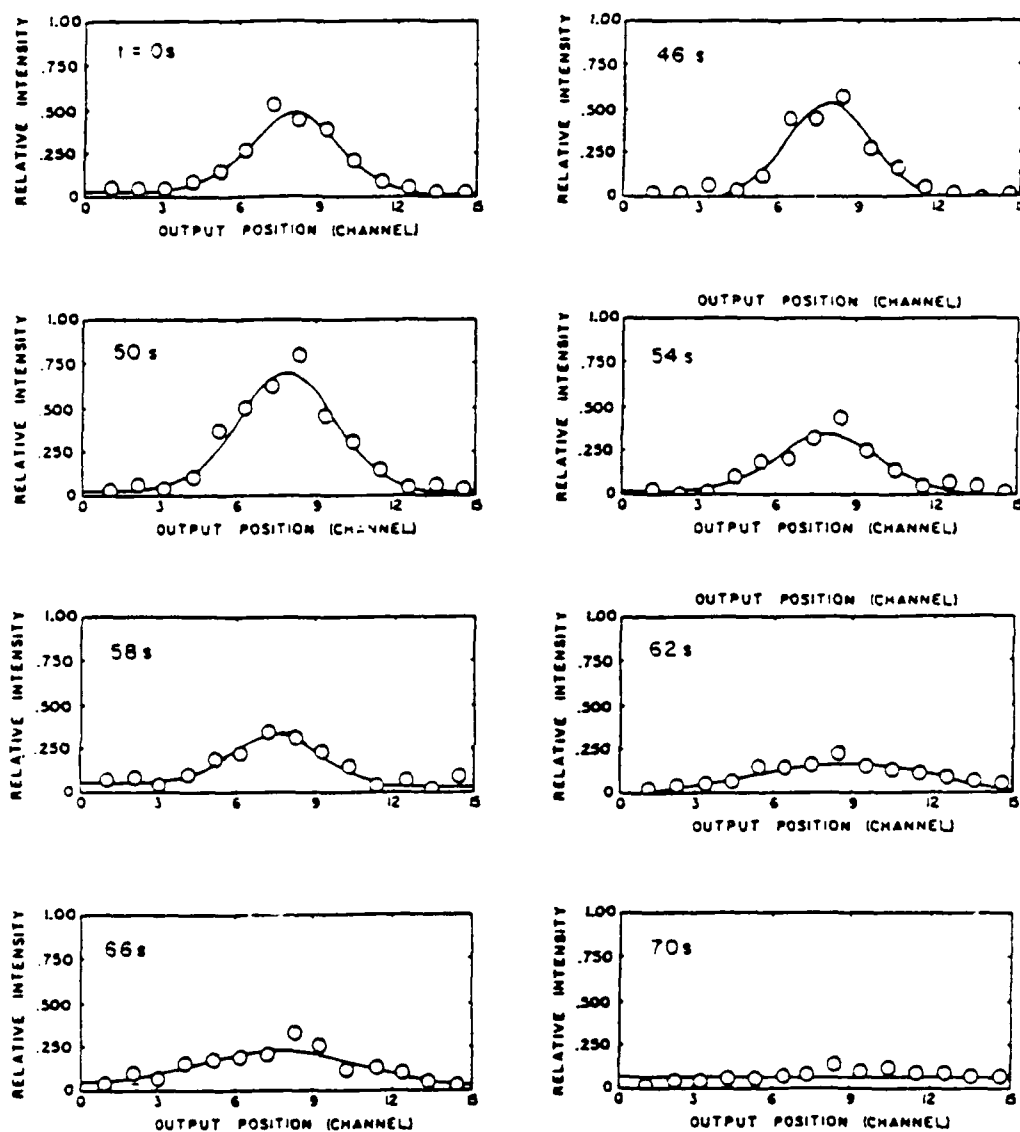


Figure A3. Beta phase (110) diffraction peaks at increasing times showing decrease in integrated intensity during the beta to alpha transformation.

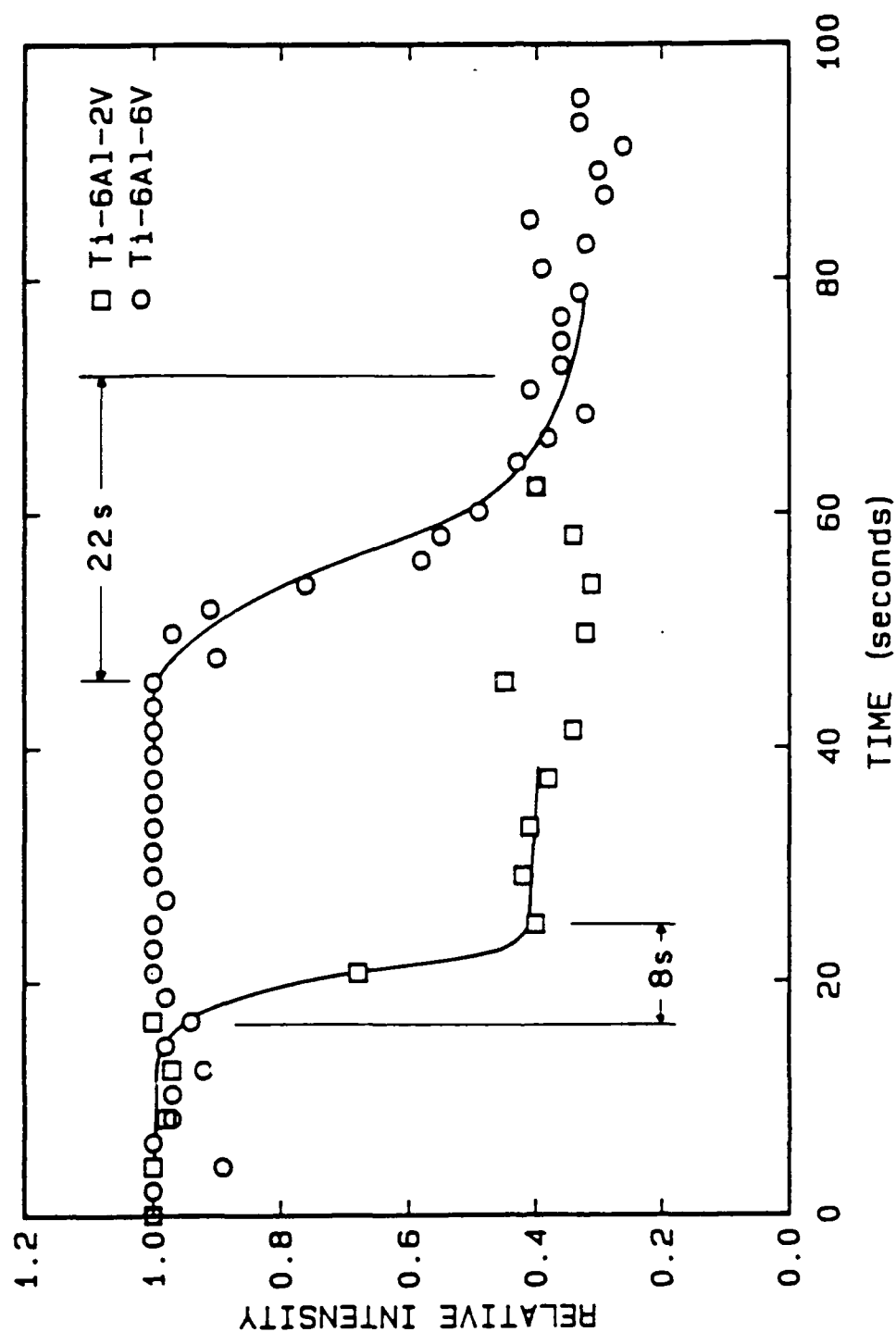


Figure A4. Relative integrated intensity of beta phase (110) diffraction peaks for Ti-6Al-2V and Ti-6Al-6V plotted against time cooling from 1200°C.

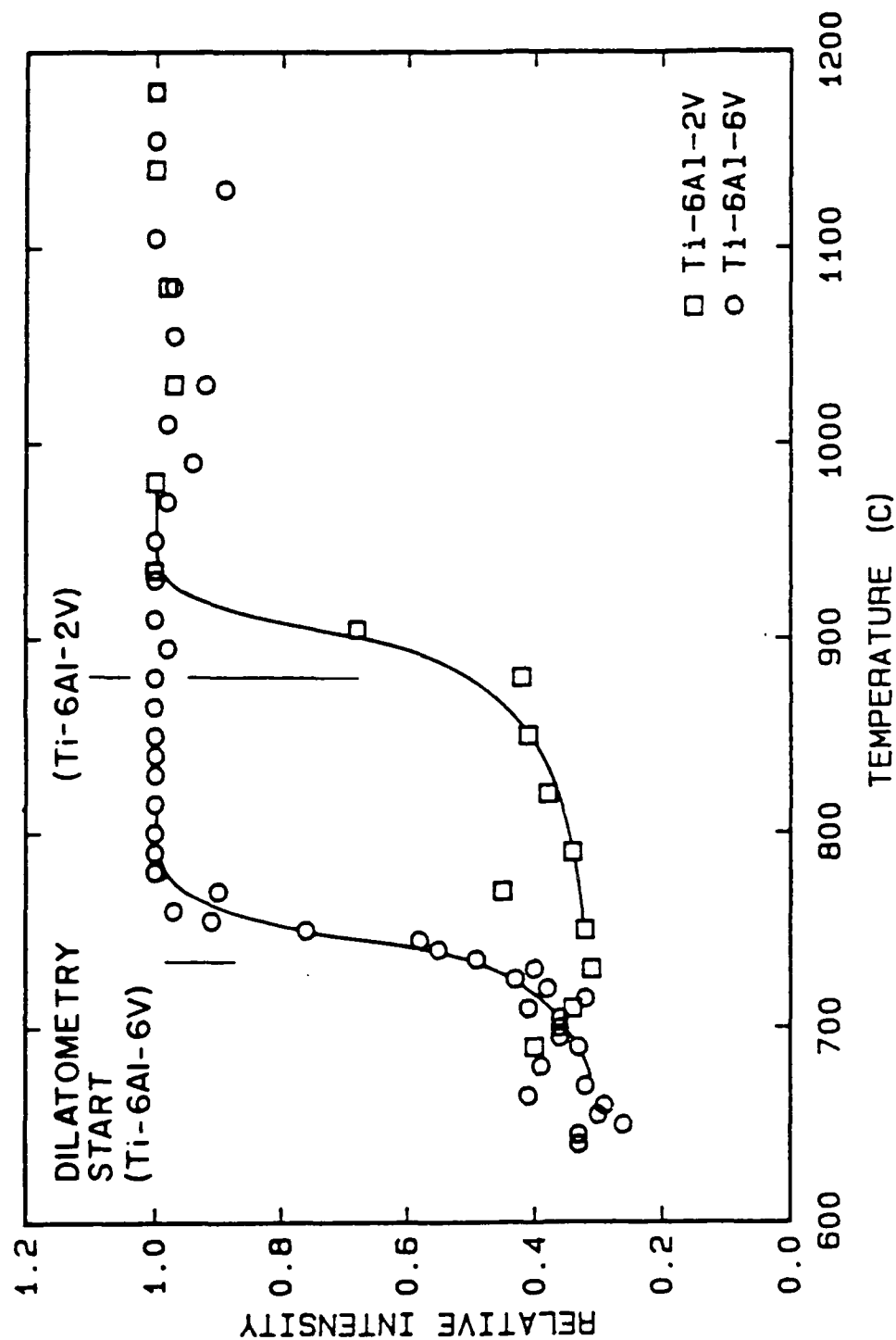


Figure A5. Relative integrated intensity of beta phase (110) diffraction peaks for Ti-6Al-2V and Ti-6Al-6V plotted against temperature during cooling from 1200°C.

DISCUSSION

Several limitations of the experimental setup, as it currently exists, are obvious. The major difficulty of the existing system is that the existing data acquisition system is not fast enough to get an accurate peak at each sampling interval. Because of this, the peak positions cannot be determined accurately. Even with the spatial limitations, the minimum counting time was approximately 1.5 seconds, barely fast enough to track the transformation in the 2V alloy. Modification of the data acquisition system is currently underway. The majority of the other difficulties with this preliminary experiment are associated with the large grain size and reactivity of the titanium sample material and hence, are easily avoided. Fortunately, the limitations imposed on this preliminary investigation were not stringent enough to prevent the successful demonstration of this technique. Figures A3 and A5 show that neutron diffraction can be used to track phase transformations, and Figure A4 shows the potential for use of this technique for transformation kinetics studies.

The greatest advantages of in-situ diffraction measurements, either x-ray or neutron, are their directness, ease, and speed. The disappearance or emergence of a grain or grains can be mapped as a function of time with a single sample. The conversion of this data to a curve of volume fraction transformed versus time then allows transformation kinetics to be quickly and easily studied under a wide variety of conditions. Several benefits of this are apparent. In addition to further study of isothermal transformation kinetics, the ability to accurately control the transformation thermal cycle and to quickly run and map the kinetics of many specimens will aid the study of non-isothermal and non-equilibrium transformations. Another way to exploit this capability is to study the effects on transformation kinetics of composition and processing modifications. Investigations such as this will aid the understanding of both the fundamental mechanics of transformations and the practical relationships between thermal cycles, alloy composition, and microstructures.

REFERENCES

1. W.A. Johnson, and R.F. Mehl: Trans. AIME, 1939, vol. 135, p. 416.
2. M. Avrami: J. Chem. Phys., 1939, vol. 7, p. 1103.
3. M. Avrami: J. Chem. Phys., 1940, vol. 8, p. 212.
4. M. Avrami: J. Chem. Phys., 1941, vol. 9, p. 177.
5. J.W. Cahn: Acta Metall., 1956, vol. 4, p. 449.
6. J.W. Cahn: Acta Metall., 1963, vol. 11, p. 561.
7. B.B. Rath: Proceedings of an International Conference on Solid-Solid Phase Transformations, H.I. Aaronson, D.E. Laughlin, R.F. Sekerka, and C.M. Wayman, eds., TMS-AIME, Warrendale, PA, 1983, p. 1097.
8. G.K. Manning and C.H. Lorig: Trans. AIME, 1946, vol. 167, p. 442.
9. J.W. Cahn: Acta Metall., 1956, vol. 4, p. 572.
10. M. Umemoto, N. Komatsubara, and I. Tamura: Proceedings of an International Conference on Solid-Solid Phase Transformations, H.I. Aaronson, D.E. Laughlin, R.F. Sekerka, and C.M. Wayman, eds., TMS-AIME, Warrendale, PA, 1983, p. 1111.
11. M.B. Kuban, R. Jayaraman, E.B. Hawbolt, and J.K. Brimacombe: Metall. Trans. A, 1986, vol. 17A, p. 1493.
12. E. Sarath Kumar Menon and H.I. Aaronson: Metall. Trans. A, 1986, vol. 17A, p. 1703.
13. L. Gerward, S. Lehn, and G. Christiansen: Texture Cryst. Sol., 1976, vol. 2, p. 95.
14. C.O. Ruud: Journal of Metals, 1979, vol. 31 (6), p. 10.
15. D. Juul Jensen and J.K. Kjems: Textures and Microstructures, 1983, vol. 5, p. 239.

16. D. Juul Jensen: Proceedings of an International Conference on Neutron Scattering in the 'Nineties, IAEA, Vienna, Austria, 1985, p. 293.
17. B.K. Damkroger, G.R. Edwards, and B.B. Rath: The Effect of Solid-State Phase Transformations on the Weldability of Titanium Alloys, paper presented at the ASM Materials Week, Orlando, Florida, 1986.

APPENDIX B

LATTICE PARAMETER MEASUREMENTS MADE USING
SYNCHROTRON RADIATION AND
NEUTRON DIFFRACTION

B.1 Synchrotron Radiation Measurements

Lattice parameter measurements were made of several titanium based alloys by Dr. M.A. Imam of the Naval Research Laboratory in Washington, D.C. (1). These measurements were made at room temperature and used the synchrotron radiation facility at Stanford University, Stanford, California. These results are presented in Table B.1.

B.2 Neutron Diffraction Measurements

Lattice parameter measurements were made at room temperature and several high temperatures using neutron diffraction. This work was done at the Danish National Laboratory at Risø. A description of the experimental apparatus is contained in Appendix I. The results of this testing are presented in Table B.2. In Table B.3, beta phase lattice parameters measured using x-ray diffraction are compared with those made using neutron diffraction.

Table B.1

Lattice Parameter Measurements Made Using
Synchrotron Radiation (114)

Alloy	Alpha Phase		Beta Phase
	a (Å)	c (Å)	a (Å)
Ti-6Al	2.934	4.680	-
Ti-6Al-4V	2.935	4.752	3.219
-6V	2.736	4.654	3.246
Ti-6Al-2Mo	2.927	4.685	3.251
-4Mo	2.881	4.716	-
-6Mo	2.715	4.797	3.228
Ti-6Al-2Nb	2.943	4.677	-
-4Nb	2.930	4.679	-
-6Nb	2.930	4.678	-

Table B.2

Lattice Parameter Measurements Made Using
Neutron Diffraction

Alloy	Temperature (°C)	Alpha Phase		Beta Phase
		a (Å)	c (Å)	a (Å)
Ti-6Al	RT	2.927	4.657	-
	1000	-	-	3.279
	1100	-	-	3.282
	1200	-	-	3.292
Ti-6Al-2V	RT	2.929	4.680	-
	900	-	-	3.277
	1100	-	-	3.286
	1200	-	-	3.286
Ti-6Al-4V	RT	2.929	4.681	-
	900	-	-	3.290
	1100	-	-	3.277
	1200	-	-	3.277
Ti-6Al-6V	RT	2.935	4.696	-
Ti-6Al-2Mo	RT	2.930	4.666	-
	900	-	-	3.277
	1000	-	-	3.281
	1100	-	-	3.285
	1200	-	-	3.290
Ti-6Al-4Mo	RT	2.935	4.671	-
	300	2.940	4.699	-
	500	2.944	4.709	-
	900	-	-	3.270
	1000	-	-	3.278
	1100	-	-	3.277
Ti-6Al-6Mo	RT	2.933	4.684	-
Ti-6Al-2Nb	RT	2.932	4.698	-

Table B.2 (cont.)

Alloy	Temperature (°C)	Alpha Phase		Beta Phase a (Å)
		a (Å)	c (Å)	
Ti-6Al-4Nb	RT	2.932	4.681	-
	200	2.937	4.717	-
	400	2.934	4.710	-
	700	2.955	4.723	-
	900	-	-	3.295
	1000	-	-	3.304
	1100	-	-	3.310
	1200	-	-	3.308
Ti-6Al-6Nb	RT	2.932	4.684	-
	1000	-	-	3.288
	1100	-	-	3.294
	1200	-	-	3.298
Ti-6211	RT	2.931	4.690	-
	1000	-	-	3.291
	1100	-	-	3.296
	1200	-	-	3.298

Table B.3

B Phase Lattice Parameters (\AA) and Cell Volumes (\AA^3)
 Measured by X-Ray and Neutron Diffraction

Alloy	Temperature ($^{\circ}\text{C}$)	X-Ray		Neutron	
		a	V	a	V
Cp Ti	1200	3.323	36.70	-	-
Ti-6Al	1200	3.313	36.37	3.292	35.68
-2V	1200	3.323	36.70	3.286	35.47
-4V	1200	3.311	36.40	3.277	35.19
-6V	1200	3.323	36.70	-	-
Ti-6Al					
-2Nb	1200	3.353	37.70	-	-
-4Nb	1200	3.329	36.90	3.308	36.21
-6Nb	1200	3.317	36.50	3.298	35.86
Ti-6Al					
-2Mo	1200	3.323	36.70	3.290	35.60
-4Mo	1200	3.314	36.40	3.308	36.21
-6Mo	1200	3.302	36.00	-	-
Ti-6211	1200	3.323	36.70	3.298	35.88
Ti-6Al					
-2V-2Nb	1200	3.302	36.00	-	-

APPENDIX C

X-RAY DIFFRACTION DATA PROCESSING METHODS
AND BASIC COMPUTER PROGRAMS

Several errors are inherent in the measurement of x-ray diffraction peak positions and hence, lattice parameters. These errors, which depend on the particular experimental technique used, are thoroughly discussed in references C and BM. As described in these references, the most severe of these inherent errors as they apply to a mechanical diffractometer are:

1. Misalignment of the instrument—the incident beam not intersecting the center of the diffractometer and $2\theta=0^\circ$.
2. Use of a flat specimen rather than one curved to follow the focusing circle.
3. Absorption of the specimen. (This is minimal with titanium because of its relatively high absorption.)
4. Displacement of the specimen from the diffractometer axis.

The error due to displacement of the specimen from the diffractometer axis is described in reference C as "usually the largest single source of error" and causes an error in d (plane spacing) given by:

$$\Delta d/d = -(D \cos^2 \theta)/R \sin \theta$$

This error can be minimized by extrapolation of lattice parameters plotted against $\cos^2 \theta / \sin \theta$. The errors resulting

from the use of a flat specimen and absorption of the specimen, on the other hand, are minimized by using an extrapolation parameter of $\cos^2\theta$. The selection of a particular extrapolation parameter will depend on the relative magnitudes of these errors. Both extrapolation parameters were tried for a specimen of unalloyed aluminum using the experimental apparatus used in this investigation. It was found that the best results were obtained with the $\cos^2\theta/\sin\theta$ extrapolation parameter. An additional extrapolation parameter, $\cos^2\theta/\sin\theta + \cos^2\theta/\theta$, known as the Nelson-Riley parameter and usually used with data from a Debye-Scherrer camera, was also tried. The results obtained with this parameter were virtually identical to those obtained with $\cos^2\theta/\sin\theta$. Therefore, the more theoretically correct parameter, $\cos^2\theta/\sin\theta$ was used throughout.

In the case of alpha titanium which has a hexagonal crystal structure, a minimum of two diffraction peaks are required to compute both the "a" and "c" parameters. A graphical extrapolation or linear regression would require the selection of diffraction peak groups having indices (001) to calculate and extrapolate the c parameter, and peak groups having indices (hk0) for the a parameter. This was not possible in this investigation due to the low diffracted intensities encountered.

In this investigation, the data was processed using a multiple regression analysis technique known as Cohen's (C) method. First, an extrapolation parameter is chosen which most completely compensates for all of the systematic errors in the experimental setup. This parameter describes the errors in calculated plane spacing as a function of diffraction angle, θ . In this investigation, a mechanical diffractometer was used, so the best extrapolation parameter was $\cos^2\theta/\sin\theta$. Based on this:

$$\Delta d/d = \cos^2\theta/\sin\theta$$

Starting with Bragg's law, $n\lambda = 2d\sin\theta$, square each side, take the log of both sides and differentiate:

$$\lambda^2 = 4d^2\sin^2\theta \text{ or } \lambda^2/4d^2 = \sin^2\theta$$

$$\ln(\lambda^2) - 2\ln(d) = \ln(\sin^2\theta)$$

$$-2(\Delta d/d) = \Delta \sin^2\theta/\sin^2\theta$$

Substituting for $\Delta d/d$ in this equation:

$$-2K(\cos^2\theta/\sin\theta) = \Delta \sin^2\theta/\sin^2\theta$$

$$-2K(\sin^2 2\theta/\sin\theta) = \Delta \sin^2\theta$$

For a hexagonal system:

$$1/d^2 = (4/3)(h^2+hk+k^2/a^2) + (l^2/c^2)$$

Combining this with Bragg's law:

$$\sin^2\theta = (\lambda^2/4)(h^2+hk+k^2/a^2) + (\lambda^2/4)(l^2/c^2)$$

It is important to note that the values of $\sin^2\theta$, a , and c in the above equation are true values, where:

$$\sin^2\theta(\text{observed}) - \sin^2\theta(\text{true}) = \Delta\sin^2\theta$$

When the expressions for $\sin^2\theta(\text{true})$ and $\Delta\sin^2\theta$ are substituted into this equation, the resulting expression is:

$$\sin^2\theta(\text{observed}) = C\alpha + B\gamma + D\beta$$

where: $\alpha = h^2 + hk + k^2$ $C = \lambda^2/3a^2$

$$\gamma = l^2$$

$$B = \lambda^2/4c^2$$

$$\beta = \cos^2\theta\sin\theta$$

$$D = -2K$$

At this point it should be noted that if a different extrapolation function is chosen, it will affect only β in the above analysis. The data for $\sin^2\theta(\text{observed})$ and the indices of the diffraction peaks are then input into equation (V) and these equations are combined and solved for a and c (C and B) using the method of least squares. This procedure involves the creation of a group of normal equations which are solved simultaneously. The normal equations in this analysis are:

$$\sum \alpha \sin^2\theta = C \sum \alpha^2 + B \sum \alpha\gamma + D \sum \alpha\beta$$

$$\sum \gamma \sin^2\theta = C \sum \alpha\gamma + B \sum \gamma^2 + D \sum \gamma\beta$$

$$\sum \beta \sin^2\theta = C \sum \alpha\beta + B \sum \gamma\beta + D \sum \beta^2$$

The above analysis procedure was combined with a subroutine for solving simultaneous equations by Choleski's method into a BASIC computer program for use on either an IBM PC or TI personal computer. This program, called ANG, is included in this appendix. The data in this

investigation processed by this program is denoted by the suffix "ANG".

A second data processing system was developed specifically to process the data generated by the neutron diffraction measurements conducted at the Danish National Laboratory at Risø. Because of their greater penetration, neutrons diffract from the entire specimen, rather than from the surface. Thus, the sources of three of the major errors inherent in mechanical diffractometry, displacement of the specimen from the diffractometer axis, absorption of the specimen, and the use of a flat rather than round specimen, can be greatly reduced by proper collimation of the incident and diffracted beams. In this case, an extrapolation parameter is no longer needed. The procedure to process this data simply combined each pair of diffraction peaks to calculate "a" and "c" and averaged these values. A BASIC computer program was written to perform this calculation, and is included in this appendix and referred to as MUL. This data processing method was originally applied to only the neutron diffraction data, but was later used with the x-ray data as well to supplement the ANG results. When presented, data processed with this program is denoted by the suffix "MUL".

Table C1 compares several sets of diffractometry data

Table C.1

Examples of Lattice Parameters Obtained With Various
Data Processing Methods

Material and Source	Processing Method	a (Å)	c (Å)	vol/cell (Å ³)
<hr/>				
Unalloyed Titanium				
Published Data				
10 lowest peaks	ANG	2.948	4.681	35.231
+0.05°	ANG	2.947	4.681	35.215
-0.05°	ANG	2.948	4.682	35.246
10 highest peaks	ANG	2.949	4.684	35.268
10 random peaks	ANG	2.950	4.684	35.300
8 lowest peaks	MUL	2.951	4.678	35.290
TIMET Ti-6Al-4V				
8 Lowest Peaks				
CSM x-ray data	ANG	2.927	4.677	34.702
	MUL	2.926	4.681	34.698
Risø neutron				
diffraction data				
	ANG	2.933	4.679	34.856
	MUL	2.929	4.681	34.770

processed by the both methods, ANG and MUL. This table shows that the results obtained with the two methods are very similar. this method. In both cases, the calculated lattice parameters can be used to back calculate theoretical diffraction peak positions. These back-calculated peak positions can then be compared with the measured values as a qualitative check of the internal consistency of the data set. Table C2 shows measured and back-calculated 2θ values for two sets of data processed by both methods. Again, the results are very similar. In both cases, the back-calculated 2θ values are within approximately 0.05° of the measured values. As will be discussed in the following Appendix, this difference is roughly the accuracy with which the chart recorder trace of intensity versus Bragg angle can be read.

Two additional methods of processing the data were briefly investigated. The first involved the use of two very intense peaks, the (011) and (112) peaks, to directly calculate "a" and "c". This system was investigated as possibly being a more consistent relative measure of cell volume than the ANG extrapolation procedure, at the expense of absolute accuracy. However, in addition to being a poor measure of absolute parameters, the use of only two peaks eliminates the internal checks in a multi-peak analysis,

Table C.2

Published and Measured Peak Positions Compared With Peak
Positions Back-Calculated From Lattice Parameters

Original Data		Back-Calculated 2 θ	
hkl	2 θ	ANG	MUL
Published Ti Data ($\lambda=1.54051$)			
010	35.06	35.11	35.08
002	38.40	38.45	38.45
011	40.15	40.20	40.17
012	53.01	53.04	53.02
110	62.96	62.98	62.93
103	70.66	70.72	70.71
112	76.29	76.27	76.22
201	77.32	77.40	77.34
TIMET Ti-6Al-4V CSM X-Ray Data			
010	35.45	35.41	35.43
002	38.53	38.49	38.47
011	40.48	40.48	40.48
110	63.59	63.58	63.61
112	76.85	76.84	76.85
201	78.16	78.13	78.16

hence requires multiple samples to insure consistent results. When a small number of samples were used, the parameters calculated by this method often varied significantly from those obtained using the extrapolation procedure. This method was used to evaluate a small number of alloys early in this investigation, but was not used in the overall data comparison.

The fourth method which was investigated briefly relied on the assumption that peak positions could be measured very accurately relative to each other. This procedure used two peak positions to calculate "a" and "c". These parameters were then used to back calculate the position of a third peak which was compared to the measured position. The data was adjusted, maintaining the original peak spacing, until the set of three peaks were located correctly to produce a consistent unit cell. Although beautiful in concept, this procedure resulted in huge shifts of the original peak positions for any and all data, and produced calculated lattice parameters which deviated severely from published or produced by any other data processing procedure. This method was not used.

BASIC Computer Program "ANG4"

```

200 'THIS SECTION IS THE CHOLESKI SUBROUTINE USED IN THE
210 'SOLUTION OF A SET OF LINEAR SIMULTANEOUS EQUATIONS
220 '** VARIABLE LISTING '**
230 ' V1 = NUMBER OF EQUATIONS (UNKNOWN)
240 ' V2-V7 = VARIABLE INDICES IN THE SUBROUTINE
250 ' W1(V1,V1), W2(V1,V1), W3(V1) = TEMPORARY ARRAYS IN THE SUBROUTINE
260 ' W4-W5 = WORKING VARIABLES IN THE SUBROUTINE
270 ' COEF(V1,V1) = COEFFICIENT MATRIX
280 ' FUNC(V1,1) = FUNCTION MATRIX
290 ' SOLUT(V1,1) = SOLUTION MATRIX
300 '
310 .....
320 '** MAKE SURE 1) THAT THE MATRICES: COEF, FUNC, SOLUT, W1, W2, **
330 '** AND W3 ARE DIMENSIONED WITH THE CORRECT VALUES IN THE MAIN **
340 '** PROGRAM ; 2) THE VARIABLES: COEF, FUNC, SOLUT, AND W ARE **
350 '** DEFINED IN DOUBLE PRECISION (DEFDBL) ; 3) THAT V IS DEFINED **
360 '** AS AN INTEGER (DEFINT). **
370 .....
380 '
385 DEFINT V,R,Z
390 GOTO 1000
401 DEFINT V
409 FOR V2=1 TO V1
410   V3=V2
420   V4=V2-1
430   IF V2=1 THEN 530
440   FOR V5=1 TO V4
450     W4=COEF(V2,V5)
460     IF V5=1 THEN 510
470     V6=V5-1
480     FOR V7=1 TO V6
490       W4=W4-W1(V2,V7)*W2(V7,V5)
500     NEXT V7
510     W1(V2,V5)=W4/W2(V5,V5)
520   NEXT V5
530   FOR V5=V3 TO V1
540     IF V2=1 THEN 610
550     W5=COEF(V2,V5)
560     FOR V7=1 TO V4
570       W5=W5-W1(V2,V7)*W2(V7,V5)
580     NEXT V7
590     W2(V2,V5)=W5
600     GOTO 620
610     W2(V2,V5)=COEF(V2,V5)
620   NEXT V5
630 NEXT V2
640 W3(1)=FUNC(1,1)
650 FOR V2=2 TO V1
660   W4=FUNC(V2,1)
670   V4=V2-1
680   FOR V5=1 TO V4
690     W4=W4-W3(V5)*W1(V2,V5)
700   NEXT V5
710   W3(V2)=W4
720 NEXT V2
730 SOLUT(V1,1)=W3(V1)/W2(V1,V1)
740 V4=V1-1
750 FOR V2=V4 TO 1 STEP (-1)

```

```
760      W4=W3(V2)
770      V3=V2+1
780      FOR V5=V3 TO V1
790          W4=W4-SOLUT(V5,1)*W2(V2,V5)
800      NEXT V5
810      SOLUT(V2,1)=W4/W2(V2,V2)
820  NEXT V2
830  IF Q = 1 THEN 1650
831  GOTO 15290
1000  PRINT "THIS IS A PROGRAM TO COMPUTE LATTICE PARAMETERS."
1010  PRINT
1030  PRINT "CRYSTAL SYSTEM? 1 FOR CUBIC, 2 FOR HEXAGONAL"
1050  PRINT
1060  INPUT Q
1070  IF Q = 2 THEN 1100
1080  PRINT "CUBIC CRYSTAL SYSTEM"
1090  GOTO 1120
1100  PRINT "HEXAGONAL CRYSTAL SYSTEM"
1120  PRINT
1130  PRINT "COPPER K-ALPHA; WAVELENGTH = 1.54184? 1 FOR YES, 2 FOR NO"
1132  PRINT
1140  INPUT WAVE
1150  IF WAVE = 2 THEN 1180
1160  L2 = 1.54184
1170  GOTO 1200
1180  PRINT "INPUT WAVELENGTH USED, IN ANGSTROMS"
1190  INPUT L2
1200  PRINT "WAVELENGTH =" L2
1220  PRINT
1230  PRINT "NUMBER OF REFLECTIONS?"
1240  INPUT R
1250  PRINT R "REFLECTIONS WILL BE ENTERED"
1255  PRINT
1256  GOTO 12000
1257  PRINT
1258  PRINT "ENTER 2-THETA, H, K, AND L, EACH SEPARATELY"
1259  PRINT
1260  LET Z = Z + 1
1270  INPUT T2(Z)
1280  INPUT H(Z)
1290  INPUT K(Z)
1300  INPUT L(Z)
1311  T2 = T2(Z)
1312  H = H(Z)
1313  K = K(Z)
1314  L = L(Z)
1315  PRINT
1320  LET T2 = (T2/360!) * 2 * 3.14159265#
1330  LET S1 = SIN (T2/2)
1340  LET S2 = S1^2
1350  LET C1 = COS (T2/2)
1360  LET C2 = C1^2
1440  IF E = 2 THEN 12150
1450  IF E = 3 THEN 12110
1460  LET B2 = C2 * S1
1470  IF Q = 2 THEN 15000
1480  LET A2 = H^2 + K^2 + L^2
1490  LET M1 = M1 + A2 * S2
1500  LET M2 = M2 + A2^2
1510  LET M3 = M3 + A2 * B2
```

```

1520 LET M4 = M4 + B2 * S2
1530 LET M5 = M3
1540 LET M6 = M6 + B2^2
1550 IF Z < R THEN 1260
1560 LET V1 = 2
1570 DIM COEF(2,2), W1(2,2), W2(2,2), W3(2), FUNC(2,1), SOLUT(2,1)
1580 LET COEF(1,1) = M2
1590 LET COEF(1,2) = M3
1600 LET COEF(2,1) = M5
1610 LET COEF(2,2) = M6
1620 LET FUNC(1,1) = M1
1630 LET FUNC(2,1) = M4
1640 GOTO 401
1650 LET C3 = SOLUT(1,1)
1660 LET A3 = SQR(L2^2/(4*C3))
1670 PRINT "IN ANGSTROMS, THE LATTICE PARAMETER IS " A3
1680 PRINT
1690 PRINT
1700 PRINT "CALCULATED 2-THETA, MEASURED 2-THETA, ABSOLUTE DIFFERENCE,"
1710 PRINT "AND PERCENT DIFFERENCE ARE"
1720 FOR ZZ = 1 TO R
1730 PRINT
1740 NWL1 = A3^2/(H(ZZ)^2 + K(ZZ)^2 + L(ZZ)^2)
1750 NWD1 = NWL1^.5
1760 NSN1 = L2/(2*NWD1)
1770 NSN1 = ATN(NSN1/SQR(-NSN1*NSN1+1))
1780 NSN1 = NSN1 * 360/(2*3.14158625#)
1790 NSN1 = 2 * NSN1
1800 NSDF = NSN1 - T2(ZZ)
1810 NSPR = (NSDF/T2(ZZ)) * 100
1820 PRINT NSN1, T2(ZZ), NSDF, NSPR
1830 NEXT ZZ
1840 PRINT
1850 PRINT "IN ANGSTROMS, THE LATTICE PARAMETER IS", A3
1860 GOTO 50000
12000 PRINT
12020 PRINT" SELECT EXTRAPOLATION FUNCTION, 1 FOR COS(THETA)^2/SIN(THETA)"
12030 PRINT "2 FOR NELSON-RILEY, 3 FOR COS(THETA)^2"
12040 INPUT E
12050 IF E = 2 THEN 12130
12060 IF E = 3 THEN 12090
12070 PRINT "COS(THETA)^2/SIN(THETA) EXTRAPOLATION FUNCTION"
12080 GOTO 1257
12090 PRINT "COS(THETA)^2 EXTRAPOLATION FUNCTION"
12100 GOTO 1257
12110 LET B2 = (SIN (T2))^2
12120 GOTO 1470
12130 PRINT "NELSON-RILEY EXTRAPOLATION FUNCTION"
12140 GOTO 1257
12150 LET T = T2/2
12160 LET N2 = (SIN (T2))^2
12170 LET B2 = N2/S1 + N2/T
12180 GOTO 1470
15000 LET A2 = H^2 + H*K + K^2
15010 LET G = L^2
15020 LET M1 = M1 + A2 * S2
15030 LET M2 = M2 + A2^2
15040 LET M3 = M3 + A2 * G
15050 LET M4 = M4 + A2 * B2
15060 LET M5 = M5 + G * S2

```

```
15070 LET M6 = M3
15080 LET M7 = M7 + G^2
15090 LET M8 = M8 + G * B2
15100 LET M9 = M9 + B2 * S2
15110 LET O1 = M4
15120 LET O2 = M8
15130 LET O3 = O3 + B2^2
15140 IF Z < R THEN 1260
15150 LET V1 = 3
15160 DIM COEF(3,3), W1(3,3), W2(3,3), W3(3), FUNC(3,1), SOLUT(3,1)
15170 LET COEF(1,1) = M2
15180 LET COEF(1,2) = M3
15190 LET COEF(1,3) = M4
15200 LET COEF(2,1) = M6
15210 LET COEF(2,2) = M7
15220 LET COEF(2,3) = M8
15230 LET COEF(3,1) = O1
15240 LET COEF(3,2) = O2
15250 LET COEF(3,3) = O3
15260 LET FUNC(1,1) = M1
15270 LET FUNC(2,1) = M5
15275 LET FUNC(3,1) = M9
15280 GOTO 401
15290 LET C3 = SOLUT(1,1)
15300 LET B3 = SOLUT(2,1)
15310 LET A3 = SQR(L2^2/(3*C3))
15320 LET A4 = SQR(L2^2/(4*B3))
15330 PRINT "IN ANGSTROMS, THE LATTICE PARAMETERS ARE"
15340 PRINT "A = " A3
15350 PRINT "C = " A4
15351 PRINT
15352 PRINT
15353 PRINT "CALCULATED 2-THETA, MEASURED 2-THETA, ABSOLUTE DIFFERENCE"
15354 PRINT "AND PERCENT DIFFERENCE ARE;"
15355 PRINT
15360 FOR Z = 1 TO R
15370 NWL1 = L(Z)^2/A4^2
15380 NWL2 = (H(Z)^2 + H(Z)*K(Z) + K(Z)^2)/A3^2
15390 NWL2 = NWL2 * (4/3)
15400 NWD1 = NWL1 + NWL2
15410 NWD1 = 1/NWD1
15420 NWD1 = NWD1^.5
15430 NSN1 = L2/(2*NWD1)
15440 NSN1 = ATN(NSN1/SQR(-NSN1*NSN1 + 1))
15450 NSN1 = NSN1 * 360/(2*3.14159625#)
15460 NSN1 = 2 * NSN1
15461 NSDF = NSN1 - T2(Z)
15462 NSPR = NSDF/T2(Z)
15463 NSPR = NSPR*100
15464 PRINT NSN1, T2(Z), NSDF, NSPR
15465 PRINT
15480 NEXT Z
15481 PRINT "A = ", A3, "C = ", A4
50000 END
```

BASIC Computer Program "MUL5"

```

10 PRINT "HCP LATTICE PARAMETERS"
11 PRINT
12 PRINT "ENTER TITLE"
13 PRINT
14 INPUT Z$
20 PRINT
30 PRINT "ENTER NUMBER OF REFLECTIONS"
40 INPUT I
50 IM = I - 1
55 TEST = 1
60 PRINT
70 PRINT I, "REFLECTIONS WILL BE ENTERED"
80 PRINT
85 PRINT "ENTER WAVELENGTH IN ANGSTROMS"
86 PRINT
87 INPUT WAVE
90 'ENTER DATA
100 PRINT "FOR EACH REFLECTION ENTER 2THETA, H, K, AND L"
110 FOR L = 0 TO IM
120 INPUT THETA(L), H(L), K(L), L(L)
130 NEXT L
140 'CALCULATE NUMBER OF PARAMETER COMBINATIONS
150 '# OF WAY TO ARRANGE N THINGS M AT A TIME IS =
160 '(N FACTORIAL) / ((M-N) FACTORIAL) * N FACTORIAL
170 R = 1 * (I-1)/2
180 'CALCULATE D SPACINGS FOR EACH REFLECTION
190 FOR L = 0 TO IM
200 THETA = (THETA(L)/720) * 2 * 3.14159265#
210 SIN2 = SIN (THETA)
240 D(L) = WAVE/(SIN2*2)
260 NEXT L
270 'CALCULATE LATTICE PARAMETER COMBINATIONS
280 'FORMULA IS: 1/D^2 = (4/3)*((H^2+HK+K^2)/A^2) + (L^2/C^2)
285 PRINT
290 FOR M = 0 TO IM
300 M1 = M + 1
310 FOR N = M1 TO IM
320 H1 = H(M)^2 + H(M)*K(M) + K(M)^2
330 H2 = H(N)^2 + H(N)*K(N) + K(N)^2
340 IF L(M) = 0 THEN 420
350 IF L(N) = 0 THEN 380
360 L2 = L(M)^2/L(N)^2
370 GOTO 560
380 A2 = (4/3)*H2*D(N)^2
390 C1 = 1/D(M)^2 - (4/3)*(H1/A2)
400 C2 = L(M)^2/C1
410 GOTO 620
420 A21 = (4/3)*H1*D(M)^2
430 AM1 = A21^.5
440 IF L(N) = 0 THEN 490
450 C1 = 1/D(N)^2 - (4/3)*(H2/A21)
460 C2 = L(N)^2/C1
470 A2 = A21
480 GOTO 620
490 A22 = (4/3)*H2*D(N)^2
500 AM2 = A22^.5
510 A(M,N) = (AM2+AM1)/2
520 TEST = 0
530 C(M,N) = 0

```

```

540 X = X + 1
550 GOTO 660
560 NUM = (4/3) * (L2 * H2 - H1)
570 DEN = L2/(D(N)^2) - 1/(D(M)^2)
580 A2 = NUM/DEN
590 C1 = 1/(D(M)^2) - (4/3) * (H1/A2)
600 IF C1 = 0 THEN 1030
610 C2 = (L(M)^2)/C1
620 A(M,N) = A2*.5
625 C(M,N) = C2*.5
660 'ACCUMULATE TOTALS FOR AVERAGES
670 A = A(M,N) + A
680 C = C(M,N) + C
690 NEXT N,M
700 'CALCULATE AVERAGES
710 AVE = A/(R-Y)
720 CVE = C/(R-X)
730 PRINT
740 PRINT
750 PRINT "THE AVERAGE PARAMETERS ARE: A(AVE) =" AVE, "C(AVE) =" CVE
760 PRINT
780 'CALCULATE THE ERRORS AND % ERRORS
790 FOR M = 0 TO 1M
800 M1 = M + 1
810 FOR N = M1 TO 1M
820 DA = A(M,N) - AVE
830 PA = (DA/AVE) * 100
840 DC = C(M,N) - CVE
850 PC = (DC/CVE) * 100
851 IF PC > 1.25 THEN 860
852 IF PA > 1.25 THEN 860
853 IF PC < -1.25 THEN 860
854 IF PA < -1.25 THEN 860
855 GOTO 1010
860 IF PC = 100 THEN 1010
861 IF PC = -100 THEN 1010
865 PRINT "REFLECTIONS:" THETA(M), H(M), K(M), L(M)
870 PRINT " " THETA(N), H(N), K(N), L(N)
880 PRINT
890 PRINT "CALCULATED: A =" A(M,N), "C =" C(M,N)
900 PRINT
910 IF TEST = 0 THEN 930
920 GOTO 960
930 PRINT "INDIVIDUAL A'S ARE: A1 =" AM1, "A2 =" AM2
940 TEST = 1
960 PRINT "DEVIATIONS: DELTA A =" DA, "DELTA C =" DC
970 PRINT
980 PRINT "PERCENTS: %A =" PA, "%C =" PC
990 PRINT
1000 PRINT
1010 NEXT N,M
1020 GOTO 15351
1030 C1 = 1/(D(N)^2) - (4/3) * (H2/A2)
1040 IF C1 = 0 THEN 1070
1050 C2 = (L(N)^2)/C1
1060 GOTO 620
1070 C2 = 0
1080 X = X + 1
1090 GOTO 620
15351 PRINT

```

```
15352 PRINT
15353 PRINT "CALCULATED 2-THETA, MEASURED 2-THETA, ABSOLUTE DIFFERENCE"
15354 PRINT "AND PERCENT DIFFERENCE ARE;"
15355 PRINT
15360 FOR L = 0 TO 1M
15370   NWL1 = L(L)^2/CVE^2
15380   NWL2 = (H(L)^2 + H(L)*K(L) + K(L)^2)/AVE^2
15390   NWL3 = NWL2 * (4/3)
15400   NWL = NWL1 + NWL2
15410   NWD1 = 1/NWL
15420   NWD1 = NWD1^.5
15430   NSN1 = WAVE/(2*NWD1)
15440   NSN1 = ATN(NSN1/SQR(-NSN1*NSN1 + 1))
15450   NSN1 = NSN1 * 360/(2*3.14159625#)
15460   NSN1 = 2 * NSN1
15461   NSDF = NSN1 - THETA(L)
15462   NSPR = NSDF/THETA(L)
15463   NSPR = NSPR*100
15464   PRINT NSN1, THETA(L), NSDF, NSPR
15465   PRINT
15480 NEXT L
15481 PRINT "A =", AVE, "C =" CVE
50000 END
```


APPENDIX D

ERRORS INVOLVED IN LATTICE INCOMPATIBILITY MEASUREMENTS

In this investigation, lattice incompatibility was calculated in two different ways. The first used the assumption that the critical incompatibility was between the supercooled beta phase and the grain boundary alpha film. In this case, the measurements relied on were the lattice parameter measurements of both phases, the beta phase dilatometry, and the temperature measurements in both sets of samples. The second lattice incompatibility calculated was between the supercooled beta and the Widmanstatten colony structure, assumed to be an equilibrium mixture of alpha and beta. In addition to the lattice parameter measurements, dilatometry, and temperature measurements, this second calculation also incorporated quantitative metallography and the dilatometric measurement of specific transformation start temperatures. Each of these measurements will be briefly discussed.

D.1 Temperature Measurement

In both the high-temperature x-ray diffraction facility and the Gleeble 1500, temperature was monitored via a 0.010 in. Pt versus Pt-13%Rh thermocouple spot welded to the sample surface. In both cases, the temperature readings have been independently checked using a second thermocouple and external signal conditioning system, and found to be reproducible to within at least 5°C. In some of the

earliest high-temperature diffractometry, a specimen configuration was used in which the thermocouple was mounted on the back side of a thick sample and contained in ceramic material. With this specimen configuration, the temperature read was significantly lower than the actual specimen surface temperature. For these samples, a calibration curve relating the actual and measured temperatures was developed and used to correct the temperature readings. In these tests, the accuracy of the temperature readings was approximately $\pm 25^{\circ}\text{C}$. Data taken with this sample configuration includes that for unalloyed titanium, Ti-6Al, Ti-6Al-4V, and some of the data for Ti-6211. In any case, an examination of the data presented in Figures 5.29-5.51 indicate that in the lattice parameter measurements, errors in sample temperature measurement are not significant.

D.2 Lattice Parameter Measurements

There are several sources of error involved in the measurement of the lattice parameters and cell volumes reported in this investigation. The most obvious source of error is involved in the use and choice of an extrapolation parameter. The magnitude of the effect this can have on calculated parameters and cell volumes can be evaluated by a comparison of published, neutron, and x-ray data processed by different methods, presented in Table D1. When the

Table D.1

Examples of Lattice Parameters Obtained With Various
Data Processing Methods

Material and Source	Processing Method	a (Å)	c (Å)	vol/cell (Å ³)
Unalloyed Titanium Published Data				
10 lowest peaks	ANG	2.948	4.681	35.231
+0.05°	ANG	2.947	4.681	35.215
-0.05°	ANG	2.948	4.682	35.246
10 highest peaks	ANG	2.949	4.684	35.268
10 random peaks	ANG	2.950	4.684	35.300
8 lowest peaks	MUL	2.951	4.678	35.290
TIMET Ti-6Al-4V 8 Lowest Peaks				
CSM x-ray data	ANG	2.927	4.677	34.702
	MUL	2.926	4.681	34.698
Risø neutron diffraction data				
	ANG	2.933	4.679	34.856
	MUL	2.929	4.681	34.770

published data for pure titanium is processed by the ANG and MUL procedures, the difference in calculated parameters is 0.003\AA , or $\pm 0.05\%$, and in cell volumes, 0.059\AA^3 , or $\pm 0.08\%$. Also included in this table are sets of Ti-64 peak positions measured by neutron and x-ray diffraction. This data is processed by both the ANG and MUL programs. For the neutron data, the calculated cell volumes differed by 0.086\AA^3 , or $\pm 0.09\%$. For the case of Ti-64 measured by x-ray diffraction, the difference between cell volumes calculated by the ANG and MUL programs was 0.004\AA^3 , or $\pm 0.005\%$. For comparison, the most theoretically correct values are the parameters calculated from the neutron diffraction data and the MUL program, and the parameters calculated from the x-ray diffraction data with the ANG program. These values differed by 0.068\AA^3 , or $\pm 0.09\%$. These results suggest that differences in parameters calculated from data from different sources are of approximately the same magnitude as the worst that can be induced by an incorrect choice of extrapolation procedure, $\pm 0.09\%$ in cell volume.

Once a data processing system has been selected as the best possible compensation for systematic experimental errors, the effect of random errors on the final parameters and cell volumes may be evaluated. A qualitative

examination of the error in determining peak position on a chart recorder trace suggested that the peak position could be determined at least as well as $\pm 0.05^\circ 2\theta$. To evaluate the effect of this error, the lowest 10 of the published 2θ positions for pure titanium were offset $+0.05^\circ$ and -0.05° and the parameters and cell volumes calculated using the ANG program. These results are also included in Table D1. It was found that the variation in calculated volume, from largest to smallest, was 0.031\AA^3 which corresponds to $\pm 0.04\%$, a smaller effect than arises from either an incorrect choice of extrapolation procedure or the variation in data from different sources.

The accuracy of the calculated lattice parameters in this investigation was further compromised by the use of low angle diffraction peaks. As with any extrapolation procedure, the accuracy of the extrapolated values is best when a small extrapolation follows a large data range. Further, as discussed earlier, the effect of errors in peak position determination will have a relatively larger effect on calculated lattice parameter when low angle reflections are used. In this investigation, only peaks with a range of 2θ from 35° to 78° had sufficient intensity to be used. With the extrapolation parameter $\cos^2\theta/\sin\theta$, it was found that this range of 2θ corresponds with a range of $\cos^2\theta/\sin\theta$

from about 3 to 1, extrapolated to $\cos^2\theta/\sin\theta = 0$. One problem that this sometimes causes is that the extrapolation procedure seems to put an inordinate amount of weight on the highest angle reflections, often the least accurately read due to their low intensity. Also, the relative intensity of various diffraction peaks varied from sample to sample. Frequently, certain peaks had too low an intensity to use.

The magnitude of the variation in the calculated parameters due to the use of different sets of peaks was investigated using the published data for pure titanium. The data was divided into three sets, one consisting of the 10 lowest angle peaks, a second consisting of the 10 highest angle peaks, and the third, a random group of 10 peaks. Each data set was processed using the ANG program and the results are included in Table D1. It was found that the difference in calculated parameters, in terms of cell volume, was found to be 0.0037\AA^3 , or an error of $\pm 0.05\%$. This error is approximately the same magnitude as that introduced by random errors in peak position determination. This error is again within the scatter due to using data from different sources or that due to incorrect compensation for systematic errors.

The above comparisons of data from different sources processed both with and without the use of an extrapolation

parameter show a variation which is, in the worst case, no greater than that seen in the published data for pure titanium, Table 5.4. Published values for pure titanium lattice parameters vary from 2.943Å to 2.953Å for "a", and from 4.679Å to 4.729Å for "c". Even in studies carefully designed to determine the most accurate lattice parameters possible (C), variations in the data are on the order of 0.002Å in "a" and 0.005Å in c, or 0.07% and 0.10%, respectively. Based on this comparison and the above analysis of the errors involved in the lattice parameter measurements, the accuracy of these measurements is estimated at $\pm 0.05\%$ of the individual parameters and $\pm 0.10\%$ of the calculated cell volumes.

D.3 Dilatometry Errors

The determination of the lattice incompatibility in this investigation used radial dilatometry to determine the size of the beta phase cooled to below the equilibrium transformation start temperature. Figures 5.49-5.51 showed that the dilatometric curves for all of the alloys could be approximated by the same curve and that this average curve agreed closely with previously published results. Because of this, the conclusion can be made that the error in the measured size of the supercooled beta lattice is not overly affected by dilatometric errors. However, these errors

apply to a certain extent to the measurement of transformation temperatures where other investigators (H) have found that they can be significant, so they are briefly listed below.

D.3.1 Misalignment of the Dilatometer

If the dilatometer is not at the sample center, it will record the dilation of material at a lower temperature, where the sample size does not change as rapidly with temperature. Also, if the dilatometer is not perpendicular to the sample, it will record the true dilation divided by the cosine of the misalignment angle. These errors vary from run to run, each time the dilatometer is re-installed on a sample.

D.3.2 Differential Barrelling

Several sample configurations were used in this investigation. The ability of these samples to overcome load on the ram imposed by the o-ring seals around the ram and expand longitudinally varied. Samples with greater hot strength and a larger cross sectional area were able to expand more longitudinally and thus had lower apparent thermal expansion coefficients. All other factors being equal, the longitudinal thermal profile is flatter for a longer sample, hence the overall expansion of the specimen is greater. If the specimen was not able to overcome the o-

ring load, the apparent thermal expansion coefficient was higher. These errors vary primarily from alloy to alloy and between different sample geometries.

D.3.3 Fixturing Errors

The largest of these are drift due to expansion of the fixturing and creep into the sample due to the clamping force of the dilatometer spring. These vary from run to run as well as from one alloy to another.

D.4 Transformation Temperature Measurements

The dilatometer errors, particularly misalignment of the dilatometer, also apply to the measurement of transformation temperatures. It was assumed that, in Gleeble testing, 1/3 of the specimen free span is at a temperature greater than 90% of the peak temperature. A common sample configuration used in the CCT diagram development was shown in Figure 4.1. This sample configuration results in a "90%" zone of approximately 8 mm. In some cases, samples were used where the "90%" zone was only approximately 4 mm. If it is further assumed that the longitudinal thermal gradient is linear within the "90%" zone, at 800°C, these two sample configurations result in thermal gradients of 20°C/mm and 40°C/mm respectively. Qualitatively, it was determined that the dilatometer can be located at the thermocouple with an accuracy of

approximately 0.5 mm. In the shorter specimens, this corresponds with a potential error of 20°C . It should be noted that the potential errors in measurement of Gleeble specimen temperatures are most significant in the ductility testing, where the specimen very rarely fails exactly at the thermocouple. For the ductility tests, the accuracy of the reported temperatures is certainly no better than $\pm 20^{\circ}\text{C}$, and probably no better than $\pm 40^{\circ}\text{C}$.

Additional errors involved in the measurement of transformation temperatures result from incorrect calibration and non-linearity of the chart recorder and the accuracy with which it can be read. Qualitatively, the chart recorder can be calibrated to within approximately 5°C if the proper scale is used and the recorder is referenced to a simulated output representing the temperature to be measured. In this investigation, 2000°C was used as full-scale deflection of the chart recorder. With this scale, temperature can be read with an accuracy of approximately $\pm 5^{\circ}\text{C}$.

The largest source of error in the measurement of transformation temperatures is involved in determining exactly where, on the chart recorder trace, the transformation starts and ends. To achieve the highest possible accuracy, the dilatometric measurements should be carefully coordinated with metallographic analysis of

quenched specimens. In this investigation, the measurement of transformation finish temperatures was further complicated by the fact the majority of the samples contained both alpha and beta at room temperature. In the case of Ti-6Al-6V, the "transformation finish" was simply too gradual to measure. In general, the finish temperatures could not be measured as accurately as could the start temperatures. Based on the above analysis and an evaluation of the repeatability of test results, the accuracy of measured transformation temperatures is estimated at $\pm 15^{\circ}\text{C}$ for the transformation start temperatures, and where reported, $\pm 25^{\circ}\text{C}$ for the finish temperatures. It must be pointed out however, that these estimates represent "worst case" values. In most cases, the accuracy of the reported values is probably much better than this.

In terms of the lattice incompatibility measurements, the only effect that an error in transformation temperature measurement will have is in the calculation of the volumetric difference between the supercooled beta and the equilibrium beta. This arises because of the large change in lattice volume with temperature that occurs near the beta transus due to the changing composition of the beta phase, Figure 5.42. As shown in Figure 5.46, this effect is largest for the vanadium containing alloys. As was

discussed, a possible modification of the lattice incompatibility calculation method is to more heavily weight the beta phase. If this is done, the error in beta to beta incompatibility due to incorrect transformation temperatures could be significant.

D.5 Quantitative Metallography

The metallographic quantity used in the lattice incompatibility calculations was the volume percent of the Widmanstatten colony structure. This quantity and the width of the colonies were also used when discussing the microstructural effects on hot ductility, Section 5.3.3. It is estimated that both quantities have an accuracy of +/- 10%. Because the range observed in both cases is very large, it is believed that the accuracy of the reported values could affect the quality of the correlations shown, but not their existence (or lack thereof).